Measurement of $\pi^+\pi^-$ Bound State Lifetime with the DIRAC Spectrometer at CERN

INAUGURALDISSERTATION

zur Erlangung der Würde eines Doktors der Philosophie

vorgelegt der

Philosophisch-Naturwissenschaftlichen Fakultät

der Universität Basel

von

Daniel Goldin

aus California, USA

Basel, 2005

Genehmigt von der Philosophisch-Naturwissenschaftlichen Fakultät
auf Antrag der Herren Professoren:

Prof. Dr. L. Tauscher, Universität Basel
Prof. Dr. L. Nemenov, CERN und JINR (Dubna)

Basel, den 20. Januar 2005

Prof. Dr. M. Tanner,
Dekan

Thesis advisor
Ludwig Tauscher

Author
Daniel Goldin

Abstract

The goal of the DIRAC experiment at CERN is to measure the lifetime of the pionium atom, $A_{2\pi}$, a bound state of a π^+ and π^- meson, through the determination of its breakup probability. The experimental data collection has taken place during several runs between 1999 and 2003. The accumulated results will allow us to determine the $A_{2\pi}$ lifetime with precision of 0.3 fs. Once this value is known, $|a_0 - a_2|$, the isospin 0 and 2 scattering lengths difference, will be determined unambiguously. On the theoretical side, the value of pionium lifetime has been obtained with high precision by the Chiral Perturbation Theory (ChPT), yielding 2.9 ± 0.1 fs and $|a_0 - a_2|$ difference yielding $0.265 \pm 0.004\,[m_\pi^{-1}]$. Our experimental approach is model-independent and, as such, will provide a crucial cross-check of these results.

In this thesis we will analyze the data taken during 2002 and 2003 runs. For these run periods the dual target method will be used for the first time to determine the value of pionium lifetime taking into account statistical and systematic uncertainties.

Contents

Acknowledgments

I gratefully acknowledge the great deal of support and help I got from the Basel University DIRAC team: Angela Benelli, Panos Kokkas, Cibrán Santamarina, Christian Schütz and Sotiris Vlachos. I have greatly benefited from the discussions I had with Valery Brekhovskikh, Leonid Nemenov, Jürg Schacher and Valery Yazkov. Special thanks go to my thesis adviser, Ludwig Tauscher, for the guidance received while working on this thesis and the vast amount of physics knowledge imparted to me during the years of working together. I am very grateful for the support I received from my parents while being away from home.

Chapter 1

Introduction

Under the experimental conditions of the DIRAC experiment, a 24 (20) GeV proton beam impinges on a thin target (or several layers of thin target foils) of the overall thickness of the order of 100 μm. Proton-target nuclei collisions may create pions through direct production and through decays of short (ρ, ω, ...) and long-lived secondaries, such as η's, K_s^0's, Λ's,.... The first two production modes may result in coherent pion pairs, whose final state interaction cross-section is enhanced by the Coulomb interaction. While most of these pairs, known as *Coulomb pairs*, are not bound, a small fraction may form a bound state, known as the *pionium atom*.

Created with an average γ of approximately 17, pionium migrates a distance of 15 μm or more encountering around 100,000 target atoms along its path. An individual pionium atom can evolve according to three different scenarios. The first one, manifestly independent of the interaction with the target material, is the *annihilation* into $\pi^0\pi^0$ with a branching ratio of 99.6%.[1] This process is mediated by the strong force. The rest of the processes are due to pionium-target atom interactions: the first one is the *excitation* (*de-excitation*) to a higher (lower) bound state, and the second is the ionization, or *breakup*. These interactions are electromagnetic.

The probabilities of annihilation, (de-)excitation (P_{dsc}) and breakup thus constitute a "complete set" of transformations for the atom, whose evolution at any moment

[1]The other decay process into $\gamma\gamma$ is negligibly small, taking up the remaining 0.4%.

in time is then governed by

$$P_{dsc} + P_{anh} + P_{br} = 1.$$

The goal of our experiment is to measure the probability of pionium *breakup*, P_{br}, or, more exactly, to measure the number of dissociated atoms from which the breakup probability is extracted. Pionium lifetime, on the other hand, is determined by the *annihilation* probability P_{anh}, being inversely proportional to it. By exploiting the "completeness" relationship above, the breakup probability can be linked to pionium lifetime for a particular choice of target. Since several target materials and thicknesses have been used throughout data taking, several values of breakup probabilities will allow us to find the value of lifetime with better precision.

Chapter 2

Theoretical Background

The theory of Quantum Chromodynamics (QCD) is the primary theory describing strong interactions. It is essentially a perturbation theory developed in analogy to QED. However, due to large values of the coupling constant and the non-Abelian nature of strong interactions, the standard QCD encounters difficulties in the low energy regime. The two most widely accepted approaches developed to remedy this problem are the lattice QCD and the Chiral Perturbation Theory (ChPT). Of the two, ChPT provides the most precise predictions by forgoing the quark and gluon degrees of freedom in favor of composite hadron interactions; hence, its results will be emphasized in this thesis.

2.1 Pion-Pion Scattering

We begin by writing the general two-body T-matrix (Fig. 2.1):

$$T_{ab;cd} = A(s,t,u)\delta_{ab}\delta_{cd} + A(t,s,u)\delta_{ac}\delta_{bd} + A(u,t,s)\delta_{ad}\delta_{bc}, \tag{2.1}$$

where $A(s,t,u), ...$ are the scattering amplitudes expressed in terms of the Mandelstam variables. In the SU(2) group representation pions constitute an isospin 1 triplet. Taking into account the two possible isospin combinations, the process $\pi^+\pi^- \to \pi^0\pi^0$ can then be represented by:

$$\left|\pi^+\pi^-\right\rangle + \left|\pi^-\pi^+\right\rangle \to \left|\pi^0\pi^0\right\rangle \tag{2.2}$$

With the aid of Clebsch-Gordan coefficients the T-matrix becomes:

$$\begin{aligned} \tfrac{1}{\sqrt{2}}\left[\langle\pi^0\pi^0\,|T|\,\pi^+\pi^-\rangle + \langle\pi^0\pi^0\,|T|\,\pi^-\pi^+\rangle\right] &= \tfrac{1}{3}\langle 2,0\,|T|\,2,0\rangle - \tfrac{1}{3}\langle 0,0\,|T|\,0,0\rangle \\ &\equiv \tfrac{1}{3}T^2 - \tfrac{1}{3}T^0 \end{aligned} \tag{2.3}$$

The isospin amplitudes T^2 and T^0 are found by applying projection operators to Eq. 2.1 to yield [1]:

$$T^0 = 3A(s,t,u) + A(t,s,u) + A(u,t,s) \tag{2.4}$$

$$T^2 = A(t,s,u) + A(u,t,s) \tag{2.5}$$

Using these with Eq. 2.3, one gets:

$$\langle T\rangle = \frac{1}{3}T^2 - \frac{1}{3}T^0 = -A(s,t,u) \tag{2.6}$$

The T-matrix and the resulting scattering length differences may be determined experimentally, as will be accomplished by the DIRAC experiment. Theoretically, they may be derived using the Chiral Perturbation theory through the explicit calculation of $A(s,t,u)$. The following section is a rough outline of the theoretical steps leading to this result.

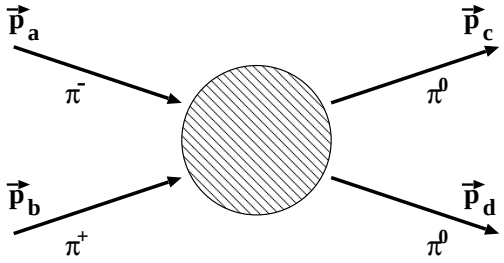

Fig. 2.1: $\pi^+\pi^-$ scattering diagram

2.2 The Chiral Perturbation Theory and Scattering Lengths

Chiral Perturbation Theory (ChPT) is an effective theory in a sense that it operates with pion fields directly, as opposed to the quark and gluon degrees of freedom.

With the two representations being equivalent, one may transform the fundamental degrees of freedom, represented by quarks and gluons, into the experimental ones, represented by pions. First, we define a pion field operator [1]:

$$U = \exp\left(i\vec{\tau}\cdot\vec{\pi}(x)/F_\pi\right), \tag{2.7}$$

where $\vec{\tau}$ are Pauli matrices, $\vec{\pi}(x)$ is the pion field and F_π is the pion decay constant, equal to 92.4 MeV. In the matrix representation the $\vec{\tau}\cdot\vec{\pi}$ term becomes:

$$\vec{\tau}\cdot\vec{\pi} = \begin{pmatrix} \pi^0 & \sqrt{2}\pi^+ \\ \sqrt{2}\pi^- & -\pi^0 \end{pmatrix} \tag{2.8}$$

With the chiral transformations defined as:

$$\psi_L \to L\psi_L \tag{2.9}$$

$$\psi_R \to R\psi_R, \tag{2.10}$$

the chiral symmetry demands that the field operator U obey the relationship

$$U \to LUR^\dagger. \tag{2.11}$$

Thus, to preserve the chiral invariance the kinematic part of the effective Lagrangian needs to be constructed exclusively with terms containing $U^\dagger U$, i.e. [2]:

$$\mathrm{Tr}[\partial_\mu U^\dagger \partial^\mu U], \quad \mathrm{Tr}[\partial_\mu U^\dagger \partial^\mu U]\,\mathrm{Tr}[\partial_\mu U^\dagger \partial^\mu U], \quad \mathrm{Tr}[(\partial_\mu U^\dagger \partial^\mu U)^2]. \tag{2.12}$$

In an abbreviated form, the effective Lagrangian can then be written as:

$$\mathcal{L}_{eff} = \mathcal{L}_2 + \mathcal{L}_4 + \mathcal{L}_6..., \tag{2.13}$$

where subscripts 2, 4, 6,... correspond to the orders of the momentum and quark mass expansion. Since it is the process of pion-pion scattering that interests us, the lowest order term

$$\mathcal{L}_2 = \frac{F_\pi^2}{4}\mathrm{Tr}[\partial_\mu U^\dagger \partial^\mu U] \tag{2.14}$$

needs to be expanded to at least the fourth order in pion fields. Using Eq. 2.7, we obtain:

$$\mathcal{L}_2 = \frac{1}{2}\partial_\mu\vec{\pi}\cdot\partial^\mu\vec{\pi} + \frac{1}{6F_\pi^2}\left[(\vec{\pi}\cdot\partial_\mu\vec{\pi})^2 - (\vec{\pi}\cdot\vec{\pi})(\partial_\mu\vec{\pi}\cdot\partial^\mu\vec{\pi})\right] + \mathcal{O}(\pi^6) \tag{2.15}$$

Expression 2.15, as it stands, describes the interactions of massless pions. However, nature indicates that the pions are, in fact, massive. To take this into account symmetry breaking terms of the form $\sim \mathrm{Tr}(U^\dagger + U)$, e.g. [2]:

$$\mathrm{Tr}(U^\dagger + U), \quad \mathrm{Tr}[\partial_\mu U^\dagger \partial^\mu U]\,\mathrm{Tr}(U^\dagger + U), ... \tag{2.16}$$

need to be introduced. The combination $U^\dagger + U$ *explicitly* violates the symmetry transformation (2.11). This and the rest of the combinations in the expression are the *perturbative*, symmetry-breaking terms that give the Chiral Perturbation theory its name. To the lowest order in symmetry breaking then:

$$\delta\mathcal{L}_{\chi SB} = \frac{F_\pi^2 M_\pi^2}{4}\mathrm{Tr}(U^\dagger + U) \simeq \text{const.} - \tfrac{1}{2}M_\pi^2(\vec{\pi}\cdot\vec{\pi}) + \frac{M_\pi^2}{24F_\pi^2}(\vec{\pi}\cdot\vec{\pi})^2, \tag{2.17}$$

where here, as throughout the text, M_π refers to the charged pion mass. Combining this with the kinematic term of Eq. 2.15 (and omitting the irrelevant constant term), the effective Lagrangian for pion-pion scattering becomes:

$$\begin{aligned}\mathcal{L}_2 &= \tfrac{F_\pi^2}{4}\mathrm{Tr}[\partial_\mu U^\dagger \partial^\mu U] + \tfrac{F_\pi^2 M_\pi^2}{4}\mathrm{Tr}(U^\dagger + U) \\ &= \left\{\tfrac{1}{2}\partial_\mu\vec{\pi}\cdot\partial^\mu\vec{\pi} - \tfrac{1}{2}M_\pi^2\vec{\pi}\cdot\vec{\pi}\right\} + \left\{\tfrac{1}{6F_\pi^2}\left[(\vec{\pi}\cdot\partial_\mu\vec{\pi})^2 - (\vec{\pi}\cdot\vec{\pi})(\partial_\mu\vec{\pi}\cdot\partial^\mu\vec{\pi})\right]\right. \\ &\quad \left. + \tfrac{M_\pi^2}{24F_\pi^2}(\vec{\pi}\cdot\vec{\pi})^2\right\}\end{aligned} \tag{2.18}$$

The term between the second pair of braces is the pion-pion interaction part of the Lagrangian. Using it one obtains the T-matrix:[1]

$$T_{ab;cd} = \frac{s - M_\pi^2}{F_\pi^2}\delta_{ab}\delta_{cd} + \frac{t - M_\pi^2}{F_\pi^2}\delta_{ac}\delta_{bd} + \frac{u - M_\pi^2}{F_\pi^2}\delta_{ad}\delta_{bc}, \tag{2.19}$$

The primary decay channel of $A_{2\pi}$ is the annihilation into two neutral pions: $\pi^+\pi^- \to \pi^0\pi^0$. The branching ratio for this process was found to be 99.6%. The next allowed decay mode $\pi^+\pi^- \to \gamma\gamma$ has a branching fraction of only 0.4% and, due to its small magnitude, is neglected in the final lifetime determination. Using the result of Eq. 2.6 for the s-channel of this process, one gets:

$$T(\pi^+\pi^- \to \pi^0\pi^0) = -A(s,t,u) = -\frac{s - M_\pi^2}{F_\pi^2}\delta_{ab}\delta_{cd} \tag{2.20}$$

[1]Following the ChPT convention, the T-matrices and the scattering lengths found throughout the text will be expressed in units of inverse *charged* pion mass, m_π^{-1}. For example, Eq.2.19 can be written explicitly as: $T_{ab;cd} = \frac{1}{M_\pi}\left[\frac{s-M_\pi^2}{F_\pi^2}\delta_{ab}\delta_{cd} + \frac{t-M_\pi^2}{F_\pi^2}\delta_{ac}\delta_{bd} + \frac{u-M_\pi^2}{F_\pi^2}\delta_{ad}\delta_{bc}\right]$ and Eq. 2.25 as $a_0^0 - a_0^2 = 3\langle T\rangle = \frac{9M_\pi}{32\pi F_\pi^2}$, with both formulas now expressed in natural units.

The $T_l^I(s)$ matrix is complex, but in the low energy regime just its real part may be considered and expanded in powers of relative momenta Q:

$$\mathcal{R}e[T_l^I(s)] = Q^{2l}(a_l^I + Q^2 b_l^I + ...) \tag{2.21}$$

The *scattering lengths* are then defined as the coefficients in the power expansion of the T-matrix in Q, and, physically, they describe the range of the strong interaction. If one reverts to Mandelstam variables *s, t, u*, the two lowest order *on-shell* scattering amplitudes for the isospin eigenstates and $l = 0$ become[2] [3]:

$$T^0 = a_0^0 + b_0^0(s/4M_\pi^2 - 1) \tag{2.22}$$

$$T^2 = a_0^2 + b_0^2(s/4M_\pi^2 - 1) \tag{2.23}$$

Thus the T-matrix of Eq. 2.6 yields to the first order of relative momenta:

$$\langle T \rangle = \frac{1}{3}(a_0^0 - a_0^2) \tag{2.24}$$

With Eq. 2.20 it is possible to obtain the values of the scattering length difference to the first order of the ChPT, as was done in the pioneering work by Weinberg in 1966 [4]:

$$a_0^0 - a_0^2 = 3\langle T \rangle = \frac{9M_\pi^2}{32\pi F_\pi^2} \tag{2.25}$$

The individual tree-level scattering lengths are then found to be:

$$a_0^0 = \frac{7M_\pi^2}{32\pi F_\pi^2} \qquad a_0^2 = -\frac{M_\pi^2}{16\pi F_\pi^2} \tag{2.26}$$

It should be noted that the pion mass parameter M_π in the expressions above gives a direct measure of both explicit and spontaneous breaking of chiral symmetry. This is the parameter that gives the Goldstone bosons (pions in the SU(2)×SU(2) ChPT) their mass through [5]:

$$M_\pi^2 \simeq \frac{1}{F_\pi^2}(m_u + m_d)\left|\langle 0\left|\overline{u}u\right|0\rangle\right|, \tag{2.27}$$

where we have shown only the first term of the expansion of M_π^2 in powers of $(m_u + m_d)$. The expression above explicitly exhibits the link between the quark and the pion

[2] The invariant and partial wave amplitudes are related through the standard expansion: $T^I(s,t,u) = \sum_l (2l+1)P_l(\cos\theta)T_l^I(s,t,u)$.

degrees of freedom. Here m_u (m_d) refers to an up (down) quark mass and the term $(m_u + m_d)$ points to the *explicit* symmetry breaking (cf. Eq. 2.17), whereas the vacuum expectation value $|\langle 0\,|\overline{u}u|\,0\rangle|$, known as the *chiral condensate*, is a signature of the *spontaneous* symmetry breakdown.

With the inclusion of perturbative corrections up to two loops, the scattering length difference (Eq. 2.25) becomes [6][7]:

$$a_0^0 - a_0^2 = 0.265 \pm 0.004\,[m_\pi^{-1}] \tag{2.28}$$

with[3]

$$a_0^0 = 0.220 \pm 0.005\,[m_\pi^{-1}] \qquad a_0^2 = -0.0444 \pm 0.0010\,[m_\pi^{-1}]. \tag{2.29}$$

The goal of DIRAC is to find the value of $|a_0^0 - a_0^2|$ experimentally and in a *model-independent way* with 5% precision.

2.3 Pionium Lifetime

In the previous section we briefly outlined how the pion-pion scattering lengths are derived from the Chiral Perturbation theory; in this section we show how they can be found through the pionium lifetime measurement. Since its decay width of $A_{2\pi}$ of ~ 0.2 eV is much smaller than its binding energy of $\sim 2 \times 10^3$ eV, the non-relativistic approach to calculate its wavefunction may be used. The Schrödinger equation for the combined potential is given by

$$(K + C + V)\Psi = E\Psi, \tag{2.30}$$

where K is the kinetic energy operator, C is the Coulomb potential and V is the potential due to strong interaction between the pions.

The probability density of the Coulomb part of the equation, $(K + C)\Psi = E\Psi$, has the standard form:

$$|\Psi_n(0)|^2 = \frac{p_B^3}{\pi n^3}, \tag{2.31}$$

[3] In standard units of length the theoretical prediction of the scattering lengths difference corresponds to 0.375 ± 0.006 fm.

where p_B is the Bohr momentum

$$p_B = \alpha M_\pi / 2 \tag{2.32}$$

expressed in terms of the fine structure constant α and the charged pion mass M_π.

Next we consider the strong part of the interaction. If one replaces $\Psi_n(0)$ with the notation Ψ^0, the complete solution of Eq. 2.30 is [8]:

$$\begin{aligned} \Psi &= \Psi^0 + (1 - P_0)\Psi \\ &= \left[1 + \tfrac{1}{E-K-C-(1-P_0)V}(1 - P_0)V\right]\Psi^0 \\ &\equiv R\Psi^0, \end{aligned} \tag{2.33}$$

where P_0 is a projection operator onto the state Ψ^0. The orbital energy shift of the $\pi^+\pi^-$ system due to the strong potential is:

$$\delta E = E - E_0 = \left\langle \Psi^0 | V R \Psi^0 \right\rangle \tag{2.34}$$

The matrix element describing forward scattering of pions (neglecting Coulomb effects) is

$$T_{00} \equiv \langle \chi_0 | T(E_+) \chi_0 \rangle = \langle \chi_0 | [\, V + V \frac{1}{E_+ - K - V + i\epsilon} V \,] \chi_0 \rangle \,, \tag{2.35}$$

where χ_0 represents the plane wave state corresponding to the relative motion of the π^+ and π^- and E_+ is the positive energy of one of the pions. Taking into account that the phase space element Ω is large for our case and setting energy E_+ to 0 in order to be able to operate with the conventional definition of the scattering lengths, one may obtain the energy level shift by considering only the real part of Eq. 2.35. Eq. 2.35 then approximates Eq. 2.34 as:

$$\delta E = \mathrm{Re} \left\langle \Psi^0 | R(0) \Psi^0 \right\rangle . \tag{2.36}$$

Since the strong interaction has a very short range, the Coulomb wavefunction Ψ^0 assumes the value at the origin and, hence, can be factorized from Eq. 2.36. Then:

$$\delta E = \left| \Psi^0(0) \right|^2 \Omega \, \mathrm{Re} \left\langle \chi_0 | R(0) \chi_0 \right\rangle . \tag{2.37}$$

Relating the $\langle \chi_0 | R(0) \chi_0 \rangle$ to the complex expression for scattering lengths $a(\pi)$ yields the value of the energy shift:

$$\delta E = -(4\pi / M_\pi) |\Psi^0(0)|^2 a(\pi). \tag{2.38}$$

Making use of the standard relationship between the decay width and the energy shift $\Gamma = -\mathrm{Im}[\delta E] \propto \mathrm{Im}[a(\pi)]$, to the lowest order the Chiral Perturbation calculation gives the following expression of the $A_{2\pi}$ *total* decay width [9]:

$$\Gamma_{\pi^0\pi^0} = 1/\tau_{A_{2\pi}} = \sum_{n=1}^{\infty} \frac{16\pi}{9}\alpha^3 \frac{p^*}{M_\pi}(a_0^0 - a_0^2)^2 \left|\Psi_n(0)\right|^2 = \sum_{n=1}^{\infty} \frac{2}{9n^3} p^*(a_0^0 - a_0^2)^2, \quad (2.39)$$

where

$$p^* = \sqrt{M_\pi^2 - M_{\pi^0}^2 - 1/4(M_\pi^2\alpha^2/n^2)} \quad (2.40)$$

and where we have reverted from $\Psi^0(0)$ to the $\Psi_n(0)$ notation.

$A_{2\pi}$ lifetime depends strongly on the energy level the atom was in before its annihilation, since $\tau_n \sim n^3$ for an ns state. Annihilation strongly favors low-n states and only occurs for the states with even orbital quantum number l, since the odd-l state decays into a pair of identical bosons are forbidden by conservation of parity.

Eq. 2.39 takes into account only the leading and next-to-leading order terms. Applying the Chiral Perturbation theory methods Gasser *et al.* [10] have taken into account higher order corrections and obtained the $1s$ *state lifetime* given by (cf. Eq. 2.39):

$$\Gamma_{\pi^0\pi^0} = \frac{2}{9}\alpha^3 p^*_{n=1}(a_0^0 - a_0^2)^2(1 + \delta_\Gamma), \quad (2.41)$$

with[4] $\delta_\Gamma = (5.8 \pm 1.2) \times 10^{-2}$. Combined with Eq. 2.29 $1s$ state lifetime is:

$$\tau_{1s} = 2.9 \pm 0.1\,\mathrm{fs} \quad (2.42)$$

This calculated value will be confronted with our experimental measurement.

2.4 Evolution of Pionium Atom Inside the Target

The atomic pair double differential production cross-section in terms of center-of-mass momentum P and relative momentum Q is given by:

$$\frac{d^2\sigma^A_{nlm}}{d\vec{P}\,d\vec{Q}} = (2\pi)^3 |\psi_{nlm}(0)|^2 \frac{E}{M} \lim_{\vec{Q}\to 0}\left(\frac{d^2\sigma^0_s}{d\vec{P}\,d\vec{Q}}\right), \quad (2.43)$$

[4] To a certain degree, the inclusion of δ_Γ undermines the claim that the $|a_0^0 - a_0^2|$ difference may be obtained from the lifetime in a model-independent way; however, this correction amounts to a 6% change in the decay width of Eq. 2.39.

where $\psi_{nlm}(0)$ refers to the wavefunction of the pionic atom (with the relative momentum $Q = 0$), E and M to the energy and mass of the $\pi^+\pi^-$ system, and $d^2\sigma_s^0/d\vec{P}\,d\vec{Q}$ to the double inclusive cross-section for pion production from the short-lived sources[5] (the contribution from the long-lived decays was neglected as they contribute to the atomic production only at the level of 1%). For the purposes of our experiment the exact knowledge of the strong production mechanism ($d^2\sigma_s^0/d\vec{P}\,d\vec{Q}$ term) is not required. Specifically, the atomic evolution in the Monte Carlo simulation can begin directly from the quantum eigenstate $\psi_{nlm}(0)$.

. As discussed in Chapter 1, once created, an $A_{2\pi}$ may evolve in three different

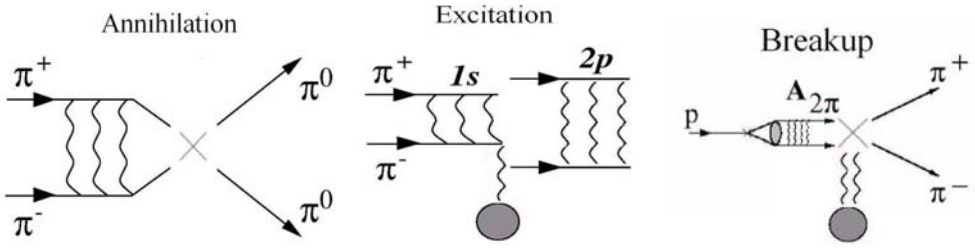

Fig. 2.2: Three evolution scenarios of the $A_{2\pi}$ inside the target.

ways: it may annihilate, be (de-)excited to a higher (lower) n-state or break up (Fig. 2.2). These evolution scenarios have been modeled in [11]-[17] using relativistic atomic transport equation and Glauber and Born scattering cross-sections. An atom was propagated spacewise through a series of discrete steps, where at the end of each interval the atom's evolution is decided based on the following expressions for the probabilities per unit length:

$$P_{anh} = \frac{1}{\lambda_{nlm}^{anh}} = \begin{cases} \frac{2M_\pi}{p_\pi n^3 \tau_{1s}}, & l = 0 \\ 0 & l = 1, 2, ... \end{cases} \tag{2.44}$$

$$P_{dsc} = \frac{\sigma_{nlm}^{n'l'm'} \rho N_0}{A} \tag{2.45}$$

$$P_{br} = \frac{\sigma_{nlm}^{\infty} \rho N_0}{A} \tag{2.46}$$

[5]Short and long-lived sources are to be discussed in more detail in the next section.

where $\sigma_{nlm}^{n'l'm'}$ and σ_{nlm}^{∞} are the excitation (de-excitation) and breakup cross-sections, respectively, ρ is the target density, A the atomic number of the target material, N_0 is the Avogadro's number, λ_{nlm}^{anh} is the mean free path before annihilation, and, finally, p_π is the atomic lab momentum. The four probabilities per unit length[6] are

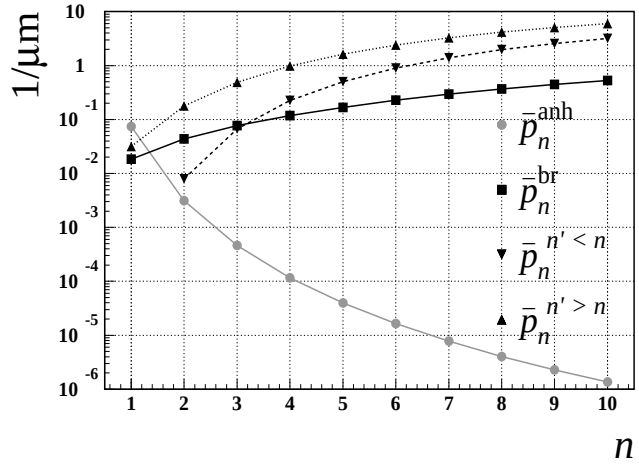

Fig. 2.3: Annihilation $\overline{p}^{anh}$, ionization $\overline{p}^{br}$, excitation $\overline{p}^{n'>n}$ and de-excitation $\overline{p}^{n'<n}$ probabilities per unit length for the Ni target as a function of atomic energy state n [17].

shown in Fig. 2.3 as a function of the principal quantum number n. According to Fig. 2.3 and as remarked in Ref. [17], the fact that the target thickness is much larger than the mean free path of the atomic pair leads to the pionium suffering many collisions with the atoms of the target resulting in excitations to successively higher n states (upturned triangles on the plot). As the physical size of the atom grows, and with it the interaction cross-section, successive excitations are more likely to result in the eventual breakup of the atom in one of the collisions (squares), with the latter constituting signal events for DIRAC.

In Ref. [17] breakup probability as a function of lifetime – a relationship analogous to the one used in this thesis – has been simulated for a 95 μm Ni target. Two different sets of Born approximations (*Born1* and *Born2* of Fig. 2.4), corresponding single photon exchanges, and the Glauber approximation, which takes into account

[6]The processes of excitation and de-excitation have different probabilities and are considered separately here.

multi-photon exchanges, have been considered. Glauber cross-section approximation, being the most comprehensive one, was chosen in obtaining this function. For this target choice using Glauber approximation, the Chiral Perturbation Theory lifetime prediction of 2.9 fs corresponds to a 45% breakup probability.

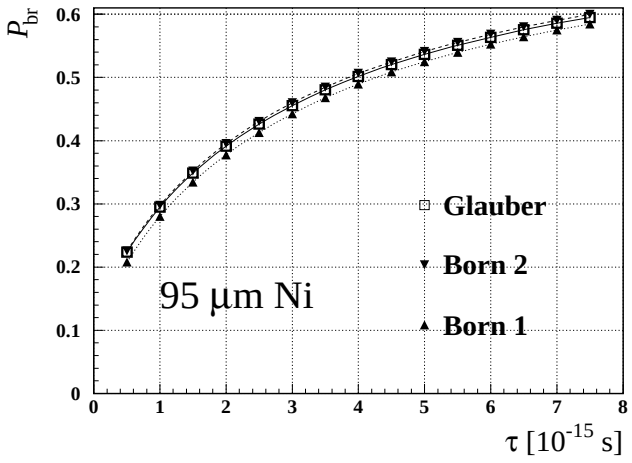

Fig. 2.4: Breakup probability as a function of pionium lifetime with the Born and Glauber approximations for a 95 μm Ni target. Note: The Glauber approximation yields the most accurate results [17].

2.5 Pionium Atoms, Atomic Pairs and Background

In our experiment the background events are treated on the same footing as the signal events, since both are directly involved in the determination of the pionium lifetime (and, thus, the scattering length difference). The experimental approach for the pionium lifetime determination was first proposed by L. Nemenov in 1985 [18]. This method of obtaining the $A_{2\pi}$ lifetime makes use of the relationship between the signal and background. It is used by our experiment to analyze the data obtained with the single layer target, which was in place up to and including the 2001 run. In this thesis we will use an alternative method, first proposed by A. Kuptsov in 2002 [20], which relies on the relationship between the signals from the single foil and multi-foil targets. The present analysis is the first direct application of the procedure.

The signal extraction performed by subtracting the simulated background from the experimental events is common to both methods, so a brief description of the sources of both is warranted here and is found below.

Pion Pair Types	Sources
Atomic pairs	*Direct production and short-lived sources (ρ's, ω's)*
Coulomb pairs	"
Non-Coulomb pairs	*Long-lived sources (η's, Λ's, K^0's)*
Accidentals	*Uncorrelated interactions (e.g., separate proton-target interactions)*

Table 2.1: Pion pairs classified by their origin.

The origins of pion pairs from the long-lived and short-lived decays have been briefly described in the Introduction. Atomic and Coulomb pairs both originate from the short-lived sources with the typical formation range of $r_{form} \sim 1/M_\pi \sim 1 \div 3$ fm. The $A_{2\pi}$'s Bohr radius given in terms of the pion mass and the fine structure constant α is $a_\pi = 2/(M_\pi \alpha) = 387.5$ fm. The binding energy is 2 keV. As mentioned previously, as result of the interaction with the target atoms pionium atoms may dissociate with a certain probability. We call these dissociated pairs **atomic pairs** and their extraction is the goal of the experiment. The rest of the identifiable pairs constitute the background.

The **Coulomb pairs** (CC) are the dominant part of the background events. The Coulomb correlation causes the enhancement of their production cross-section relative to that of the incoherent pairs. Their high production rate is confirmed experimentally

by fitting the background events.

Long-lived decays are one of the two sources of incoherent pion pairs. Neither atomic nor Coulomb pairs are likely to be produced in such interactions. The typical pion pair formation distance in this case is on the order of $r_{form} \sim 1000$ fm. Due to their nature, these pairs of pions are given the name **non-Coulomb** pairs (NC).

The second mode of the incoherent pion pair production is the trivial one, where pion pairs originate from spacewise uncorrelated interactions, such as separate proton-target nuclei collisions. These are called **accidental** pairs (ACC).

To avoid confusion between different pion pair types and their sources we summarize the nomenclature in Table 2.1.

2.6 Production of Background Pairs

Both atomic and Coulomb pairs originate from the same short-lived decays. Thus, we expect their production cross-sections to be quite similar. Indeed, for the CC pairs we have:

$$\frac{d^2\sigma_{CC}}{d\vec{P}\,d\vec{Q}} = A_c(Q)\frac{E}{M}\left(\frac{d^2\sigma_s^0}{d\vec{P}\,d\vec{Q}}\right), \tag{2.47}$$

where

$$A_c(Q) = \frac{2\pi M_\pi \alpha/Q}{1 - \mathrm{e}^{-2\pi M_\pi \alpha/Q}}, \tag{2.48}$$

is the *Coulomb correlation function* for point-like sources, which replaces the atomic wavefunction in Eq. 2.43. This function depends on the relative momentum of the two pions and is simply the ratio of the probability densities of the final (plane wave) and initial wavefunctions, which are the solutions to the Schrödinger equation for the central potential problem [19]. The experimental conditions make this function finite in the low Q region and modify its shape due to the apparatus acceptance and resolution.

As mentioned previously, the non-Coulomb pairs and accidental pairs are formed by incoherent pions. In Chapter 6 we will elaborate on the production mechanisms for these events.

2.7 Experimental Results

Experimentally, the most precise measurement of the scattering lengths has been performed recently by the E865 experiment at Brookhaven Alternating Gradient Synchrotron [22]. A K_{e4} decay branch $K^{\pm} \to \pi^+\pi^- e^{\pm}\nu_e(\overline{\nu}_e)$ was considered. The experiment obtained the $\delta_0^0 - \delta_1^1$ phase shift difference, which, using Roy equation [21] and chiral symmetry constraints, yielded the value of a_0^0:

$$a_0^0 = 0.216 \pm 0.013\,(\text{stat.}) \pm 0.002\,(\text{syst.}) \pm 0.002\,(\text{theor.}). \tag{2.49}$$

Thus, a_0^0 was determined with 6% precision. In its calculation the ChPT predictions had to be relied on (as can be inferred from the presence of the theoretical uncertainty in the result above).

A value of the $\pi\pi$ scattering length a_0^2 was found in a model-dependent way by an experiment performed at TRIUMF, which analyzed the process $\pi^+ p \to \pi^+\pi^+ n$ near the production threshold [23]. Pion data were accumulated for several energy values ranging from 172 MeV to 200 MeV. a_0^2 was found to be:

$$a_0^2 = -0.040 \pm 0.003. \tag{2.50}$$

The value was determined with the 7.5% precision and is in agreement with the ChPT prediction (Eq. 2.29).

To summarize, the experimental data determining the scattering lengths or scattering length difference is sparse. DIRAC's model-independent measurement of $a_0^0 - a_0^2$ should provide a true test of the ChPT predictions. Should this value turn out to be different from the predicted one, the entire ChPT framework may need to be revised.

Chapter 3

DIRAC Experimental Setup

The DIRAC experiment [24] is located on the T8 proton beam line of the CERN's PS complex. The incident protons have the momentum of 24 GeV/c. A fraction of the secondary particles produced as a result of interactions with the target material enter a secondary beam channel inclined 5.8° with respect to the primary beam (Fig. 3.1). The horizontal and vertical acceptance of the channel is ±1°. Secondary particles resulting from collisions between proton beam and a thin target (of the order of 100 μm in thickness) are registered by 3 coordinate detectors: Microstrip Gas Chambers (MSGC), scintillating fiber detector (SFD) and the ionization hodoscope (IH) (Fig. 3.2). Charged secondaries are subsequently separated by the 1.6 Tesla magnet into the positive and negative arms. The downstream detectors in each arm comprise vertical and horizontal hodoscopes (VH and HH), drift chambers (DC), Cherenkov detector (CH), and preshower (PSH) and muon counters (MU).

3.1 Beam Line and Target Station

The proton extraction for the PS beam line is accomplished in a slow extraction mode with the spill duration between 400 and 500 ms [24]. Between 1999, the first period of data taking, and the present time the beam intensity is fixed at several values ranging between $0.6 \cdot 10^{11}$ and $1 \cdot 10^{11}$ protons per spill, with the value of intensity depending on the choice of the target. The beam spot on the target is elliptical

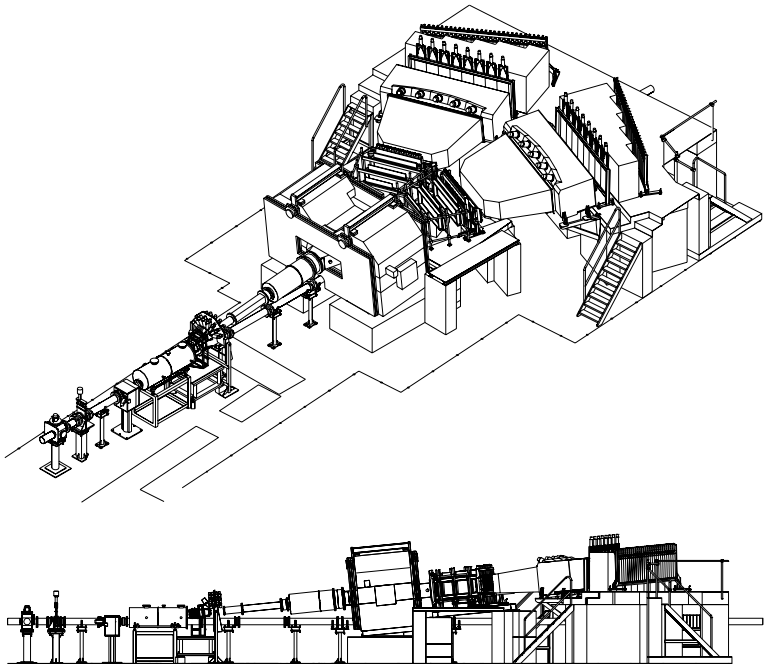

Fig. 3.1: Isometric and side view of the DIRAC experimental setup.

in shape, with dimensions of $1.6 \times 3.2\,\mathrm{mm}$. In the run period between 1999 and 2003 three different target materials with 4 different thicknesses were used: platinum ($28\,\mu$m), nickel (94 and $98\,\mu$m) and titanium ($250\,\mu$m).

Two beam pipes constitute the secondary particle channel upstream of the spectrometer magnet (Fig. 3.2). The first pipe of length of 0.611 m is placed with one of its ends immediately following the target station. The cross-sectional area of this volume was chosen to be large and free of any radiation shielding in order to reduce scattering off the walls of the tube into the main acceptance area of the setup. A 1.5 m gap which follows the first beam pipe contains three upstream detectors: MSGC, SFD and IH. The gap is followed by the collimator and the second beam pipe, 2.7 m long. The collimator consists of stainless steel blocks placed in front of the second beam pipe arranged to form a rectangular aperture. The opening limits the geometrical acceptance of the setup to $\pm 1^\circ$.

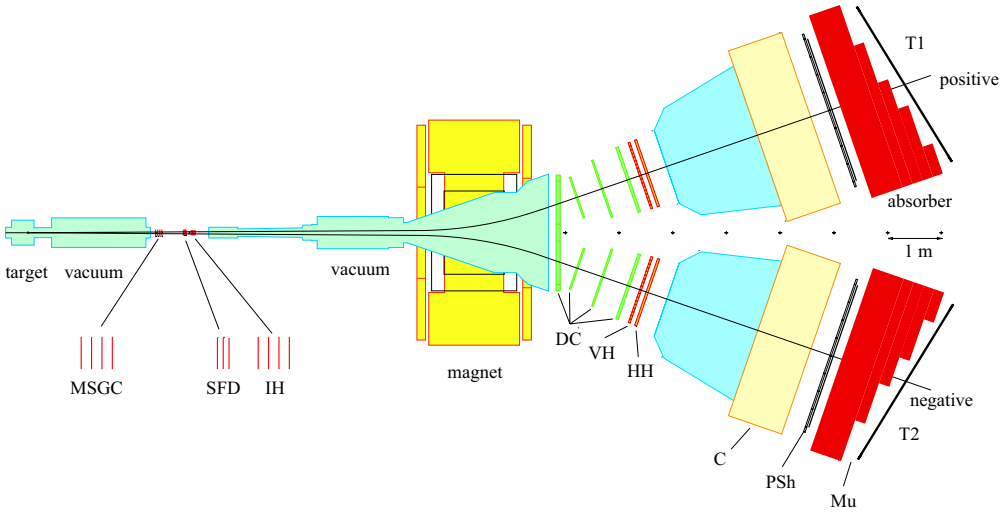

Fig. 3.2: Top view of the setup. Detectors: Microstrip Gas Chambers (MSGC), scintillating fiber detector (SFD), ionization hodoscope (IH), 1.6 Tesla magnet, drift chambers (DC), vertical hodoscopes (VH), horizontal hodoscopes (HH), Cherenkov detectors (C, or CH), preshower detectors (PSH) and muon counters (Mu).

3.2 Upstream Detectors

Three tracking devices, the microstrip gas chambers (MSGC), the scintillating fiber detector (SFD) and the ionization hodoscope (IH), are used to improve the precision of the relative momentum determination by the downstream detectors. Both SFD and MSGC are also essential in providing the coordinates of the effective beam position used in the momentum reconstruction. Additionally, these detectors also aid in distinguishing background particles and particles resulting from decays outside the target. The ADC signals provided by the ionization hodoscope (IH) are used to separate single from double track events. Both SFD and IH are also involved in triggering (see Chapter 3). Below we describe the upstream detectors in more detail.

3.2.1 Microstrip Gas Chambers

MSGC was designed to provide coordinates of double tracks close to their origin in the target. In its function the MSGC is roughly similar to a multiwire proportional chamber: both consist of an array of anodes and cathodes measuring the electrical

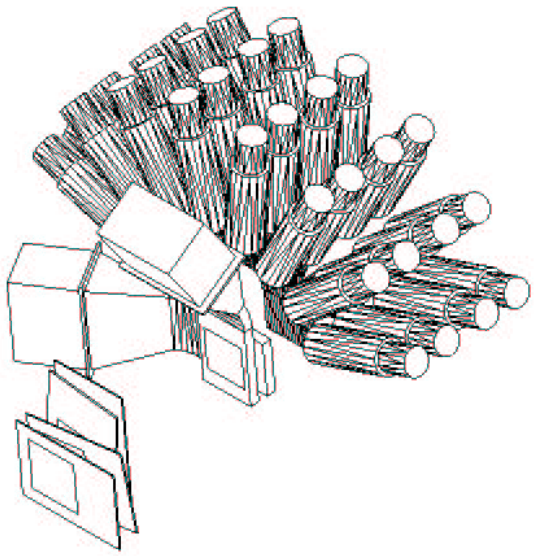

Fig. 3.3: Upstream detectors. From left to right: the microstrip gas chambers (MSGC), scintillating fiber detector (SFD) and ionization hodoscope (IH).

discharge produced by the passage of charged particles through gas. However, unlike the MWPC's anode wires, MSGC utilizes metal strips fixed on a glass substrate by means of photolithography [26]. The alternating anode and cathode strips run parallel to each other, forming two comb-like patterns.

The principle of operation of the device in our experiment is the following. The first signal amplification stage of the detector is the so-called *GEM*, or Gas Electron Multiplier, plate (Fig. 3.4). This plate consists of an insulating foil sandwiched between two thick metal layers [27]. The GEM is perforated by circular holes forming a staggered pattern. The two metal layers are held at high potential difference creating a strong electrostatic field within the holes. An electron produced somewhere in the gas volume will first encounter the electric field produced by the GEM holes and may ionize the atoms of the gas producing an electron avalanche.

The avalanche electrons, in turn, are attracted by the field produced by the positive strips (anode) on the glass substrate. At a sufficiently close distance to it (high field strength) the primary avalanche may start a secondary one. Thus the single electron signal becomes doubly amplified.

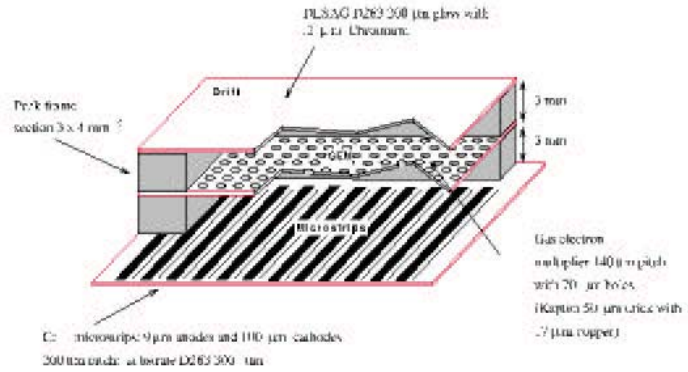

Fig. 3.4: The MSGC detector layout.

Due to the fact that its mobility in the insulating substrate is highly reduced, the resulting cloud of positive ions tends to cluster around a cathode. This accumulation of charge can sometimes result in sparking between adjacent strips. However, due to the double stage amplification inside the MSGC, the cathode-anode voltage can be reduced, thereby significantly reducing the chance of sparking.

The MSGC detector is located at 3.1 m downstream of the target and consists of 4 planes: X, Y, U and V, oriented at 0, 90, 5 and 85 degrees, respectively, relative to the horizontal (X) axis [24]. The function of U and V planes is to resolve the ghost combinations of hits produced by the X and Y planes.

The active area of each plane is 10.24×10.24 mm. The drift plane, which serves as the trigger electrode for a particle originating in the target, is made of Chromium-coated layer of glass of 200 μm thickness. The GEM layer consists of a kapton core of 50 μm thickness clad by 4 μm thick copper layers on both sides. The diameter of GEM's staggered holes is 50 μm and their relative spacing is 140 μm. The microstrips are 9 μm and 100 μm wide and of 200 μm pitch. The following voltages are applied: -3 kV to the drift plate, -410 V to the cathodes, and the anodes are grounded. The gas employed in the detector is a mixture of Ar and DME in the 60/40 proportion. The overall gain of the detector is around 3000.

The MSGC is read out by three motherboards: analog, control and VME. The

signal arriving from an anode strip is sent to a preamplifier channel on the so-called *Analog Pipeline Chip*, or the APC, and stored in an analog capacitor-based pipeline memory. The analog signals coming from the APC's are digitized by the ADC circuitry. The APC's are controlled by the Field Programmable Gate Arrays (FPGA's) located on the control board. Each FPGA controls 4 APC's using the control sequence produced by the VME board. Its second function is to perform the discrimination of the digitized signal and to store the useful signals above the discriminator thresholds. The signals from the VME board are read out during the dead time between the proton spills.

Under normal run conditions the single-track resolution of the MSGC is around 200 μm. When combined with the 3 planes of the SFD, the overall single-track efficiency of 99% is obtained.

3.2.2 The Scintillating Fiber Detector

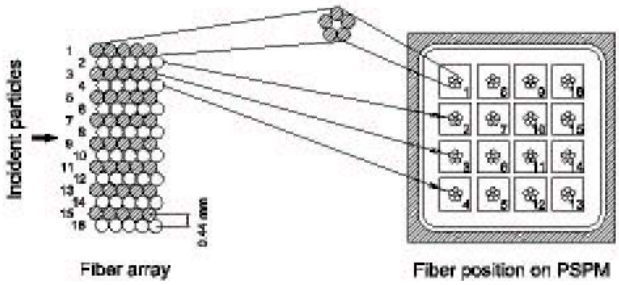

Fig. 3.5: Layout of the Scintillating Fiber Detector (SFD). Each SFD channel (one fiber wide, 5 fibers deep) is attached to to the matrix-type PSPM via clear fiber light guide. Each PSPM contains 16 channels.

The Scintillating Fiber Detector (SFD) is a coordinate detector used in track reconstruction upstream of the magnet. It consists of 3 planes, X, Y and U, rotated 45° relative to the x or y axis. The overall dimensions of the detector are 10.4×10.4 cm. The X and Y planes are composed of 240 fiber channels of 0.44 mm in effective diameter, and the U plane contains 320 channels of 0.43 mm in effective diameter. Each channel is 1 fiber wide and 5 fibers deep, as shown in Fig. 3.5. A bundle

of 5 fibers forming one channel is connected to via a clear fiber light guide to the photomultiplier by means of optical epoxy.

SFD fibers measure from 70 to 150 mm in length and the light guide is about 300 mm long. Due to this relatively short propagation distance[1] and the good insulating characteristics of the cladding material and the epoxy[2], the combined attenuation losses in the fiber channels and the light guide were found to be negligible.

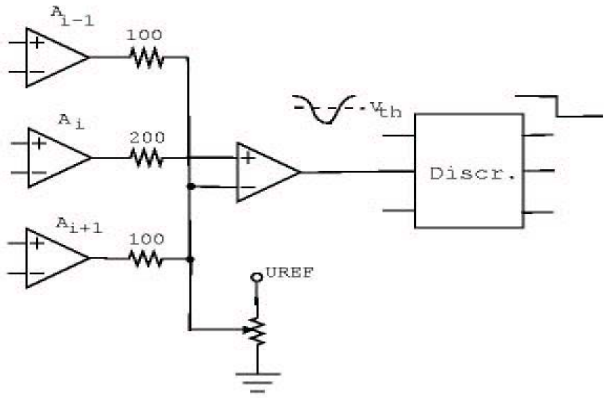

Fig. 3.6: A simplified schematic of one cell of the peak-sensing circuit. The signal from the central channel A_i is compared to the adjacent channels A_{i-1} and A_{i+1}: $2A_i - (A_{i-1} + A_{i+1}) vs. U_{thr}$ [30].

The clear fibers of the light guide are glued directly onto the photocathode of the photomultiplier. The photomultipliers used are 16-channel Hammamatsu H6568 position-sensitive photomultipliers (PSPM's). This particular model has been selected due to its superior technical characteristics, such as the fast rise time of ≈ 0.7 ns and low level of noise of 1-2 noise pulses per second.

The configuration of the PSPM readout has been adapted from the RD-17 experiment at CERN. It consists of the so-called peak-sensing circuit (PSC) [28], which compares the signals from three adjacent channels (Fig. 3.6). The $2A_i - (A_{i-1} + A_{i+1})$ difference is compared to the externally preset threshold value U_{thr}. The discriminator produces 1 or 0 depending on the threshold value.

[1] Attenuation loss is related to the *attenuation length*, defined as the distance for the light intensity to fall to $1/e$ of the original value. For most standard scintillators this length is on the order of 1 m [25].

[2] Light transmission through the epoxy was found to exceed 90% [29].

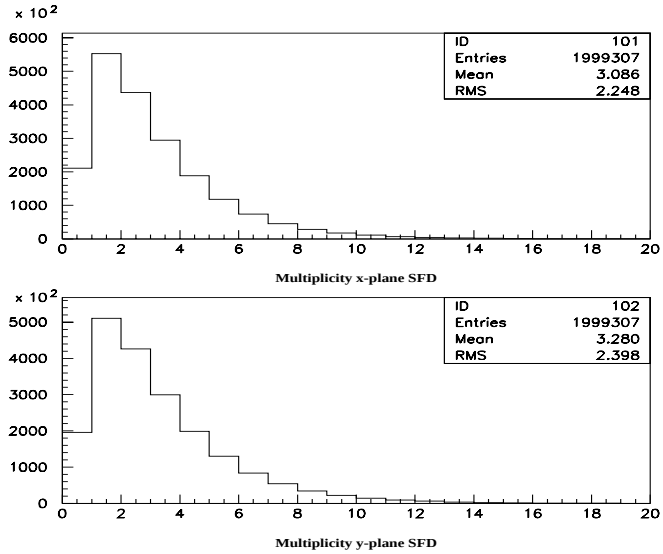

Fig. 3.7: SFD X and Y plane pion multiplicities per event.

The advantages of the peak-sensing circuitry are good cross-talk and noise rejection in the adjacent channels. However, in the case of two adjacent channels registering particle hits, one or both hits may be rejected by the PSC. For the most recent threshold settings, a complete loss of hits when two or one was expected is observed in about 9% of the events. About 2% of cross-talk and noise is found after the action of the PSC (see Appendix A). The time resolution of the SFD, as tested with pion pairs, was found to be 2 ns (Appendix B). In Fig. 3.7 we show pion multiplicities in the X and Y planes of the SFD.

3.2.3 The Ionization Hodoscope

The hits in the SFD detector are used mainly to adjust the upstream part of the tracks found in the drift chambers downstream of the magnet. Additionally, one needs to ensure that for the final selection only the ones originating from the target are taken. An event with two hits belonging to two tracks in one plane of the SFD does not present a serious problem for the tracking algorithm. However, frequently a situation arises when only one hit corresponding to two tracks is found. It may be

caused by either the inefficiency of the SFD when one of the two hits was lost or a simple fact that two particles may have traversed a single SFD channel. In order to determine exactly how many particles crossed the SFD, the ADC information from the ionization hodoscope is used (see Fig. 5.3).

The ionization hodoscope, like the SFD, is a scintillation-type detector. Its overall size is $11 \times 11\, cm^2$ and it consists of 2 X and 2 Y planes arranged in the X-Y-X-Y sequence. Each plane contains 16 plastic slabs, 11 cm long, 7 mm wide and 2 mm thick [31]. The choice of plastic was BC-408 for faster scintillation light response and $30\,\mu$m mylar was used as cladding for each slab to improve optical isolation.

The slab pattern in each X (and Y) plane is staggered relative to each other, covering the $60\,\mu$m interslab gaps due to cladding, which further enhances the acceptance of the detector[3].

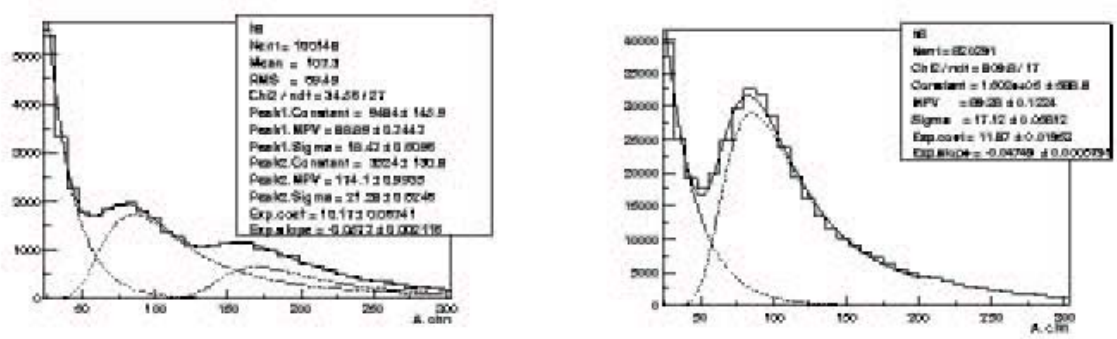

Fig. 3.8: ADC counting rates for electron pairs (left) and pion pairs (right). Single and double ionization peaks may be observed for the case of electrons.

The FEU-85 photomultipliers were chosen to maximize the quantum efficiency, defined as the number of emitted electrons per incident photon. They were placed in optical contact along the side face of the slab, as opposed to the standard end-face readout. Analysis of this readout configuration has shown that the light collection efficiency has been improved by about 50%. Analog pulse height and duration are

[3]The older (1999-2001) version of the IH included only two planes, one X and one Y plane, with 16 slabs each. The acceptance of this configuration was somewhat worse due to 0.5 mm interslab gaps, which were not covered by another pair of planes.

transformed into the ADC and TDC signals by the LeCroy ADC 4300B and TDC 3377, respectively.

The single track resolution tests of the ionization hodoscope have been performed by [31]. Due to the single/double ionization event overlap shown in Fig. 3.8 the double ionization threshold was chosen to keep the contamination of the single ionization events small while keeping as many double ionization events as possible. For this study a threshold corresponding to a 10% loss of doubles and 15% contamination of singles was chosen. With this criterion double ionization in two slabs in each X plane was found to be around 72% and double ionization in a pair of slabs in Y plane is 76%. These two figures determine the efficiency of the IH in the context of our experiment. The same analysis determined the time resolution of the IH to be around 1 ns.

3.3 Magnet and the Downstream Detectors

The spectrometer magnet is followed by the downstream detectors located in the positive and negative arms. The axes of symmetry of both arms are located 19° to the left and right relative to the Z axis. The acceptance area covered by each arm is 11°. Downstream detectors provide information essential in reconstructing the zeroth order tracks offline and are used for online triggering (described in the next chapter). Primary track reconstuction is accomplished in the drift chambers using the information from the vertical and horizontal hodoscopes. Preshower and Cherenkov detectors are used to filter out the unwanted electrons coming from the upstream area. The muon detector is used as a veto to reject muon pairs faking a $\pi^+\pi^-$ signal.

3.3.1 Magnet

MNP21/3 spectrometer magnet separates positive and negative secondaries coming from the upstream area. The dimensions of the magnet's cavity is 0.5 m (height), 1.5 m (width) and 1.1 m (depth). The *bending power* of the magnet, which is proportional to the magnetic field strength and the depth of the magnet's cavity ($\int B \cdot dl$), is in our case 2.2 T·m. The accuracy of the momentum determination dp/p is in the

range from 2.8×10^{-3} to 3.3×10^{-3} depending on the momentum.

3.3.2 Drift Chambers

The drift chamber setup (DC) supplies the information essential for track reconstruction. The setup incorporates 7 modules. The first one (DC1), closest to the magnet, is common to both tracks and consists of 6 chamber planes arranged in the X-Y-W-X-Y-W sequence, with W planes rotated 11.3°. with respect to the x axis [24]. DC2 (X-Y), DC3 (X-Y) and DC4 (X-Y-X-Y) modules are identical in design and are placed in the left and right arms. The respective dimensions of the drift chambers are 0.8×0.4 m^2, 1.12×0.4 m^2, 1.26×0.4 m^2, 0.8×0.4 m^2. The distance between the center of the first Y plane of DC1 and the geometric center of DC4 provides a 1.6 m lever arm. Six measurement points, together with a sufficiently long lever arm, allows us to accurately reconstruct the downstream tracks. Schematic diagram of a

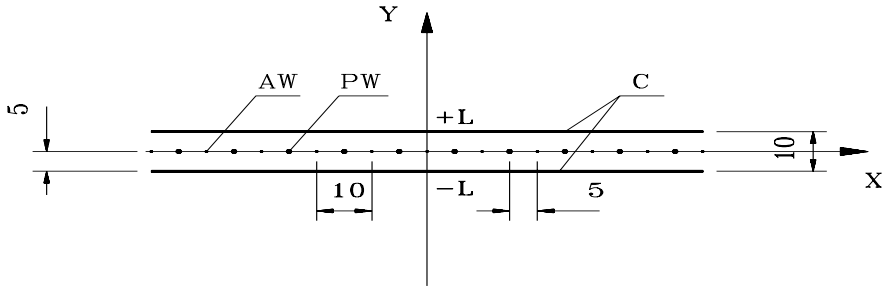

Fig. 3.9: Schematic diagram of a drift plane. Abbreviations: AW: anode wires, PW: potential wires, C: cathode foil. Dimensions are in mm.

drift plane is shown in Fig. 3.9 and Fig. 3.10. A charged particle generates a fast pulse in the vertical hodoscope defining a reference time t_0 for the TDC counters. A particle ionizes the gas mixture, $\mathrm{Ar}(\sim 50\%) + \mathrm{C_4H_{10}}(\sim 50\%) + \mathrm{H_2O}(\sim 0.5\%)$, and the electrons start drifting towards the anode wire. If the electron drift time is Δt, then the current position of the particle in the drift chamber is given by

$$x = \int_{t_0}^{t_0+\Delta t} u(t)dt,$$

where $u(t)$ is the drift velocity. A histogram of the drift time spectrum (proportional to $u(t)$) and its integral (proportional to the particle position x) in one of the X planes

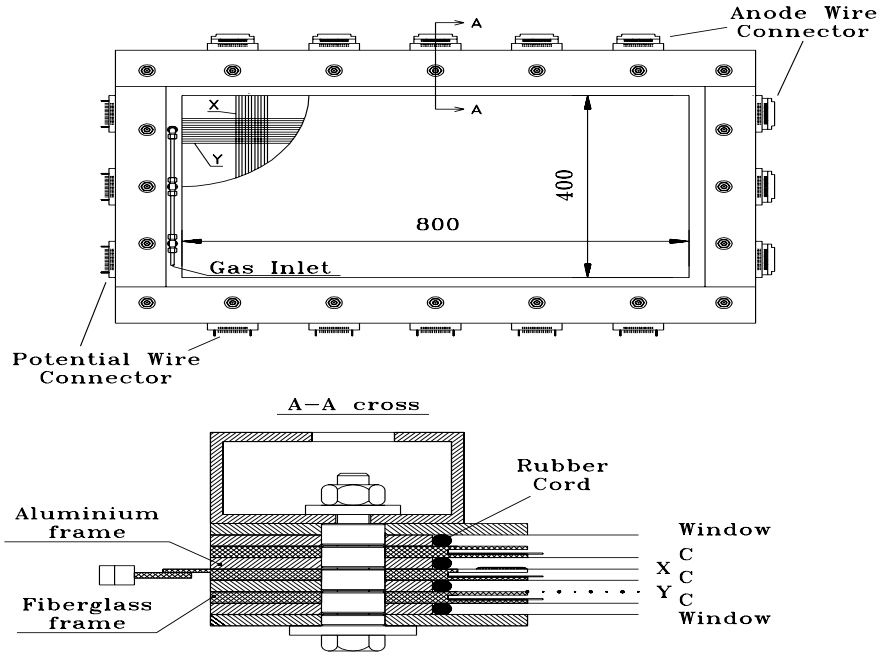

Fig. 3.10: Top: drift chamber design (top). Nomenclature bottom: X - X plane, Y - Y plane, C - cathode foils.

is shown in Fig. 3.11.

Drift chamber time information is read out by time-to-digital converters (TDCs) mounted directly on the DC frames simplifying the hardware design and reducing electronic noise due to cabling [32][33]. The TDC boards are connected to the Drift Chamber Processor (DCP) and the VME buffer memory. Depending on the DCP decision (T4 trigger, described in Chapter 3) an event is either accepted or discarded. In the former case the event is kept and transfered to the VME buffer.

The overall characteristics of the drift chambers are: space resolution of the order of 90 μm and tracking efficiency is 99%, with the 1% inefficiency due to missing signals in one of the drift planes.

3.3.3 Vertical Hodoscope

Since pion pairs constituting the signal and prompt background are characterized by very small time differences, $\Delta t = [-0.5, 0.5]$ ns, a precision timing detector

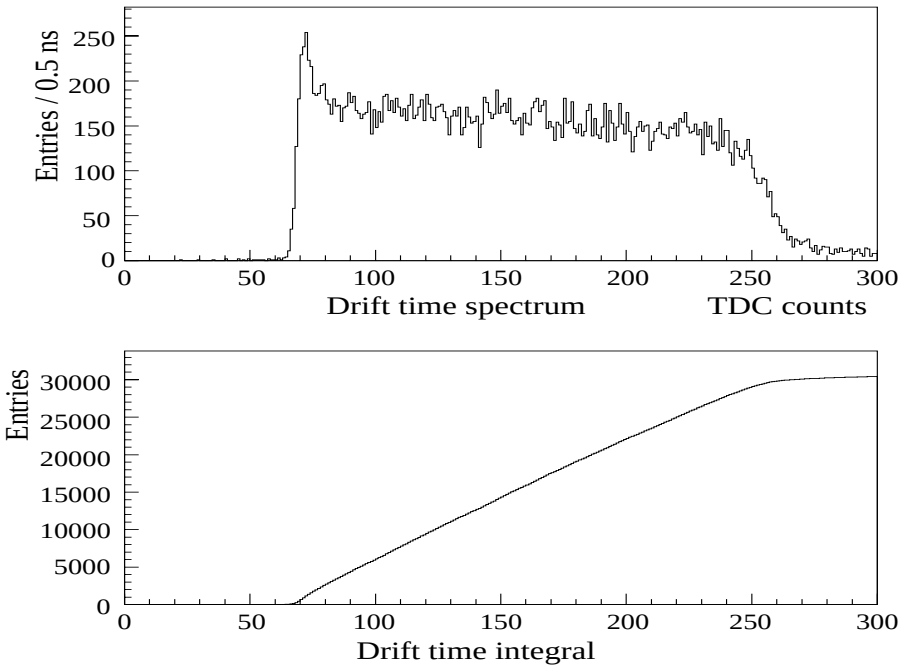

Fig. 3.11: Drift time spectrum (top) and its integral (bottom) for the X plane in right arm of DC3. Horizontal axis is in TDC channels, with each channel corresponding to 0.5 ns.

downstream of the magnet is required. This role is fulfilled by the vertical hodoscope (VH). Its precision in our experiment was better than 200 ns (Fig 3.12), making it sensitive enough to measure the signal and prompt background events.

We also made use of the VH data in the time interval between $\Delta t_{VH} = [-15, -5]$ ns. These data were used to cross-check our Monte Carlo simulations of accidental pion pairs and pairs coming from the long-lived sources in the target.

Online, the main purpose of the vertical hodoscope was to provide the timing gate for the rest of the detectors. The width of this gate was set to 40 ns. The same signal started the level-0 trigger (T0) and activated higher-level triggers.

Additionally, good timing capability of the vertical hodoscope allowed us to separate $\pi^+\pi^-$ events from contamination by $\pi^- p$ pairs. A lab momentum *vs.* Δt_{VH} distribution, shown in Fig. 3.13, made it possible to set a momentum cut of $P_{lab} < 4$ GeV/c, safely below the point where the curved band of $\pi^- p$ meets the vertical band of $\pi^+\pi^-$ pairs. During normal data taking we were also able to distingush and collect $\pi^- K$ events, which may at a later stage be used for the analysis of πK atoms.

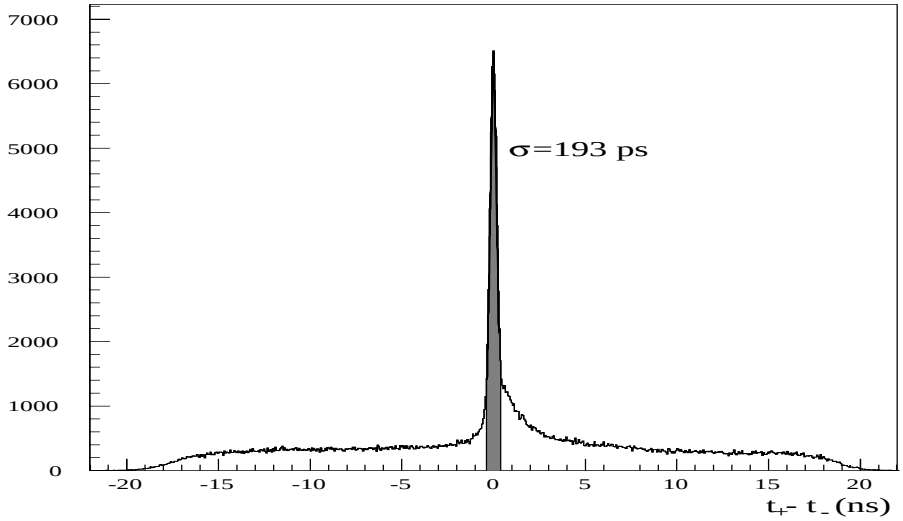

Fig. 3.12: Time difference for the particle pairs measured by the vertical hodoscope planes in the positive and negative arms of the spectrometer (2001 distribution for the single layer Ni target is shown). Gaussian fit of the peak yields the resolution of the vertical hodoscope of 193 ps. The shaded area corresponds to 2σ interval ($[-0.5, 0.5]$ ns) where the signal and prompt background events are found. The shoulder on the right side of the peak is due to the πp events, in which protons travel slower than pions.

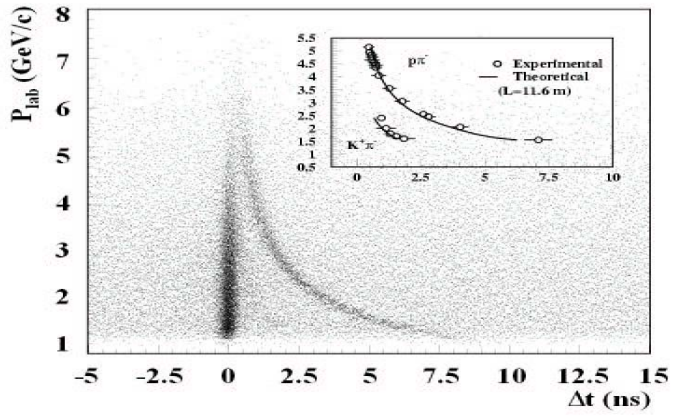

Fig. 3.13: Reconstruced laboratory momentum of particle pairs *vs.* positive-negative arm time differerence as measured by the vertical hodoscope. The main plot and the inset obviate the need to apply a momentum cut $P_{lab} < 4$ GeV/ to $\pi^+\pi^-$ events in the $[-0.5, 0.5]$ ns time interval in order to separate them from πp pairs.

Physically, the VH consists of 18 vertical scintillation BICRON BC420 slabs located in the positive and negative arms and measuring 40 cm in length, 7 cm in width and 2.2 cm in thickness [34][24]. Scintillation light passes through two fishtail light guides fixed at both ends of the slab to two 12-dynode Hamamatsu R1828-10 photomultipliers. By feeding the signal from both ends of the slab to a CAEN C561 meantimer a position insensitive time measurement is achieved. Time jitter is minimized by using LeCroy L3420 constant fraction discriminators. Time digitization is performed by 4303 time-to-FERA converters. Pulse height is digitized by ADC 4300B.

The relevant technical characteristics of the vertical hodoscope are: time resolution of 193 ps for $\pi^+\pi^-$ pairs and 99.5% single hit detection efficiency in the positive arm and 98.8% in the negative one.

3.3.4 Horizontal Hodoscope

The design of the horizontal hodoscope is analogous to that of the vertical hodoscope. Online, the information from the horizontal hodoscope is used by the coplanarity trigger (described in more detail in the following chapter). Offline, the device aids in track reconstruction.

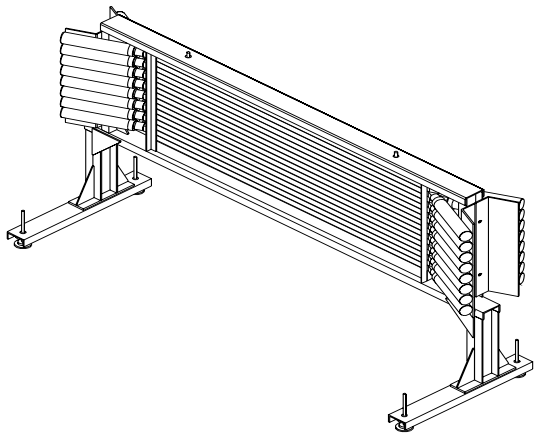

Fig. 3.14: Horizontal hodoscope.

The positive and the negative sides of the hodoscope consist of 16 horizontally-oriented scitillating slabs measuring $130 \times 2.5 \times 2.5$ cm^2 (length×width×thickness) covering the area of 40×130 cm^2. Analogously to the vertical hodoscope, each slab is read out on both ends by photomultipliers. Philips model XP2008 was used for this purpose. The rest of the electronics is identical to the one used for the vertical hodoscope.

The single hit detection efficiency of the horizontal hodoscope is 96.6% and the time resolution is 320 ns.

3.3.5 Cherenkov Counters

The Cherenkov radiation occurs when the velocity of the charged particle exceeds the velocity of light in a dielectric medium (c/n). A charged particle polarizes atoms in its wake resulting in emission of coherent radiation. The direction of the emitted light is related to the particle's velocity and the index of refraction as [25]:

$$cos(\theta_{Ch}) = \frac{1}{\beta n} \tag{3.1}$$

Most charged particles detectable by the Cherenkov counter in our experiment have a value of β on the order of 1. For these conditions a material with a low index of refraction, such as gas, is required. In fact, nitrogen was used as a radiator in the experiment yielding $\theta_{Ch} = 1.4°$ at normal temperature and pressure.

DIRAC's Cherenkov detector is found downstream of the horizontal hodoscope and used primarily to veto electrons resulting from pair productions in the upstream area. There are 5 gas-filled counters in each arm containing 4 curved light-focusing mirrors and a pair of photomultipliers [35]. The counter entrance has dimensions of 74×86 cm^2, and its exit dimensions are 74×100 cm^2. The ADC signals from the photomultipliers are read out by LeCroy 4300B ADC units [24]. The photomultiplier signal is passed through the discriminators and is used in triggering.

Since the signature of an electron pair closely resembles that of the pion pair and its production rate is several orders of magnitude greater than that of the latter, a very efficient electron rejection rate is required. The detector performance is illustrated in

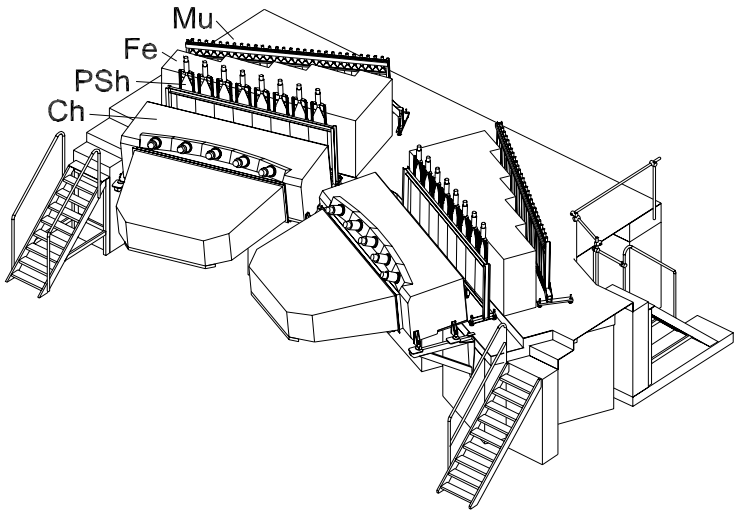

Fig. 3.15: Cherenkov (Ch), preshower (PSh) and muon detector(Mu) with an iron (Fe) absorber in front.

terms of the ADC count rate in Fig. 3.16[4]. After the careful adjustment of the ADC threshold corresponding to the number of photoelectrons in the photomultiplier, the detection efficiency for electrons was found to be 99.9% with a residual admixture of pions of 0.1%.

3.3.6 Preshower Detector

A small fraction of electrons in the downstream part escape undetected by the Cherenkov counter. To get rid of the undesirable electron background a preshower detector (PSH) was installed downstream of the Cherenkov detector. The function of the detector is to register the electromagnetic showers in the early stages of formation. It is well known that the electromagnetic showers develop much earlier than the hadronic ones. The nuclear interaction length for the lead absorber used in our experiment is given by [37]

$$\lambda_I = 35\,\mathrm{g\,cm^{-2}} A^{1/3},$$

[4]Cherenkov electron spectra after applying the pion trigger can also be found in Appendix C.

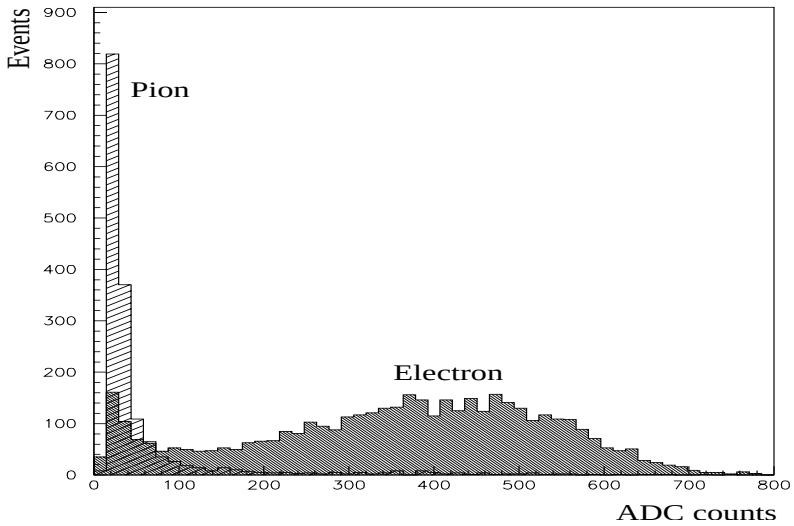

Fig. 3.16: Pion and electron peaks shown in terms of the ADC counts. Note that the first pion peak is virtually indistinguishable from the ADC pedestal values.

which yields a value of approximately 18 cm, whereas the radiation length

$$X_0 = \frac{716.4\,\mathrm{g\,cm^{-2}}A}{Z(Z+1)\ln(287/\sqrt{Z})}$$

gives a value of around 6 mm (A is the atomic mass and Z the atomic number of the absorber). Due to the large difference between X_0 and λ_I, an electron and a pion can be easily distinguished after passing through a relatively thin absorber. In DIRAC 16 Pb absorbers are installed in each arm with thickness ranging from 10 mm ($2X_0$) for the two outermost slabs and 25 mm ($5X_{rad}$) for the rest (Fig. 3.17) [36].

A corresponding scintillating slab (of the type BC-408 and dimensions 35×75 cm^2 and 1 cm in thickess) registers whether the particle started a shower (electron) or produced the signal corresponding to a minimum ionizing particle (pion) [24]. 10 mm thick Plexiglas light guides transmit the light to the EMI-9954 photomultipliers. The PM output is split by the LeCroy 428F FIFO into two signals: one is attenuated and passed to the LeCroy analog-to-digital converter 4300B and the second to the leading-edge discriminator (LeCroy 4416) with the threshold preset for electron/pion triggering.

The PSH's double track detection efficiency, defined by the presence of a hit when the downstream track can be reconstructed in drift chambers, was found to be around

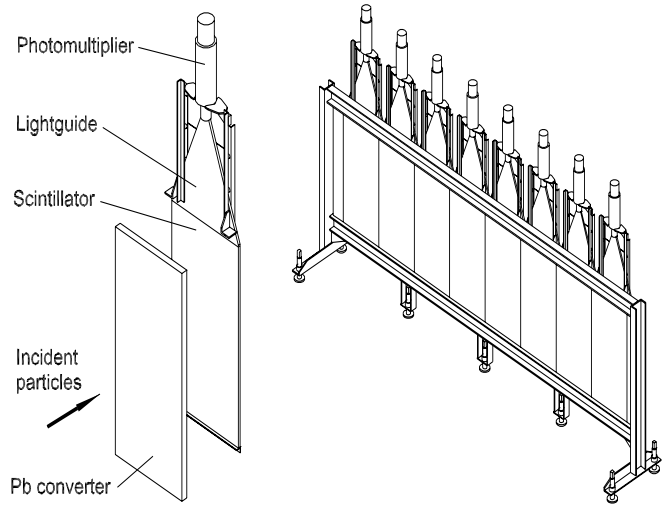

Fig. 3.17: Preshower detector components.

98.7% [38]. Its electron rejection capability is 85% with the 5% loss of the pion signal [24]. When combined with the ADC signal from the Cherenkov detector, the PSH's overall electron rejection efficiency approaches 100%.

3.3.7 Muon Detector

Like the electrons, the muons may fake the low relative momentum pion events produced in the target area. Most of the muons originate from pion decays, with only a small fraction resulting from other decays and direct $\mu^+\mu^-$ production.

The pion-muon separation is performed by the last detector downstream of the magnet, the muon detector (MU). The iron absorbers with thicknesses varying from 60 to 140 cm are placed in front of the detector in order to absorb hadrons and hadronic showers in their entirety. (Thicker absorbers were placed closer to the central axis of the experiment where higher momentum particles are found.) Two planes consisting of 28 scintillating slabs of dimensions $75 \times 12 \times 0.5$ cm were installed immediately following the absorbers.

In order to filter out the background events due to the presence of the nearby beam dump, the signal is recorded only in the case when it is detected by both MU

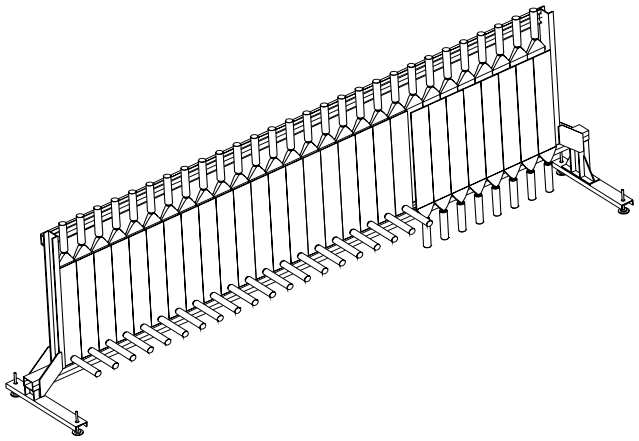

Fig. 3.18: Layout of the muon counters in one arm. Due to space constraints some of the scintillating slabs are coupled directly to the photomultipliers, avoiding the light guides.

planes. However, due to the relatively high probability of misidentification, the muon events are tagged without being rejected, to be later analyzed offline.

Bialcaline FEU-85 photomultipliers followed by CAEN C808 constant fraction discriminators and CAEN C561 meantimers are used to process the scintillation light. The latter arrives to the electronics via the fishtail-type light guides or by direct coupling to the scintillating slabs (made twice as thick as the rest to compensate for the loss of the light yield).

A 10% reduction in a $\pi^+\pi^-$-triggered events was observed after subtraction of $\mu\pi$ and $\mu\mu$ events [39]. Time resolution of the muon detector was found to be 1.3 ns.

Chapter 4

Trigger System

The secondary particles resulting from the PS proton beam-target atoms collisions result in single count rates of a few times 10^5 counts/sec in the downstream detectors to a few times 10^6 counts/sec in the upstream detectors. The processing capability of the data acquisition system (DAQ) is around 2000 events/spill [24]. Thus a trigger system capable of rate reduction by a factor of around 1000 becomes a necessity. The trigger system employed in the DIRAC experiment provides such a reduction factor by selecting pion pair events with a small opening angle and low relative momentum.

Since the beginning of data-taking for our experiment, the trigger setup has undergone several modifications. Below we consider only the latest version of the trigger employed in the 2001-2003 runs, as the one relevant for the data analysis found in later chapters.

4.1 Pretrigger (T0)

The function of the T0 trigger is to provide an initial gate for the DNA and RNA triggers to start processing an event. The following logic sequence is employed:

$$(VH1 \cdot VH2) \cdot (PSH1 \cdot PSH2),$$

where $VH1 \cdot VH2$ and $PSH \cdot PSH2$ correspond to the left/right arm time coincidences between at least one pair of vertical and preshower detector slabs, respectively. The

"coincidence window" defined as the time difference between a pair of hit slabs in the negative arm and the trigger hit in the positive arm of each detector has been set at ±20 ns. This window width is the same as the one for the level 1 trigger, T1. To improve the time response of the T0 trigger the VH signals are read out directly from the discriminator outputs before they arrive to the meantimers.

4.2 Trigger T1

The T1 trigger [43] fulfills the following tasks:

- Separates events containing an electron pair from the non-electron ones.
- Selects events only in the case when signals in both detector arms are present.
- *Coplanarity* condition: if the signals in both arms of the horizontal hodoscope (HH) are found, the trigger takes only the events where left/right arm slab difference is less than 2 slabs (Fig. 4.1). This condition restricted the event selection to the ones with small spatial separation in the y direction, and, hence, small Q_y.

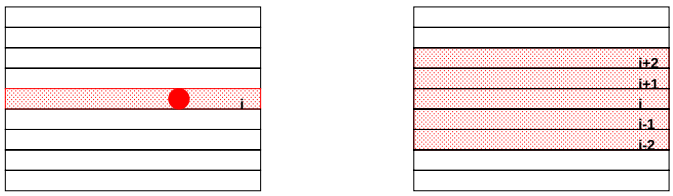

Fig. 4.1: Coplanarity selection by the T1 trigger. If a hit was registered in slab i in one of the arms, the coplanarity subtrigger selects events only if the $i-2 \leq i \leq i+2$ criterion in the other arm was satisfied.

In addition to the pion pair events, our experiment collects e^+e^-, $\Lambda \rightarrow p + \pi^-$, $K^+ \rightarrow \pi^+\pi^+\pi^-$, $K^- \rightarrow \pi^-\pi^-\pi^+$ events.

e^+e^- data used for calibration purposes for tuning Cherenkov, preshower and ionization detector thresholds. T1 has the capability to separate electron and non-electron pair events by requiring:

$$CH1 \cdot PSH1$$

for an electron event in a given spectrometer arm, and

$$\overline{CH1} \cdot PSH1$$

for non-electron events[1] (such as pion pairs), where CH stands for Cherenkov signal ($\overline{CH}$ corresponds to the absence of the signal in the Cherenkov detector) and PSH for preshower detector signal(s). Since the overall timing of an event is started by a signal in the vertical hodoscope (VH), electron signature in one arm is defined by the following signal coincidence:

$$VH1 \cdot HH1 \cdot CH1 \cdot PSH1 = e1,$$

whereas for non-electron events the trigger logic is:

$$VH1 \cdot HH1 \cdot \overline{CH1} \cdot PSH1 = \overline{e1}.$$

The T1 pion pair trigger provides a reduction factor of 2 relative to the minimum bias events (defined as $VH1 \cdot IH$). The decision time of the trigger is around 15 ns.

4.3 DNA and RNA Neural Network Triggers

The DNA (DIRAC Neural Atomic) trigger [44] is a processing system based on the neural network algorithms. The neural network was trained to select particle pairs with low relative momenta: $Q_x < 3\,\mathrm{MeV}/c$, $Q_y < 10\,\mathrm{MeV}/c$ and $Q_L < 30\,\mathrm{MeV}/c$. Events that do not satisfy at least one of these conditions are rejected.

The detectors employed in the trigger are shown in Fig. 4.2. DNA processes hit patterns from the vertical hodoscopes VH1, VH2, the x-planes of the ionization hodoscope IH and, optionally, the preshower detectors PSH1 and PSH2.

DNA is able to handle events with up to 2 hits in each vertical hodoscope VH and up to 5 hits in each IH x-plane. If the number of hits exceeds these values in any of these detectors, DNA accepts the event for further offline evaluation. In the case

[1]The analogous logic is applied to the negative arm, i.e. $CH2 \cdot PSH2$. Here, as everywhere throughout this section index "1", for the positive detector arm, may be interchanged with index "2", for the negative arm.

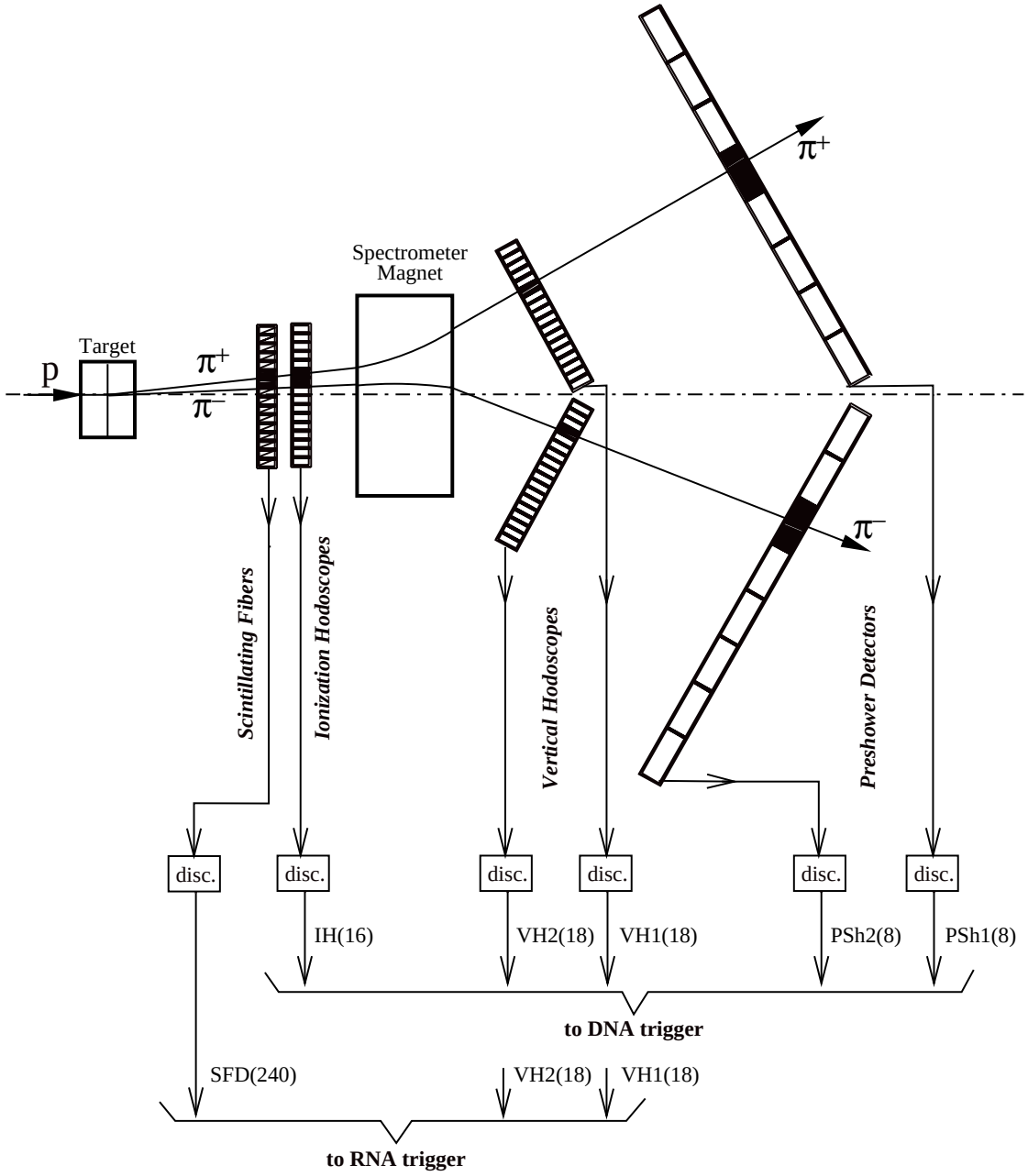

Fig. 4.2: DIRAC detectors used for the neural network triggers DNA and RNA. Numbers of signals from each detector are given in parentheses.

there is only 1 hit in an IH plane, it is assumed that two particles cross the same IH slab.

Each of the two IH planes is used independently in combination with both arms of the vertical hodoscope. To evaluate this information two identical arrays of electronic modules were used: the interface and decision card, the neural network cards and the POWER-PC VME master CPU card (Motorola MVME 2302). The subdecisions of the two parts are combined in a logical OR to minimize inefficiency due to interslab gaps in the IH.

A DNA-selected event is only processed by the processor if it is also accepted by T1 trigger. The DNA rejection factor is around 2.3 with respect to T1. Its efficiency in the low Q region is 94%. The trigger decision time is around 210 ns.

To increase the selection efficiency, the DNA logic at the later stage of the experiment was supplemented with the RNA trigger system. The RNA operation is similar to that of the DNA. Instead of the IH data, RNA uses the information from the X-plane of the scintillating fiber detector SFD (Fig. 4.2). Finer granularity upstream of the magnet (0.5 mm in SFD compared with 6 mm in IH) provides higher trigger efficiency for pion pairs with small opening angles. The RNA decision time is 250 ns.

The OR between DNA and RNA provides a rejection factor of 1.9–2.0. The combined trigger results in an increased efficiency in the low Q range of 99%.

4.4 T4 Trigger

Trigger 4 is the final trigger stage. Its tasks are twofold: straight line track reconstruction in the the drift chamber x-planes and the relative momentum determination. T4 processing starts when an event is accepted by the T1 trigger.

T4 processing is performed by two submodules: the track finder and track analyzer. The track finder (an identical processor is used for each arm) operates only with hit wire numbers from all the drift chamber x-planes, the values of drift times are not used. A diagram of the T4 operation is shown in Fig. 4.3.

The track finder logic is based on the endpoint algorithm. Drift chamber planes X1 (or X2) and X5 (or X6) are used as the base planes for track search (there are

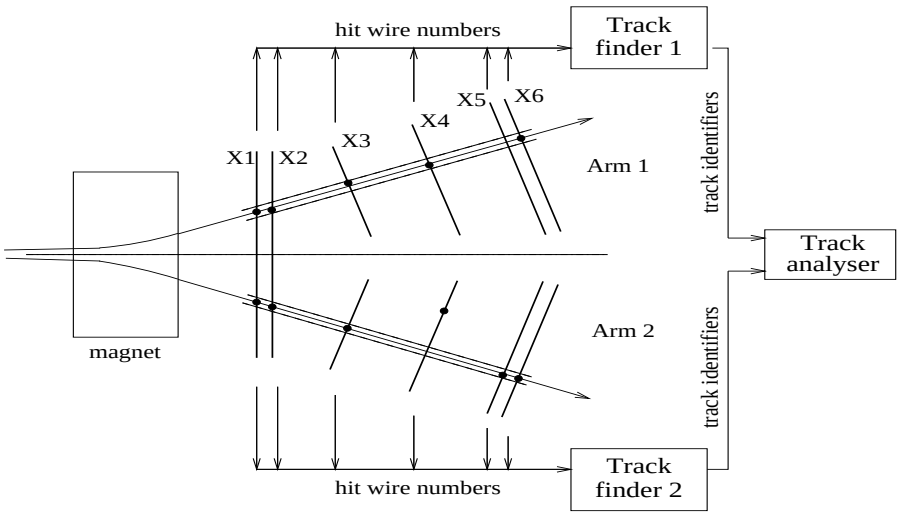

Fig. 4.3: T4 trigger block diagram. Only the drift chamber X-planes involved in T4 are shown.

a total of 6 X-planes in each spectrometer arm). Pairs of hits in the base planes are taken as end points for straight line fits. A track is found if the number of hits within a predetermined range away from the fit (allowed hit window) exceeds a certain fixed value. The window width and position for every plane, as well as the minimum number of hits per track (a commonly used value is 4), can be easily adjusted. A unique number, called the "track identifier", containing the encoded numbers of the hit wires in the base planes, is associated with the track. Parasitic combinations (i.e. repeated track identifiers) are suppressed.

If tracks are identified in both arms, the track analyzer proceeds with the event evaluation. The look-up memory of the track analyzer contains all possible combinations[2] of the track identifiers for pion pairs with relative momenta $Q_L \leq 30\,\mathrm{MeV}/c$ and $Q_x \leq 3\,\mathrm{MeV}/c$. The track analyzer then compares track identifiers from both arms with the content of the look-up memory tables. If a relevant combination is found, the T4 processor generates a "Track Found" signal which starts the data transfer to the VME buffer memories. Otherwise, CLEAR and RESET signals are applied to the DAQ and trigger systems.

[2]These "allowed" combinations were obtained with Monte Carlo methods using the precise geometrical description of the setup.

The T4 decision time varies depending on the complexity of the event. The decision times range 1.5 μs for simple events to more than 20 μs for the more complicated ones, with the average around 3.5 μs. T4 provides a rejection factor of around 5 with respect to the T1 rate or around 2.5 with respect to DNA/RNA. The T4 efficiency in the low Q region exceeds 99%.

4.5 Combined Trigger Operation and Performance

The overall trigger combining all the subtriggers described above are shown in Fig. 4.4. A positive decision of the T1 trigger starts DNA+RNA and the T4 triggers. If

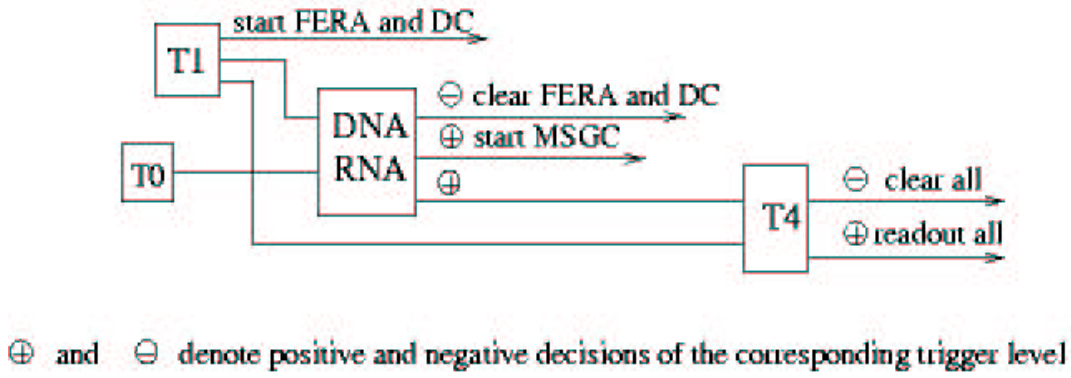

Fig. 4.4: Multilevel trigger system employed by DIRAC in the 2001-2003 runs.

DNA+RNA issues a negative decision, the data stored in the drift chamber branches and FERA modules responsible mainly for the ADC and TDC information are cleared; otherwise, a positive signal is sent to T4 and the MSGC. We note that the MSGC processing time is relatively long, thus it is started after the entire trigger chain, including the T4, has accepted the event. If an event has passed the T4 selection it is loaded into the VME buffers to be processed offline.

The complete (DNA+RNA)·T4·T1 trigger is found to be 98% efficient in the $Q_l < 22$ MeV/c region and 95% efficient for $Q_l < 30$ MeV/c, where $Q_x < 3$ MeV/c and $Q_y < 3$ MeV/c. Distributions reflecting the performance of the individual trigger stages are shown in Fig. 4.5-4.8.

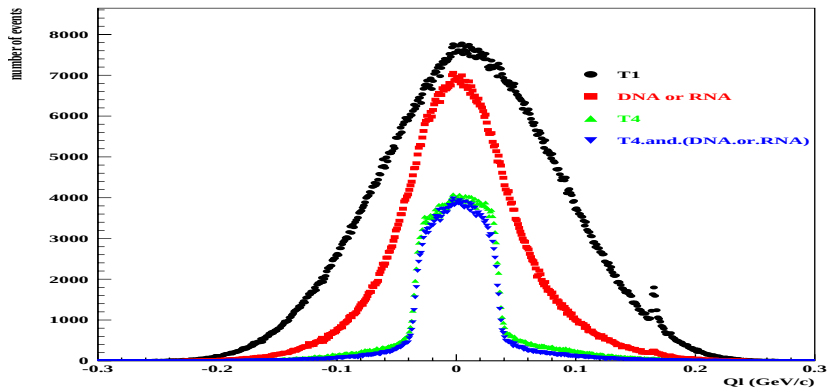

Fig. 4.5: Action of T1, DNA+RNA, T4 and the combined trigger illustrated for the Q_l events. The triggers preserve as many low Q_l events as possible. (An enhancement due to Λ decays is seen on the right-hand side of the plot.)

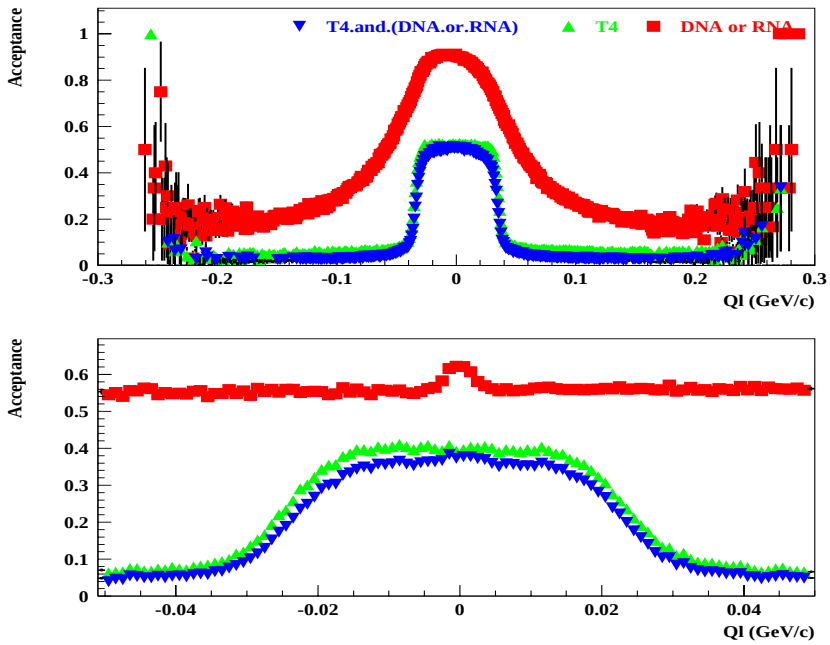

Fig. 4.6: Ratio of the Q_l distributions after the action of DNA+RNA, T4 and the combined trigger over the T1-accepted events with the requirement of one reconstructed track in each spectrometer arm. Bottom graph shows the low Q_l region.

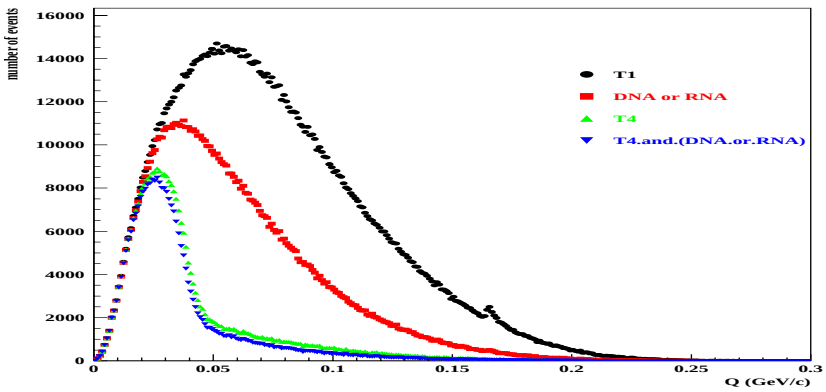

Fig. 4.7: Action of T1, DNA+RNA, T4 and the combined trigger illustrated for the Q events. The triggers preserve as many low Q events as possible. (An enhancement due to Λ decays is seen on the right-hand side of the plot.)

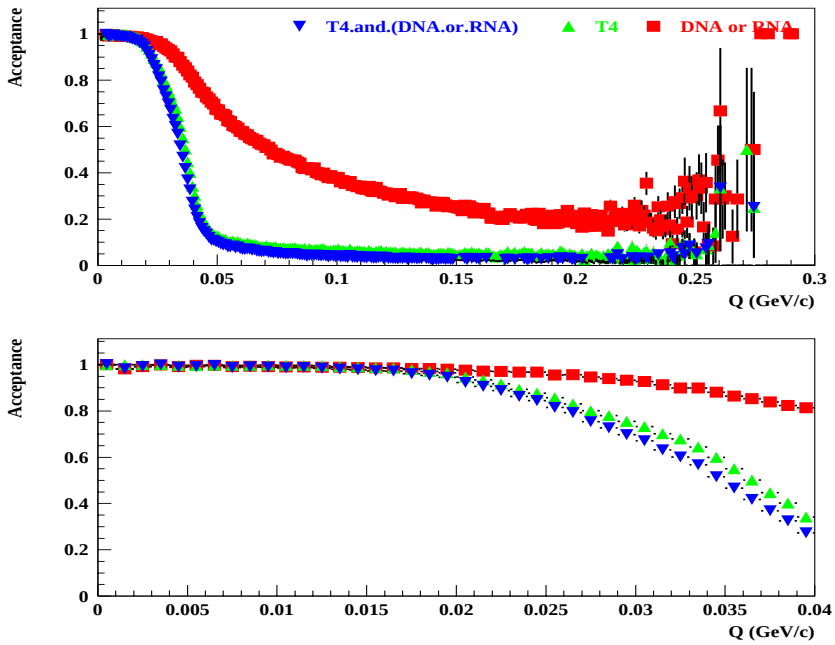

Fig. 4.8: Ratio of the Q distributions after the action of DNA+RNA, T4 and the combined trigger over the T1-accepted events with the requirement of one reconstructed track in each spectrometer arm. Bottom graph shows the low Q region in detail.

Chapter 5

Track Reconstruction

The offline tracking is performed by the ARIANE software package [52]. The tracking procedure is split, roughly, into two stages: the downstream stage with DC providing the primary track reconstruction information and the upstream one with the SFD supplying most of the upstream information[1]. Below we provide a more detailed description of the track reconstruction algorithm.

5.1 Downstream Stage

A downstream track candidate is reconstructed first in the drift chambers (DC's). Initially, horizontal and vertical degrees of freedom are considered separately. A linear track candidate is found when at least one hit per horizontal plane is found on both ends of the DC setup (DC1 and DC4) (Fig. 5.1) [45]. A search range centered around the linear fit is then used to find hits lying close to the track in the other horizontal planes. The same procedure is repeated for the vertical DC planes. If the total number of hits within the search range is less than 4 for either vertical or horizontal set of planes, the track candidate is rejected; otherwise, the hits in the horizontal and vertical planes are matched using the inclined drift planes. A drift chamber track is found if the horizontal/vertical matching was successful. Frequently, hit wire

[1]Some downstream information provided by DC is also used in the upstream stage of reconstruction (see below).

distributions allow for more than one DC track possibility. "Extra" hits may appear due to noise or stray particles crossing the detector. For the tracking purposes, we take only the events with maximum of 2 tracks per DC arm (for data analysis only the events with one track per are selected), provided that, in addition, they point to the magnet's aperture.

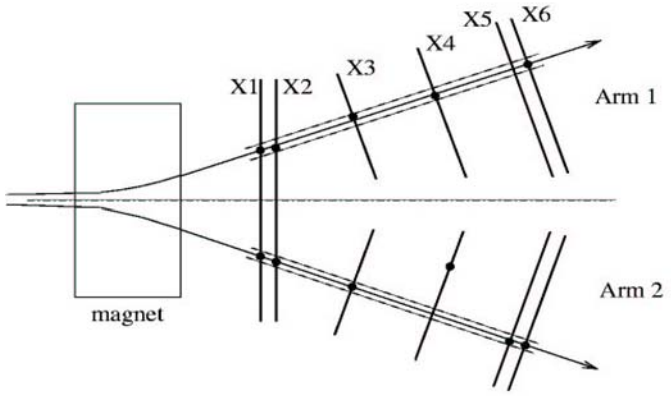

Fig. 5.1: Drift chamber tracking shown with a few allowed hit configurations and the search range.

The magnetic field map in the spectrometer magnet has been measured and described with 4 polynomials with 5 parameters each to an accuracy of 10^{-4}. Using these, the spatial track parameters are projected to the center of the beam spot at the target, yielding a zeroth-order estimate of particle's momentum.

A more precise determination of momentum is made with the zeroth order track and the precise the DC hit positions determined from drift times. The number of accepted tracks is further reduced by applying the χ^2 confidence limits.

5.2 Upstream Stage

Following the χ^2 selection and, in analogy to the DC track fitting procedure, an upstream hit search window relative to each track is defined. Spacewise, the upstream detector hit search range is defined by:

$$\Delta x\,(\Delta y) = \pm\left(0.2 + \frac{4.8}{p_{lab}\,[\mathrm{GeV}/c]}\right)\ \mathrm{cm}, \tag{5.1}$$

where the first term gives the uncertainty in the beam position and the second is determined the multiple scattering and the uncertainties in the magnetic field measurements. The timewise constraint is defined by the time of flight between the vertical hodoscope and the SFD and by the VH's resolution $\Delta t = \pm 4\,\text{ns}$. This value corresponds to about 3σ acceptance.

Using the Taylor expansion of momenta relative to the track - hit distance, each track is then subsequently adjusted so that it passes through a hit closest to it.

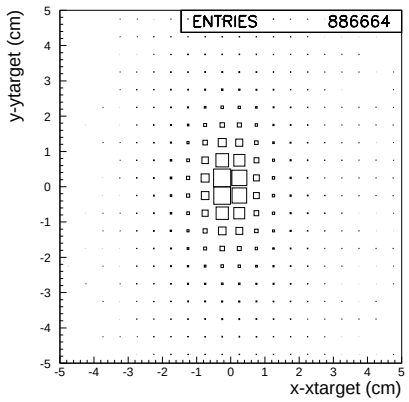

Fig. 5.2: Δy vs. Δx distances between pairs of tracks in the target plane.

In the next step, all available pairs of tracks are considered, where the origin of each track is restricted to a 15 mm interval from the center of the beam spot. The tracking may subsequently proceed in one of the two ways. In the *standard* tracking procedure [46], Kalman filter fit [47] starting from the DC's down to the first MSGC plane is made, exhausting all available hit information. A "vertex fit" is made where a pair of tracks are constrained to intersect the central plane of the target within a preset distance. A pair of tracks is selected based on the threshold confidence test. This procedure does not rely on the precise knowledge of the beam position and width. In the *modified* tracking method, the target itself provides another measurement point for the Kalman filter and the uncertainty in its position is defined by variations in beam intensity across the target [48][49]. A cut on the distance (15 mm) between a track and the center of the beam spot on the target leads to the final track selection.

Fig. 5.2 illustrates the distribution of distances between pairs tracks in the target plane.

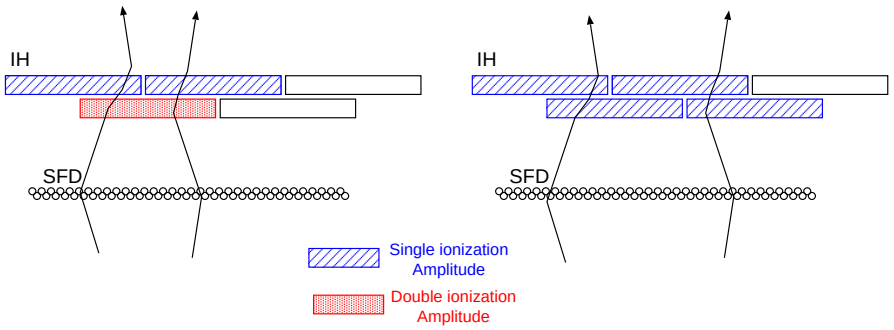

Fig. 5.3: Some of the IH hit/amplitude configurations allowed by the event selection procedure.

In order to reduce the probability of hit-track misidentification, in this analysis only the events with a maximum of 2 hits in the SFD satisfying the criteria above were selected. The ionization hodoscope amplitudes were then checked (Fig.5.3). An event was accepted if two IH hit slabs with amplitudes exceeding the single ionization threshold or a single slab with an amplitude equal to or exceeding double ionization threshold were found. If the number of hits within a SFD search window was one, the event was taken if at least one doubly ionized slab was found.

As an illustration of the accuracy of the tracking procedure we show the reconstructed invariant mass of the Λ particle (Fig. 5.4). The $\pi^- p$ decays of Λ were taken with a signature of one downstream track per spectrometer arm and the $[0, 1.3]$ ns TOF difference between the two arms. The invariant mass $M_\Lambda = \sqrt{m_\pi + p_{CM}} + \sqrt{m_p + p_{CM}}$ fit by the Gaussian superimposed onto the linear background yields $M_\Lambda = 1115.790 \pm 0.031$ (stat.) MeV/c^2 with $\sigma_{M_\Lambda} = 0.395 \pm 0.007$ (stat.) MeV/c^2 [45].

Within the limits imposed by the detector efficiencies, the dominant type of events are single track events. The results for the 2001 run show that 92% of the tracks in the negative spectrometer arm were single track events and 96% in the positive one[2].

[2]The left/right arm discrepancy can be explained by the presence of protons in the positive arm.

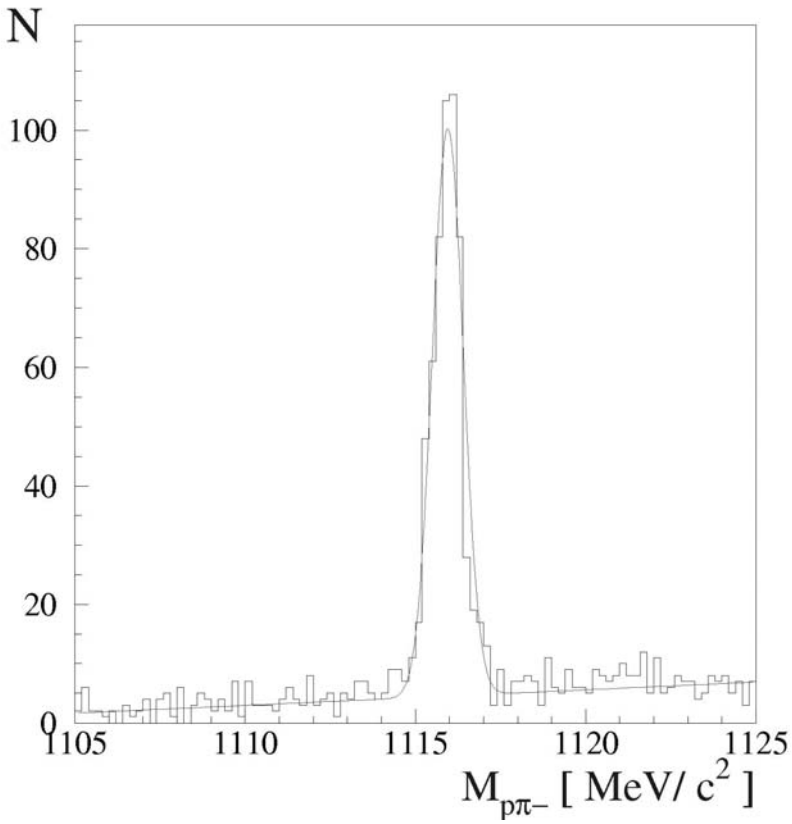

Fig. 5.4: Reconstructed Λ mass. Gaussian fit yields $M_\Lambda = 1115.790 \pm 0.031\,(\text{stat.})$ MeV/c^2 with $\sigma_{M_\Lambda} = 0.395 \pm 0.007\,(\text{stat.})$ MeV/c^2.

Chapter 6

Signal Extraction

Below we describe the process of signal extraction. Since the background distributions, save for the accidental events, cannot be extracted they must be generated using the Monte Carlo techniques. We will discuss in detail how the atomic pair and background spectra are generated. Once these events are propagated through the setup and digitized by the offline software, they can be used to find the atomic pair signal by subtracting the MC background from the experimental prompt ($\Delta t_{VH} = [-0.5, 0.5]$ ns) spectra. In both cases, the MC events and the experimental data are subjected to the identical set of cuts, also found in this chapter.

6.1 Monte Carlo Event Generators

In what follows we describe the Monte Carlo simulated atomic pair signal and the three types of background events: Coulomb, non-Coulomb and accidental. We place a special emphasis on how the signal and background, used as an MC input, was generated at the target level[1].

Input files corresponding to each of the four types of events containing initial momentum vectors of the pion pairs and the coordinate of the point of production were produced[2].

[1]The generator code was written by C. Santamarina and is described in [53].

[2]Due to their origin from the uncorrelated proton-target nucleus collisions, a *pair* of coordinates was produced for the case of accidental pairs.

6.1.1 Atomic Pairs

In order to simulate the breakup cross-section found in Eq. 2.43 one needs to specify P and Q distributions. For convenience the polar coordinate representation was chosen. A set of two coordinate vectors $(|\vec{P}|, \theta, \phi)$ and $(|\vec{Q}|, \theta', \phi')$ then completely specifies the atomic pair in momentum space.

P *vs.* θ dependence was found from the experimental data using prompt events in the interval $[-0.5, 0.5]$ ns. We note that the spectrometer acceptance distorts the P distribution at breakup, and, thus, in order to recover the initial P spectrum the acceptance correction needs to be applied to the experimental distribution. To this end, a *uniform* (P, θ) distribution with soft geometric cuts was generated and passed through the GEANT-DIRAC simulation. Experimental prompt pion spectrum was then divided by the "acceptance-distorted" uniform distribution yielding the P distribution at the generation point. In Fig. 6.1 we show distributions before and after applying the correction. Fig. 6.2 shows the final P *vs.* θ spectrum.

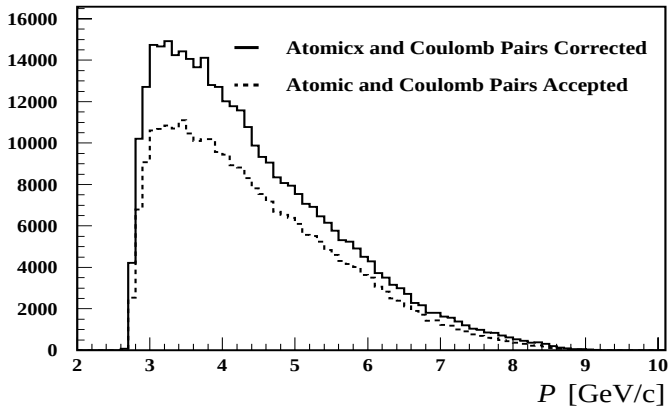

Fig. 6.1: Atomic and Coulomb lab momentum distributions before (dashed) and after (solid) applying the acceptance correction.

Q *vs.* θ' dependence has been parametrized and is given by [54]:

$$\frac{d^2\sigma^{1s}}{dQ\, d\theta'} \propto \frac{x\exp\left(-4x^{-1}\tan^{-1}x\right)\sin^{2l+1}\theta'}{(x^5+1)^5(1-\exp\left(2\pi/x\right))} \tag{6.1}$$

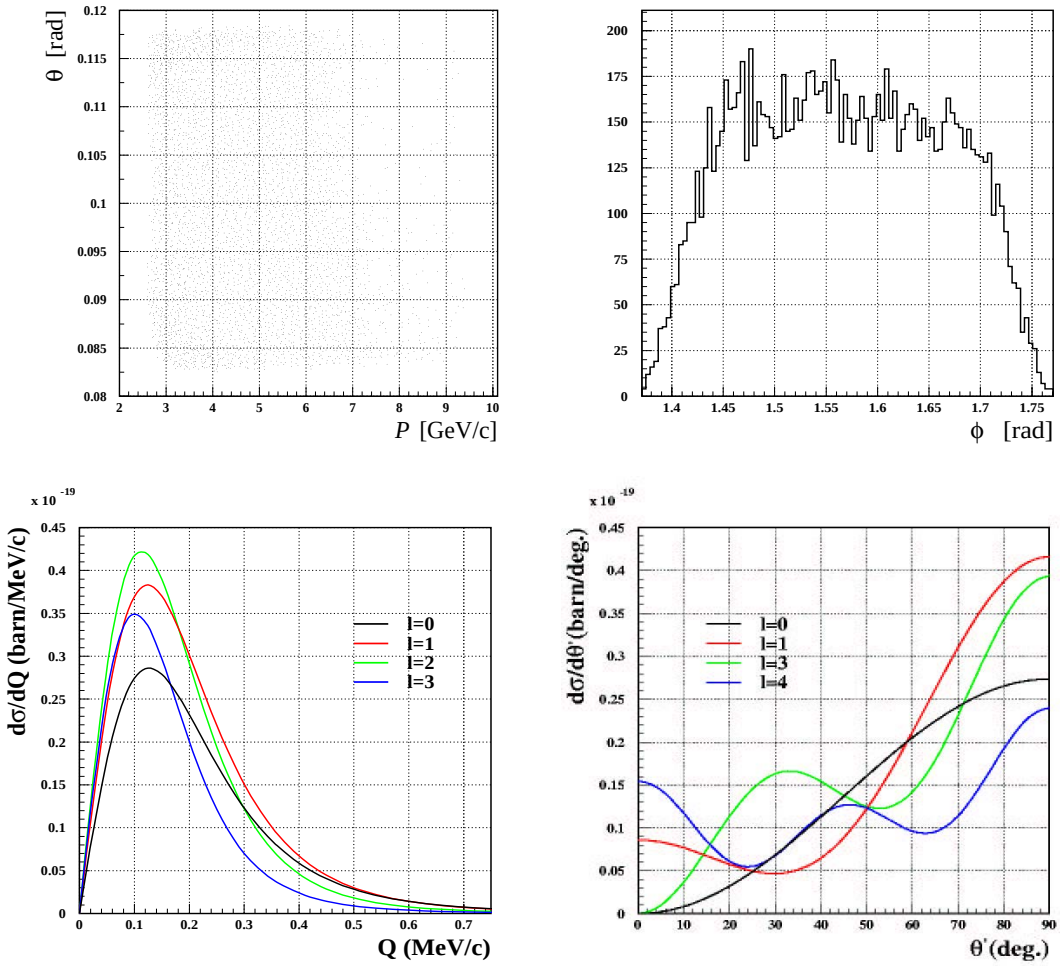

Fig. 6.2: Input distributions used to pion pairs at the point of their formation. Top row distributions are used to generate both the atomic and Coulomb pairs. Top left: θ *vs.* CM lab momenta. Top right: a small sample of events showing input ϕ distribution. The gradual drop-off around the edges corresponds to lower probability of detecting pion pairs downstream which pass close the edges of the acceptance region upstream. Bottom row: differential cross-sections as a function of Q and θ' for different values of orbital quantum number l.

$$\frac{d^2\sigma^{2s}}{dQ\,d\theta'} \propto \frac{x(x^2+1)\exp\left(-4x^{-1}\tan^{-1}2x\right)\sin^{2l+1}\theta'}{(4x^2+1)^6(1-\exp\left(2\pi/x\right))}, \tag{6.2}$$

where the first equation refers to the $A_{2\pi}$ breakup from the $1s$ state and the second from the $2s$ state and where M_π is the pion mass, α is the fine structure constant and $x \equiv Q/M_\pi\alpha$. For the higher n states x was taken to be $Q/2nM_\pi\alpha$ [55]. A sample parametrization for $n = 4$ state is shown in Fig. 6.2.

The breakup cross-section 2.43 does not exhibit azimuthal dependence, thus ϕ and ϕ' are generated according to uniform distributions (Fig. 6.2).

To be usable by the GEANT simulation, center-of-mass and relative momenta of the atomic pairs are converted to individual lab momenta through the generic relationship:

$$\frac{d^2\sigma}{d\vec{P}\,d\vec{Q}} = \frac{E}{M}\frac{d^2\sigma}{d\vec{p_1}\,d\vec{p_2}} \tag{6.3}$$

The breakup probability as a function of traversed distance Z inside the target has been described in Chapter 1. The $A_{2\pi}$ dissociation point is then generated according to the distribution in Fig. 6.3. Generated $\vec{p_1}$ and $\vec{p_2}$ and position of the origin are written to the input file.

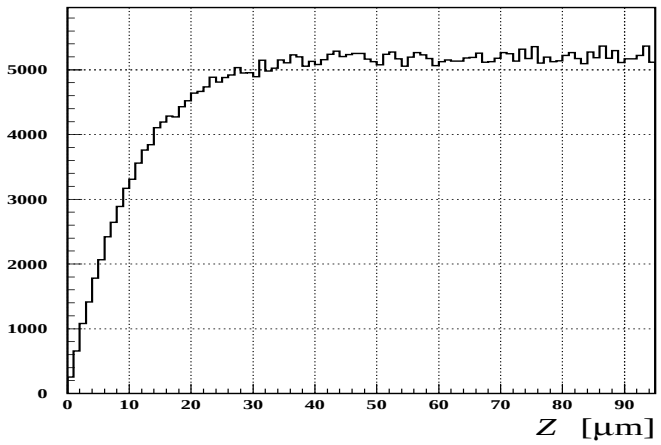

Fig. 6.3: $A_{2\pi}$ breakup rate as a function of the breakup position in the target.

6.1.2 Coulomb Pairs

Due to their identical origins with atomic pairs (cf. Section 2.6), center-of-mass momenta weights of Coulomb pairs at production are also described by Fig. 6.2.

The relative momentum parametrization is:

$$\frac{d^2\sigma_{CC}}{dQ\,d\theta'} = \frac{2\pi M_\pi \alpha/Q}{1-\mathrm{e}^{-2\pi M_\pi \alpha/Q}} Q^2 \sin\theta', \tag{6.4}$$

where $Q^2 \sin\theta'$ is the phase space element in spherical coordinates. We note that the CC production cross-section can be thought of as the accidental pion pair distribution (Section 6.1.4) enhanced by the Coulomb correlation function of Eq. 6.4. Due to the fact that, unlike the $A_{2\pi}$, Coulomb-correlated pairs are created in an unbound state, the Q *vs* θ' and point-of-production (Z) distributions are uniform. Analogously to atomic pairs, $\vec{P}$ and $\vec{Q}$ are converted to $\vec{p_1}$ and $\vec{p_1}$ (Eq. 6.3) and recorded in an input file along with their Z coordinate.

6.1.3 Non-Coulomb Pairs

The lab momenta of the non-Coulomb pairs are obtained by combining DIRAC experimental data with FRITIOF6 simulation of hadron-nuclei interactions [56].

In order to obtain the non-Coulomb pair contribution to the prompt ($\Delta t_{VH} = [-0.5, 0.5]$ ns) events, the signal-free relative momentum region $5 < Q < 10$ MeV/c was chosen (the signal is over 99% contained in the $Q < 4$ MeV/c interval). In this interval:

$$\frac{d^2\sigma_{exp}}{d\vec{P}\,d\vec{Q}} = \frac{d^2\sigma_{CC}}{d\vec{P}\,d\vec{Q}} + \frac{d^2\sigma_{NC}}{d\vec{P}\,d\vec{Q}} + \frac{d^2\sigma_{ACC}}{d\vec{P}\,d\vec{Q}} \tag{6.5}$$

In order to reconstruct the NC momentum distribution, the accidental distribution is subtracted from $\frac{d^2\sigma_{exp}}{d\vec{P}\,d\vec{Q}}$ and the Coulomb-correlated background is then used to express $\frac{d^2\sigma_{NC}}{d\vec{P}\,d\vec{Q}}$.

The accidental pion distribution, having its origin in the independent proton-target nucleus interactions, is unchanged, regardless of whether one takes events with small or large time separation. Since the extraction of accidentals in the prompt region is not feasible, P-distribution in the $\Delta t_{VH} = [-15, -5]$ ns interval was used.

Taking into account the fact that the Coulomb pairs originate from short-lived decays and non-Coulomb pairs from long-lived ones, one can rewrite Eq. 6.5 as:

$$\frac{d^2\sigma'}{d\vec{P}\,d\vec{Q}} = \omega_s(P)\frac{d^2\sigma}{d\vec{P}\,d\vec{Q}} + (1-\omega_s(P))\frac{d^2\sigma}{d\vec{P}\,d\vec{Q}} = \frac{d^2\sigma_s}{d\vec{P}\,d\vec{Q}} + \frac{d^2\sigma_l}{d\vec{P}\,d\vec{Q}} \tag{6.6}$$

where $d\sigma'/d\vec{P}d\vec{Q} = d\sigma_{exp}/d\vec{P}d\vec{Q} - d\sigma_{ACC}/d\vec{P}d\vec{Q}$, and $\omega_s(P)$ and $\omega_l(P)$ indicate the momentum-dependent fraction of the short-lived and long-lived sources, respectively, obtained using FRITIOF6 ($\omega_l = 1 - \omega_s$ is plotted in Fig. 6.4). The Coulomb background is reconstructed as described in the previous section and $dN_{ACC}/\vec{P}$ is reconstructed as shown in Section 6.1.4. Thus, the NC contribution is defined.

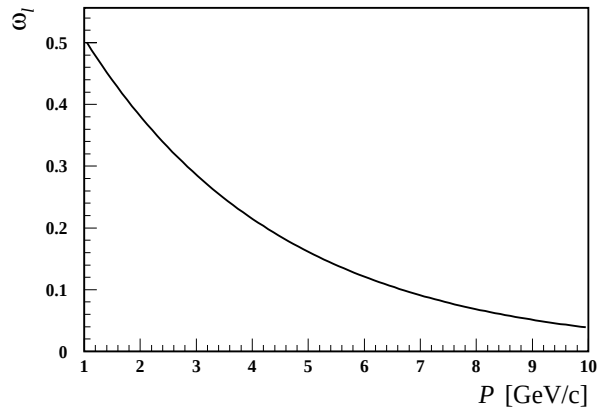

Fig. 6.4: The momentum dependent fraction of pion pairs from long-lived sources, $\omega_l(P)$.

6.1.4 Accidental Pairs

The accidental pair generator is the simplest of the four generators. Due to the uncorrelated nature of accidental pions the Q distribution is defined purely by phase space:

$$\frac{d^2N_{ACC}}{dQ\,d\theta} \propto Q^2 \sin\theta \tag{6.7}$$

$\Delta t_{VH} = [-15, -5]$ ns time interval was used to extract $\vec{p_1}$ and $\vec{p_2}$ directly from the data. Z-distribution is once again uniform.

6.1.5 Comparison of the Input Distributions

In Fig. 6.5 we show the input lab momentum distributions for one of the pions for the AT, CC, NC and ACC events. As is evident from the figure, the only distribution with a lab momentum significantly different from the rest is the NC distribution. The softer NC spectrum is attributable to the fact that the non-Coulomb pairs result from the long-lived decays and the pion pair is forced to share its phase space with several other decay products (see Section 2.5).

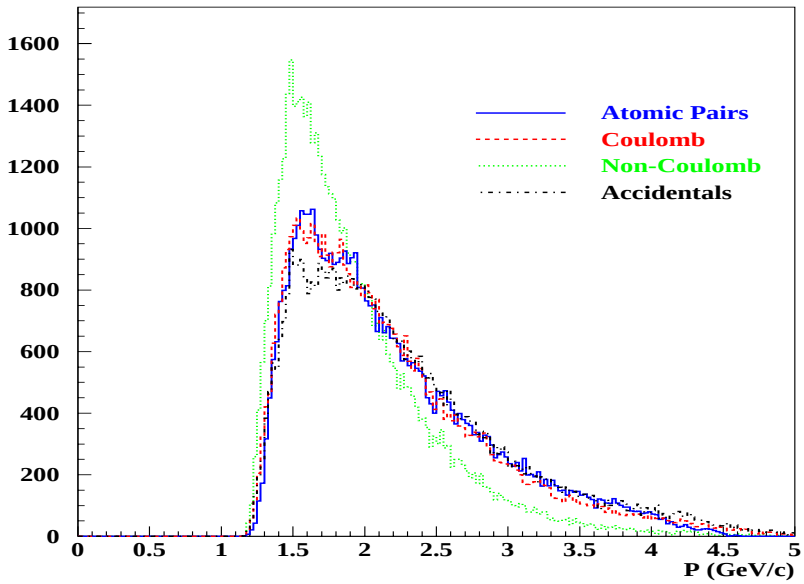

Fig. 6.5: Single pion lab momenta distributions for 50,000 AT, CC, NC and ACC input events. NC distribution has a softer spectrum due to phase space constraints.

In Fig. 6.6 we show the input relative momenta distributions in four momentum projections. Due to the fact that the pion pairs (top two rows) resulting from pionium dissociations are highly correlated, the AT spectra have the lowest relative momenta. The correlation peak may observed for the Coulomb pairs; the enhancement is especially evident for the Q_x, Q_y and Q_l distributions (bottom two rows). The Q distribution of CC pairs is seen to increase linearly with Q for low Q values (see Eq. 6.4) . Due to their incoherent nature, the relative momenta of non-Coulomb

and accidental events are virtually indistinguishable (unlike the P_{lab} spectra). The pure phase space distribution in Q_l for those can be observed. In the same interval the accidental and non-Coulomb distribution is proportional to the phase space factor Q^2. The rest of the Q shape follows the geometrical acceptance of the apparatus.

6.2 Event processing

Once the input events had been generated, they were processed with GEANT-DIRAC, a GEANT3-based simulation of the DIRAC setup [51]. Therein a pion pair was propagated through the various detector materials. Resulting detector hits and times-of-flight were written into a buffer file. This information was subsequently digitized and converted to realistic detector responses by the ARIANE offline package [52]. The same package was also employed to perform track reconstruction (see Chapter 5) for the Monte Carlo events, treating them identically to the experimental data. Below we describe a set of applied cuts and the modification to the simulated SFD response, which was performed to ensure that the signal extraction could proceed correctly.

6.2.1 Event Selection Criteria

To improve the signal-to-background ratio the events suitable for further analysis were subject to the following selection criteria:

- Maximum two SFD hits in the hit search range of the X and Y plane were allowed. (The hit search range was defined by the window $\pm(0.2 + \frac{4.8}{P[GeV/c]})$ cm from the point where the 0th-order track (DC track projected onto the target) intersected the SFD plane (see Chapter 4).

- Only the events containing one DC track per arm were taken. If two tracks in one arm is found, the earlier one (the one that most likely produced a trigger) was taken. Events with higher track multiplicities are rejected. Combination of

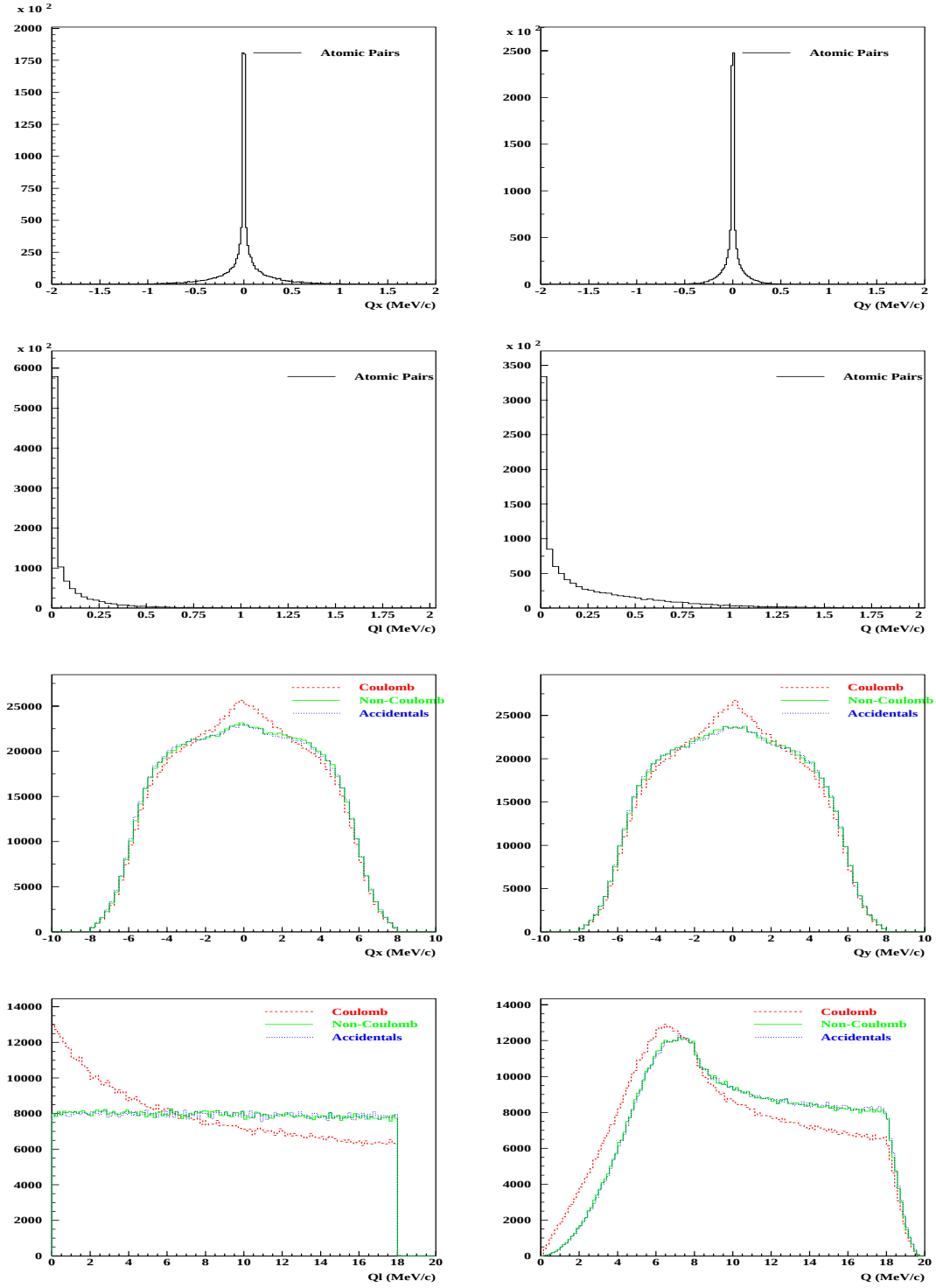

Fig. 6.6: MC input distributions at production. Top two rows: atomic pairs. Bottom two rows: background pairs. Transverse relative momentum cuts $Q_{trans} < 8$ MeV/c and a $Q_l < 18$ MeV/c have been applied. The effects of the first cut can be observed in the gradual tapering off of Q_x and Q_y distributions starting around 6 MeV/c. The effect of this cut can also be observed in a cusp around 6 MeV/c in Q, with the rest of the Q spectrum dominated by the Q_l component. (The distributions shown have been normalized to 10^6 events.)

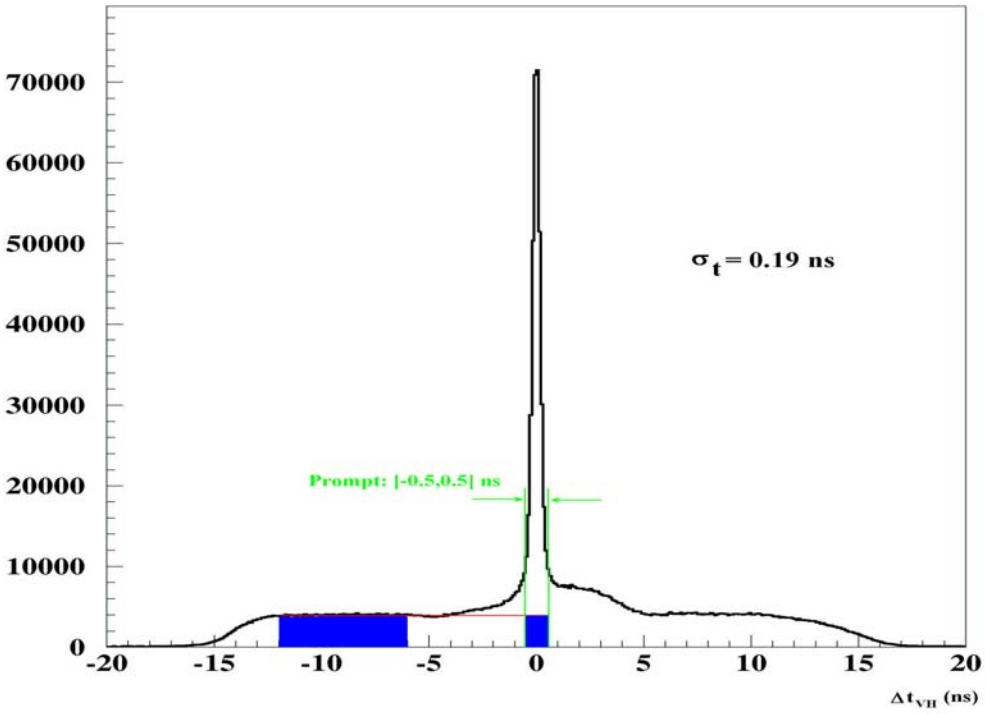

Fig. 6.7: Triggered pion pair time difference between the negative and positive arms as measured by the vertical hodoscope (2002 distribution for the single layer Ni target is shown). The fraction of accidentals in the prompt region of $[-0.5, 0.5]$ ns is found by straight line extrapolation of accidentals in the interval $[-12, -6]$ ns. (The irregular shape to the right of the peak is due to the timing gate misalignment for the 2002/2003 runs (cf. Fig 3.12).)

this and the previous cuts reduces the initial number of events by roughly 60%, this number being strongly dependent on the run conditions.

- Events with identified electron tracks in the downstream area of the setup were removed. (While most of the electron events are rejected by the T1 trigger, the undetected events due to detection inefficiency may be rejected offline by setting the pion threshold at 75 ADC counts in the negative arm and 62 counts in the positive. Sample contamination due to these events constitute only a fraction of a percent.)

- Events with identified muon tracks [39] in the downstream area of the setup were removed. (The muon contamination is found to be about 10%).

- The following relative momentum cuts were applied: $Q_{trans} < 4$ MeV/c and $|Q_l| < 15$ MeV/c[3]. The first cut is found to be broad enough to entirely contain signal events, and the second was chosen to optimize the stability region of the MC-simulated background while keeping the the Q_l (and Q) range large enough to provide an accurate background fit.

- Only **prompt** events defined by the $-0.5 < \Delta t < 0.5$ ns time difference between the negative and positive arm of the vertical hodoscope were kept (Fig.6.7).

We emphasize that the same set of cuts were applied to the experimental as well as the Monte Carlo distributions.

6.2.2 Simulating the SFD response

As mentioned previously, the scintillating fiber detector plays a crucial role in the track fitting procedure. How well its response is simulated has a direct effect on the Q_x, Q_y and, hence, on the Q distribution, in particular, its low value region, where

[3]This cut was applied at the final stage of selection. The set of cuts $|Q_x| < 6$ MeV/c, $|Q_y| < 6$ MeV/c and $|Q_l| < 45$ MeV/c is applied at the first stage of event selection, followed by the stronger final cuts $Q_{trans} < 4$ MeV/c and $|Q_l| < 15$ MeV/c.

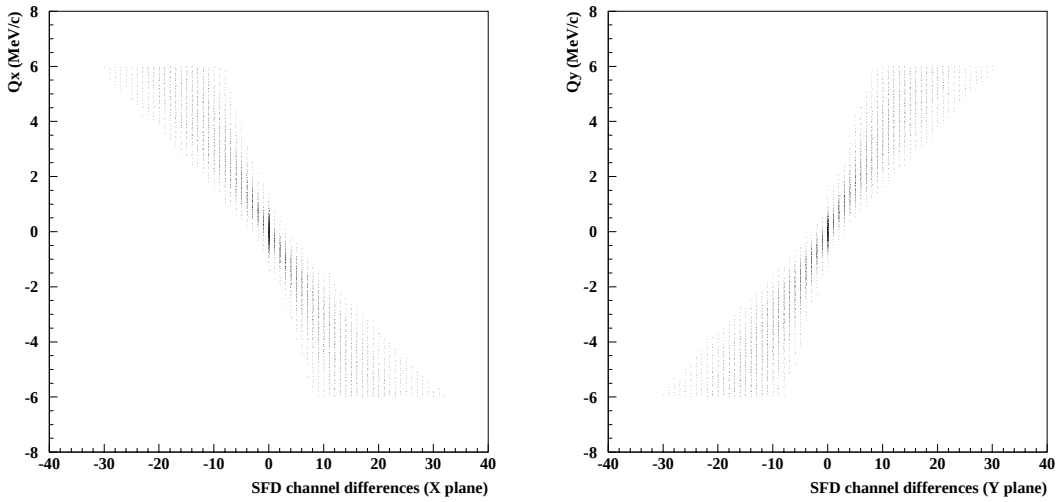

Fig. 6.8: X and Y projections of relative momenta *vs.* SFD hit fiber differences in the X and Y plane, respectively. Each hit fiber difference can be seen to set a range where a corresponding Q can be found. The events shown here satisfy the selection criteria of the previous section, with the exception of the looser $|Q_x| < 6$ MeV/c, $|Q_y| < 6$ MeV/c cuts (evidenced by the sharp horizontal cutoffs).

the signal can be found. Fig. 6.8 illustrates the importance of the SFD X and Y plane[4] performance in determining the transverse components of relative momenta.

As described in Section 3.2.2, the SFD readout is performed by the peak-sensing circuit (PSC), whose function is to simultaneously process amplitudes from a channel "triplet" applying $2A_i-(A_{i-1}+A_{i+1}) \lessgtr U_{thr}$ logic, where A_i, A_{i-1} and A_{i+1} are the hit amplitudes and U_{thr} is a DC threshold. While it considerably reduces cross-talk, this algorithm has a non-negligible probability of rejecting a valid signal. For example, two particles having grazed a pair of neighboring fibers, may produce a pair of signals A_i and A_{i-1} of comparable magnitude. The PSC logic may then reject either A_i or A_{i-1} if $2A_i - (A_{i-1} + A_{i+1}) < U_{thr}$ or $2A_{i-1} - (A_{i-2} + A_i) < U_{thr}$. In essence, the action of the algorithm in this case is to "merge" two hits into one.

Fig. 6.9 illustrates the effect of merging on the SFD hit fiber differences for the hits associated with the track. The dips at +1, -1 point to the removed hits, and the excess height at 0 indicates that the pair of tracks has been forced to pass through a

[4]The SFD U plane was not used in track reconstruction.

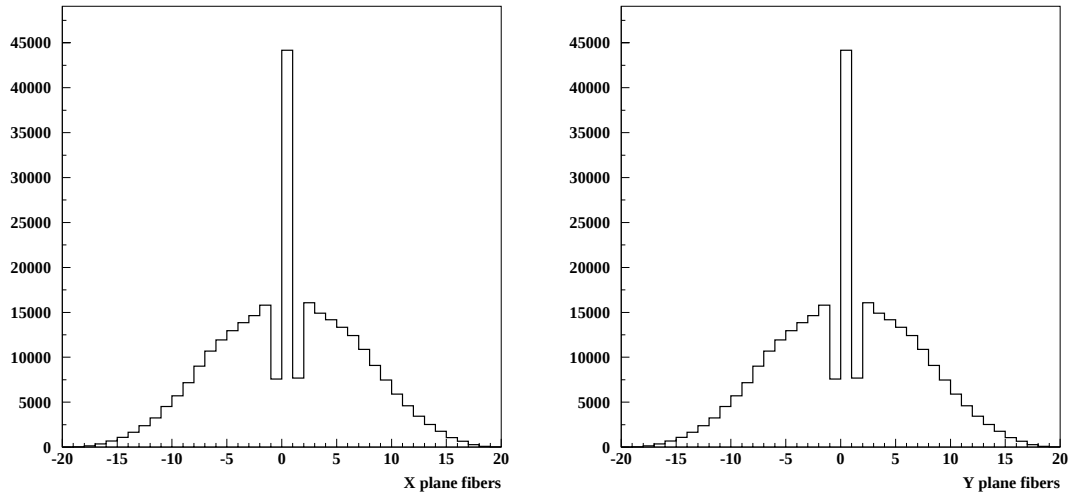

Fig. 6.9: SFD hit fiber differences in the X and Y plane. The central peak and the adjacent dips show the effects of the peak sensing circuit.

single hit after the merging. It has been verified that the combined size of the dips is roughly equal to the excess height of the peak above the rest of the SFD distribution.

The relative weights of the three bins in the $[-1, +1]$ experimental hit difference interval were taken as a basis for simulating the SFD merging for the MC-generated background (CC, NC and ACC). After the digitization in ARIANE, once a pair of hit fibers was found to be adjacent, a random number was generated according to the central 3 hits in the distribution above. In the event when the random number was 0, one of the MC hit fibers was eliminated (whether it was the left adjacent channel or the right channel, was decided, once again, by generating two random weights based on the relative heights of the experimental -1 and +1 bins). The same experimental -1, 0, 1 weights were applied to all three background distributions.

The peak at 0 channel difference was treated differently depending on the type of tracking used. The Monte Carlo SFD distributions were found to agree better with the experimental data for the modified tracking than the standard one. If one adds the MC Δ_{SFD} distributions in correct proportions found from the fits, one obtains the plot as shown Fig. 6.11. For the *standard* tracking SFD peak value at 0 was adjusted by changing the IH double ionization thresholds after the tracking was completed.

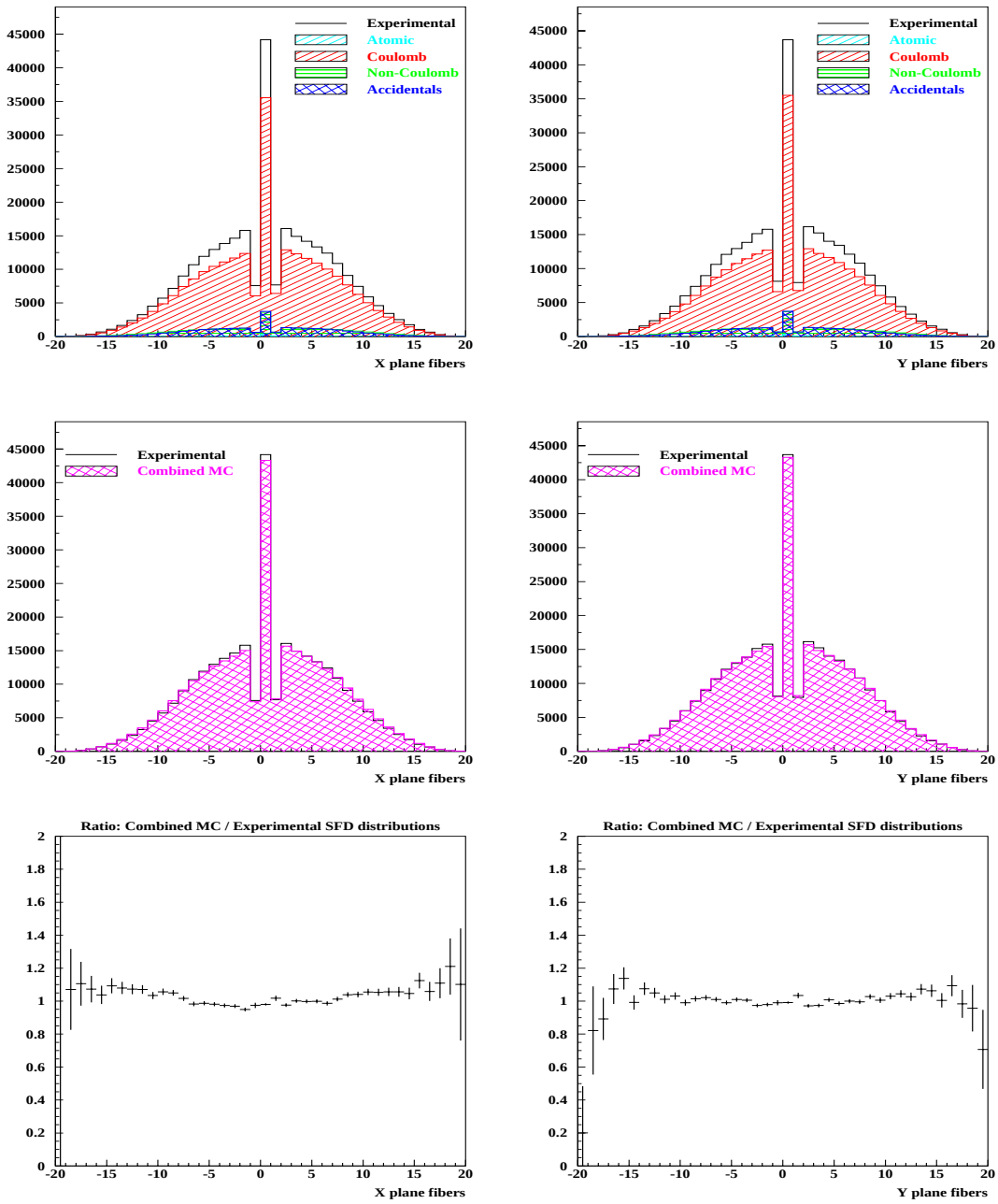

Fig. 6.10: SFD X and Y plane hit differences with modified tracking. Top row: experimental, MC background and MC atomic pairs distributions shown separately with their correct contributions to the prompt signal (described in detail later in this section). Middle row: Comparison of the combined MC (cross-hatched plots) and the experimental distributions. Bottom row: ratio of the combined MC to the experimental distributions. The area around the central peak is seen to be in agreement; away from it the MC distributions are found to be slightly wider than the experimental ones.

Changing the values of the double ionization cut changes the number of the accepted single hit events (peak at 0). Thus, the former were adjusted in such a way that the ratio of the sum of the bins located at -2. and +2., to the sum of three central bins (-1., 0., 1.) for the MC SFD distribution yields the same result as the analogous ratio for the experimental distribution. This procedure has the effect of redistributing the signal events without influencing the signal-free regions, thus, as a result, the integral number of atomic events is unchanged (cf. Fig. 6.8).With the *modified* tracking the double ionization thresholds were based on the experimental values and were preset before the tracking was performed.

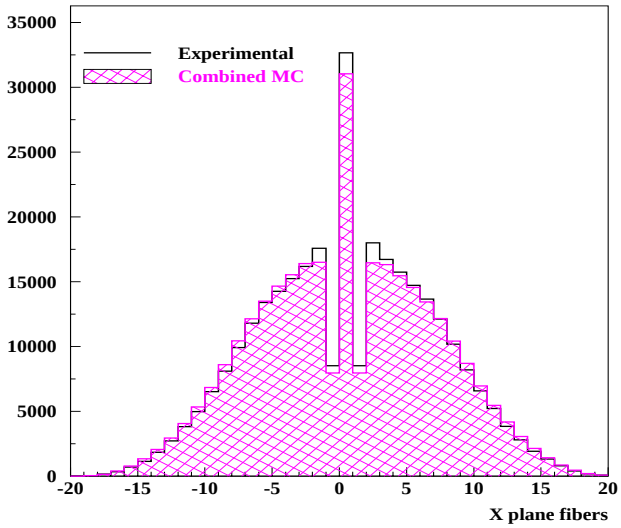

Fig. 6.11: Standard Tracking: SFD hit fiber differences for the X plane with MC distributions added together. The central three bins show the discrepancy between the Monte Carlo and experimental data.

With both methods we have considered the single hit inefficiency, which occurs when a particle passes through a single fiber without the hit being registered. This probability was estimated to be 7.6% (Appendix A and [40]) and thus the same percentage of MC-digitized hits were removed[5].

The results of applying the merging procedure and single hit inefficiency are shown

[5]Additional inefficiency due to the SFD background has been studied and simulated, but has not been shown to have a significant effect on the final results (see Appendix C and Ref. [41])

in Fig. 6.10. The atomic pair and background distributions seen in the figure are given in proportions obtained from fitting Q_l and Q spectra described later in the chapter. We see that the overall Monte Carlo shape and the merging/single hit inefficiency has been simulated correctly and that the MC events reproduce well the experimental SFD hit difference distributions.

6.3 Signal Extraction

In Fig. 6.12 we show the Q_x, Q_y and Q_{trans} ($= \sqrt{Q_x^2 + Q_y^2}$) components of the experimental and Coulomb-correlated distributions after the cuts described in Section 6.2.1 have been applied. As is evident from the plots, the Coulomb background

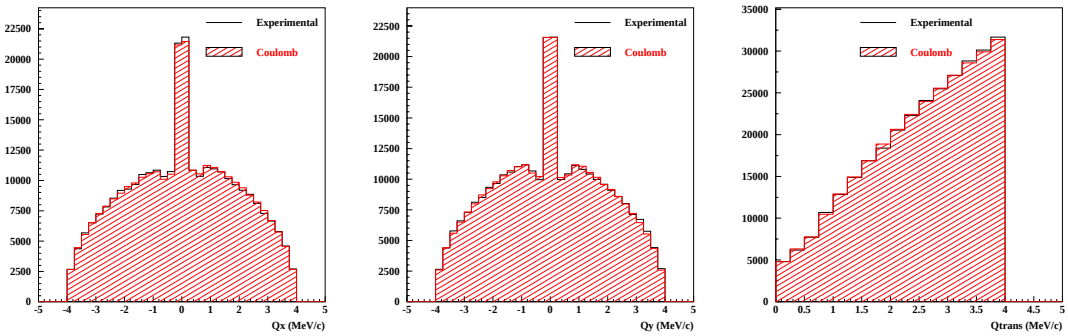

Fig. 6.12: Q_x, Q_y and Q_{trans} components of relative momenta for the experimental data (unshaded histogram) and Coulomb pairs (cross-hatched histogram) are virtually identical. Signal extraction from these relative momenta components is not feasible. (The central peak and the adjacent dips are caused by the peak-sensing circuit and reflect the shapes in Fig. 6.10)

is virtually indistinguishable from the prompt experimental spectra. Therefore, we conclude that the signal extraction cannot be accomplished with any of the transverse relative momenta components, and the relative momenta projections containing a longitudinal component need to be considered.

Indeed, the Q_l and Q projections do yield the observable excess number of events in the low value regions (Fig. 6.13). It must be noted that the accidental and non-Coulomb spectra have very similar shapes due to the fact that the pairs of pions, which produce these events, originate from uncorrelated sources. This similarity in shape

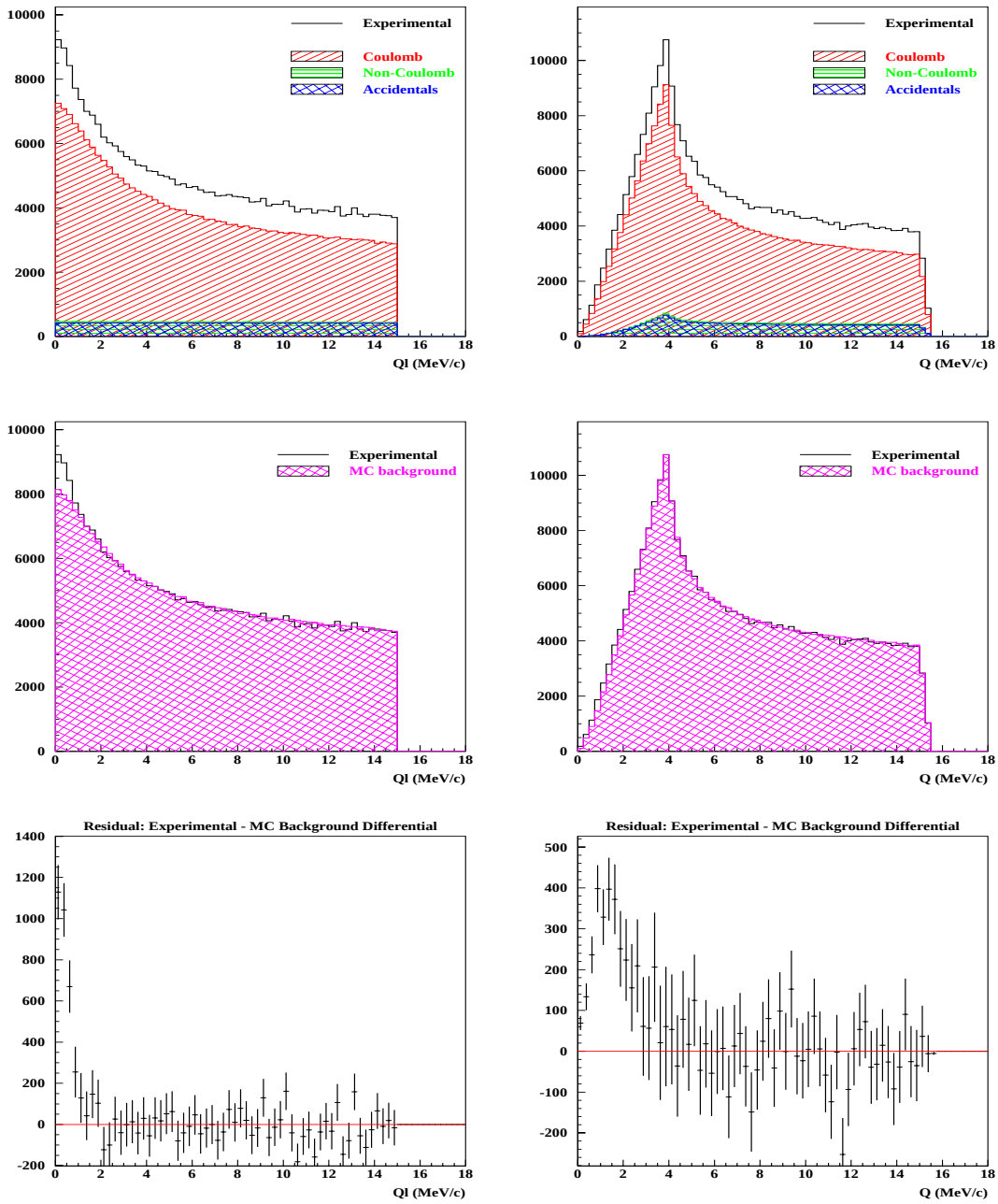

Fig. 6.13: Signal and MC background for the 2002 experimental data with modified tracking. Q_l and Q components of relative momenta for the experimental distributions, as well as the Coulomb, non-Coulomb and accidental pairs are shown (top row). The accidental and non-Coulomb distributions have a very similar shape in Q_l and Q. However, the accidental contribution is fixed by a parameter determined from real data, and since Coulomb and non-Coulomb shapes are distinct, the background can be fit to the experimental data yielding the signal for Q_l and Q (middle row). Bottom row: results of subtracting the MC background from the experimental distributions. The atomic pair peak is clearly visible on top of the background difference centered around 0.

could adversely affect the accuracy of the background fit. Fortunately, due to the fact that the accidental contribution can be extrapolated from the experimental data (described in more detail in Section 7.2) and the fact that Coulomb and non-Coulomb shapes are distinct, background fitting can be performed without any hindrance.

With the accidental distribution fixed, *CC and NC spectra (Fig. 6.13) can be fitted in the intervals where the atomic signal vanishes*, i.e. for $|Q_l| > 2$ MeV/c and $Q > 4$ MeV/c. As a result of the fit, a clear excess of experimental events in the $|Q_l| \leq 2$ MeV/c and $Q \leq 4$ MeV/c intervals can be observed. The atomic pair signal (the dissociated atoms) is found by a simple subtraction of the MC background from the experimental events.

Chapter 7

Dual and Single Target Methods

The single layer target configuration was used by the experiment until the end of the 2001 run. For the 2001 run, which has produced the most stable results so far, our experiment collected data with 94 μm and, subsequently, with the 98 μm single layer Ni target. For this run period the atomic pair signal was extracted by exploiting the relationship between the number of atomic and the number of Coulomb pairs produced in a target subject to a relative momentum cut [45][46]. Below we describe this method in more detail as well as the alternative procedure, which relies on the combination of a single-foil and multi-foil targets, the **dual target method**. This configuration was introduced in 2002 and consisted of a segmented Ni target consisting of 12 planes separated by 1 mm gap [50]. The combined 96 μm thickness of all the planes was chosen to be approximately equal to that of the single layer 98 μm Ni target. The dual target procedure will be used in this thesis to analyze the 2002 and 2003 data. It should be noted, that the data collection for the 2001 and 2002 runs were performed with the 24 GeV proton beam, whereas in 2003 20 GeV beam was used. Between 2001 and 2002 the setup has undergone one change, when the SFD U plane was introduced.

7.1 Breakup Probability with the Single Target Method

As described previously, the breakup probability is defined as the ratio of the number of atomic pairs resulting from the $A_{2\pi}$ breakups over the initially produced number of $A_{2\pi}$'s[1]:

$$P_{br} = n_A/N_a \tag{7.1}$$

The initial number of atoms N_a, an unknown quantity, can be expressed via the number of produced Coulomb pairs N_{CC} with Q at the point of breakup less than 2 MeV/c and the proportionality factor, K-factor, $K_{th} = 0.615$ [18]:

$$P_{br} = \frac{n_A}{K_{th} N_{CC}(Q_{init} < 2\,MeV)} \tag{7.2}$$

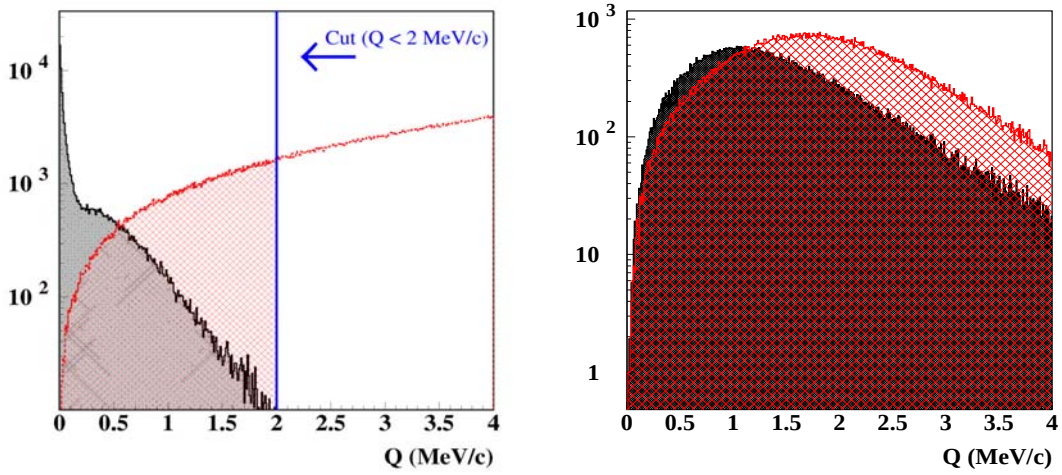

Fig. 7.1: Atomic and Coulomb pair Q distributions at the origin (left). Same distributions after track reconstruction (right). Shape smearing after reconstruction is mainly due to multiple scattering in the target.

The number of atomic pairs n_A is determined from the experimental events after applying cuts on the reconstructed relative momentum distributions. For kinematic reasons, an identical cut needs to be applied to the Monte Carlo CC distributions.

[1]For simplicity, from here on we will occasionally omit the differential rates: e.g., instead of $\sum_i n_A(Q_i)$, we will use simply n_A.

The Q distribution at the origin Q_{init}, shown in Fig. 7.1, is greatly distorted by the apparatus acceptance and multiple scattering in the target and the setup. Additionally, the applied trigger, and detector and tracking inefficiencies also modify the original distribution. Thus, the relative momentum at breakup cannot be substituted for the reconstructed relative momenta.

And, in order to take these effects into account, the breakup probability must be redefined in terms of the *effective* K-factor K_{eff} as:

$$P_{br} = \frac{n_A(Q < Q_{cut})}{K_{eff} N_{CC}(Q < Q_{cut})}, \tag{7.3}$$

where Q is the reconstructed relative momentum. We note that Eq. 7.2 and Eq. 7.3 can be equally well applied to the longitudinal component of the relative momentum, Q_l. The value of Q_{cut} is determined iteratively by scanning over different values of Q and Q_l distributions until the atomic pair yield from both spectra converges and stabilizes. The convergence of the atomic signal for is Q and Q_l is illustrated in Table 7.1 for 2001 data [46].

	n_A	N_{CC}	K_{eff}
Total produced	599267	14892663	
Produced with $Q^{init} < 2$ MeV/c	594799	315568	
$Q < 2$ MeV/c	105451±124	61694±16	0.5535±0.0007
$Q < 3$ MeV/c	125913±145	158948±41	0.2565±0.0003
$Q < 4$ MeV/c	131300±150	307297±79	0.1384±0.0002
$\|Q_l\| < 1$ MeV/c	120872±140	128173± 33	0.3054±0.0004
$\|Q_l\| < 2$ MeV/c	130217±149	237736± 61	0.1774±0.0002

Table 7.1: Detected atomic (n_A) and Coulomb pairs (N_{CC}) for the 94 μm target (run 2001) with reconstructed Q and Q_l, where the setup acceptance, trigger and reconstruction efficiencies are taken into account. The atomic pair yield for Q and Q_l converges for $Q < 4$ MeV/c and $|Q_l| < 2$ MeV/c, i.e. when the signal integrated out completely [46].

Combining Eq. 7.2 with Eq. 7.3, the experimental K-factor is obtained:

$$K_{eff} = K_{th} \frac{n_A(Q < Q_{cut})}{n_A} \frac{N_{CC}(Q_{init} < 2\,MeV)}{N_{CC}(Q < Q_{cut})}. \tag{7.4}$$

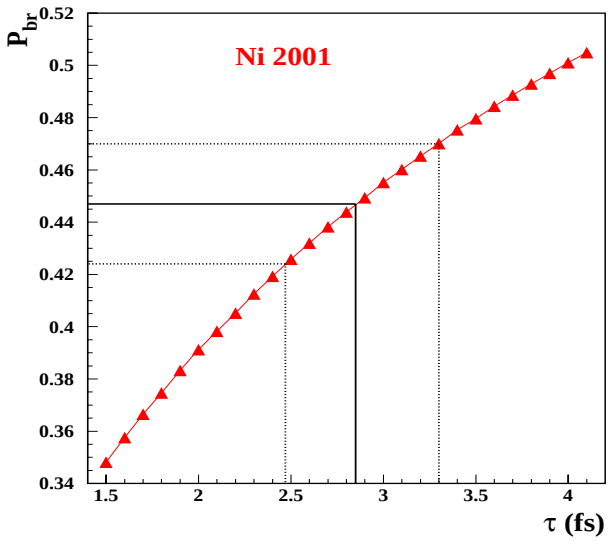

Fig. 7.2: Pionium breakup probability *vs.* lifetime dependence for Ni 2001 data. Shown is the 0.447 breakup probability corresponding to 2.85 fs lifetime value.

With the efficiencies defined as $\epsilon_A = \frac{n_A(Q<Q_{cut})}{n_A}$ and $\epsilon_{CC} = \frac{N_{CC}(Q<Q_{cut})}{N_{CC}(Q<2)}$, breakup probability of Eq. 7.3 becomes:

$$P_{br} = \frac{\epsilon_{CC}}{\epsilon_A} \frac{n_A(Q < Q_{cut})}{K_{th} N_{CC}(Q < Q_{cut})} \tag{7.5}$$

After performing the analysis, similar to the one that presented in Table 7.1, the breakup probability can be found using Eq. 7.5. For 2001 single layer Nickel data the breakup probability was found to be [46]:

$$P_{br} = 0.447 \pm 0.020\,(\text{stat.}) \pm 0.009\,(\text{syst.}), \tag{7.6}$$

Using breakup probability *vs.* lifetime parametrization shown in Fig.7.2, the value of lifetime was found to be:

$$\tau = 2.85^{+0.48}_{-0.41}\ \text{fs}. \tag{7.7}$$

7.2 Overview of the Dual Target Method

The multilayer target configuration is shown schematically in Fig. 7.3. The absence of material in the interlayer gaps of the multilayer target forces the pionium

atoms to decay into two neutral pions, as the competing processes of excitation and breakup do not interfere in these regions. Since the traversed thicknesses of the target material in the single and multilayer configurations are very similar, the relative momenta distributions of the atomic pairs have the same shape, but *lower* peak value due to the annihilations, and the background distributions are *unaffected* by the choice of target. Experimentally, this difference can be observed in the form

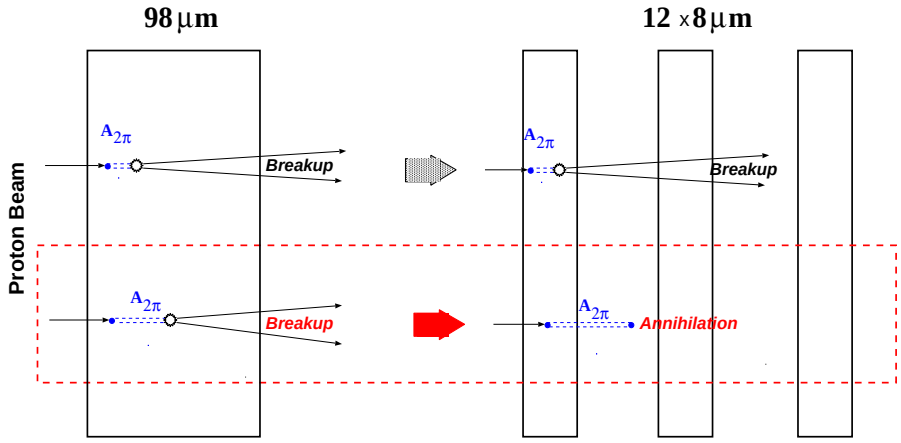

Fig. 7.3: Diagram showing single layer (left) and multilayer (right) target configurations. Pionic atoms formed in the multilayer target have a higher annihilation probability in the interlayer gaps, hence the breakup yield from the multilayer is lower than from the single layer target.

of an excess number of the low-Q events in the single layer target distribution over the multilayer one (Fig. 7.4). The equivalence of the single and multilayer backgrounds is illustrated in Fig. 7.5, where we compare the Q_l and Q yields for single and multilayer *experimental* accidental ($\Delta t_{VH} = [-11, -6]$ ns) events. The comparison of *Monte Carlo-simulated* prompt background events (Coulomb, non-Coulomb and accidentals) for the single and multilayer targets may be found in Appendix C. As is evident from the plots in Fig. 7.4 and 7.5 and Appendix C, utilizing the single foil target results in more dissociated pairs, while the rates and the shapes of the background pair distributions are the same for both target configurations.

We will begin the main part of our analysis by normalizing single layer experimental background Q_l and Q distributions to the multilayer ones (the inverse operation is,

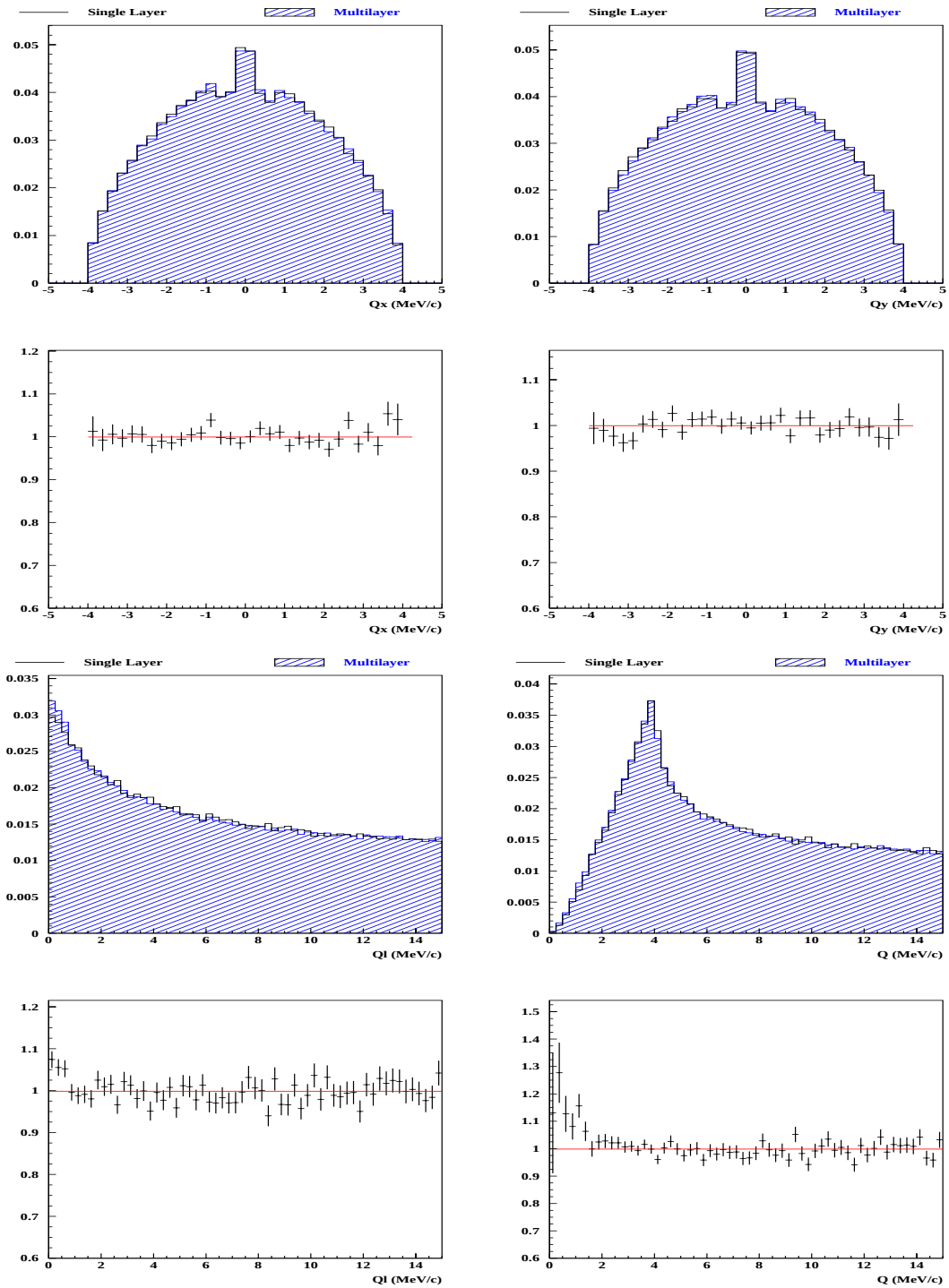

Fig. 7.4: Single and multilayer target distributions with the ratios of the former over the latter. (Single layer distribution is normalized to multilayer one in the signal free region.) Excess events in Q_l and Q corresponding to the excess atomic pair signal in the single layer target can be observed in Q_l and very prominently in Q projections, while the ratios in the signal-free intervals are flat indicating that the single and multilayer backgrounds are identical. The corresponding signal enhancements in Q_x and Q_y cannot be distinguished (see Section 6.3). (2002 events with standard tracking are shown.)

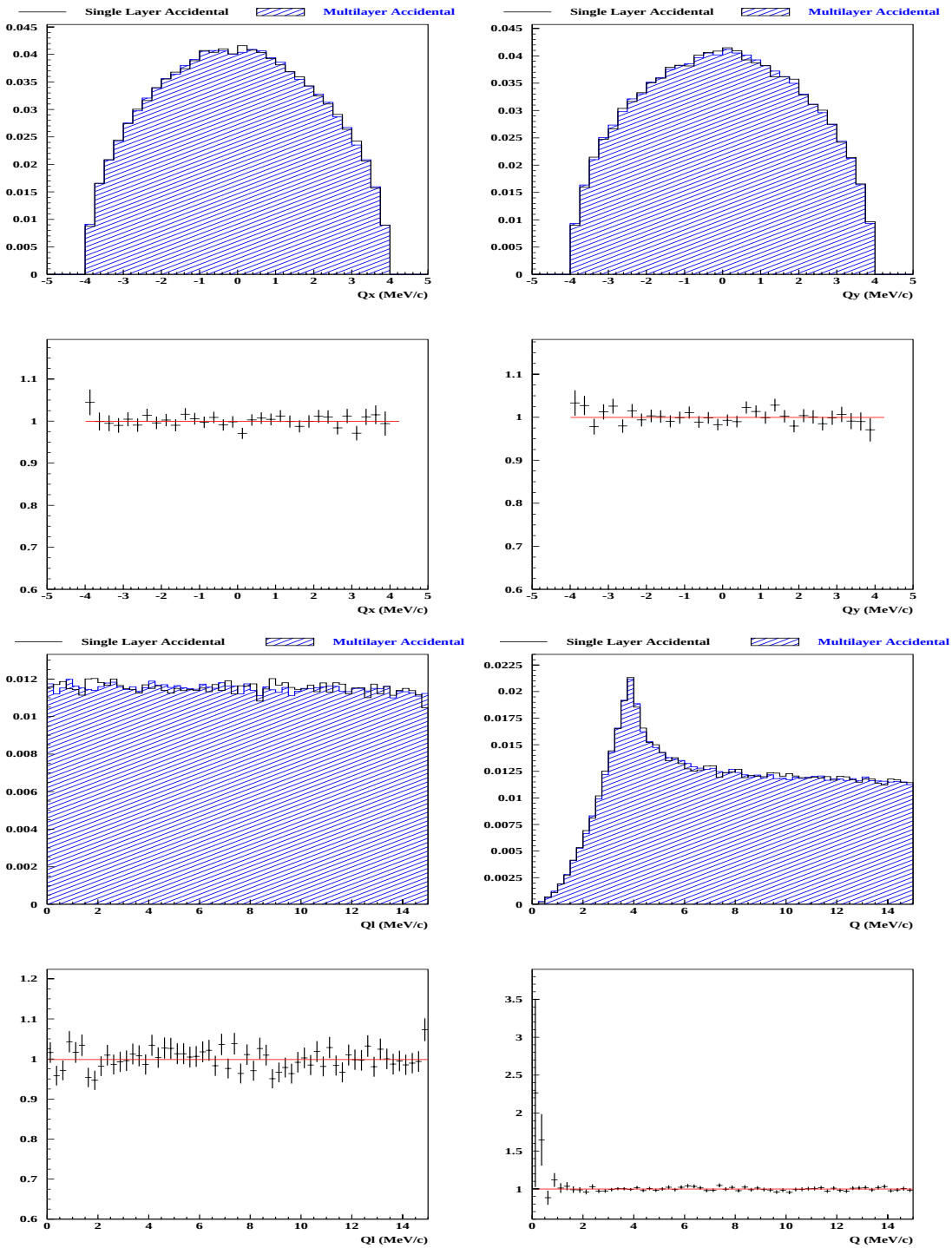

Fig. 7.5: Single to multilayer relative momenta components (normalized to 1) and the ratios of the 2002 experimental accidental ($\Delta t_{VH} = [-11, 6]$ ns) events (standard tracking). Flatness of the ratios confirms that the single and multilayer backgrounds are virtually identical.

obviously, equally valid), this operation being permitted by their equivalence. This, as discussed previously, amounts to normalizing the corresponding experimental spectra in the signal-free regions, $Q_l > 2$ MeV/c and $Q > 4$ MeV/c. Taking into account the definition of breakup probability (Eq. 7.1), one then has:

$$\frac{dN^s_{exp}(Q)}{dQ} = \frac{dN^s_{at}(Q)}{dQ} + \frac{dN_B(Q)}{dQ} = P^s_{br}\frac{dN^{init}_{at}(Q)}{dQ} + \frac{dN_B(Q)}{dQ} \tag{7.8}$$

$$\frac{dN^m_{exp}(Q)}{dQ} = \frac{dN^m_{at}(Q)}{dQ} + \frac{dN_B(Q)}{dQ} = P^m_{br}\frac{dN^{init}_{at}(Q)}{dQ} + \frac{dN_B(Q)}{dQ}, \tag{7.9}$$

where $dN^s_{at}(Q)/dQ$ and $dN^m_{at}(Q)/dQ$ are the atomic pair yields from the single and multilayer targets, respectively, N^s_{at} and N^m_{at} replace the n_A and N^{init}_{at} takes place of N_a in Eq. 7.1, P^s_{br} and P^m_{br} are the single and multilayer breakup probabilities, and $dN_B(Q)/dQ$ denotes the background distribution.[2] It should be noted that, in addition to the backgrounds being identical, the number of created atoms N^{init}_{at} is also the same for both types of targets due to their identical composition and overall thickness.

Taking the difference of Eq. 7.8 and 7.9, one then has:

$$\frac{dN^s_{exp}(Q)}{dQ} - \frac{dN^m_{exp}(Q)}{dQ} = \frac{dN^s_{at}(Q)}{dQ} - \frac{dN^m_{at}(Q)}{dQ} = (P^s_{br} - P^m_{br})\frac{dN^{init}_{at}(Q)}{dQ} \tag{7.10}$$

We note that in this expression the normalized single and multilayer backgrounds cancel out and one is left with the pure difference of atomic signals. Thus, the single-multilayer experimental difference allows us to observe the atomic pair signal in the "cleanest" possible way. For improved statistical accuracy, this differential will be fitted with the MC-simulated atomic pair signal. We call the corresponding fit parameter δ.

One may also define a new quantity, the *ratio of breakup probabilities*, ρ. Then:

$$\rho \equiv \frac{P^s_{br}}{P^m_{br}} = \frac{P^s_{br}\sum_i N^{init}_{at}(Q_i)}{P^m_{br}\sum_i N^{init}_{at}(Q_i)} = \frac{\sum_i N^s_{at}(Q_i)}{\sum_i N^m_{at}(Q_i)}, \tag{7.11}$$

Hence, the determination of the ratio of the atomic signal strengths leads directly to the ratio of single-to-multilayer breakup probabilities.

[2] In this chapter Q should be understood to mean both the longitudinal and the total relative momenta components.

The value of ρ may be found by fitting the so-called "pure" background. This background corresponds to the distribution in which the signal has been eliminated:

$$\rho\frac{dN^m_{exp}(Q)}{dQ} - \frac{dN^s_{exp}(Q)}{dQ} = \rho\left[\frac{dN^m_{at}(Q)}{dQ} + \frac{dN_B(Q)}{dQ}\right] - \left[\frac{dN^s_{at}(Q)}{dQ} + \frac{dN_B(Q)}{dQ}\right] \quad (7.12)$$

$$= (\rho - 1)\frac{dN_B(Q)}{dQ},$$

Here the N_B spectra constructed out of the Monte Carlo-simulated Coulomb, non-Coulomb and accidental events will be fitted to the experimental Q_l/Q distributions on the left-hand side of Eq. 7.12.

The combination of δ, the difference of breakup probabilities, and ρ, their ratio, completely specifies the individual values of P^s_{br} and P^m_{br}. But since the direct functional dependence of P^s_{br}/P^m_{br} on the pionium lifetime has been calculated, the individual probabilities will not be of concern to us here. The lifetime can then, in principle, be determined directly from the "pure" background fit in Eq. 7.12; however, in order to improve the precision of our final result, the experimental differential (described above) and the sum of the single and multilayer spectra have been added to the evaluation of ρ. The sum of the single and multilayer spectra distributions can be expressed as:

$$\frac{dN^s_{exp}(Q)}{dQ} + \frac{dN^m_{exp}(Q)}{dQ} = \left[\frac{dN^s_{at}(Q)}{dQ} + \frac{dN^m_{at}(Q)}{dQ}\right] + 2\frac{dN_B(Q)}{dQ} \quad (7.13)$$

$$= (P^s_{br} + P^m_{br})\frac{dN^{init}_{at}(Q)}{dQ} + 2\frac{dN_B(Q)}{dQ},$$

The experimental distributions found on the left-hand side of Eq. 7.13 will be fitted with the MC-simulated background spectra (corresponding to the $2dN_B(Q)/dQ$ term) and the atomic pair shape (corresponding to $dN^s_{at}(Q)/dQ + dN^m_{at}(Q)/dQ$ distributions). We call the fit parameter corresponding to the $dN^s_{at}(Q)/dQ + dN^m_{at}(Q)/dQ$ term σ.

The final value of the ratio of breakup probabilities will be obtained by simultaneously fitting Eq. 7.10, 7.12 and 7.13. We note that in the combined fit three fitting parameters will be used: δ, ρ and ω. The last parameter, to be discussed in more detail in the following chapter, describes the contribution of Coulomb pairs to the

sum of Coulomb and non-Coulomb backgrounds.[3] We also note that one of the three fit parameters, δ, ρ and σ, described previously is superfluous and can be expressed in terms of the other two. We have chosen to eliminate σ, by expressing it through:

$$\sigma = \frac{\delta(\rho+1)}{\rho-1}. \tag{7.14}$$

With this relationship σ enters the combined fit not as an independent fit parameter, but rather as a constraint.

7.3 The Dual vs. Single Target Method

The critical advantage of using the dual target procedure over the single target method is in significant reduction of the overall systematic error. By considering the *ratio* of breakup probabilities, as opposed to calculating each separately, one eliminates the need for both the K-factor and for a precise description of the Coulomb background in the low Q region (Eq. 7.1 and 7.11), which enters crucially in the determination of the breakup probability (Eq. 7.3). From Eq. 7.3 and 7.5 it is obvious that any uncertainty in determining the shape of the Coulomb pairs in the low Q region will be amplified by a sizeable K-factor, significantly reducing the precision of the determination of the breakup probability. Additionally, with the dual target method one disposes of the need to perform cut optimizations, such as the ones found in Table 7.1. Other potential sources of the systematic error, such as the reconstruction efficiencies ϵ_{CC} and ϵ_A, are also eliminated. In the final section of the next chapter we will apply the so-called *finite size correction function* to the Coulomb pairs and demonstrate that the atomic pair yield is significantly less sensitive to the background shape with the single/multilayer procedure compared to the standard method.

[3] ω found here and in the rest of this work relates the same distributions as ω_s of Eq.6.6.

Chapter 8

The Dual Target Analysis

In what follows we discuss three different Monte Carlo fits to the experimental data, which will lead to the ratio of single to multilayer breakup probabilities for the 2002 and 2003 run data samples. In this work we analyze separately two tracking procedures, *standard* and *modified*, which, together with the two run periods, make up four data sets. Run period and tracking method uncertainties will be discussed in the section describing the systematic effects. The final value of the single/multilayer ratio of breakup probabilities and the resulting lifetime is quoted by performing a simultaneous fit on all four data sets.

8.1 Choice of the MC Simulation and the Overall Statistics

In 2002 data collection was performed with the 24 GeV incident proton beam, whereas in 2003 data were collected with 20 GeV protons. At the time of this analysis, the 20 GeV MC simulation was not yet available; in its place we use 2002 24 GeV simulation to fit 2003 experimental data. In Fig. 8.1 we compare the essential prompt single layer 24 GeV distributions with their counterparts of 20 GeV. The fact that the ratios of the Q_l and Q distributions are flat outside the signal regions and the values of χ^2 obtained from the Monte Carlo fits found later in the chapter indicate that the

use of the 24 GeV MC simulation to fit 20 GeV data is a reasonable approximation. However, more significant deviations are observed in the low-Q region pointing to the fact that a more precise analysis using the 20 GeV simulation for the 2003 run might be required.

In Table 8.1 we summarize the experimental and Monte Carlo statistics subject to the cuts described in the previous chapter.

Tracking	Standard		Modified	
	2002	2003	2002	2003
Exp. Single Layer	311170	100451	293987	95507
Exp. Multilayer	141503	94084	137009	89905
Atomic Pairs	100454		231622	
Coulomb Pairs	865427		1976242	
Non-Coulomb Pairs	578702		842622	
Accidentals	609720		892000	

Table 8.1: Top: Number of the experimental and Monte Carlo events after applying the cuts in Chapter 5.

8.2 Signal Extraction with Two Targets

In the next three sections we will show how the experimental Q_l and Q distributions may be fitted in order to find the ratio of single to multilayer breakup probabilities. Only two of the three fits below are truly independent, with the third one serving to improve the accuracy of the final result.

8.2.1 Single/Multilayer Target Differential

The single/multilayer target method allows us to observe the atomic pair signal in the most unbiased and straightforward way, and at the same time justify the assertion that the multilayer setup yields lower number of atomic pairs. First, we normalize the single layer background to the multilayer one by integrating Q_l distributions for both targets in the interval outside the signal region, i.e. $2 < |Q_l| \leq 15$ MeV/c.

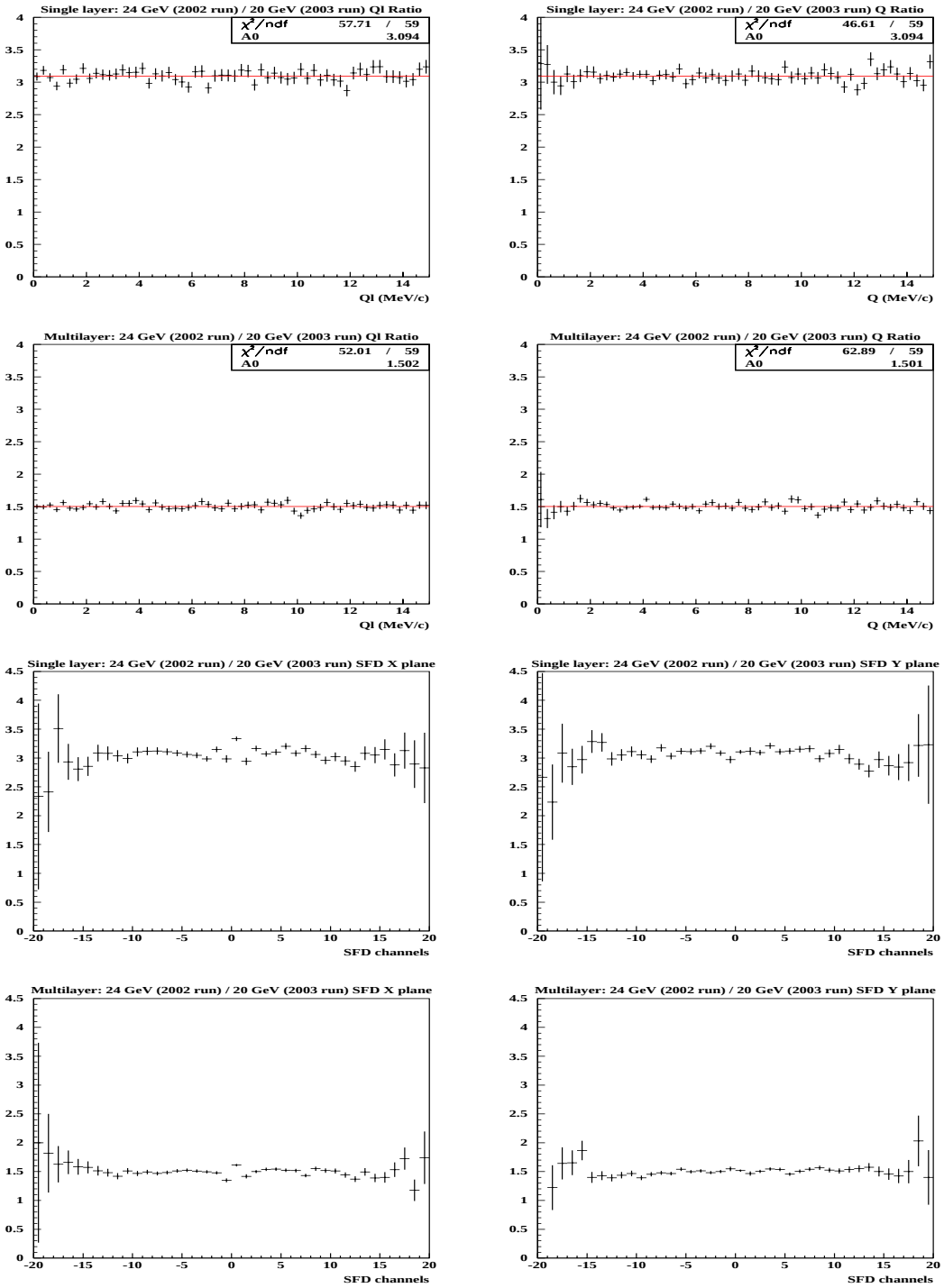

Fig. 8.1: Comparison of the 20 with the 24 GeV spectra for the single and multilayer targets. Top two rows: Ratios of Q_l and Q distributions are flat everywhere in Q_l and the signal-free regions of Q. There are, however, more sizable fluctuations in the low-Q region that might affect the uniformity of the signal. Bottom two rows: Hit channel differences for the events with two hits per SFD plane. The curvature of the SFD X and Y plane hit channel distributions are possible indications of the differences in signal strengths in the low relative momentum region.

The ratio of the sum of the multilayer events over the single layer one gives us the normalization constant ϵ, i.e.:

$$\epsilon = \sum_{i=9}^{60} N^m(Q_l^i) / \sum_{i=9}^{60} N^s(Q_l^i). \tag{8.1}$$

(Here, as throughout the chapter, 0.25 MeV/c binning is used. Thus the summation in the $2 < |Q_l| \leq 15$ MeV/c region corresponds to summation of bins 9 through 60.) The values of ϵ for 2002 and 2003 runs were determined to be

$$\epsilon\,(\text{Run2002}) = 0.4575 \pm 0.0016 \qquad \epsilon\,(\text{Run2003}) = 0.9415 \pm 0.0048 \tag{8.2}$$

for the *standard* tracking procedure; whereas for the *modified* tracking these values were:

$$\epsilon\,(\text{Run2002}) = 0.4684 \pm 0.0017 \qquad \epsilon\,(\text{Run2003}) = 0.9452 \pm 0.0049 \tag{8.3}$$

By multiplying Q_l and Q components of the experimental *single layer* distribution by the corresponding value of ϵ we obtain the plots, similar to those shown in Fig. 7.4. The low Q excess events and the equivalence of the single and multilayer backgrounds are especially pronounced after the single-multilayer subtraction (Fig. 8.3). The atomic pair enhancement is thus clearly visible on top of the background differential centered around zero.

The atomic pair shape fits in Q_l and Q shown in Fig. 8.2 have been made by minimizing the single/multilayer differential with respect to the MC-reconstructed atomic shape. Below we give the corresponding χ^2 function being minimized:[1]

$$\chi^2 = \sum_{i=1}^{60} \frac{[(\epsilon N^s(Q_i) - N^m(Q_i)) - \delta N_{at}(Q_i)]^2}{(\epsilon\sigma_{N^s(Q_i)})^2 + \sigma^2_{N^m(Q_i)}} \tag{8.4}$$

In the expression above N^s and N^m correspond to the experimental single and multilayer spectra, N_{at} stands for the MC-reconstructed atomic shapes, and Q_i is an individual bin value of the Q_l or Q spectra. $\sigma_{N^s(Q_i)}$ and $\sigma_{N^m(Q_i)}$ refer to the statistical errors of the experimental single and multilayer distributions. The values of the

[1] The fitting procedure was performed using the MINOS subroutine, available as a part of MINUIT [58] package (CERNLIB library).

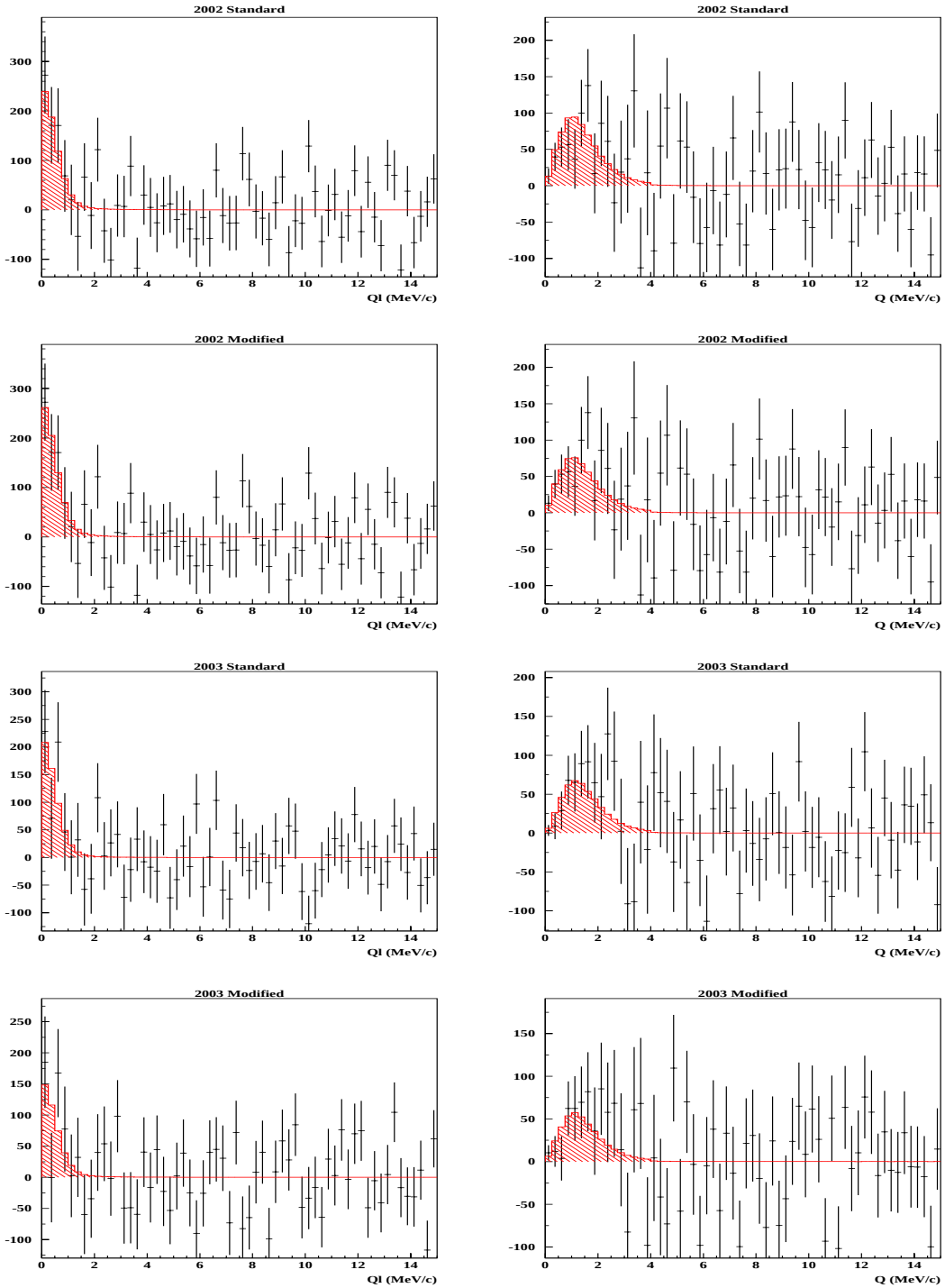

Fig. 8.2: Normalized single - multilayer differentials obtained with the standard and modified tracking procedures. Top two rows refer to the 2002 run, bottom two rows to the 2003 run. Also shown is the fitted MC-generated atomic pair events with the fit parameters found in the top Table 8.2. Atomic pair shape fits the differential within errors, however, the former is seen to be slightly narrower than the latter. Single and multilayer backgrounds match, as witnessed by the flatness of the differential outside the signal region.

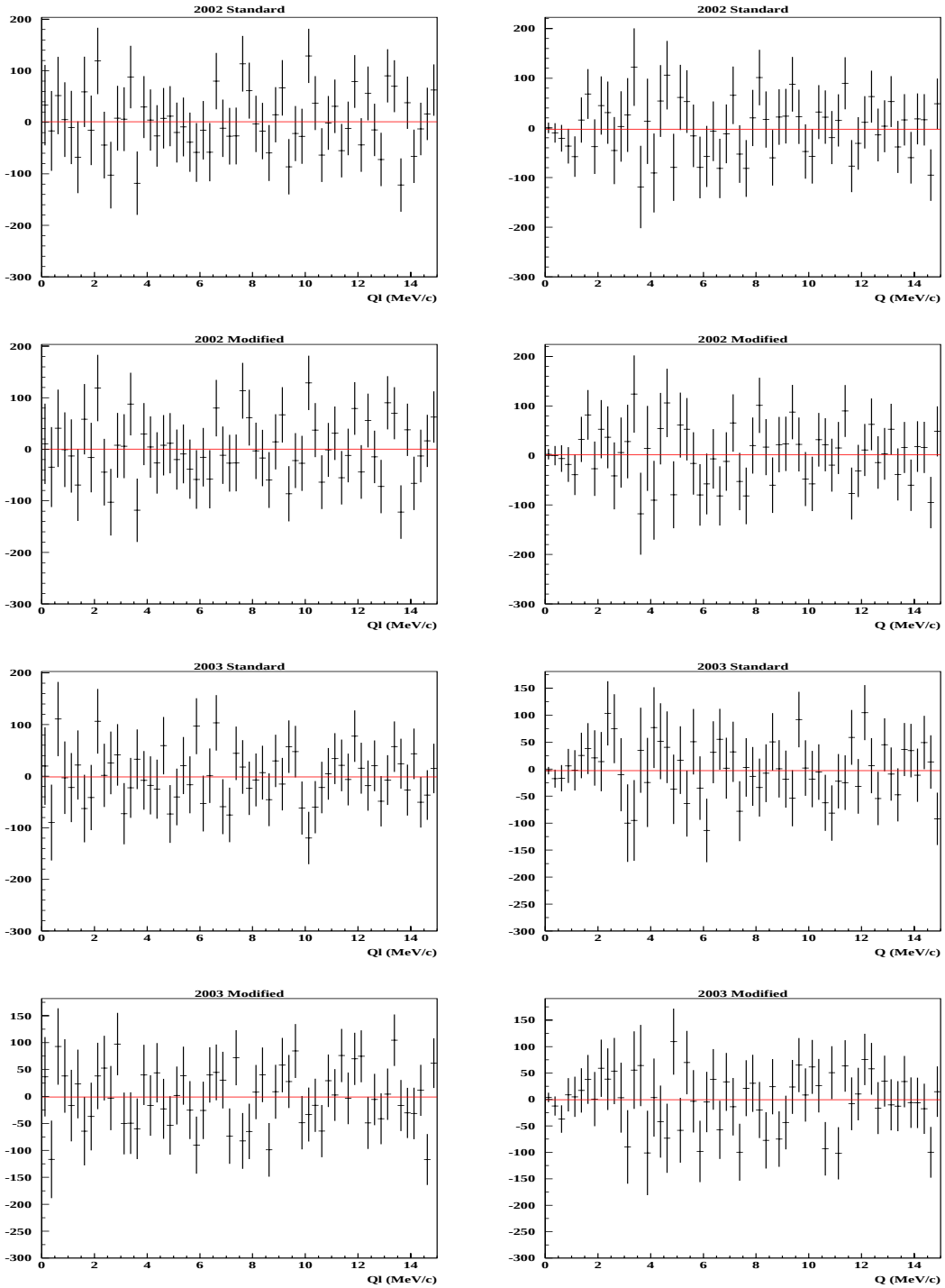

Fig. 8.3: Atomic pair events subtracted from the experimental differentials (Fig. 8.2). The slightly narrower atomic pair shape observed in Fig. 8.2 does not result in observable systematic deviations from 0 in the signal region.

	2002		2003	
Tracking	Q_l	Q	Q_l	Q
Standard	918 ± 109	722 ± 81	565 ± 103	483 ± 79
Modified	744 ± 111	545 ± 81	423 ± 104	407 ± 79

	2002		2003	
Tracking	$Q_l \leq 2$	$Q \leq 4$	$Q_l \leq 2$	$Q \leq 4$
Standard	846 ± 207	962 ± 235	490 ± 196	528 ± 221
Modified	704 ± 205	670 ± 234	370 ± 192	511 ± 217

Table 8.2: Top: Number of events from the *MC-simulated atomic pair fit* to the single-multilayer event differences for Q_l and Q with standard and modified tracking. Bottom: *Experimental single-multilayer differential* integrated from 0 to 2 MeV/c in Ql and 0 to 4 MeV/c in Q (the signal region).

fit parameter δ for various tracking procedures and run periods can be found in the top Table 8.2.[2] The numbers shown have been obtained by fitting the MC signal in the entire available fitting range, i.e. 0 to 15 MeV/c. Due to the high statistics of the MC-generated atomic pairs, the fit results were found to be virtually unchanged (with fluctuations of only a few events), regardless of the fit region.

In the bottom Table 8.2 the experimental differential integrated from 0 to 2 MeV/c in Ql and 0 to 4 MeV/c in Q is shown. The atomic pair yield from all the spectra should be approximately the same if the signal is completely contained by the Q_{trans} and Q_l cuts. The tabulated values of the atomic pair fit and the experimental differential show an overall agreement in Q_l and Q within 1σ uncertainty. Fig. 8.3 illustrates how well the simulated atomic pair shape reproduces the experimental differential. The atomic shape can be seen to slightly underestimate the width of the experimental signal (Fig. 8.2), however, as Fig. 8.3 indicates, this does not result in severe systematic deviations from zero.

[2]The relative uncertainties in ϵ, constituting a fraction of a percent for all four data samples, do not affect the fit parameters at the level of accuracy used here and, thus, have been neglected.

8.2.2 Signal from the Fit to the Extracted Background

In Section 8.2.1 the single-multilayer target Q_l and Q spectra led to the "pure" atomic signal. In this section we discuss how the signal can be obtained by con-

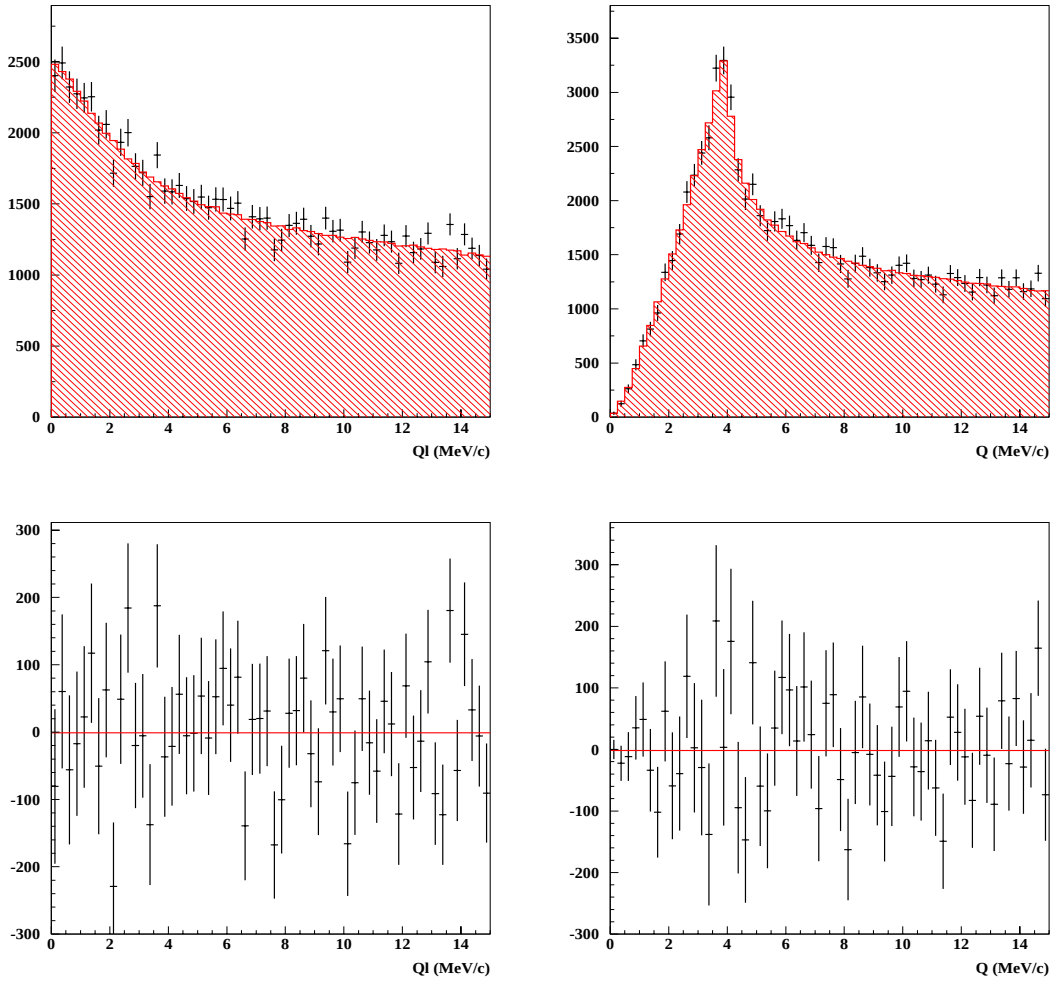

Fig. 8.4: Top: Extracted experimental background (2002 run with modified tracking is shown here) and the Monte Carlo fit. Bottom: Experimental - MC background differences. The flatness in the signal-free region indicates that the MC background correctly reproduces the experimental one.

structing the "pure" background. We define N_{at}^{s} and N_{at}^{m} as the atomic signal from the single layer and multilayer targets, respectively. The prompt experimental signal

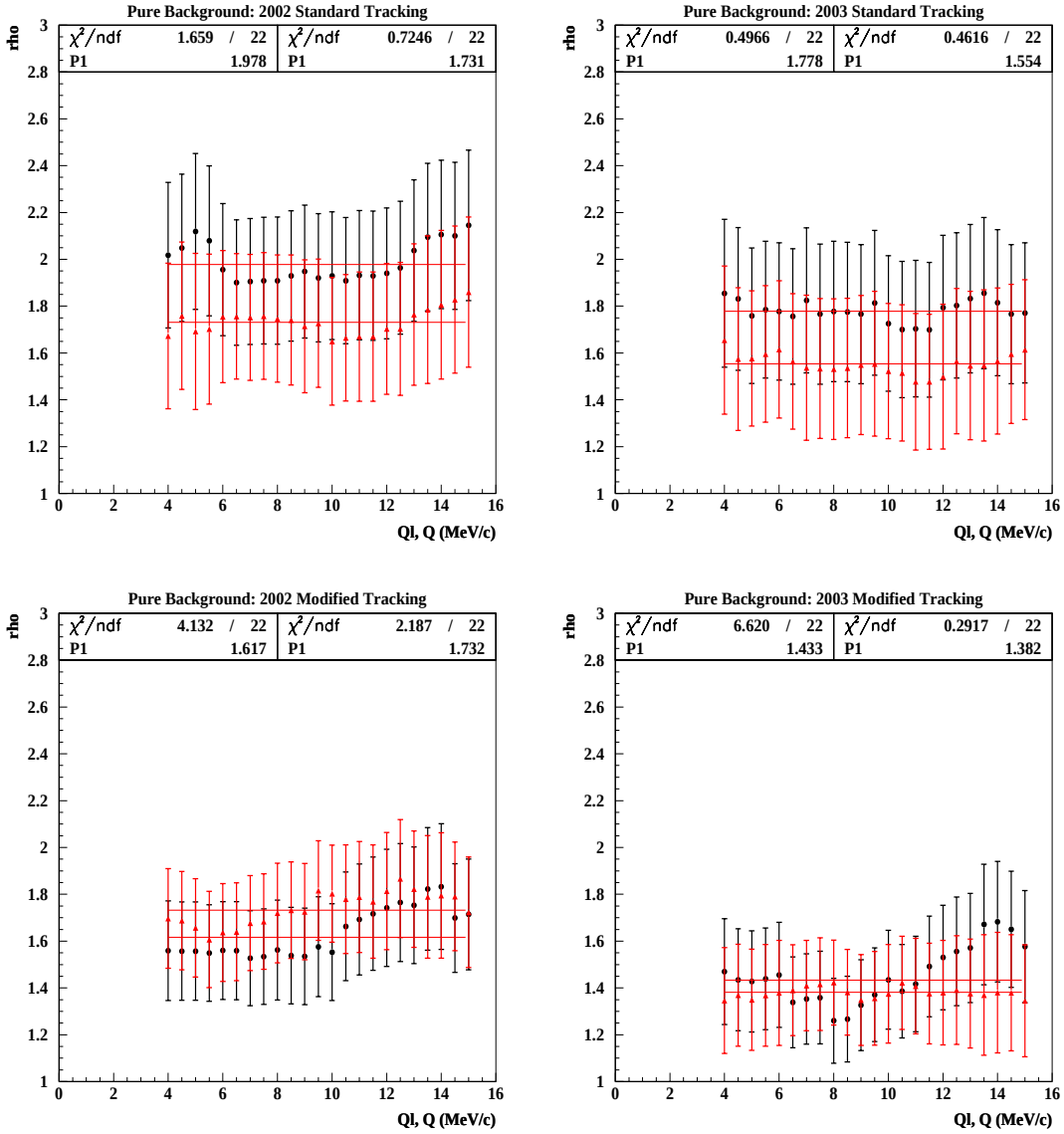

Fig. 8.5: Values of fit parameter ρ corresponding to the single/multilayer breakup probability ratio plotted as a function of the fit range in Q_l (filled circles) and Q (upturned triangles).

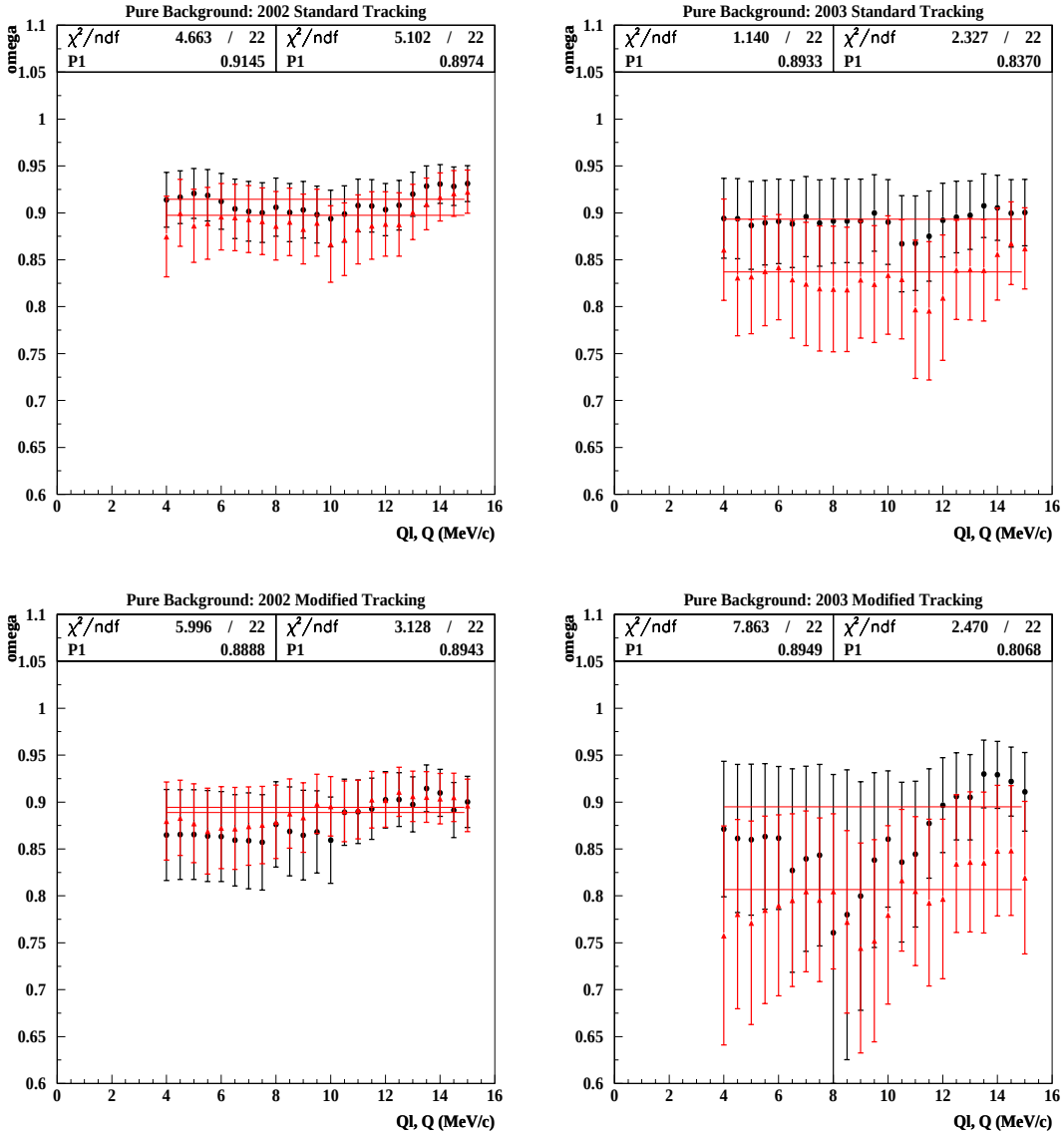

Fig. 8.6: Values of the fit parameter ω corresponding to the Coulomb/non-Coulomb background proportion plotted as a function of the fit range in Q_l (filled circles) and Q (upturned triangles).

can be written as

$$N^s_{exp}(Q_i) = N^s_{at}(Q_i) + N^s_B(Q_i) \quad (8.5)$$

$$N^m_{exp}(Q_i) = N^m_{at}(Q_i) + N^m_B(Q_i), \quad (8.6)$$

where N^s_B and N^m_B are single and multilayer background yields, respectively. We multiply Eq. 8.5 by the background normalization constant ϵ defined in the previous section and Eq. 8.6 by:

$$\rho \equiv \frac{\epsilon \sum N^s_{at}(Q_i)}{\sum N^m_{at}(Q_i)}, \quad (8.7)$$

(where $\sum N^s_{at}$ and $\sum N^m_{at}$ are the integral number of *signal* events in single and multilayer targets in the entire fitting range, in our case $Ql, Q \in [0, 15]$ MeV/c) and subtract Eq. 8.5 from Eq. 8.6 . We thus eliminate the signal events and obtain the expression for the *pure*, or *extracted*, background:

$$\rho N^m_{exp}(Q_i) - \epsilon N^s_{exp}(Q_i) = \rho N^m_B(Q_i) - \epsilon N^s_B(Q_i) \quad (8.8)$$

As before, the summation can be applied to both Q_l and Q distributions. Recalling that the single and multilayer target composition and thicknesses are the same, we observe that Eq. 8.7 can be rewritten as the ratio of the single to multilayer breakup probabilities, i.e.:

$$\rho = \frac{\epsilon \sum N^s_{at}(Q_i)/N^{init}_{at}(Q_i)}{\sum N^m_{at}(Q_i)/N^{init}_{at}(Q_i)} = P^s_{br}/P^m_{br}. \quad (8.9)$$

We note that the single and multilayer experimental backgrounds cannot be extracted directly from the prompt distributions. Thus, one has to rely on the MC-simulated spectra. Taking into account the contribution of the Coulomb, non-Coulomb and accidental events the MC background can be written as:

$$N_B(Q_i) = (1 - \phi_{acc})[\omega N_{cc}(Q_i) + (1 - \omega)N_{nc}(Q_i)] + \phi_{acc} N_{acc}(Q_i) \quad (8.10)$$

The overall normalization constant is 1, as is the normalization for the individual background components. ϕ_{acc}, the percentage of the accidental events in the prompt distribution, can be determined as described in the caption to Fig. 6.7. ω is a measure of the background composition and refers to the fraction of Coulomb events in the combined Coulomb and non-Coulomb sample.

Combining Eq. 8.8 with Eq. 8.10 the corresponding χ^2 to be minimized becomes:

$$\chi^2 = \sum_{i=1}^{60} \frac{[(\rho N^m(Q_i) - \epsilon N^s(Q_i)) - \beta_1 N_B(Q_i)]^2}{(\rho\sigma_{N^m(Q_i)})^2 + (\epsilon\sigma_{N^s(Q_i)})^2} \tag{8.11}$$

with the background normalization constant β_1 given by:

$$\beta_1 = \sum_{i=1}^{60} [\rho N^m(Q_i) - \epsilon N_s(Q_i)] \tag{8.12}$$

and N_B given by Eq. 8.10. (As in the previous section $\sigma_{N^s(Q_i)}$ and $\sigma_{N^m(Q_i)}$ refer to the statistical errors of the experimental single and multilayer distributions.)

In Fig. 8.4 we show the extracted background (corresponding to the left-hand side of Eq. 8.8) together with its Monte Carlo fit (right-hand side of Eq. 8.8) for the 0 to 15 MeV/c fit range in Q_l and Q. In order to improve the statistical accuracy the extracted experimental background was fitted for a set of fit ranges, from 4 up to 15 MeV/c for the Q_l and Q relative momenta projections. The values of fit parameters ρ and ω *vs.* fit ranges are plotted in Fig. 8.5 and 8.6. One may observe considerable fluctuations of ρ around the straight line fit, as well as systematic differences between the pairs of relative momenta components, run periods and tracking methods. The systematic effects will be considered later in the chapter. One should note, however, that the values of ρ and ω are in agreement when their corresponding statistical errors are taken into consideration. Since no convergence of parameters ω and ρ at any fit range was observed, the final value of ρ is to be averaged over all the fit ranges.

8.2.3 Signal from the Sum of Single and Multilayer Spectra

Signal extraction from the sum of single and multilayer spectra is "redundant" in a sense that the fit parameters for this method can be found in the other two fits or expressed in terms of them. Thus, fitting of the summed distributions is performed simultaneously with the rest. The procedure is straightforward: we fit the sum of the single and multilayer Q and Q_l spectra with the Monte Carlo-simulated background and the atomic pair signal. We point out that the evident advantage of fitting the sum of the single and multilayer distributions, as opposed to fitting each target spectra individually, is in significant reduction of statistical error.

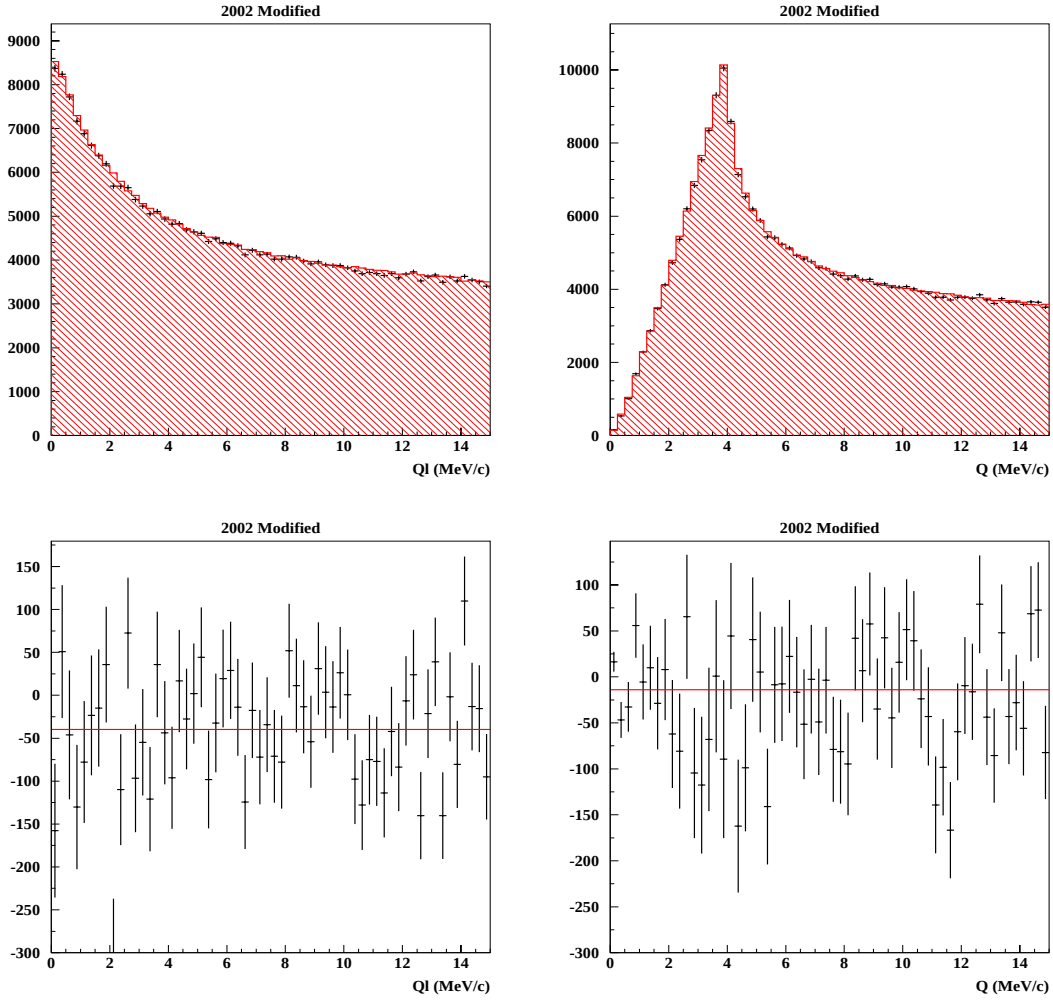

Fig. 8.7: Top: Sum of the experimental prompt single and multilayer Q_l and Q distributions (2002 run with modified tracking) with their Monte Carlo fits. Bottom: Experimental - MC background fit differential.

χ^2 for the summed distributions yields:

$$\chi^2 = \sum_{i=1}^{60} \frac{[(\epsilon N_s(Q_i) + N_m(Q_i)) - (\sigma N_{at}(Q_i) + \beta_2 N_B(Q_i))]^2}{(\epsilon\sigma_{N_s(Q_i)})^2 + e^2_{N_m(Q_i)}} \tag{8.13}$$

The nomenclature for the Monte Carlo components is the same as in the previous two sections. β_2 is the background normalization, analogous to expression 8.12:

$$\beta_2 = \sum_{i=1}^{60}[N_m(Q_i) + \epsilon N_s(Q_i)] - \sigma \tag{8.14}$$

The last term in the expression above is the fit parameter σ, which removes the signal events from the sum of the experimental single and multilayer distributions.

In Fig. 8.7 we plot the summed experimental distributions fitted with the Monte Carlo-simulated background and atomic pair distributions in the range of 0 to 15 MeV/c. As we have done for the case of the extracted background, the summed spectra were fitted for a number of fit ranges, from 4 up to 15 MeV/c in Q_l and Q. The values of fit parameters σ and ω *vs.* fit ranges are plotted in Fig. 8.8 and 8.9. There are no considerable fluctuations in σ around the mean, which is to be expected since the high-statistics MC atomic pair signal is included in the fit and the slight fluctuations are caused only by the variations in fit range. There are, however, sizable systematic differences in Q_l and Q signals, the differences being especially pronounced for 2002 modified tracking, where the values of ω and σ fall between 1 and 2σ's. The results of the tracking methods are consistent between each other within one standard deviation, except for, once again, the 2002 run with modified tracking, where the values of σ and ω for the relative momentum component Q lie between 1σ and 2σ away from the Q_l values and the standard tracking results. The values of ω (proportion of Coulomb pairs in the non-accidental pairs) are seen to be consistent with the extracted background fit (Fig. 8.6), with the summed distributions yielding smaller statistical errors. Once again, no convergence of parameters ω and ρ at any fit range was observed.

As mentioned previously, the fit parameters for the summed distributions are not independent of the previous two fits. Parameter ω also appears in the extracted background. Parameter σ can be re-expressed in terms of ρ and δ found in the

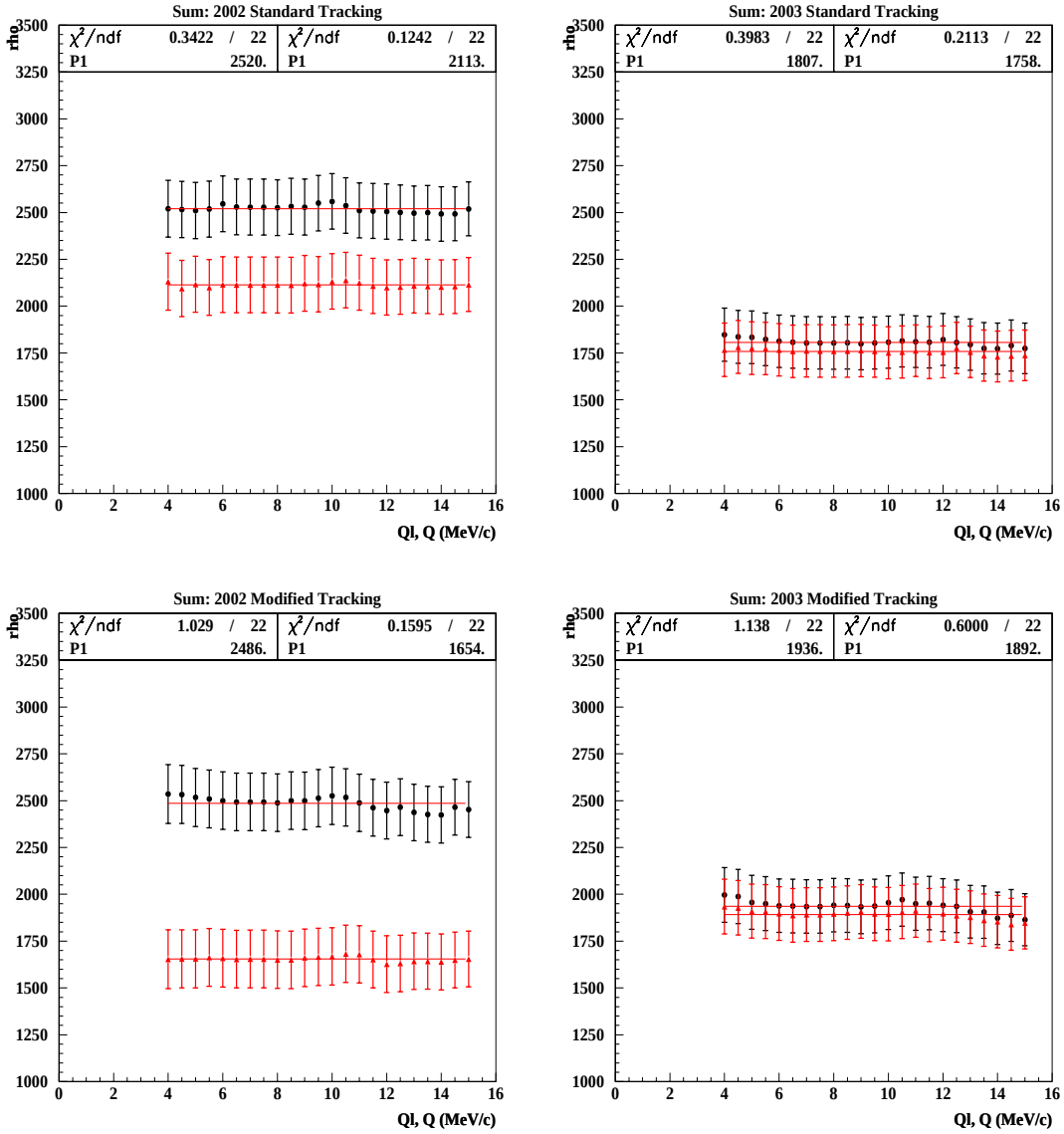

Fig. 8.8: Values of fit parameter ρ corresponding to the single/multilayer breakup probability ratio plotted as a function of the fit range in Q_l (filled circles) and Q (upturned triangles).

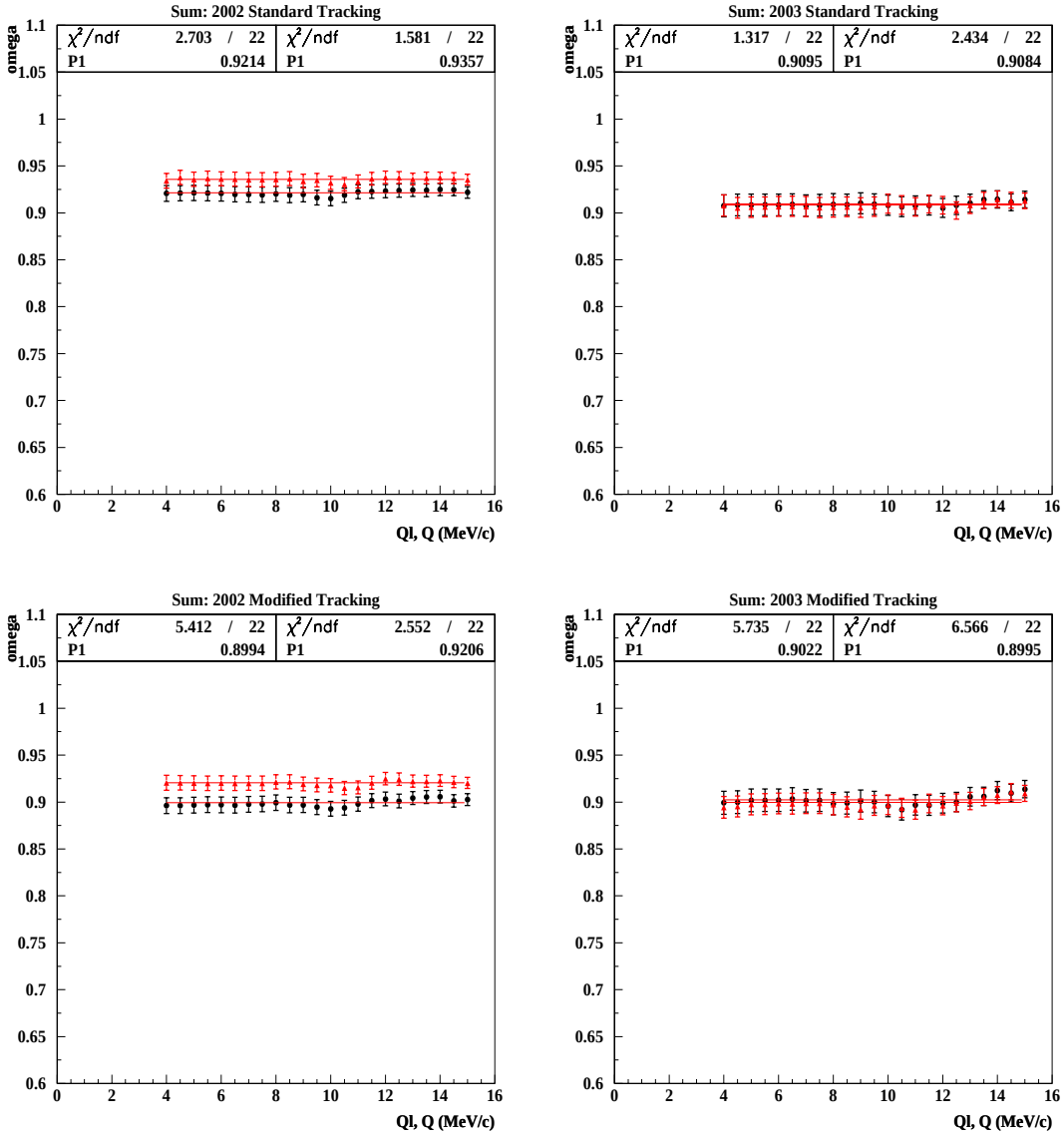

Fig. 8.9: Values of the fit parameter ω corresponding to the Coulomb/non-Coulomb background proportion plotted as a function of the fit range in Q_l (filled circles) and Q (upturned triangles).

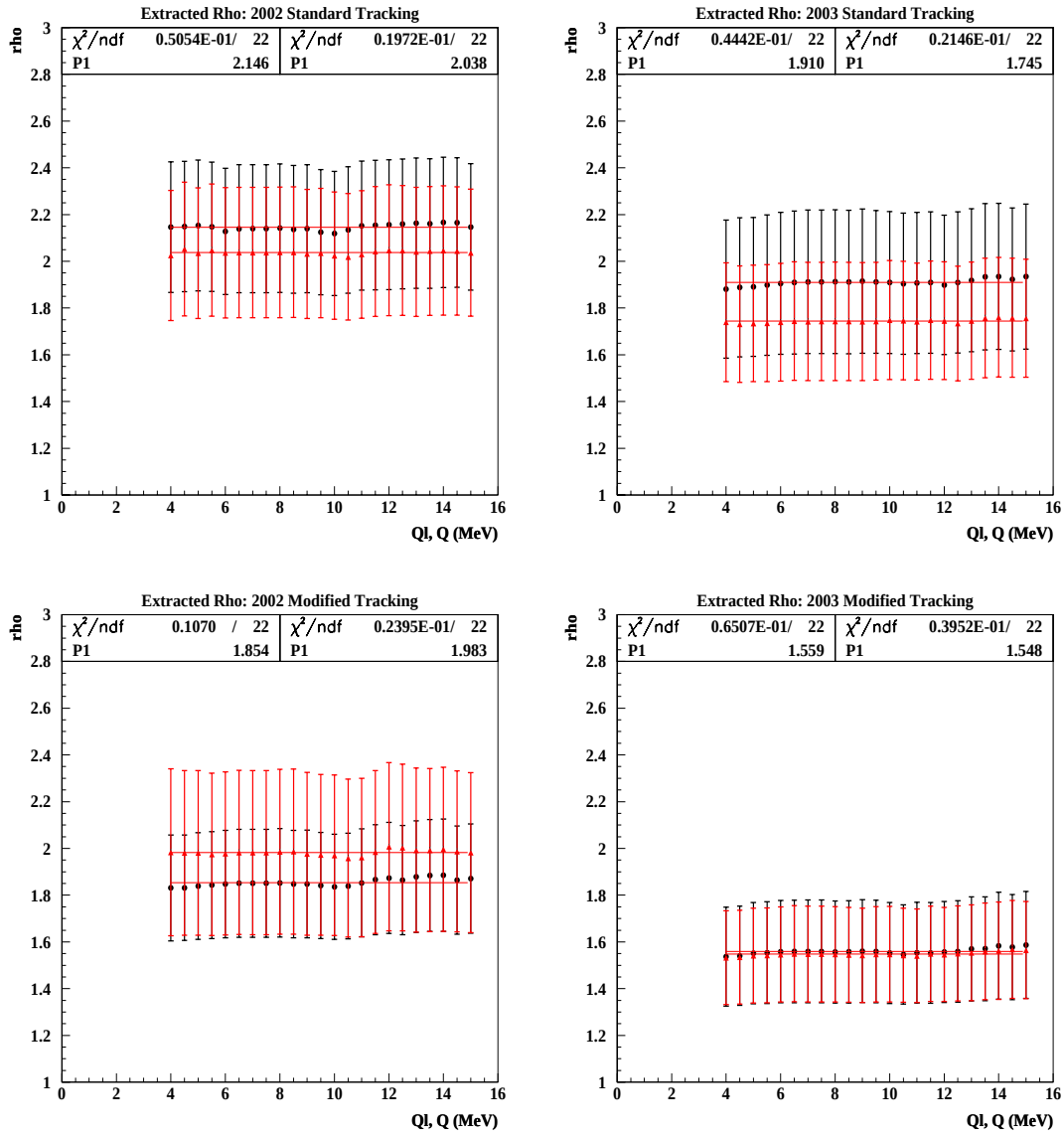

Fig. 8.10: Values of the ratio of single/multilayer signals (corresponding to the fit parameter ρ above) extracted from the fits to the sum and difference of the single and multilayer backgrounds plotted as a function of the fit range in Q_l (filled circles) and Q (upturned triangles).

previous two sections. From

$$\sigma = \epsilon \sum N_{at}^{s}(Q_i) + \sum N_{at}^{m}(Q_i) \tag{8.15}$$

$$\delta = \epsilon \sum N_{at}^{s}(Q_i) - \sum N_{at}^{m}(Q_i) \tag{8.16}$$

we get:

$$\rho = \epsilon \sum N_{at}^{s}(Q_i) / \sum N_{at}^{m}(Q_i) = \frac{\sigma + \delta}{\sigma - \delta} \tag{8.17}$$

Using the values of δ found in the top Table 8.2 and σ values from this section, we obtain the values of "extracted ρ" (Fig. 8.10). Due to the stability of parameters δ and ρ, the extracted ρ appears to be less prone to fluctuations as the one found for the pure background case (Fig. 8.5). Despite sizeable systematic uncertainties, the values of ρ extracted from the sum/difference fits and the pure background are generally found to be in 1σ agreement for both tracking methods and the two run periods.

8.3 Combined Fits

In this section we combine the individual Q_l and Q fits and perform the simultaneous Q_l and Q fit for each type of tracking and run period. These fits, in turn, will be combined to yield an overall value of the breakup probability and lifetime with their corresponding statistical errors.

In Sections 8.2.1-8.2.3 we have introduced four parameters δ, ρ, ω and σ. We redefine one of the "redundant" parameters, σ, as b_{at} and use it as a constraint rather than a fit parameter. Using Eq. 8.17:

$$b_{at} \equiv \sigma = \frac{\delta(\rho + 1)}{\rho - 1} \tag{8.18}$$

Making this substitution in the minimization of Eq. 8.13, the set of χ^2 to be simul-

taneously minimized in terms of δ, ρ and ω becomes:

$$\chi_1^2 = \sum_{i=1}^{60} \frac{[(\epsilon N^s(Q_i) - N^m(Q_i)) - \delta N_{at}(Q_i)]^2}{(\epsilon\sigma_{N^s(Q_i)})^2 + \sigma^2_{N^m(Q_i)}} \tag{8.19}$$

$$\chi_2^2 = \sum_{i=1}^{60} \frac{[(\rho N^m(Q_i) - \epsilon N^s(Q_i)) - \beta_1 N_B(Q_i)]^2}{(\rho\sigma_{N^m(Q_i)})^2 + (\epsilon\sigma_{N^s(Q_i)})^2} \tag{8.20}$$

$$\chi_3^2 = \sum_{i=1}^{60} \frac{[(\epsilon N_s(Q_i) + N_m(Q_i)) - (b_{at} N_{at}(Q_i) + \beta_2 N_B(Q_i))]^2}{(\epsilon\sigma_{N_s(Q_i)})^2 + e^2_{N_m(Q_i)}}. \tag{8.21}$$

Fitting the differential (Eq. 8.4), summed distributions and the extracted background (Eq. 8.11) one obtains more stable values ρ and ω (shown in Fig. 8.11 and 8.12). The overall 1σ agreement between the Q_l and Q projections, run periods and tracking procedures is evident. Also evident are the systematic differences between the four sets of plots. Of the four types of spectra, the 2003 modified tracking results deviate more from the rest.

As a further illustration of the level of agreement of the fit parameters ρ and ω, we plot one against the other on the 70% C.L. contour plots (Fig 8.13). The area of intersection of the contours indicates where the combined overall value of ρ and ω may be found. Since both parameters are only weakly correlated, one representing the signal ratio and the other background composition, we do not expect the axes of the contours to have a significant slope, which is, indeed, the case. For an even clearer picture of the statistical and systematic errors and the area of agreement by combining Q_l and Q distributions. 70% C.L. contour plots are shown in Fig. 8.14.

Finally, all the fits may be combined into one simultaneous fit that yields the overall ratio of single to multilayer breakup probabilities with its statistical error. In Table 8.3 we show the values of ρ and ω for different fit ranges. Taking the weighted mean over the rho values in the fit ranges in Table 8.3 and averaging of the statistical errors one obtains the ratio of single to multilayer breakup probabilities:

$$\rho = P^s_{br}/P^m_{br} = 1.811 \pm 0.248, \tag{8.22}$$

while the Coulomb contribution to the non-accidental background, ω, is:

$$\omega = 0.917 \pm 0.014. \tag{8.23}$$

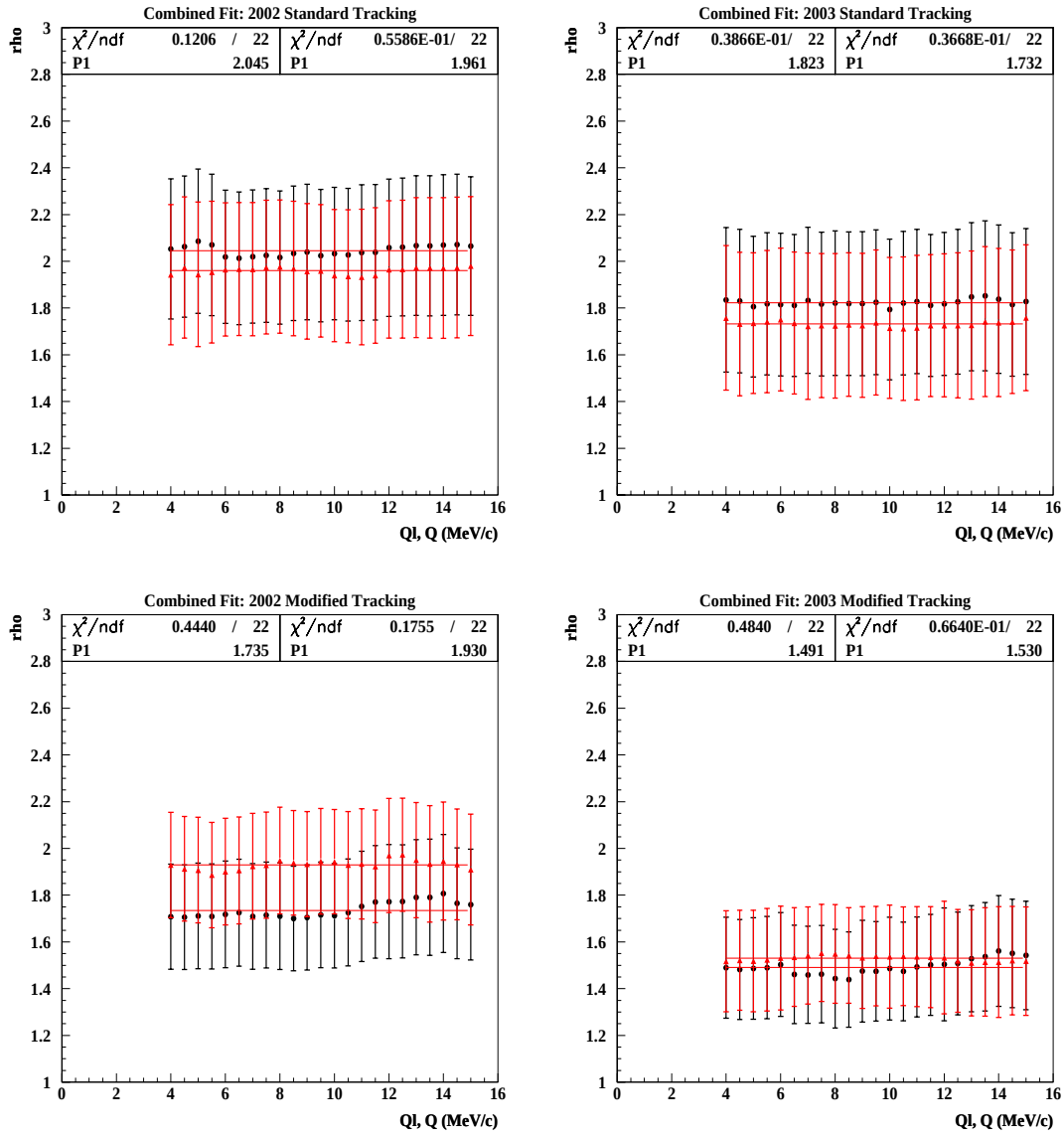

Fig. 8.11: Values of the ratio of single/multilayer signals (corresponding to the fit parameter ρ above) extracted from the fits to the sum and difference of the single and multilayer backgrounds plotted as a function of the fit range in Q_l (filled circles) and Q (upturned triangles).

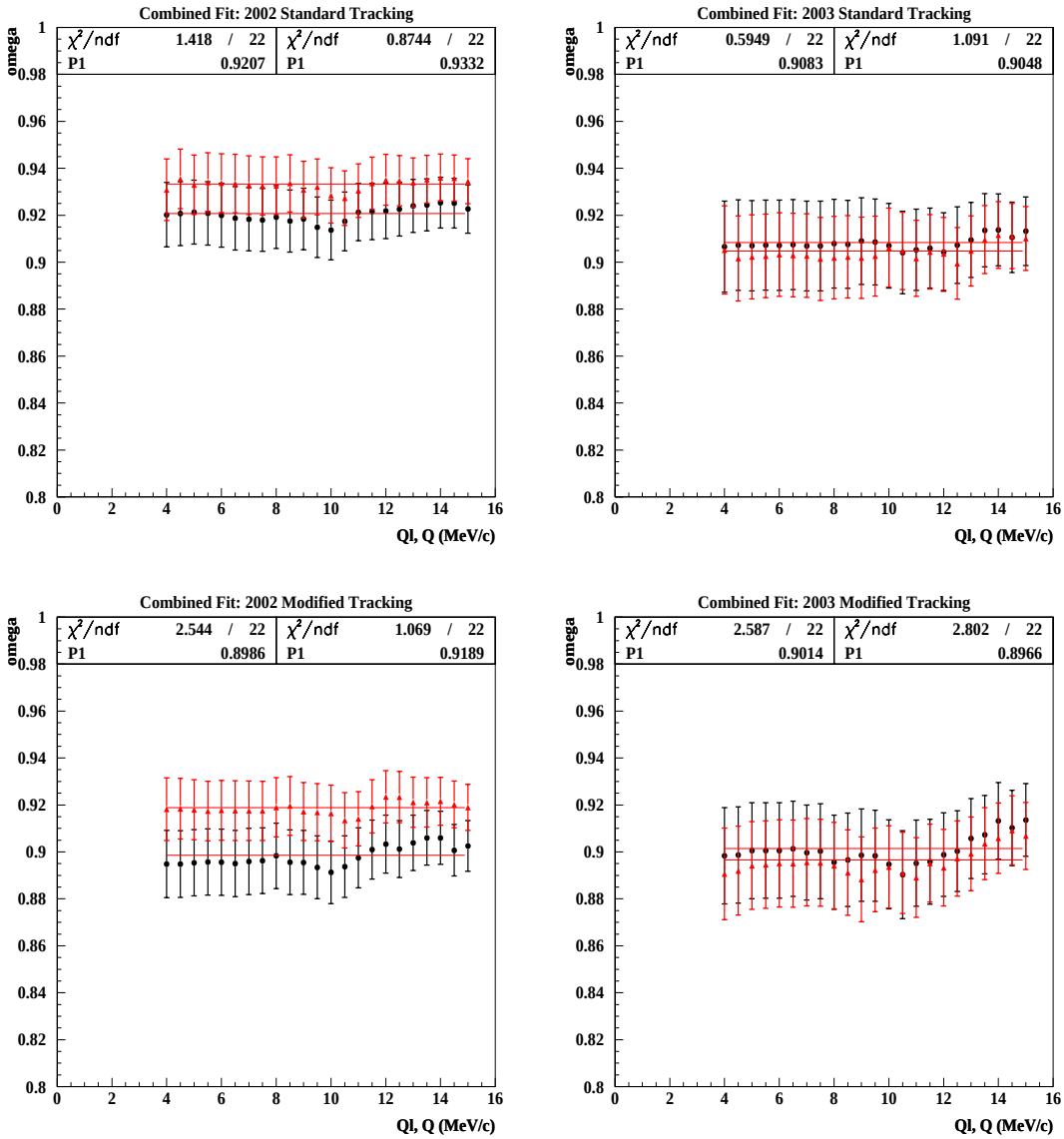

Fig. 8.12: Proportion of Coulomb pairs in the Coulomb + non-Coulomb background (corresponding to the fit parameter ω above) extracted from the fits to the sum and difference of the single and multilayer backgrounds plotted as a function of the fit range in Q_l (filled circles) and Q (upturned triangles).

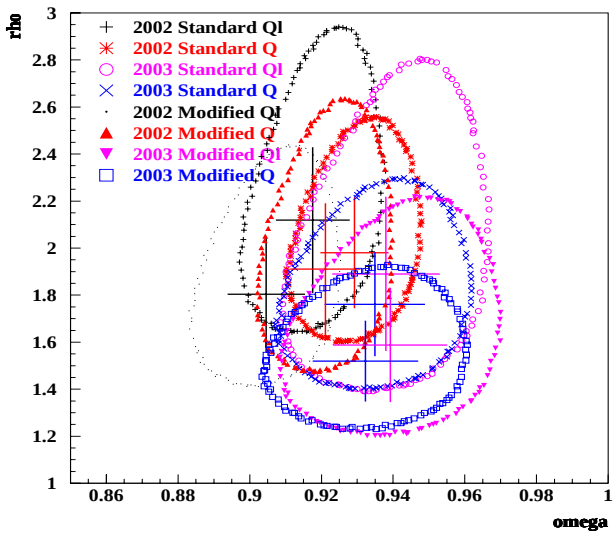

Fig. 8.13: Mean values of ρ *vs.* ω fit parameters with statistical errors (large crosses) for Q_l and Q distributions fitting the differential, extracted background and and summed distributions simultaneously. 70% C.L. contours for each fit are shown.

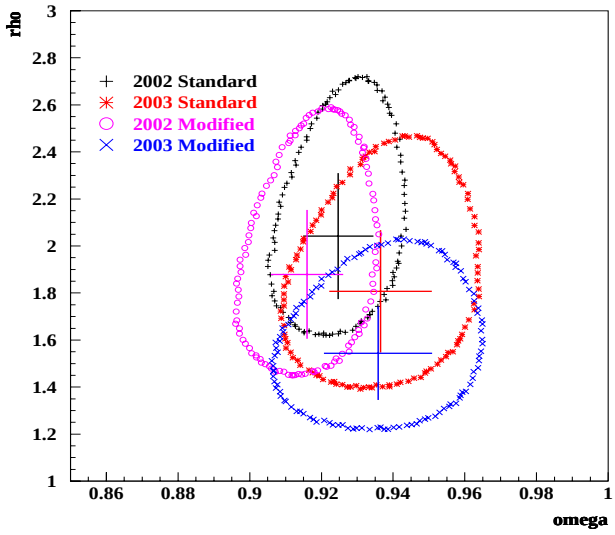

Fig. 8.14: Mean values of ρ *vs.* ω fit parameters with statistical errors (large cross) combined by year and type of track fit. 70% C.L. contours for each fit are shown.

Q_l, Q (MeV/c)	χ^2	χ^2/ndf	ω	ρ
4.0	35.24	1.215	0.9149 ± 0.0155	1.806 ± 0.248
4.5	38.73	1.174	0.9156 ± 0.0151	1.804 ± 0.247
5.0	42.93	1.160	0.9156 ± 0.0150	1.801 ± 0.247
5.5	45.44	1.108	0.9158 ± 0.0150	1.802 ± 0.247
6.0	50.21	1.116	0.9158 ± 0.0150	1.807 ± 0.248
6.5	54.87	1.120	0.9155 ± 0.0150	1.800 ± 0.246
7.0	58.34	1.101	0.9153 ± 0.0149	1.801 ± 0.246
7.5	61.65	1.082	0.9152 ± 0.0149	1.807 ± 0.247
8.0	65.95	1.081	0.9157 ± 0.0148	1.806 ± 0.247
8.5	69.48	1.069	0.9151 ± 0.0146	1.802 ± 0.246
9.0	72.74	1.054	0.9143 ± 0.0145	1.803 ± 0.245
9.5	77.10	1.056	0.9138 ± 0.0143	1.807 ± 0.246
10.0	82.10	1.066	0.9126 ± 0.0141	1.800 ± 0.244
10.5	86.93	1.073	0.9119 ± 0.0138	1.801 ± 0.243
11.0	91.15	1.072	0.9138 ± 0.0136	1.807 ± 0.246
11.5	95.92	1.078	0.9166 ± 0.0133	1.810 ± 0.247
12.0	99.84	1.074	0.9178 ± 0.0131	1.824 ± 0.251
12.5	103.28	1.065	0.9178 ± 0.0128	1.825 ± 0.251
13.0	106.63	1.056	0.9189 ± 0.0125	1.828 ± 0.252
13.5	111.33	1.060	0.9207 ± 0.0123	1.829 ± 0.254
14.0	114.01	1.046	0.9218 ± 0.0120	1.833 ± 0.255
14.5	117.46	1.039	0.9203 ± 0.0117	1.823 ± 0.251
15.0	123.59	1.056	0.9198 ± 0.0115	1.824 ± 0.251

Table 8.3: Combined fit results for 2002 and 2003 data with standard and modified tracking procedures. The first column indicates the upper bound of the fit range starting from 0.

The relative error in ρ is thus 13.6% and in ω is 1.5%. In Fig. 8.15 we show the mean values of ρ and ω with their standard deviations and the contour plots corresponding to 70%, 90% and 95% confidence limits on both variables.

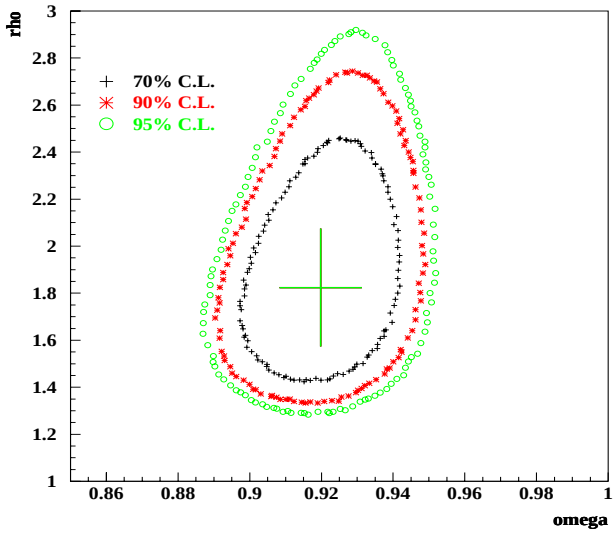

Fig. 8.15: Combined mean values with standard deviations for fit parameters ρ and ω obtained for 2002 and 2003 run periods with standard and modified tracking (large crosses). Contour plots correspond to 70%, 90% and 95% confidence limits on both parameters.

8.4 Analysis of the Systematic Effects

In the subsequent sections we will evaluate the contribution of the systematic errors on the final value of the ratio of breakup probabilities. The influence of the signal differences obtained with Q_l and Q distributions, run period/tracking uncertainties, sensitivity of the fits on the ω fit parameter, the sensitivity on the MC-simulated atomic signal shape, and, finally, the influence of the accidental contribution on the fits will be examined. In all cases some variation on the combined fits given by Eq. 8.19 - 8.21 will be performed.

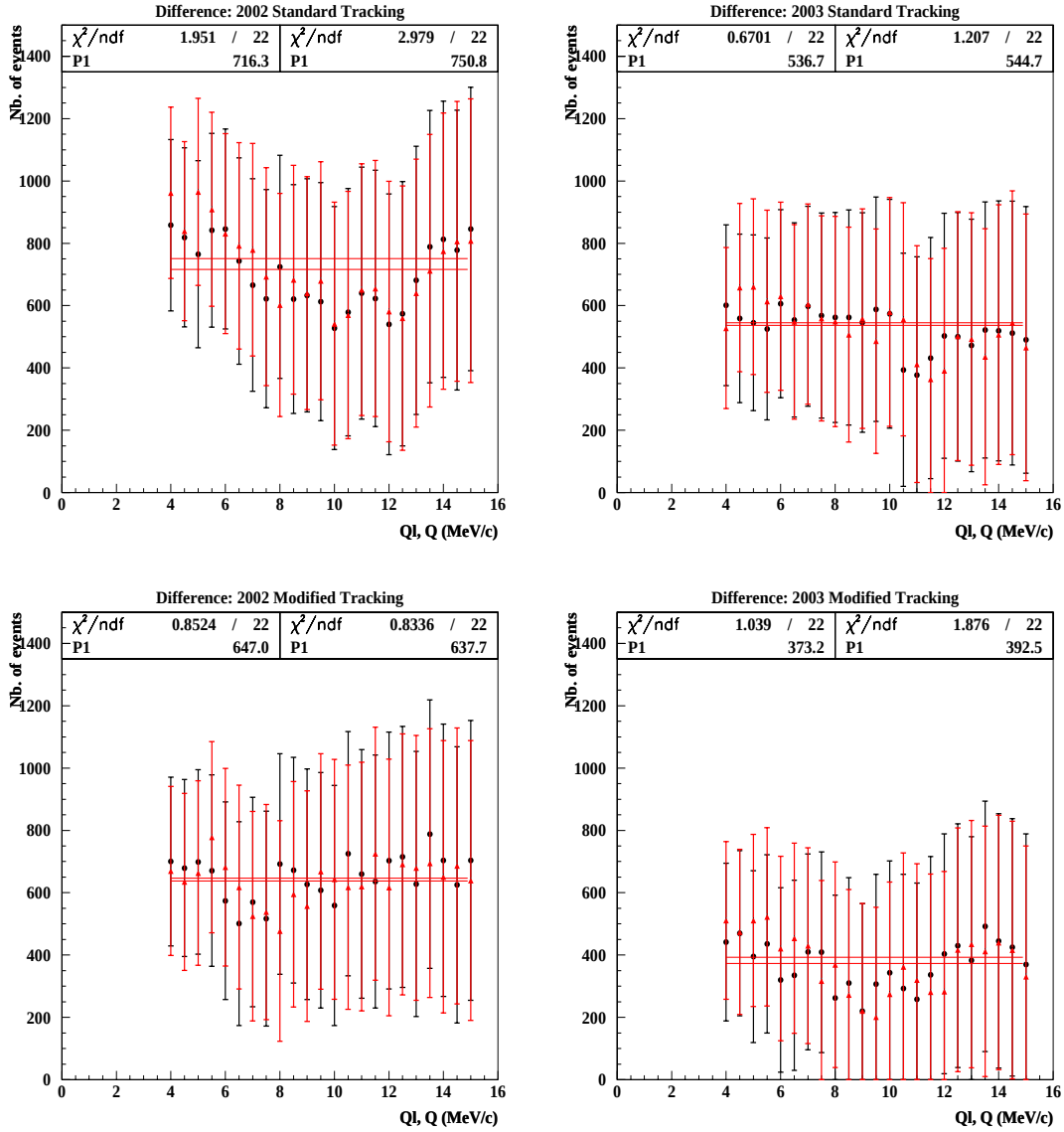

Fig. 8.16: *Experimental* differentials (residual) plotted as a function of the fit range in Q_l (filled circles) and Q (upturned triangles).

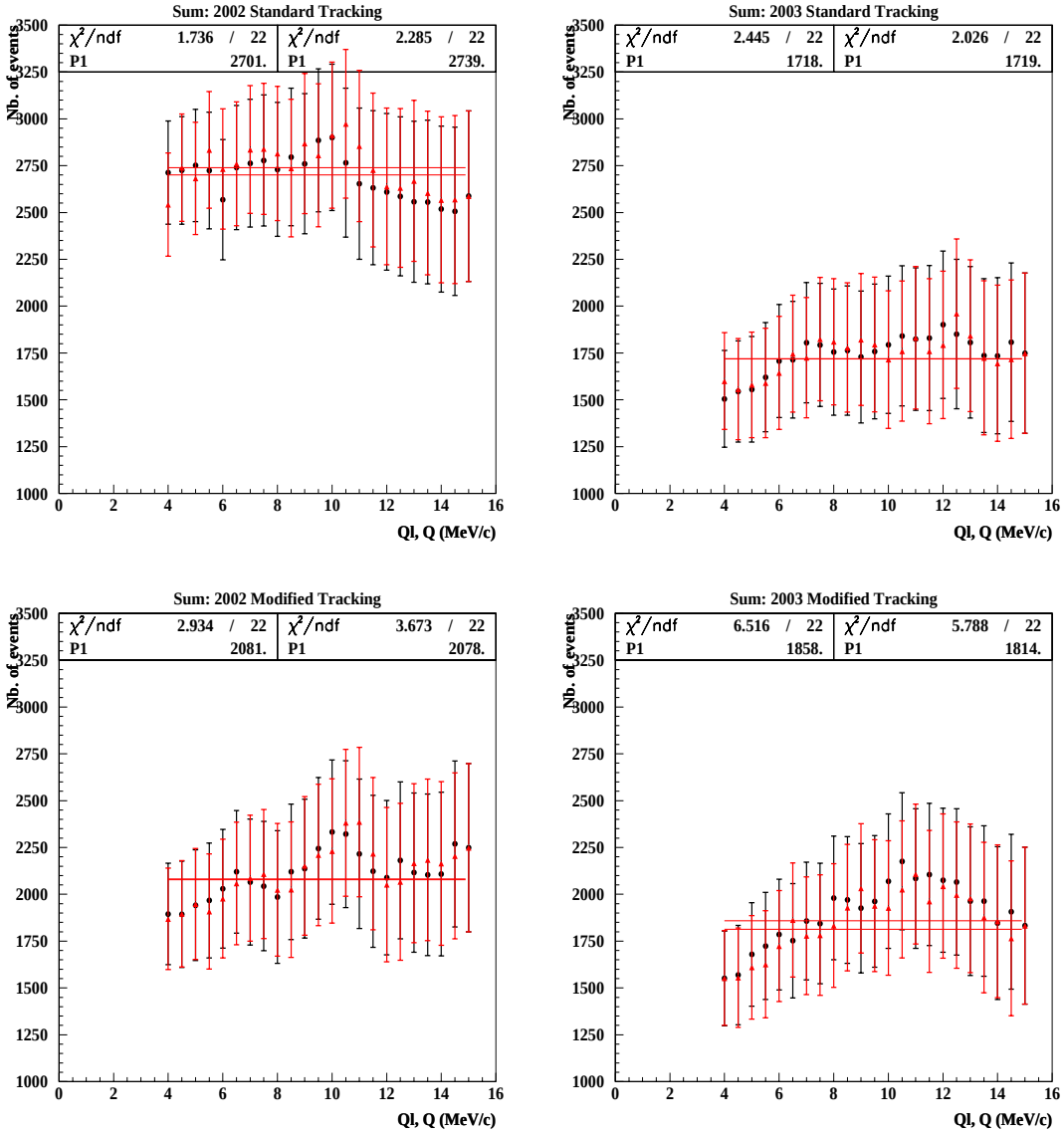

Fig. 8.17: *Experimental* signal (residual) from the summed distributions plotted as a function of the fit range in Q_l (filled circles) and Q (upturned triangles).

8.4.1 Systematic Error due to Q_l/Q Differences

From the previous sections it is evident that the systematic discrepancies between the signals obtained from the Q_l and Q distributions do exist. We can broadly classify the possible sources of the systematic error into experimental and Monte Carlo-related. The experimental discrepancy should be especially visible in the low Q region where the influence of the transverse component of the relative momentum Q_{trans} is significant. (It may be recalled that, unlike Q_l, Q_{trans} is affected by the performance of the upstream detectors, such as the SFD.)

We first consider the experimental differential, such as the one found in the bottom Table 8.2, and instead of only fitting the regions $0 \leq Q_l \leq 2$ MeV/c and $0 \leq Q \leq 4$ MeV/c, we fit both momentum projections for the set of intervals from 4 to 15 MeV/c (with the same lower bound at 0). The results are shown in Fig. 8.16.

In the next step we attempt to find the experimental signal from the summed distributions. This amounts to subtracting the MC background from the experimental signal (cf. Eq. 8.13):

$$N_{at}^{exp} = [\epsilon N_s(Q_i) + N_m(Q_i)] - \beta_2 N_B(Q_i), \tag{8.24}$$

where β_2 and N_B contain fit parameters σ and ω. We keep ω fixed at the mean value 0.917 (Eq. 8.23). The value of σ is left to vary freely. Its exact value is immaterial for the purposes of this study as it only enters through the overall normalization constant β_2 where it contributes only at 1% level. The results for N_{at}^{exp} are shown in Fig. 8.17.

Considering the close agreement between the Ql and Q residuals in Fig. 8.16 and 8.17 one observes that the Q/Q_l signal bias found in Table 8.2 and Fig. 8.8: (a) cannot be caused by deficiencies in tracking, and (b) is not due to any biases in the MC-simulated background since it also enters in the reconstruction of the residuals. Thus, we conclude that the Q_l/Q signal differences are affected mostly by the discrepancies in the Monte Carlo simulation of the atomic pair signal occurring at the level of event generation and/or the digitization of detector responses. The accuracy of the latter would not be as significant for the background reconstruction due to much larger variations in relative momenta. Below we quantify the systematic uncertainty in ρ for the Q_l and Q relative momenta projections.

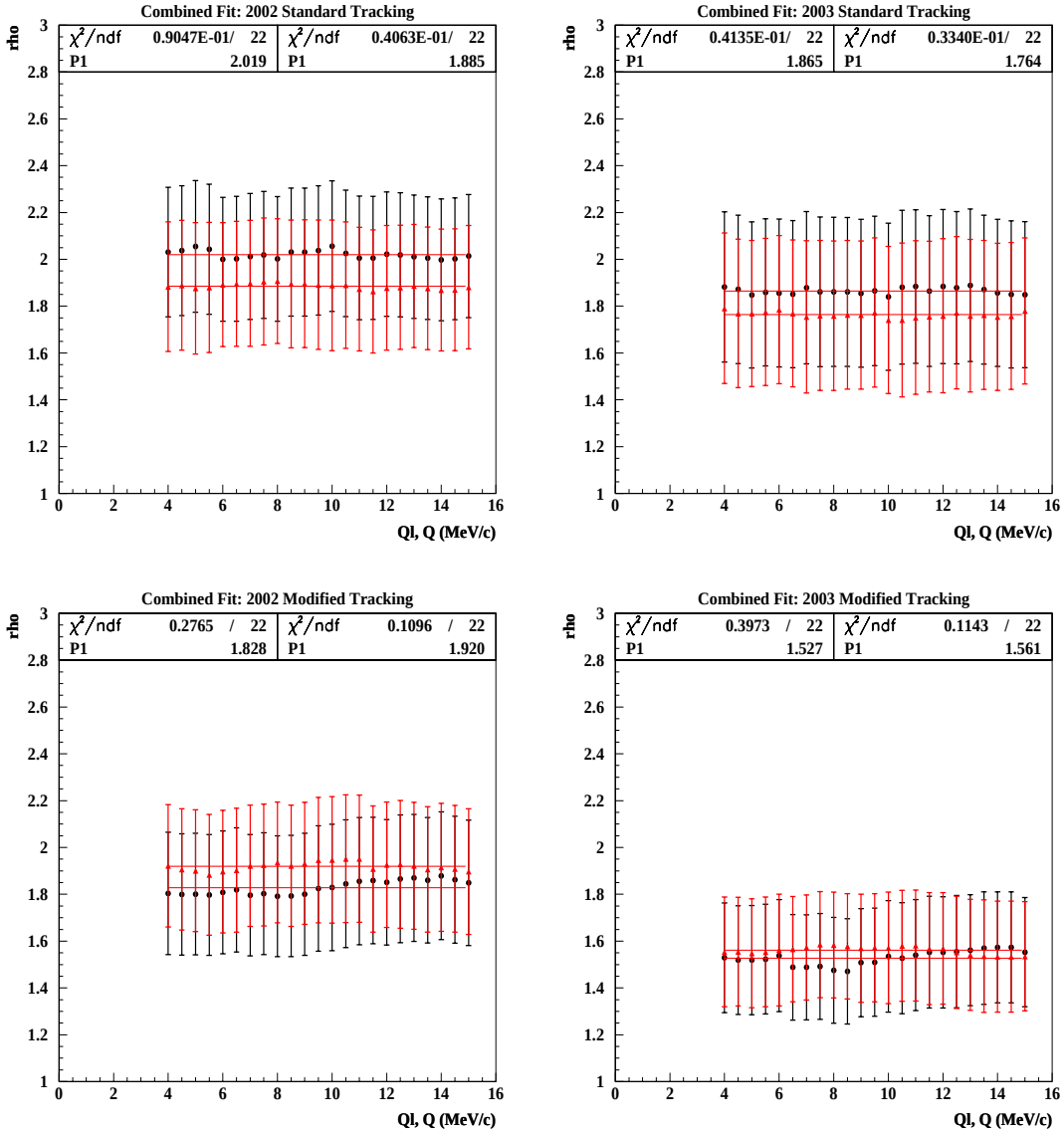

Fig. 8.18: Evaluating the systematic error in ρ due to Q_l/Q differences. Combined ρ distributions plotted analogously to Fig. 8.11, but with ω fixed at the overall fit value of 0.917.

In order to evaluate the systematic error due to the Q_l/Q differences, we perform the simultaneous fit described by Eq. 8.19 - 8.21, first in Q_l, then in Q projection. We keep the value of ω fixed at the value of 0.917 obtained with the overall combined fit. The resulting ρ fits are shown graphically in Fig. 8.18.

To evaluate the systematic error we take the "extreme case scenario" with the largest deviation between Q_l and Q values. From the four figures above, 2002 standard tracking yields the biggest deviation. From the linear fits, the difference is 0.134. Assuming that the systematic error in ρ is uniformly distributed leads to the standard deviation:

$$\sigma_{\Delta Q} = 0.1344/\sqrt{12} = 0.0388 \tag{8.25}$$

This error is thus about 2.1% of the mean value and 16% of the combined statistical error (Eq. 8.22).

8.4.2 Systematic Uncertainty Due to Tracking/Run Period

One may observe that the relatively large deviations in signal exist not only between the two tracking methods, but also between run periods for both tracking types. These discrepancies make it difficult to estimate the systematics due to the standard and modified tracking. The most conservative solution is to perform a combined Q_l/Q fit (Eq. 8.19 - 8.21) for each year and tracking type separately and estimate the systematic uncertainty taking the largest deviation in the value of ρ. The value of ω is kept fixed at the value of 0.917, as in the previous section. From Fig. 8.19 we conclude that the largest $\Delta\rho$ occurs between 2002 standard tracking and 2003 modified tracking procedures. From the fits we obtain:

$$\sigma_{\text{fits}} = 0.3899/\sqrt{12} = 0.1126 \tag{8.26}$$

We note that the error is relatively large, being 6.2% of the mean and 45.3% of the statistical error. It is most likely due to the atomic signal itself and not the simulated background, which is relatively stable, as will be shown in the following section. We also note that this error is independent of $\sigma_{\Delta Q}$, as the latter quantifies the relative spread in the Q_l/Q components *within* individual tracking procedures and

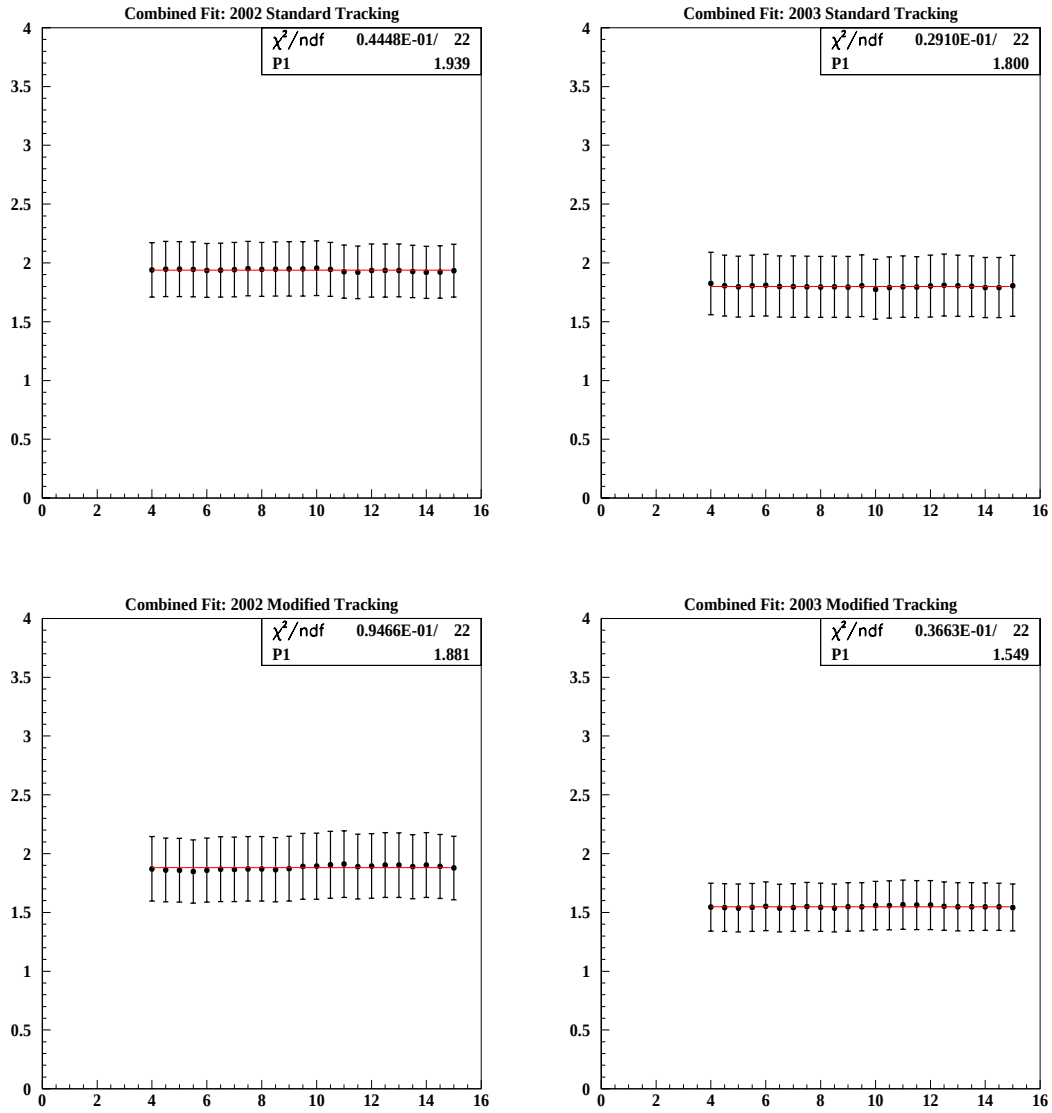

Fig. 8.19: Evaluating the systematic error caused by tracking and/or run period differences. Combined ρ distributions plotted analogously to Fig. 8.11, but with ω fixed at the overall fit value of 0.917.

run periods, as opposed to differences *between* run periods and tracking types. Hence, these two uncertainties may be combined in a straightforward way for the final error estimate.

8.4.3 Signal Sensitivity to the Background Composition

In the previous section we have discussed the influence of Q/Q_l systematics on the signal, in this section we will concentrate on the background composition. As is evident from Sections 8.2.3 and 8.2.2, the systematic deviations in ω depend on the Q_l or Q component of relative momenta. We split the combined fit of Eq. 8.19 - 8.21 into Q_l and Q components and fix the value of ρ at its overall mean of 1.811 (Eq. 8.22). The value of δ is seen to be virtually independent of the upper fit limits, but varies only with momentum projection, run period and tracking type. It is thus left unfixed. With these conditions, the following ω distribution is obtained (Fig. 8.20). From the fits in the left Fig. 8.20, the systematic error for ω is 0.0022.

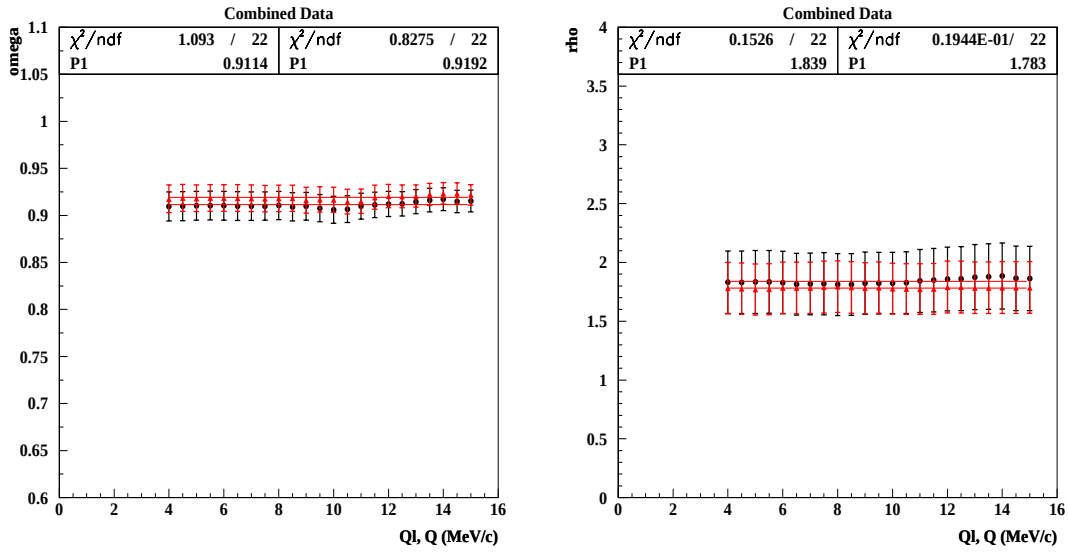

Fig. 8.20: Systematic error in ω (left) and ρ (right) for Q_l (filled circles) and Q (upturned triangles) projections.

In order to find the systematic effect on the values of ρ, we "unfix" ρ and fix ω, first, at the values of Q_l, then the values of Q found in the previous step. The

recorded values of ρ for the Q_l and Q distributions are shown graphically on the right in Fig. 8.20.

The systematic spread in values of ρ is about 0.0565 yielding the systematic error:

$$\sigma_\omega = 0.0565/\sqrt{12} = 0.0163 \tag{8.27}$$

The systematic error in background composition is then about 6.6% of the statistical error of Eq. 8.22 and about 0.9% of the mean. Qualitatively, one might expect that a small systematic error in ω leads to a small error in ρ for several reasons:

1. Due to its physical meaning as the ratio of Coulomb pairs to the sum of non-Coulomb and Coulomb pairs and due to the fact that Coulombs dominate over non-Coulombs by a ratio of about 8:1, ω is inherently stable. That is to say that any small fluctuations in *non-Coulomb* pairs would be negligible and any small fluctuations in Coulomb pairs are compensated by the ratio itself.

2. Even if one neglects the overall predominance of the Coulomb pairs, in the low Q and Q_l regions the Coulomb pair contribution would still be dominant: the non-Coulomb distribution is flat in Q_l and can be compensated by the Coulomb distribution, and the non-Coulomb spectrum grows as Q^2 in Q, as opposed to the linear Q-dependence for the Coulomb pairs.

8.4.4 Signal Shape Systematics

Below we examine the influence of the signal shape on ρ. The signal shape was changed by increasing the GEANT-preset mean multiple scattering angle by 20%. We consider only one run year, 2002, and use the standard and modified tracking methods. This results in broader signal distributions in Q_l and Q, as shown in Fig. 8.21.

The combined fits were performed with and without the increased multiple scattering. The recorded change in ρ is 0.0193 (Fig. 8.22). The systematic error is then

$$\sigma_{\text{shape}} = 0.0190/\sqrt{12} = 0.0055, \tag{8.28}$$

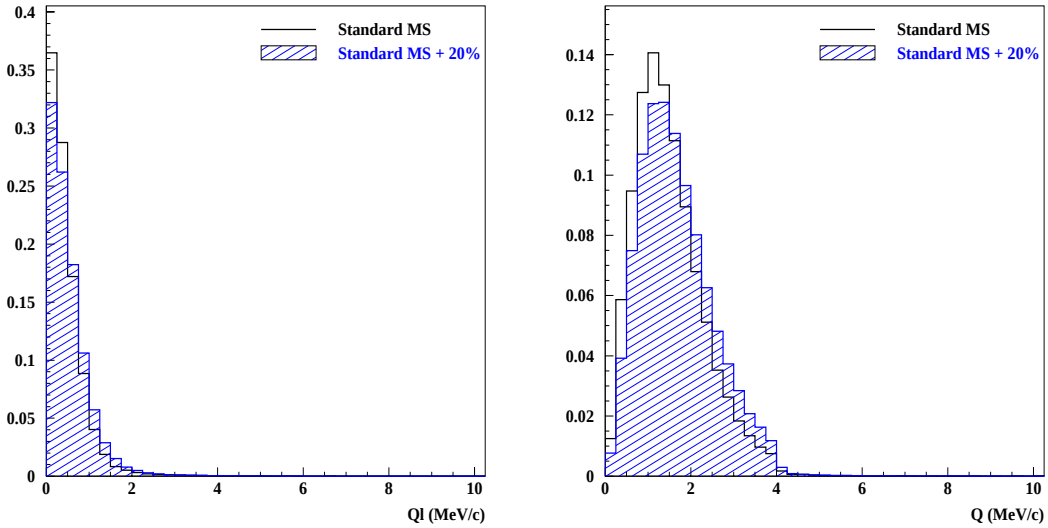

Fig. 8.21: MC-simulated atomic pair signal with standard multiple scattering and with the mean scattering angle increased by 20%.

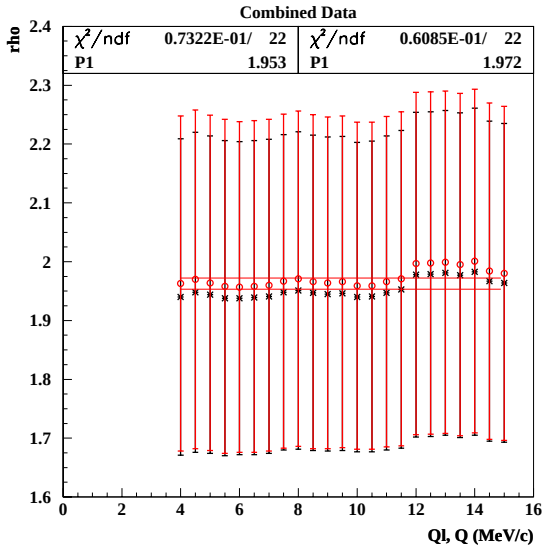

Fig. 8.22: Systematic differences in ρ due to signal shape. Asterisks indicate distributions with the standard GEANT multiple scattering, circles – 20% increase in the average multiple scattering angle.

making it about 0.3% of the mean and 2.2% of the statistical error. Thus, a wider MC-simulated atomic pair distribution would not significantly alter the overall results.

Although the end goal of this study was not as much the influence of multiple scattering on the final result, as its sensitivity to the signal shape, a few words must be said on the multiple scattering. Its effects were examined as a part of 2001 data studies [46], where the average multiple scattering angle was successively changed by +5%, −5% and +10% and applied to both the signal and the background distributions at the level of GEANT simulation. It was found that adding 5% to the scattering angle provides the best fit to the experimental data. The increase in atomic breakup probability due to this was found to be $\Delta P_{br} = 0.0006$, which corresponds to 0.1% of the mean value of 0.447. This systematic deviation is thus negligibly small and will not be considered in this thesis.

8.4.5 Systematic Error Due to the Accidental Contribution

Finally, we consider the influence of the accidental contribution on the final result of the ratios of breakup probabilities. We considered the variations in the level of the accidental pairs for the single and multilayer targets, as well as fluctuations due to the run period and the tracking type. The lower limit of 7.5% and the upper limit of 9.5% was found to describe the extreme cases. With these two values the combined fit of Eq. 8.19 - 8.21 was performed. The results are shown in Fig. 8.23

From the linear fits

$$\sigma_{acc} = 0.0017357/\sqrt{12} = 0.0005, \tag{8.29}$$

making this systematic contribution 0.02% of the mean and 0.2% of the statistical error. That this contribution to the systematic error takes on such a small value is explainable by the same reasoning as given to the Coulomb contribution at the end of Section 8.4.1.

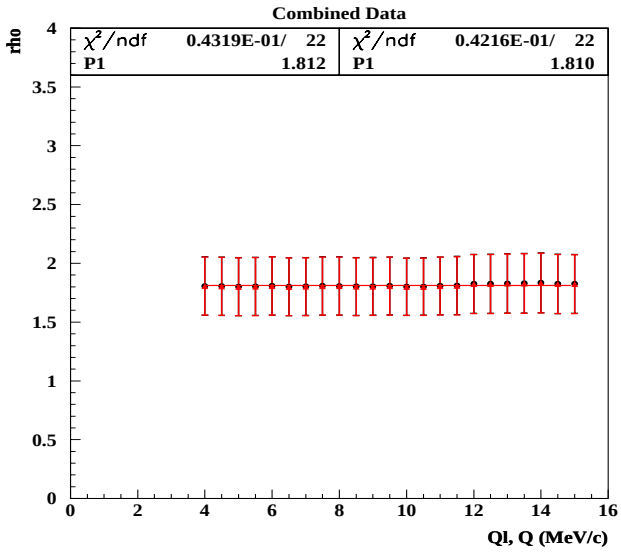

Fig. 8.23: Variation in the signal due to the 7.5% and 9.5% accidental contributions.

8.5 Finite Size Correction Function

In this section we will try to justify the claim that the dual target provides more stable results than the standard method of signal extraction by considering the effects of introducing a finite size correction function to modify the distribution of the Coulomb pairs.

The Coulomb pair differential cross-sections found in Eq. 2.47 assume zero distance between the pions at the moment of their formation. R. Lednický and J. Smolik [57] have proposed a more realistic model where the non-zero formation distance resulting from the pion pair decays of the short, medium and long-lived particles was considered. The correction for the Coulomb enhancement function of Eq. 2.47 has been parametrized as [46]:

$$F_{fs}(Q) = 1.0017 - 0.0285\,[(1 + (0.278 \cdot Q)^2)^{-0.421} - 1] \tag{8.30}$$

Hence, the modified production rate of the CC pairs is given by

$$\frac{dN_{CC}}{dQ} \propto F_{fs}(Q) A_c(Q) Q^2. \tag{8.31}$$

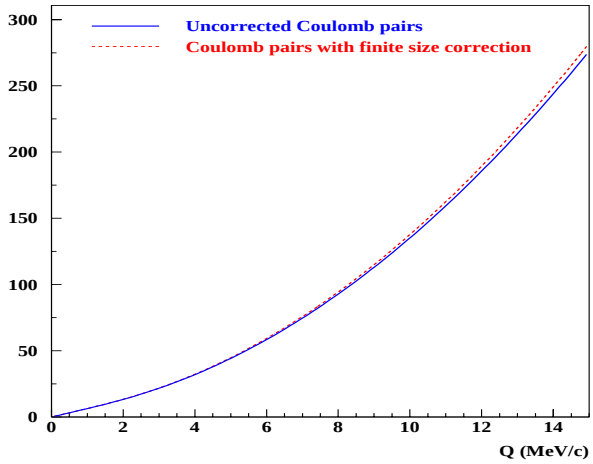

Fig. 8.24: Coulomb pair distribution at production with and without the applied finite size correction function.

In Fig. 8.24 this parametrization is shown in graphical form. For comparison we also plot the standard parametrization $dN_{CC}/Q \propto A_c(Q)Q^2$ used throughout the text.

We apply the finite size correction function F_{fs} to the *reconstructed* Coulomb events and graph the results in the form of ratios of the finite-size corrected over the non-corrected Q_l and Q spectra (Fig. 8.25). (The finite-size corrected Q_l distribution was obtained by numerically integrating the corresponding Q distribution with respect to Q_{trans} over the interval where the atomic pair signal is found, i.e. over 0 to 4 MeV/c.)

One can use thus modified Coulomb spectra to reconstruct the signal using the combined fit of the sum, difference and the extracted background, in the same manner as performed previously in the chapter. The resulting values of the fit parameters ρ and ω are plotted for different fit ranges on the right side of Fig. 8.26. The unmodified Coulomb distributions are shown on the left side of the figure. As is evident from Fig. 8.25, the parametrization F_{fs} gives more weight to the Coulomb pairs in the signal-free regions. This effect is clearly confirmed by Fig. 8.26, where the Coulomb/non-Coulomb parameter ω is increased by about 5% for both, Q_l and Q, distributions.

Despite the presence of the depression in the signal region of the parametrization

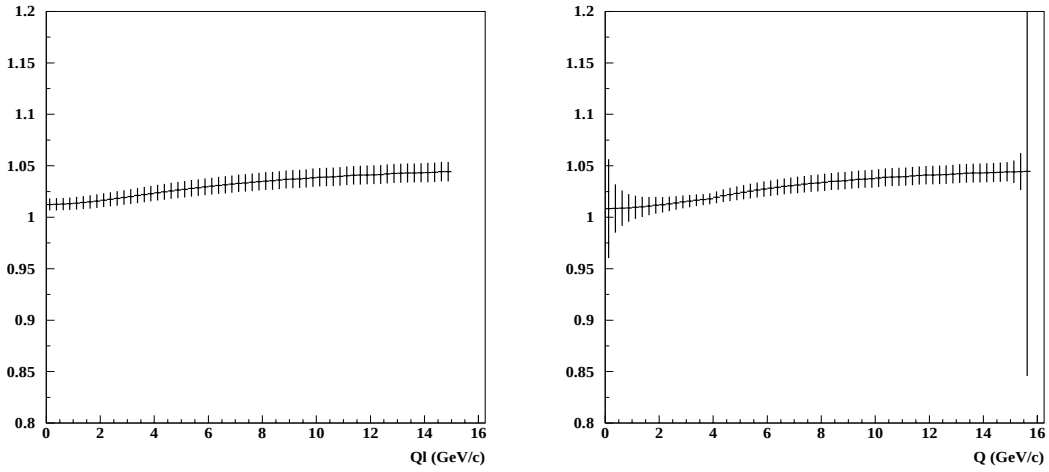

Fig. 8.25: Q_l and Q ratios of the finite-size modified Coulomb distributions after reconstruction over the standard, unmodified, spectra.

F_{fs}, its effects on the atomic pair signal cannot be easily estimated by eye due to the fact that the function has a slope of the opposite sign to the experimental prompt distributions (e.g., see Fig. 6.13). In fact, the increased ρ leads to *decreased* signals from both single and multilayer targets. Using N_{at}^s and N_{at}^m for the signal yields from the single and multilayer targets, respectively, and ΔN_{at} as the change in the atomic signal, one may make a rough estimate of the effect of the finite size correction on the single and multilayer target signal strengths. We consider the Q values in Fig. 8.26 and with

$$\rho = \frac{N_{at}^s + \Delta N_{at}}{N_{at}^m + \Delta N_{at}} = 2.006 \tag{8.32}$$

$$\rho = \frac{N_{at}^s}{N_{at}^m} = 1.930, \tag{8.33}$$

obtain $\Delta N_{at}/N_{at}^s = -3.9\%$ and $\Delta N_{at}/N_{at}^m = -7.6\%$. Thus the signal from both targets is decreased slightly. A similar conclusion was reached in Ref. [46] for 2001 single layer data. The number obtained in this work resulted from the signal strengths obtained directly from the residual events, analogous to the ones discussed in Section 8.4.1, before and after applying the finite size correction. From the Q_l values we obtain $\Delta N_{at}/N_{at}^s = -2.5\%$ and $\Delta N_{at}/N_{at}^m = -4.4\%$. With the more exact evaluation

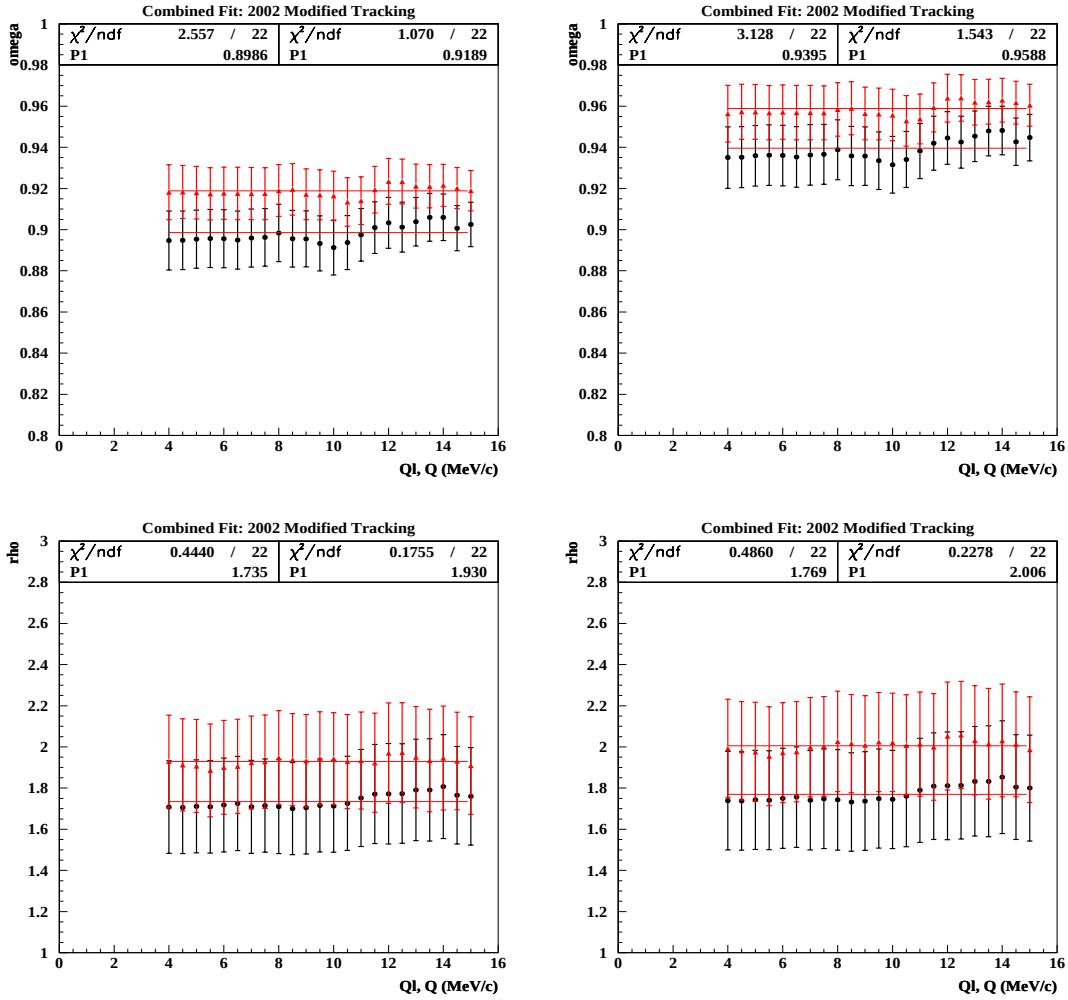

Fig. 8.26: The finite size correction effects. Combined fits for ρ and ω shown before (plots on the left) and after (right) applying the finite size correction weights. Q_l (filled circles) and Q (triangles) distributions are shown.

of 2001 data a decrease of 4.6% in the signal from the Q and 5.9% from the Q_l events was observed, the results comparable with our rough estimates of 3.9% and 2.5%.

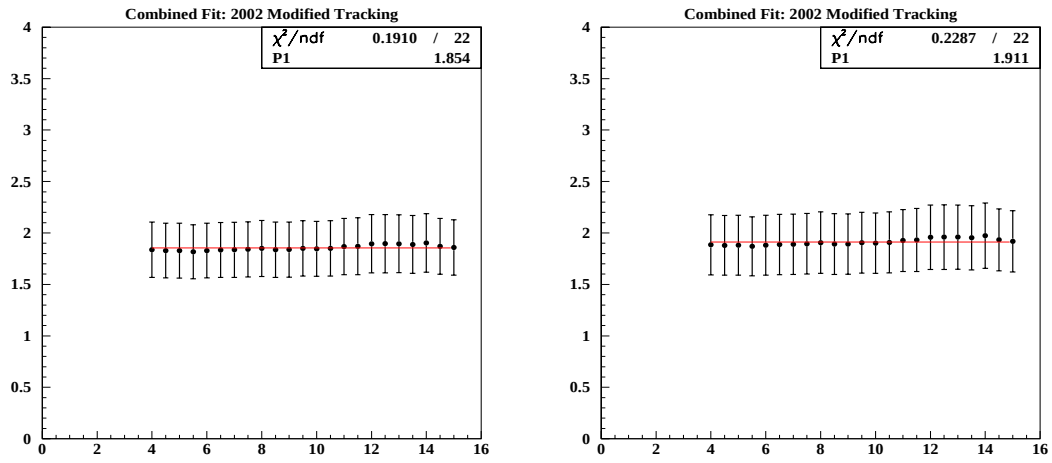

Fig. 8.27: Combined Q_l/Q ρ fits with 2002 modified tracking without (left) and with (right) the finite size correction function applied to the Coulomb pairs.

Performing a simultaneous fit in Q_l and Q with the finite-size corrected Coulomb pairs yields a value of ρ of 1.91, while the unmodified fit gives the value of 1.85 (Fig. 8.27). Using the breakup probability ratio *vs.* pionium lifetime parametrization (see Fig. 8.28, discussed in more detail below) one finds that those correspond to 2.33 and 2.64 fs lifetime, respectively, a 0.31 fs *increase* in lifetime. For the 2001 data [46] the lifetime values of 2.85 before the correction and 2.29 fs after applying the correction leads to a 0.51 fs *decrease* in lifetime. Thus, the single/multilayer target method is significantly less sensitive to the background shape than is the standard method of signal extraction, as claimed previously.

8.6 Breakup Probability and Pionium Lifetime

With all the statistical and systematical uncertainties accounted for (see Table 8.4 for the summary of the systematic errors), we are now ready to give the overall ratio of single to multilayer breakup probabilities and give the final value of the $A_{2\pi}$ lifetime.

Sources of Error	Description	σ_{sys}
Q_l/Q differences ($\sigma_{\Delta Q}$)	Q_l and Q difference in signals strengths	0.0388
Tracking/run period deviations (σ_{fits})	Signal uncertainty induced by tracking type/run period systematics	0.1126
Coulomb background composition (σ_{ω})	Influence on the signal of the Coulomb pair contribution to the background	0.0163
Signal shape systematics (σ_{shape})	Changing signal shape by increasing the average multiple scattering angle by 20%	0.0055
Accidental contribution (σ_{acc})	Influence on the signal of the accidental pair contribution to the background	0.0005
Total		0.1203

Table 8.4: Sources of systematic error of breakup probability with their corresponding contributions.

The ratio of the breakup probabilities is:

$$\begin{aligned} P^s_{br}/P^m_{br} &= 1.811 \pm 0.248\,(\text{stat.}) \\ &\quad \pm 0.0388\,(\sigma_{\Delta Q}) \pm 0.1126\,(\sigma_{\text{fits}}) \pm 0.0163(\sigma_{\omega}) \\ &\quad \pm 0.0055\,(\sigma_{\text{shape}}) \pm 0.0005\,(\sigma_{acc}) \\ &= 1.811 \pm 0.248\,(\text{stat.}) \pm 0.120\,(\text{sys.}) \\ &= 1.811 \pm 0.276. \end{aligned}$$

In terms of the relative errors, the statistical error is about 13.7% of the mean, the systematic error is about 48.5% of the statistical and 6.6% of the mean.

The atomic breakup probability dependence on lifetime for a 95 μm target has been calculated using Glauber approximation [17] and is described in more detail in Chapter 1. Similar calculation was performed for the 98 μm single layer and 96 μm multilayer targets. The parametrization of the ratio of the single to multilayer breakup probabilities P^s_{br}/P^m_{br} *vs.* $1s$ state lifetime τ is given by

$$P^s_{br}/P^m_{br} = [1.3596 + 0.25582\tau - 0.015523\tau^2][1 - \exp(-2.9404\tau^{1/2})]. \tag{8.34}$$

The ratio of the single to multilayer breakup probabilities P^s_{br}/P^m_{br} is plotted in Fig. 8.28. With the calculated value of the ratio breakup probabilities the parametrization 8.34 yields the value of the lifetime[3]

$$\boxed{\tau_{Ni_{02/03}} = 2.14^{+1.57}_{-1.08}\ \text{fs (tot.)}} \tag{8.35}$$

For comparison we also give the value of the lifetime with only the systematic errors taken into account:

$$\tau_{Ni_{02/03}} = 2.14^{+0.61}_{-0.52}\ \text{fs (sys.)} \tag{8.36}$$

Thus, we see that the statistical error is the one that heavily influences the error, being a few times larger than the systematic one.

C. Santamarina [60] had estimated the influence of 1% uncertainty (two dashed curves in Fig. 8.28) in estimating the target thickness on the breakup probability/lifetime relationship. This more conservative estimate yields:

$$\tau_{Ni_{02/03}} = 2.14^{+1.61}_{-1.10}\ \text{fs (tot.)} \tag{8.37}$$

[3]It should be noted that $\tau < 1.8$ fs has been excluded at 90% C.L. by the previous measurement at Serpukhov [59].

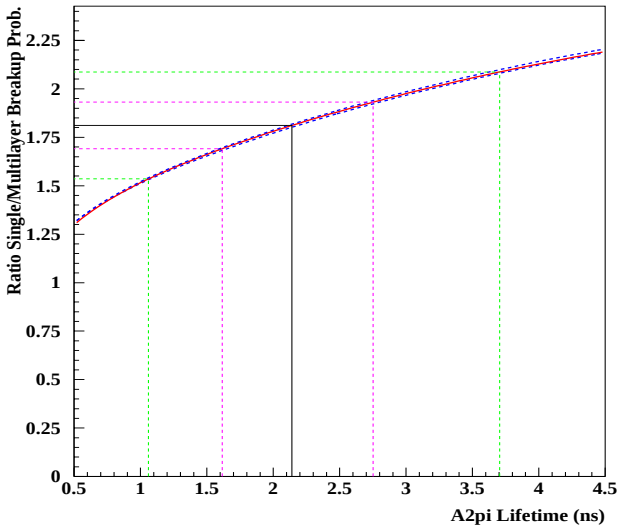

Fig. 8.28: Ratio of single/multilayer breakup probability *vs.* $A_{2\pi}$ lifetime. The dashed bands correspond to the systematic uncertainty introduced by 1% fluctuations in target thicknesses. Mean value of lifetime is shown, along with the systematic errors (a set of dashed lines closest to the mean) and the total error (statistical and systematic ones combined).

8.7 Statistical and Systematic Errors

The combined uncertainty of the ratio of breakup probabilities found in the previous section was calculated by simply combining the statistical and systematic errors in quadrature and taking a square root of the result. In this short section we discuss the validity of this approach.

Statistical and systematic errors may be combined in a rigorous way by using *convolution*, or *folding*, of errors. Mathematically convolution of two functions f and g is defined by the following expression:

$$f * g = \int_{-\infty}^{\infty} f(x)g(u-x)dx \tag{8.38}$$

In our case the number of input distributions is not two, but six, one corresponding to the statistical error and five corresponding to the various systematic ones (Table 8.4). The convolution procedure then, as applied to our case, is necessarily iterative. In the first step, the first systematic uncertainty ($f(x)$), which is assumed to be represented by a uniform distribution, is taken. It is then folded with the statistical

error ($g(u-x)$) represented by a Gaussian. This results in a convolution, which is, in turn, folded with the second systematic error. The procedure is repeated until all the the systematic errors have been accounted for. The final combined (convolved) error is shown on the left side of Fig. 8.29. The Gaussian distribution corresponding to the statistical error and the convolution of the systematic errors are also shown for comparison. The standard deviation of the folding is found to yield 0.276, which, with the given precision, exactly matches to the total error of P^s_{br}/P^m_{br} found in the previous section. If one considers the convolutions of the systematic errors (uniform distributions) (shown separately on the right-hand side of Fig. 8.29), one obtains 0.120, which is, again, the same value as obtained by simply adding the systematic errors in quadrature.

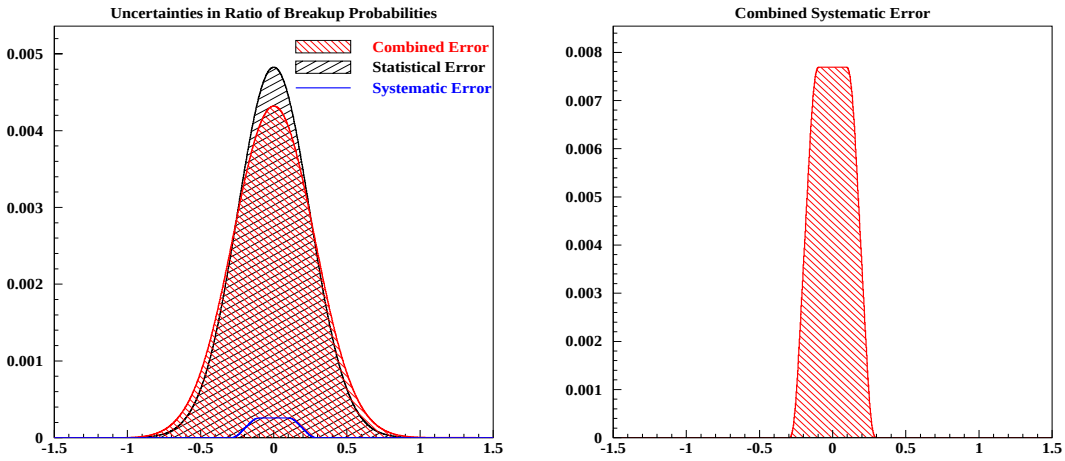

Fig. 8.29: Right: Statistical, systematic and folded (statistical and systematic) error distributions for the P^s_{br}/P^m_{br} ratio. Left: folded systematic error (composed of five uncertainties found in Table 8.4). All distributions shown are normalized to 1.

The agreement of the overall error and the combined systematic error with the values found previously is unsurprising if one considers an important property of the variance of the convolution. It can be proven that its variance is equal to the sum of the variances of its component functions. In particle physics one operates with the interval where a given value may be found with the 68.1% probability, which we'll call δ. In the case of Gaussian distribution δ coincides with the standard deviation,

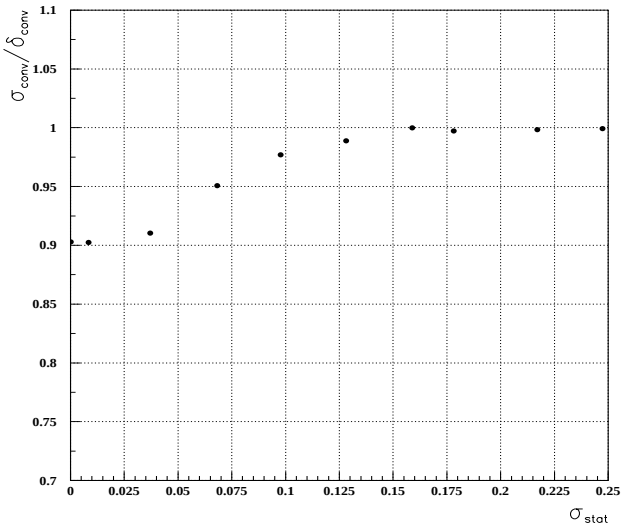

Fig. 8.30: Ratio of uncertainties of the combined (folded) error distribution $\sigma_{conv}/\delta_{conv}$ *vs.* the standard deviation of the Gaussian-distributed statistical error.

denoted here by σ; however, this correspondence does not necessarily hold true for any distribution. In our case, this is illustrated by the convolution under consideration. In Fig. 8.30 we plot the ratio of $\sigma_{conv}/\delta_{conv}$ of the convolution of the statistical and systematic errors (Fig. 8.29) as a function of the standard deviation (σ_{stat}) of the statistical error distribution. One observes that, while the σ_{stat} is significantly larger (the plateau between 0.158 and 0.248) than the standard deviation of the combined systematic error σ_{sys}, σ_{conv} and δ_{conv} coincide. Whereas, for example, for $\sigma_{stat} = 0.068$ the difference between σ_{conv} and δ_{conv} grows to 5% and the maximum difference of 10% is obtained when σ_{stat} is reduced to 0. Thus, we see that, when the statistical error distribution is appreciably wider than the systematic one, the convolution function has then the properties of a Gaussian, i.e. δ_{conv} and σ_{conv} coincide and the overall statistical and systematic errors could be added in quadrature. However, in general, the most rigorous method of obtaining δ_{conv}, valid for all combinations of σ_{stat} and σ_{sys} is not through an addition of squares of uncertainties, but through computing the interval corresponding to 68.1% area of the systematic/statistical error convolution. To summarize the results of the section: due to the width of the statistical relative

to the systematic distribution, the simple addition of the squares of uncertainties found in the previous section is a valid approach, however, with statistical errors comparable to or less than the combined systematic error, a convolution of errors needs to be considered.

8.8 Breakup Probabilities from the Q_l and Q Distributions Separately

As mentioned previously in the chapter, the simulated atomic pair signal slightly underestimates the results obtained with experimental data. Higher statistics obtained during the 2001 run make this effect even more apparent (Fig. 8.31). It is not immediately clear from the figure which momentum projection makes a better match to the experimental residual signal. Neither can an immediate conclusion be drawn from the physics standpoint. While it is true that Q_l is less affected by multiple scattering than the Q component due to the transverse nature of multiple scattering, the Q measurement is more precise due to the track information supplied by the upstream detectors. Due to the reasons found at the end of this section, we consider the combined Q_l/Q fit to yield the most precise results. However, for the sake of completeness and as a consistency check, in this section we will attempt to extract signals from the Q_l and Q spectra separately.

First, we perform a combined fit described by Eq. 8.21 for the Q_l projection only. Fig. 8.32 shows the results of the fit leading to the following values of ρ and ω:

$$\rho = 1.841 \pm 0.279 \text{ (stat.)} \tag{8.39}$$

$$\omega = 0.912 \pm 0.015 \text{ (stat.)} \tag{8.40}$$

The mean value of ρ is seen to be slightly higher than the one found from the combined Q_l/Q fit ($\rho = 1.811$). The statistical error on ρ is then about 15.1%, making it slightly larger than 13.7% found with the combined Q_l/Q fit.

To estimate the systematic error due to run year/tracking differences we fix ω at 0.912 (Eq. 8.40). The resulting plots may be found in Fig. 8.34. The largest spread

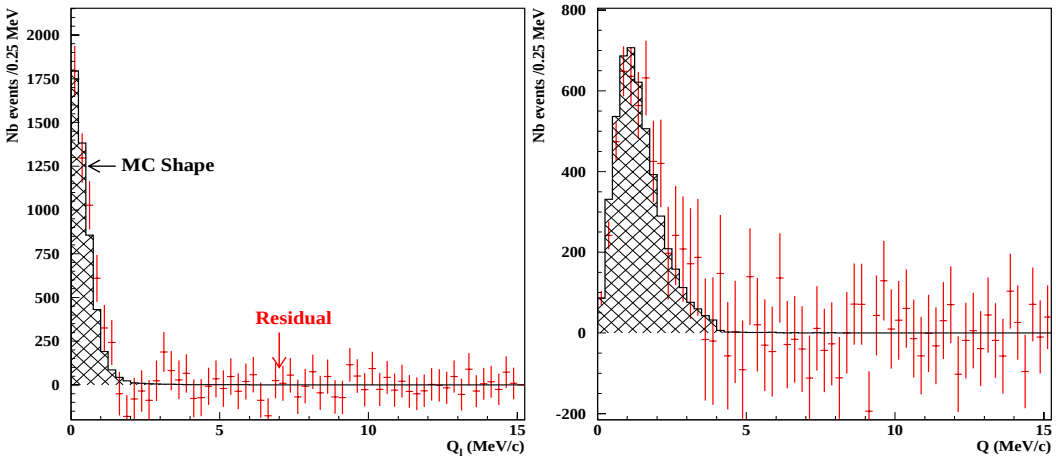

Fig. 8.31: Experimental signals (residuals) with the corresponding MC simulated atomic pair distributions in Q_l and Q. The MC events have not been fitted, but rather superimposed with their integrated number equal to the experimental residuals. (2001 data with modified tracking is shown.)

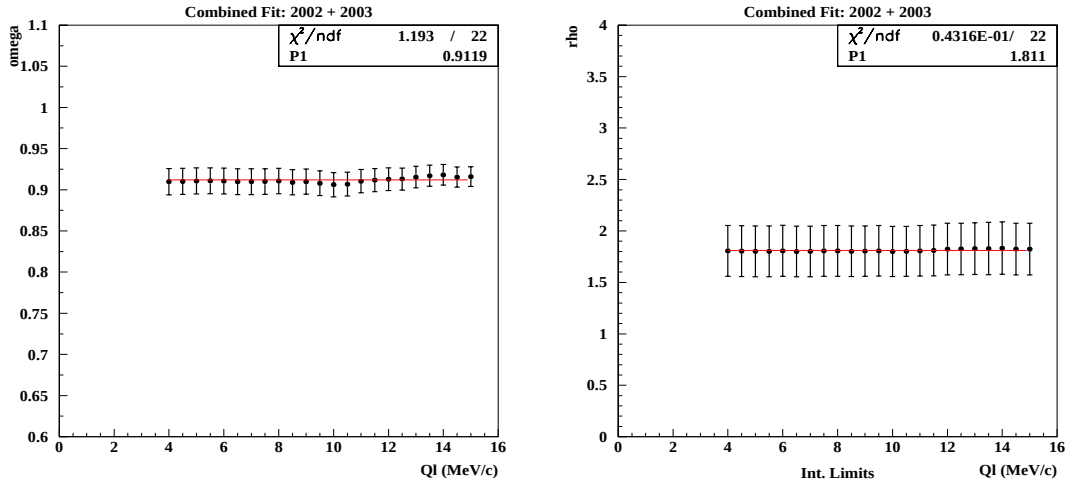

Fig. 8.32: Combined ω and ρ fits for 2002 and 2003 run periods with standard and modified tracking obtained using only Q_l spectra.

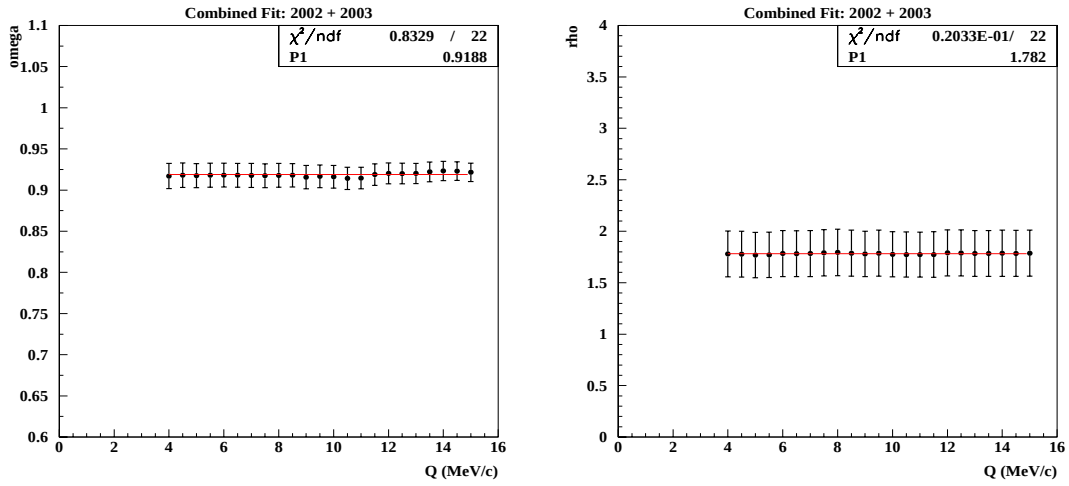

Fig. 8.33: Combined ω and ρ fits for 2002 and 2003 run periods with standard and modified tracking obtained using only Q spectra.

in fit values is between the 2002 run with standard tracking and the 2003 data with modified tracking. The systematic uncertainty yields:

$$\sigma_{\text{fits}} = 0.4691/\sqrt{12} = 0.1354, \tag{8.41}$$

corresponding to a 7.3% error with respect to ρ.

In analogy with the Q_l spectra, we now consider the combined fits with the Q spectra alone. The fit values for each range can be found in Fig. 8.33. Below we show the fit-range averaged values of ω and ρ.

$$\rho = 1.782 \pm 0.223\,(\text{stat.}) \tag{8.42}$$

$$\omega = 0.919 \pm 0.014\,(\text{stat.}) \tag{8.43}$$

The statistical error for ρ is about 12.5% with respect to the mean.

Analogously to the discussion above, we fix the value of ω at 0.912. From the fits (Fig. 8.35) we find the systematic error due to tracking/run period for the Q distributions to be:

$$\sigma_{\text{fits}} = 0.3307/\sqrt{12} = 0.0955, \tag{8.44}$$

corresponding to a 5.5% relative error.

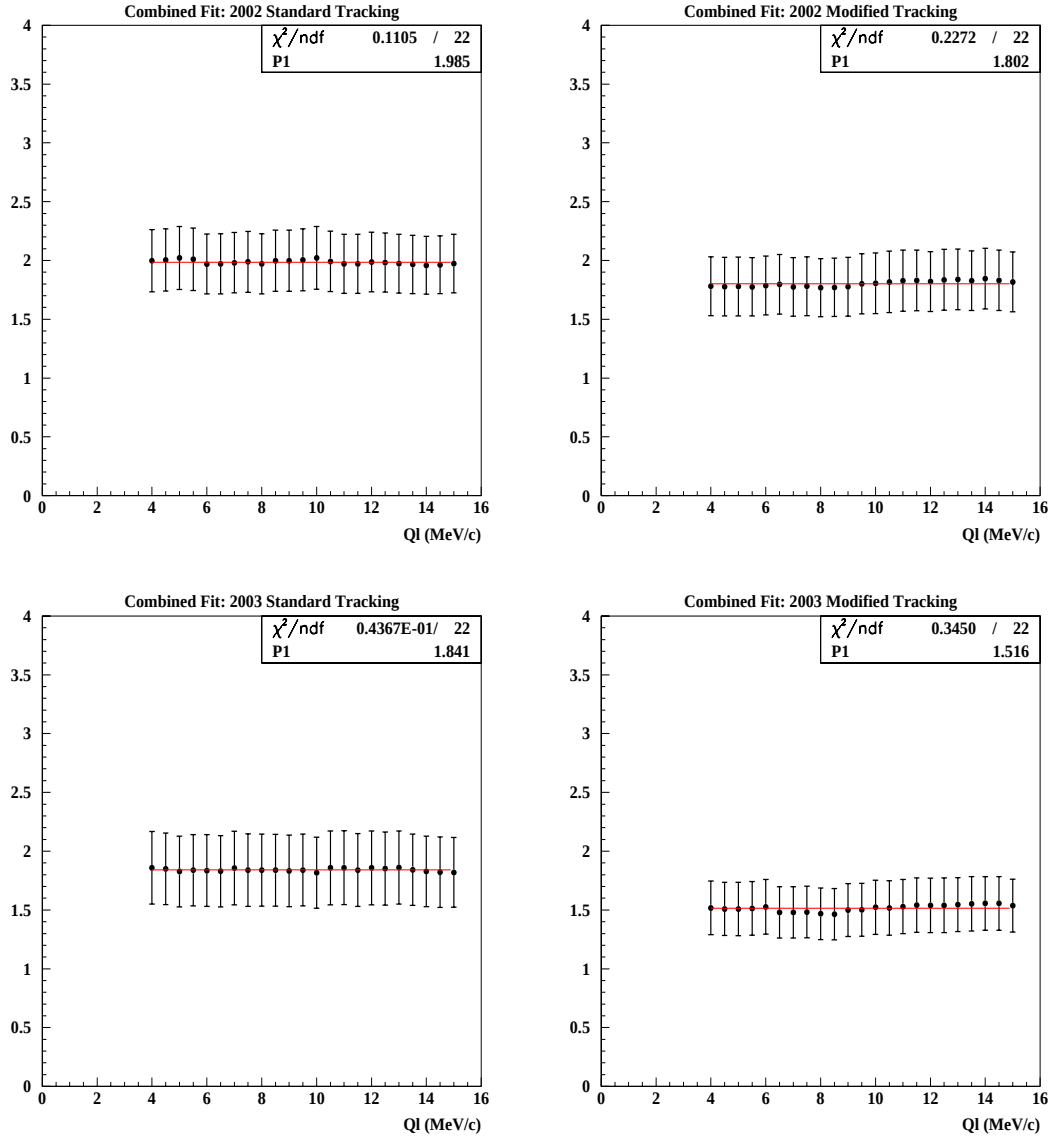

Fig. 8.34: Values of ρ obtained exclusively from the Q_l spectra. ω was held fixed at 0.912 obtained from the simultaneous Q_l fits.

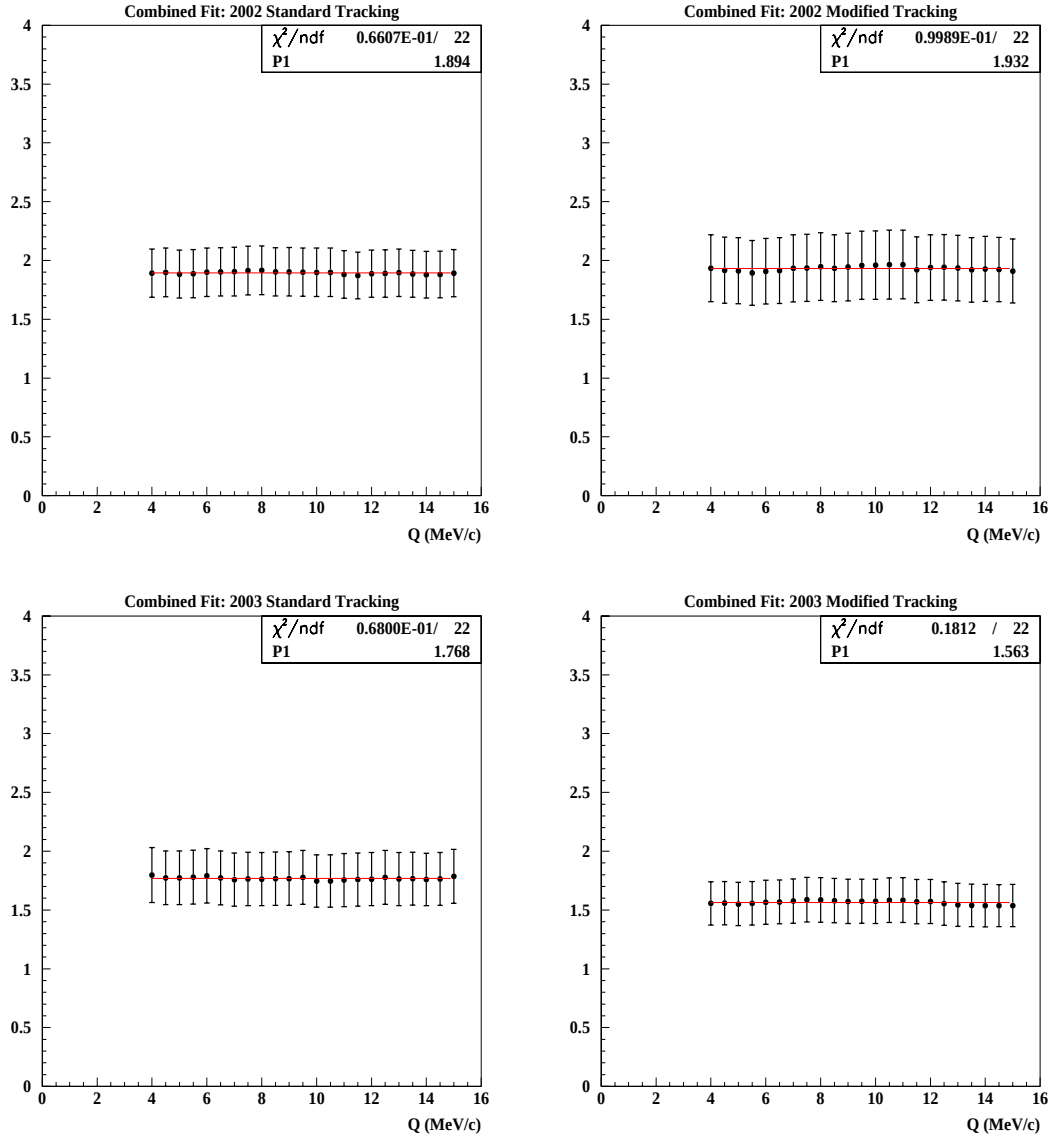

Fig. 8.35: Values of ρ obtained exclusively from the Q spectra. ω was held fixed at 0.919 obtained from the simultaneous Q fits.

Thus, as desired, we find that the Q_l and Q mean values and the statistical and systematic uncertainties of ρ and ω straddle the corresponding values from the combined Q_l/Q fits found in Section 8.6. Although the accuracy of the statistical and systematic uncertainties obtained from the Q spectra alone appears to exceed that of the Q_l and Q_l/Q methods, based on the relative advantages and disadvantages of both (as discussed in the beginning of the section) we consider the Q_l/Q analysis to be the most precise one. The combined Q_l/Q method can be regarded as an "average" of the separate Q_l and Q analyses, its systematic error taking into account any discrepancies between the two (see Sections 8.4.1 and 8.4.2).

Chapter 9

Summary

In this work have analyzed the data sample collected by the DIRAC experiment during 2002 and 2003 run periods. We have employed the single/multilayer target method to find the ratio of pionium atom breakup probabilities. It has been shown to yield:

$$P_{br}^{s}/P_{br}^{m} = 1.811 \pm 0.248\,(\text{stat.}) \pm 0.120\,(\text{sys.}), \tag{9.1}$$

with the systematic error being 6.6% of the mean and 48% of the statistical error. The ratio of breakup probabilities then led us to the value of lifetime of the $1s$ state of the $A_{2\pi}$:

$$\tau_{Ni_{02/03}} = 2.14^{+1.65}_{-1.12}\ \text{fs}, \tag{9.2}$$

$\tau_{Ni_{02/03}}$ is found to agree within 1σ with the 2001 run period [46] result of

$$\tau_{Ni_{01}} = 2.85^{+0.48}_{-0.41}\ \text{fs}. \tag{9.3}$$

This value was obtained using the K-factor method, where the signal was found by exploiting the relationship between the Coulomb and atomic pairs. The same method can be applied individually to the single and multilayer targets for the 2002/2003 run period and the respective atomic breakup probabilities and the resulting lifetime can be calculated and would serve as a cross-check of our results.[1]

[1]This analysis has not been performed for this thesis.

Higher accuracy of the 2001 lifetime determination can be explained by higher experimental statistics and steeper slope of the breakup probability *vs.* lifetime dependence, compared to the one for the ratio of breakup probabilities *vs.* lifetime curve used in this thesis. With the 1σ uncertainties taken into account the 2001 and 2002/2003 lifetimes are seen to agree. The agreement of both values with

$$\tau_{1s} = 2.9 \pm 0.1 \text{ fs} \tag{9.4}$$

predicted by the Chiral Perturbation theory is also observed.

Using $\tau_{Ni_{02/03}}$ one may also estimate the $|a_0^0 - a_0^2|$ scattering lengths difference for the 2002/2003 run period (cf. Eq. 2.39). Its magnitude is found to be:

$$|a_0^0 - a_0^2| = 0.308^{+0.119}_{-0.081}\,[m_\pi^{-1}], \tag{9.5}$$

which is within 1σ agreement with the Chiral Perturbation theory prediction:

$$|a_0^0 - a_0^2| = 0.265 \pm 0.004\,[m_\pi^{-1}]. \tag{9.6}$$

Bibliography

[1] B. R. Holstein, "Chiral Perturbation Theory: a Primer," arXiv:hep-ph/9510344.

[2] V. Koch, "Aspects of chiral symmetry," Int. J. Mod. Phys. E **6**, 203 (1997) [arXiv:nucl-th/9706075].

[3] B. R. Martin, D. Morgan, G. Shaw, "Pion-pion Interactions in Particle Physics," Academic Press (1976).

[4] S. Weinberg, "Pion Scattering Lengths," Phys. Rev. Lett. **17**, 616 (1966).

[5] M. Gell-Mann, R. J. Oakes and B. Renner, "Behavior Of Current Divergences Under SU(3) X SU(3)," Phys. Rev. **175**, 2195 (1968).

[6] J. Gasser and H. Leutwyler, "Chiral Perturbation Theory To One Loop," Annals Phys. **158**, 142 (1984).

[7] G. Colangelo, J. Gasser and H. Leutwyler, "The pi pi S-wave scattering lengths," Phys. Lett. B **488**, 261 (2000) [arXiv:hep-ph/0007112].

[8] S. Deser, M. L. Goldberger, K. Baumann and W. Thirring, "Energy Level Displacements In Pi Mesonic Atoms," Phys. Rev. **96**, 774 (1954).

[9] T. R. Palfrey and J. L. Uretsky, "Photoproduction And Detection Of The Two Meson Bound State," Phys. Rev. **121**, 1798 (1961).

[10] J. Gasser, V. E. Lyubovitskij, A. Rusetsky and A. Gall, "Decays of the pi+ pi- atom," Phys. Rev. D **64**, 016008 (2001) [arXiv:hep-ph/0103157].

[11] L. G. Afanasev and A. V. Tarasov, "Breakup of relativistic pi+ pi- atoms in matter, Phys. Atom. Nucl. **59**, 2130 (1996) [Yad. Fiz. **59**, 2212 (1996)].

[12] L. Afanasev, A. Tarasov and O. Voskresenskaya, "Total interaction cross sections of relativistic pi+ pi- atoms with ordinary atoms in the eikonal approach," J. Phys. G **25**, B7 (1999).

[13] Z. Halabuka, T. A. Heim, K. Hencken, D. Trautmann and R. D. Viollier, "Coulomb excitation and breakup of pi+ pi- atoms at high energies," Nucl. Phys. B **554**, 86 (1999).

[14] T. Heim *et al.*, "Coherent and incoherent atomic scattering: formalism and application to pionium interacting with matter," J. Phys. B **33** (2000) 3583.

[15] T. Heim *et al.*, "Pionium interacting with matter: magnetic terms and relativistic corrections," J. Phys. B **34** (2001) 3763.

[16] M. Schumann *et al.*, "Excitation cross sections for pionium in the Glauber approximation," J. Phys. B **35** 2683 (2002).

[17] C. Santamarina, M. Schumann, L. G. Afanasyev and T. Heim, "A Monte Carlo Calculation of the Pionium Break-up Probability with Different Sets of Pionium Target Cross Sections," J. Phys. B. At. Mol. Opt. Phys. **36**, 4273 (2003) [arXiv:physics/0306161].

[18] L. L. Nemenov, "Elementary Relativistic Atoms," Sov. J. Nucl. Phys. **41**, 629 (1985) [Yad. Fiz. **41**, 980 (1985)].

[19] L. D. Landau and E. M. Lifshitz, Quantum Mechanics (Non-relativistic Theory), 3rd Edition, Pergamon Press 1976.

[20] "Two target method for the lifetime measurement," L. Afanasyev, A. Kuptsov, V. Yazkov, DIRAC Note **02-08**.

[21] S. M. Roy, "Exact Integral Equation For Pion Pion Scattering Involving Only Physical Region Partial Waves," Phys. Lett. B **36**, 353 (1971).

[22] S. Pislak *et al.*, "High statistics measurement of K(e4) decay properties," Phys. Rev. D **67**, 072004 (2003) [arXiv:hep-ex/0301040].

[23] M. E. Sevior *et al.*, "Measurement Of The H (Pi+, Pi+ Pi+) N Cross-Section Very Near Threshold And Chiral Symmetry," Phys. Rev. Lett. **66**, 2569 (1991).

[24] B. Adeva *et al.* [DIRAC Collaboration], "DIRAC: A high resolution spectrometer for pionium detection," Nucl. Instrum. Meth. A **515**, 467 (2003) [arXiv:hep-ex/0305022].

[25] R. Fernow, "Introduction to Experimental Particle Physics," Cambridge University Press, 1986.

[26] A. Oed, "Position Sensitive Detector With Microstrip Anode For Electron Multiplication With Gases," Nucl. Instrum. Meth. A **263**, 351 (1988).

[27] B. Adeva, C. Burgos, J. A. Castro, F. Gómez, T. Núñez, A. Pazos, M. Pló, P.Vázquez "MSGC Detector DIRAC experiment," DIRAC Note **99-04**.

[28] A. Gorin *et al.*, "Peak-Sensing Discriminator For Multichannel Detectors With Cross-Talk," Nucl. Instrum. Meth. A **452**, 280 (2000).

[29] A. Gorin *et al.*, "Status Report on the SFD, SciFi detector group" DIRAC Note **96-12**.

[30] A. Gorin, Private communication (2002).

[31] G. Bitsadze, V. Brekhovskikh, A. Kuptsov, V. Lapsin, V. Rykalin, L. Tauscher, M. Zhabitsky, "The Ionisation Hodoscope of the DIRAC Experiment," Nucl. Instrum. Meth. A **533**, 353 (2004).

[32] V. Karpukhin, "Drift chambers electronics," DIRAC Note **95-05**.

[33] L. Afanasyev and V. Karpukhin, "Drift chamber readout system of the DIRAC experiment," Nucl. Instrum. Meth. A **492**, 351 (2002) [arXiv:hep-ex/0208011].

[34] B. Adeva *et al.*, "The Time-Of-Flight Detector Of The Dirac Experiment," Nucl. Instrum. Meth. A **491**, 41 (2002).

[35] M. Bragadireanu *et al.*, "A Prototype Threshold Cherenkov Counter For Dirac," Nucl. Instrum. Meth. A **426**, 254 (1999).

[36] M. Pentia, Gh. Caragheorgheopol, M. Ciobanu, D. Pop and C. Rusu, "Preshower detector commissioning along with DIRAC set-up," DIRAC Note **99-03**.

[37] K. Hagiwara *et al.* [Particle Data Group Collaboration], "Review Of Particle Physics," Phys. Rev. D **66**, 010001 (2002).

[38] M. Pentia, "Preshower detector for DIRAC experiment," `http://dirac.web.cern.ch/DIRAC/psh`.

[39] V. Brekhovskikh, M. V. Gallas, "Muon identification in DIRAC experiment," DIRAC Note **01-02**.

[40] D. Goldin, L. Tauscher, "Scintillating fiber detector efficiency study," DIRAC Note **03-02**

[41] D. Goldin, L. Tauscher, "Scintillating fiber detector background study and simulation," DIRAC Note **02-06**

[42] L. Afanasyev *et al.*, "The multilevel trigger system of the DIRAC experiment," Nucl. Instrum. Meth. A **491**, 376 (2002) [arXiv:hep-ex/0202045].

[43] L. G. Afanasev, V. V. Karpukhin, A. V. Kulikov and M. Gallas, "First level trigger of the DIRAC experiment," Nucl. Instrum. Meth. A **479**, 407 (2002).

[44] P. Kokkas, M. Steinacher, L. Tauscher and S. Vlachos, "The neural network first level trigger for the DIRAC experiment," Nucl. Instrum. Meth. A **471**, 358 (2001).

[45] B. Adeva *et al.* [DIRAC Collaboration], "Detection of $\pi^+\pi^-$ Atoms with the DIRAC Spectrometer at CERN," Phys. G: Nucl. Part. Phys. **30**, 1929 (2004) [arXiv:hep-ex/0409053].

[46] Ch. P. Schütz, "Measurement of the Breakup Probability of $\pi^+\pi^-$ atoms in a Nickel Target with the DIRAC Spectrometer," Ph.D. Thesis, University of Basel, Basel (2004).

[47] P. Maybeck, Stochastic Models, Estimation and Control, Volume 1, Academic Press, New York (1979)

[48] Ch. P. Schuetz and L. Tauscher, "The Basel tracking algorithm in the DIRAC experiment," DIRAC Note **03-06**.

[49] Ch. P. Schuetz and L. Tauscher, "The BASEL SFD Y prediction method in the DIRAC experiment," DIRAC Note **02-04**.

[50] A. Benelli, D. Goldin, C. Santamarina, Ch. P. Schuetz, L. Tauscher, S. Vlachos "Systematic errors in the DIRAC experiment," DIRAC Note **03-01**.

[51] P. Zrelov and V. Yazkov, "The GEANT-DIRAC simulation program," `http://zrelov.home.cern.ch/zrelov/dirac/montecarlo/instruction/_instruct26.html`.

[52] D. Drijard, M. Hansroul and V. Yazkov, "The DIRAC Offline User Guide," `http://dirac.web.cern.ch/DIRAC/Userguide.html`.

[53] C. Santamarina and Ch. P. Schütz, "Determination of the Experimental k-Factor," DIRAC Note **03-09**.

[54] L. Afanasyev, "Observation of $\pi^+\pi^-$ Atoms," Ph.D. Thesis, JINR, Dubna (1997)

[55] T. A. Heim, K. Hencken, M. Schumann, D. Trautmann and G. Baur, Proceedings of the HadAtom '01, Workshop 13, `http://www.arxiv.org/ps/hep-ph/0112293`.

[56] V. V. Uzhinskii, 1996 JINR preprint E2-96192, Dubna.
B. Andersson *et al.*, Nuclear Physics **B 281** (1987) 289.
B. Nilsson-Almquist and E. Stenlund, Comp. Phys. Comm. **43** (1987) 387.

[57] R. Lednický and J. Smolik, Private communication (2003).

[58] F. James and M. Roos, "'Minuit' A System For Function Minimization And Analysis Of The Parameter Errors And Correlations," Comput. Phys. Commun. **10**, 343 (1975).

[59] L Afanasyev, O. Voskresenskaya, V. Yazkov, "Ratio of Production Cross-sections of the Oppositely Charged Pions in Free and Bound States," JINR Communications **P1-97-306**.

[60] C. Santamarina, Private communication (2002).

Appendix A

Scintillating Fiber Detector Efficiency Study

The scintillating fiber detector (SFD) provides information essential for momentum determination and MSGC clustering. It is crucial to assess the efficiency of this detector as the event reconstruction cannot proceed if the SFD response is inaccurate or missing. We analyze this response by examining single and close lying double track events, in which we rely on the ADC values registered by the ionization hodoscope (IH) and the zeroth-order track reconstruction with drift chambers downstream of the magnet. Spring 2001 and Summer 2000 data samples with 10 million events taken with a mixed trigger $(DNA.or.T3).and.T1_{\pi\pi copl}.or.T1_{ee}or.T_{\Lambda}.or.T_{Kaon}$ were used. The experiment was run with different SFD thresholds during these two run periods. Since the T2 trigger was active at the time, 1999 data could not be analyzed.

A.1 Procedure

At the start of our procedure, we use the hit slabs in both planes of the ionization hodoscope to localize one or two particles that have crossed the detector within a small horizontal spatial iterval. Since the distance between the IH and the SFD is small and the amount of material between them is low, we assume the lateral displacements

between the SFD and the IH due to multiple scattering in the SFD or the MSGC to be small. Moreover, we rely on the fact that the particles originate from the target area. Events that are selected meet the following conditions:

- *Pion triggers.* Only the events with pion trigger marks are selected. As an additional "clean-up measure" we eliminate events containing electrons in the Cherenkov detector (see Fig. A.3) and muon tracks using the preshower and muon detectors.[1] We note that the prompt events may also contain protons ($p \geq 3.5$ GeV/c), which, similar to pions, are minimum ionizing.

- *Ionization hodoscope cuts:* Require ADC signals from the overlapping hit slabs in both planes of the IH as shown in Fig. A.1. And in the case of:
  (a) Single ionization: Require ADC signal in the range between 100 and 180 (Fig .A.4).
  (b) Double ionization: Require ADC signal above 250.

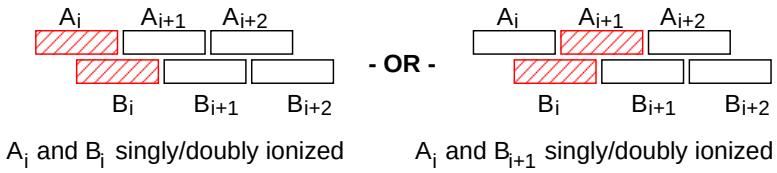

Fig. A.1: Double ionization configuration in the IH.

- *Timing of the hits:* We choose with time difference of -0.5 to 0.5 ns between the left and the right arm of the vertical hodoscope. Additionally, only the hits in the x-plane of the SFD and both planes of the ionization hodoscope which correspond to the TDC signal between 5 and 10 ns are taken. We constrain the time difference between the two planes of the ionization hodoscope to ± 2 ns. (In Fig. A.2 we show timing for plane 1 of the IH; plane 2 and the SFD timing are very similar.)

[1] Muon tracks were eliminated using the method described in [39].

- In the case of double ionization we require only one occurence of the doubly ionized slab per event in each plane. This ensures that only one pair of particles traveling close to each other is identified.

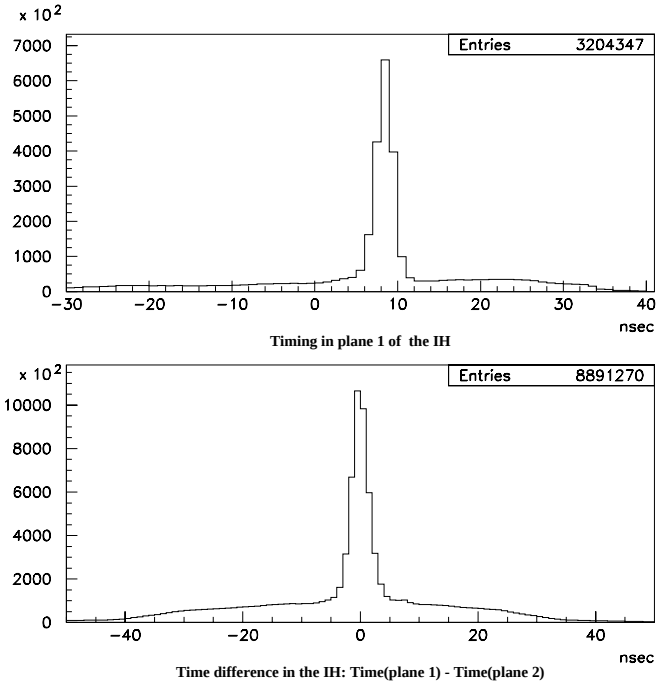

Fig. A.2: Timing of prompt events.

A.2 Identifying "active areas" of the SFD

In the first step of our analysis we localize the "active areas" of the SFD, i. e. the regions where one should look for hits corresponding to the two slab overlap area shown in Fig. A.1. In each case when the double ionization criterion in the ionization hodoscope is satisfied, we record all the hit channels in the x-plane of the SFD for this event. The result can then be graphed in the form of a scatter plot and the hit distributions in the SFD per IH slab (i.e. a projection of the scatter plot onto the SFD hit axis) (Fig. A.6 and A.7). The SFD projection plots enable us to find the

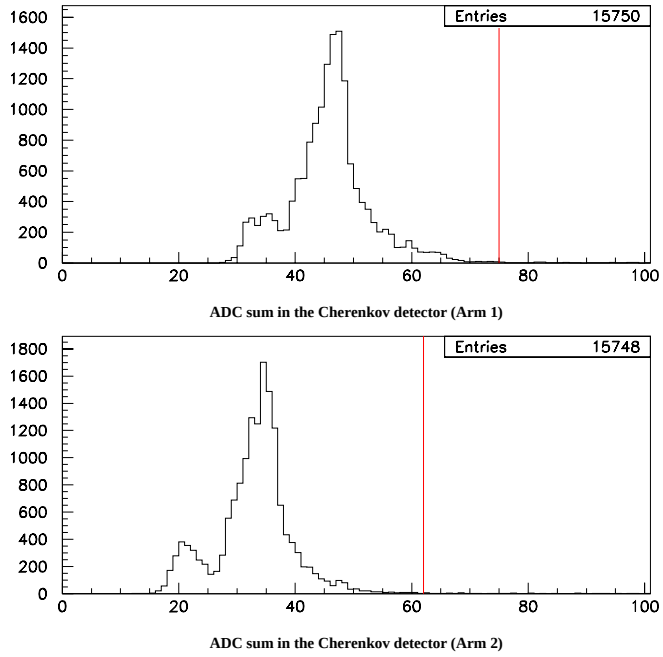

Fig. A.3: ADC signal in the Cherenkov detector after the $\pi^+\pi^-$ trigger has been applied. Signals below 75 in Arm 1 and below 62 in Arm 2 (thresholds marked with the vertical line) are rejected in this analysis.

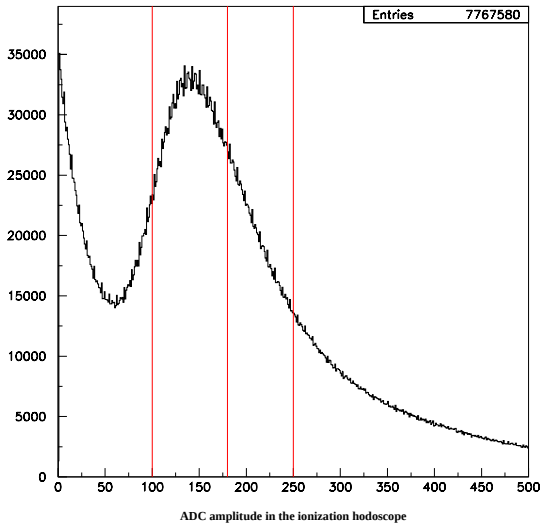

Fig. A.4: ADC signal in the ionization hodoscope. Single ionization cut corresponds to the region between 100 and 180 ADC counts and and double ionization to amplitudes above 250.

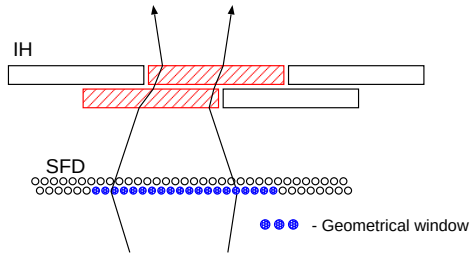

Fig. A.5: Geometrical window definition.

positions of the peak areas as a function of the IH slab number.

Knowing a window position, we can now obtain a precise value of its width. Due to multiple scattering we expect this width to be slightly broader than the overlap area of 3.3 mm between the slabs in the ionization hodoscope (Fig. A.5). Indeed we find this to be true when we cycle over the same events plotting the distance between the center of each window and the hits closest to it. The result for the cases of single (left) and double ionization (right) is shown in Fig. A.8. In the first row we plot the closest hit - window center distance in units of SFD channels, in the second the distances of 2 closest hits to the window center (closest hit - center and next-to-closest hit-center, both in the same plot) and in the third row 3 closest hits. It is evident that the width of the active areas (to which from here onward we will refer to as the "geometrical windows") can now be fixed at 10 channels (± 5 channels centered around 0), or approximately 4.5 mm. As expected, one observes a rise in background hits as one advances from a single closest to three closest hits. The peaks correspond to the window we are looking for and the areas outside are the background hits which we can discard. The shapes of the graphs are fairly symmetrical and the maxima are centered around 0 indicating that the geometrical window was indeed found correctly.

A.3 Efficiencies

By counting hits inside and outside a geometrical window whenever two overlapping singly (doubly) ionized signals in the IH are registered, we find the combined

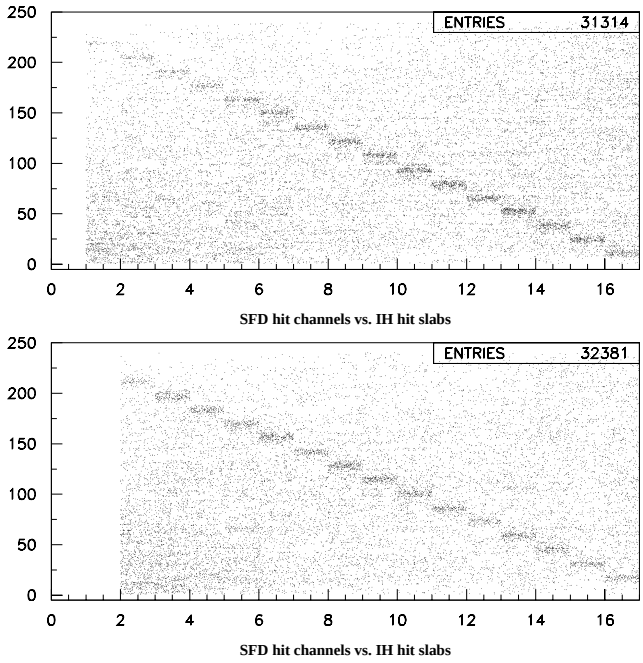

Fig. A.6: Scatter plots of SFD vs. IH hits. Top graph corresponds to the left-hand side configuration in Fig. A.1, bottom graph to the right-hand side.

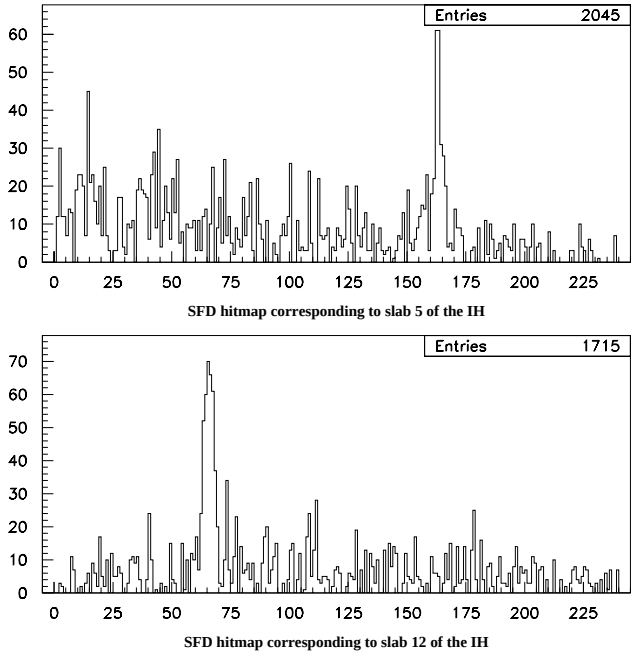

Fig. A.7: SFD projections.

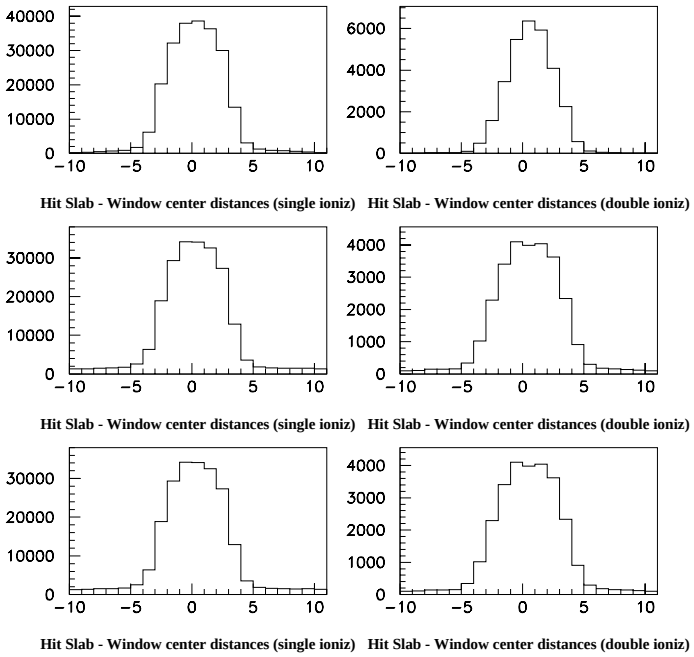

Fig. A.8: Hit slab - window center distances in units of SFD channels. Top: closest hit, center: 2 closest hits, bottom 3 closest hits to window center distances

window multiplicity (Fig. A.9). In Table A.1 we show these results in numerical form.

For the single ionization case the imposed cuts reduce the original sample of 10 million events by a factor of 2.5×10^{-2} in the year 2001 and by 1.2×10^{-3} in the year 2000. The number of events with no signal when one was expected is registered in 10% of the events in 2001 and in 26% of the events in 2000. We also note that the single hit events dominate the statistics as expected and that only about 3.4% of the events in 2001 (1.6% in 2000) have two or more hits within the geometrical window.

For the case of double ionization the reduction factor is 3.3×10^{-3} for 2001 runs and about 3.5×10^{-3} for the year 2000. We observe events with no signal when one was expected in 7.6% of the cases in 2001 and in 30.3% in 2000. As expected, most of the remaining cases have one or two hits within the geometrical window. There is a sharp increase in the number of double hits in 2001 with respect to 2000 (25% in 2001 compared to only 9% in 2000).

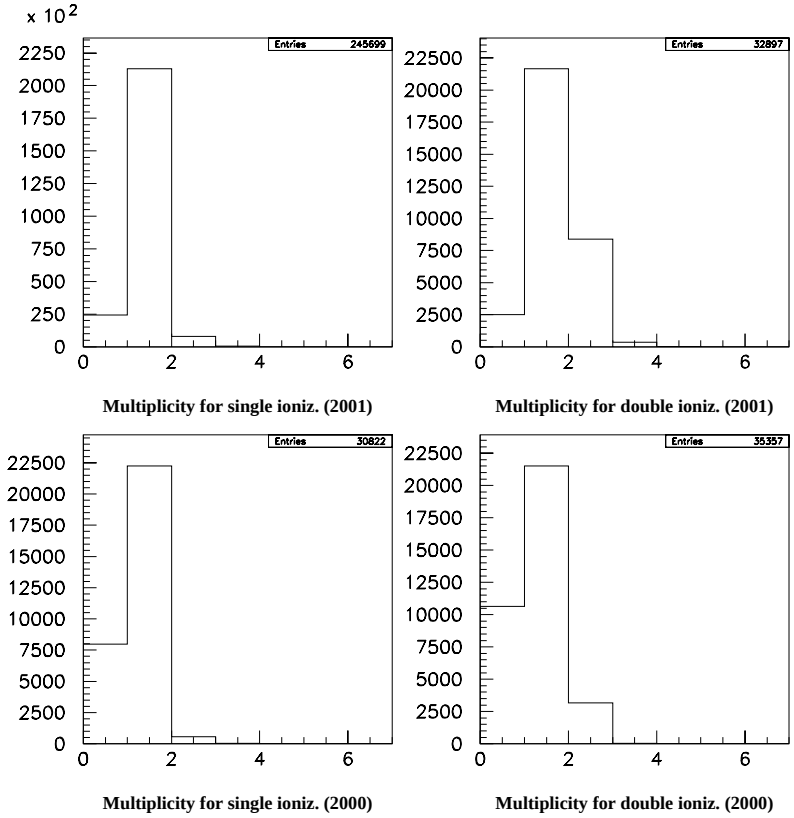

Fig. A.9: Multiplicity inside geometrical windows.

Run	Total	**Mult. 0**	Mult. 1	Mult. 2	Mult. > 2
2001 (%)	100%	**9.92±0.06%**	86.6±0.2%	3.26±0.04%	0.182±0.009%
(events)	245699				
2000 (%)	100%	**25.9±0.3%**	72.2±0.5%	1.80±0.08%	0.078±0.016%
(events)	30822				

Run	Total	**Mult. 0**	Mult. 1	Mult. 2	Mult. > 2
2001 (%)	100%	**7.62±0.15%**	65.8±0.4%	25.4±0.3%	1.10±0.06%
(events)	32897				
2000 (%)	100%	**30.1±0.3%**	60.9±0.4%	8.96±0.16%	0.127±0.018%
(events)	35357				

Table A.1: Window multiplicities with statistical errors for single ionization (top) and double ionization events (bottom).

A.4 Efficiencies with Tracking

The results in the tables above could be refined further if for every single ionization event in the overlapping IH slabs one also requires the presence of a zeroth-order track and, in the case of of double ionization, two tracks upstream of the magnet.[2] The region of the SFD where each track is "allowed" to pass is determined by multiple scattering downstream. Its width, set to 2σ, is found to be $1.6/P_{tot}$ cm, where P_{tot} is the total lab momentum of the zeroth-order track. The center of this new window, which we will call the "track window", is the midpoint of the overlap region of two singly (doubly) ionized IH slabs (Fig. A.10). The track window width can be shown to vary from 9 SFD channels, which is close to the the geometrical window size of 10 channels, to about 30 channels (4.5 mm to 13.5 mm range) (Fig. A.11).[3] In addition,

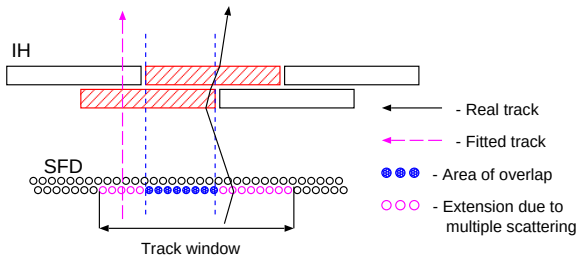

Fig. A.10: Track window definition.

to make sure that only the hits corresponding to tracks are selected we restrict our sample even further by applying the same sized track window to the y-plane of the SFD[4] and require the single and double track events to have at least one hit inside and the timing of the hits to be between 5 and 10 ns.

Whenever a track passes through the track window in the single ionization case (for double ionization we require two tracks to pass through their respective track

[2]At this stage of tracking the drift chamber fit extended upstream and connected by a straight line to the target (assumed at the origin).

[3]If one compares and plots position and width of the track window with that of the geometrical window, one finds that the geometrical window is entirely contained within the track window in 97% of the selected events.

[4]Multiple scattering downstream of the magnet is approximately the same in the x and y direction.

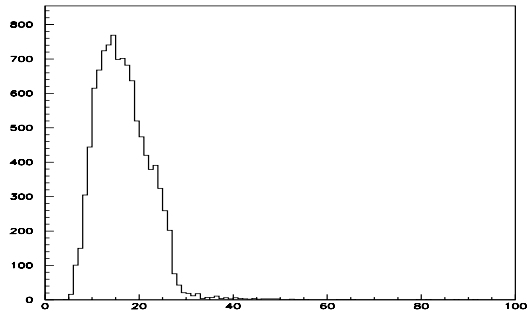

Fig. A.11: Track window width distribution.

windows), the y-plane spatial restrictions, and the initial time constraints imposed on the ionization hodoscope and the x-plane of the SFD are satisfied, we record the appropriate hits in the x-plane. One of the effects of these restrictions is a reduction in the background outside the geometrical window. In Fig. A.12 (2001 data) we compare distances of the hits closest to the window center - the position of the window center with and without the track requirement for the case of double ionization. The percentage of hits outside the $\pm$ 5 channel window is around 4% in the latter case, and about 1% in the former. For the single ionization the decrease in background hits is smaller and is around 1%.

For comparison with Fig. A.8 we also plot closest hit - window center distances for different locations of the tracks relative to the track windows (throughout this part of the analysis we do require the presence of at least one downstream track for the events with single ionization and at least 2 tracks for the events with double ionization) (Fig. A.13, A.14).

One can now plot multiplicities inside the geometrical window (Fig. A.15) and construct a table similar to Table A.1 (Table A.2).

To summarize the rest of the results, the single track requirement reduces the statistics in Table A.1 by a factor of 4.6 in 2001 and by a factor of 7.2 in 2000. For the double ionization events this factor is around 12 in 2001 and 19 in 2000. The track constraint did not have a significant effect on single ionization, but contributed

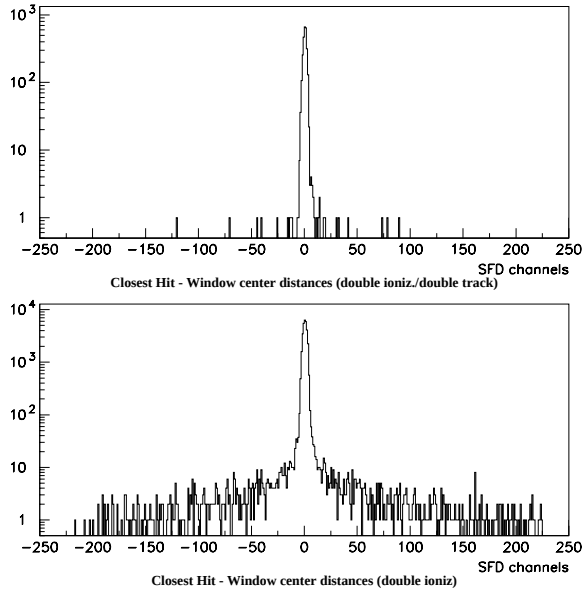

Fig. A.12: Double ionization: closest slab - window center distributions for events with (top) and without (bottom) the track requirement. The bottom plot is the expanded version of Fig A.8.

Run	Total	**Mult. 0**	Mult. 1	Mult. 2	Mult. > 2
2001 (%)	100%	**8.35±0.12%**	88.2±0.4%	3.29±0.08%	0.164±0.017%
(events)	53769				
2000 (%)	100%	**19.7±0.6%**	78.0±1.3%	2.28±0.22%	0.020±0.020%
(events)	4914				

Run	Total	**Mult. 0**	Mult. 1	Mult. 2	Mult. > 2
2001 (%)	100%	**2.82±0.32%**	42.3±1.2%	52.6±1.4%	2.23±0.29%
(events)	2731				
2000 (%)	100%	**21.2±1.1%**	54.7±1.7%	23.9±1.1%	0.165±0.095%
(events)	1814				

Table A.2: Window multiplicities with statistical errors for single ionization with 1 track in a track window (top) and double ionization events with 2 tracks in a track window (bottom).

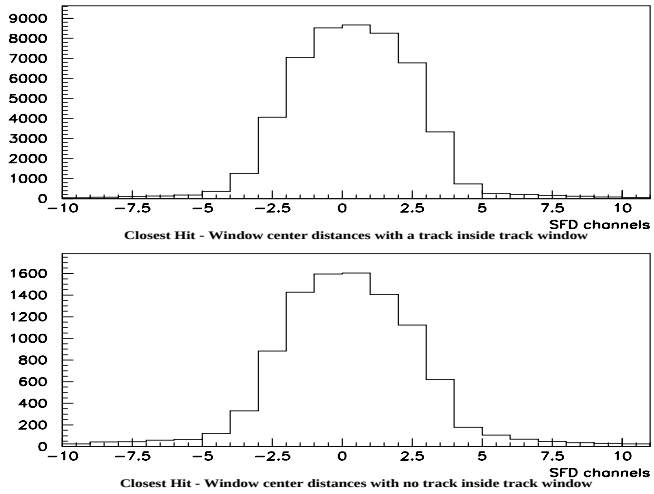

Fig. A.13: Single ionization: closest slab - window center distributions (2001 data).

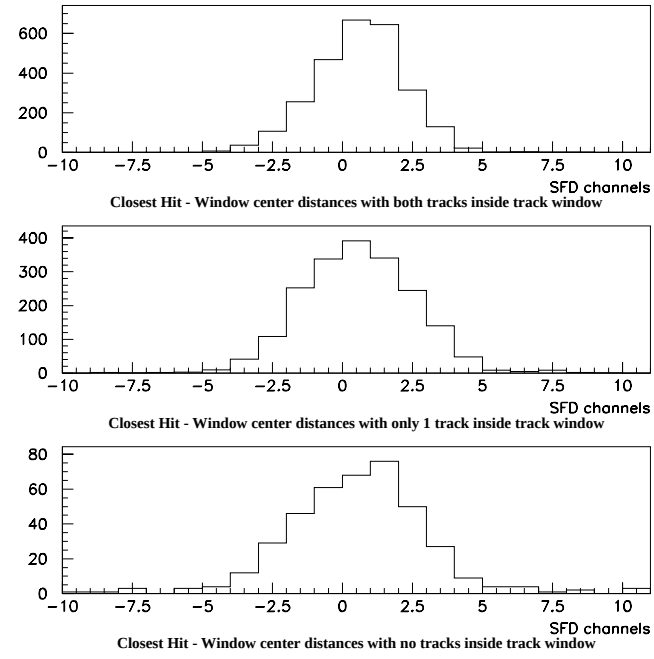

Fig. A.14: Double ionization: closest slab - window center distributions (2001 data).

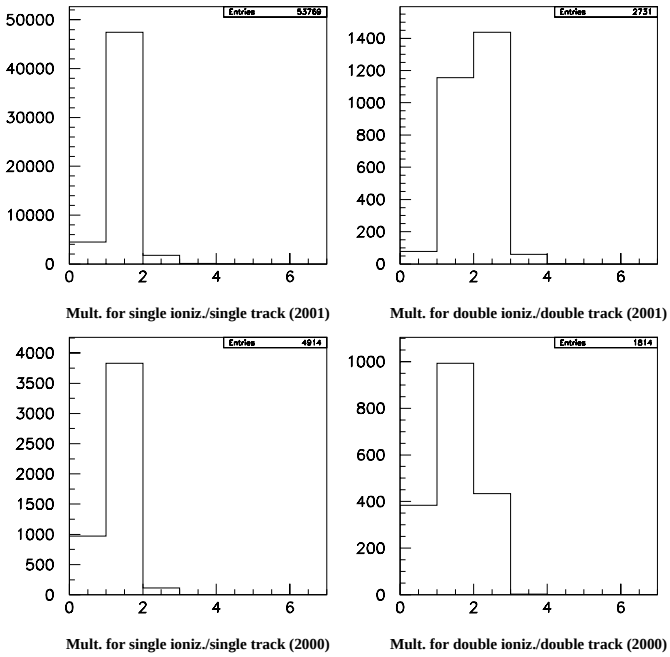

Fig. A.15: Multiplicity inside geometrical windows with the track requirement.

to a large drop in double ionization inefficiency (multiplicity 0) from 7.6% to 2.8% in 2001 and from 30% to 21% in 2000. The effect of decreased SFD thresholds in 2001 can be observed through a relationship between the number of double hits relative to the number of single hits: with the track requirement the number of double hits exceeds that of the singles for 2001 data whereas the opposite is true for the previous year (the time correlated neighboring hit channels were merged into a single hit or not registered at all due to higher threshold values). Lastly, another effect of lower SFD thresholds which becomes more evident with the track constraint, is the increase in the number of double ionization events with multiplicity higher than 2. Such events were registered in 2.23±0.29% of the cases in 2001 as compared to 0.165±0.095% in 2000.

A.5 Conclusions

Since the goal of the experiment is to detect a pair of charged particles, we will summarize the efficiencies obtained with double ionization. By examining prompt events within allowed hit ranges in the SFD satisfying a double ionization requirement in the ionization hodoscope we calculate of the efficiency to detect at least one particle in 2001 run to be about 92% with no track requirement, 97% with one. For double ionization events with 2 track requirement the efficiency of detecting one or two hits with the active area of the SFD is 91% with no track constraints and 95% with the track constraint. The cross-talk (i.e. double hits in SFD with the singly ionized slab in the IH) is observed in 2.2% of the events (with the track requirement on). For the year 2000 the two particle detection efficiency was 70% with and 79% without the track constraint. Cross-talk was close to 0, consistent with higher threshold settings.

Appendix B

Scintillating Fiber Detector Background Study and Simulation.

We present the results of the background study in the x- and y-planes of the scintillating fiber detector (SFD) and describe the method of separating the background into correlated and uncorrelated hits. The simulation based on these results was added to the existing PSC code. Overall simulated SFD performance is compared to the experimental one.

B.1 Separating Particles and Background

We begin by considering a geometric window defined roughly as a projection of the overlap area of two ionization hodoscope (IH) slabs in plane 1 and plane 2 onto the x-plane of the SFD (Fig. 1). An equivalent projection of two IH slabs in plane 3 and 4 onto the y-plane of the SFD is also considered[1]. Due to multiple scattering inside and prior to the SFD the window width is slightly larger than the IH overlap area and is found to be about 10 SFD channels (around 4.4 mm)[2].

[1]For more details on the determination of the geometrical window size see Appendix A.

[2]The geometrical window was analyzed for the old IH slab geometry, with a narrower slab width corresponding to narrower geometrical window for plane 1 and 2 relative to 3 and 4. The application of the same width to plane 3 and 4, therefore, represents a tighter cut on the allowed SFD hits leaving the results unaffected.

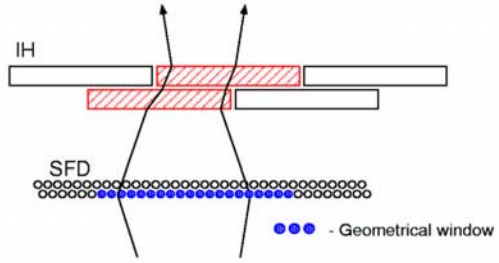

Fig. 1: Geometrical window definition.

In the first part of our analysis we look for a way to separate timewise correlated hits from the uncorrelated ones. To this end we:

1. Select events with a singly ionized pair of overlapping IH slabs in plane 1 and 2 (plane 3 and 4).

2. Find a geometrical window in the x-plane (y-plane) of the SFD that corresponds to this overlap area.

3. Record the time differences between all the hits inside the geometrical window and each IH slab.

This analysis was performed on 2001 minimum bias (VH1·IH) data. Below (Fig. 2) we plot the time differences between the x-plane and planes 1 and 2 of the ionization hodoscope. The mean and the standard deviation of the Gaussian fits to the graphs give us the allowed time interval for the particle to travel between the two detectors. We call SFD hits inside the interval (set to 2σ) *time-correlated* and outside the interval *time-uncorrelated*.

Out of the array of time-correlated (particle) hits we pick one, which we refer to as the *reference hit* (Fig. 3). (This selection is done randomly to avoid topological bias.) Subsequently, an essentially inverse procedure is performed: we look for another hit in the x (y) plane of the SFD, and, if one is located, IH slabs in the first (third) and the second (forth) plane directly across from it are examined. If timing in at least one of the IH slabs is within 2σ from the mean value obtained above (time-correlated signal) and the ADC signal in at least one of the IH slabs is higher than 70, the SFD

hit is ascribed to a particle background. If none of the two slabs satisfy the above conditions, the hit is identified with uncorrelated background.

We are now able to plot the distances between the reference hit and the rest of the hits in the event along with the corresponding differences in time and classify them according to the background type (Fig. 4).

Qualitatively the two types of background are quite different. The uncorrelated background hit distance graph shows an approximately triangular background shape pointing to a uniform hit distribution, the conclusion supported by the hit map in Fig. 5. A very sharp peak on both sides of the reference hit gap for both the uncorrelated and correlated events corresponds to a single particle crossing two SFD channels, in addition to a certain amount of crosstalk. The presence of correlated particles contributes to a broad peak for the correlated events.

B.2 Simulating SFD Noise Response

The simulation takes as its input the hits corresponding to the generated par particle tracks and the TDC signals provided by the output of the peak-sensing circuit (PSC) simulation. The algorithm for the simulation is outlined in the flow chart below (Fig. 6). The task of the background subroutine is to jitter the original TDC counts and provide additional background hits along with corresponding TDC signals in the x and y-planes of the SFD based on the results above. The call to the background procedure can be turned on or off by setting BackgroundSimuMC to True or False in the FFreadInput cards (to be available in Ariane version 304-21).

Below we show an example of the typical PSC output in terms of multi multiplicity, hit and TDC distributions for accidental $\pi^+\pi^-$ events. If the background simulation is enabled, the subroutine begins by smearing the TDC signal based on the time jitter obtained from real data. Time jitter distribution was found by considering an SFD hit generated by a single e^+ track in the minimum bias (VH1·IH) run (Fig. 8). It is obtained by subtracting the SFD TDC signal from the mean signal in the vertical hodoscope (taking into account VH's own jitter). The action of the simulation is to simply generate a jitter value for each hit and add it to the unjittered time provided

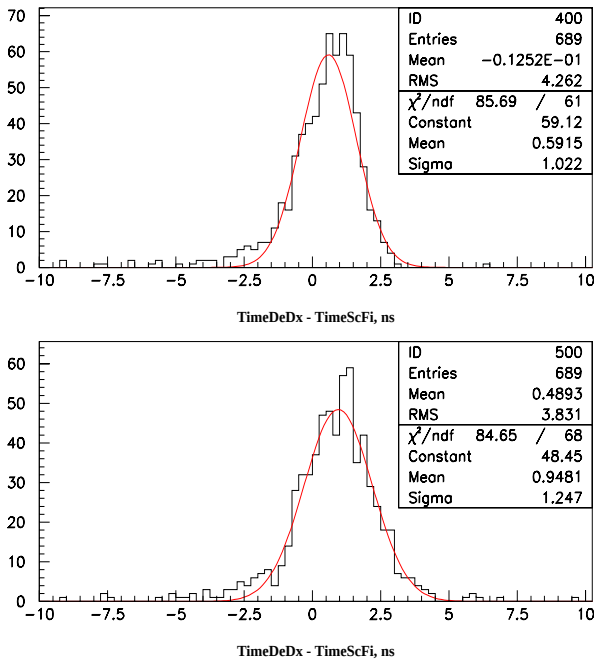

Fig. 2: Time correlations between x-plane of the SFD and plane 1 and 2.

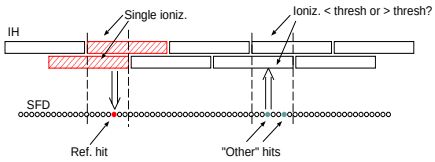

Fig. 3: Separating correlated and uncorrelated background.

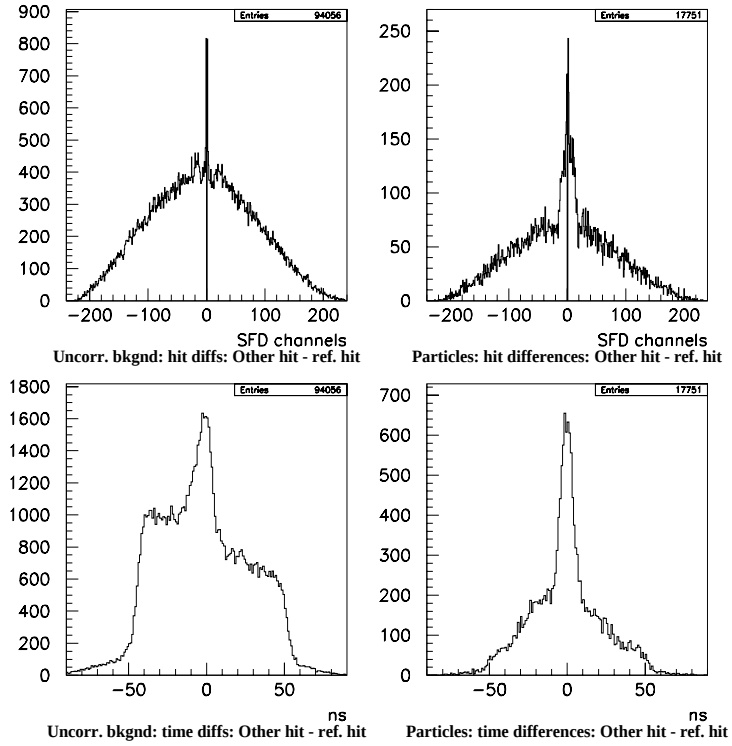

Fig. 4: Time and hit differences for correlated and uncorrelated background.

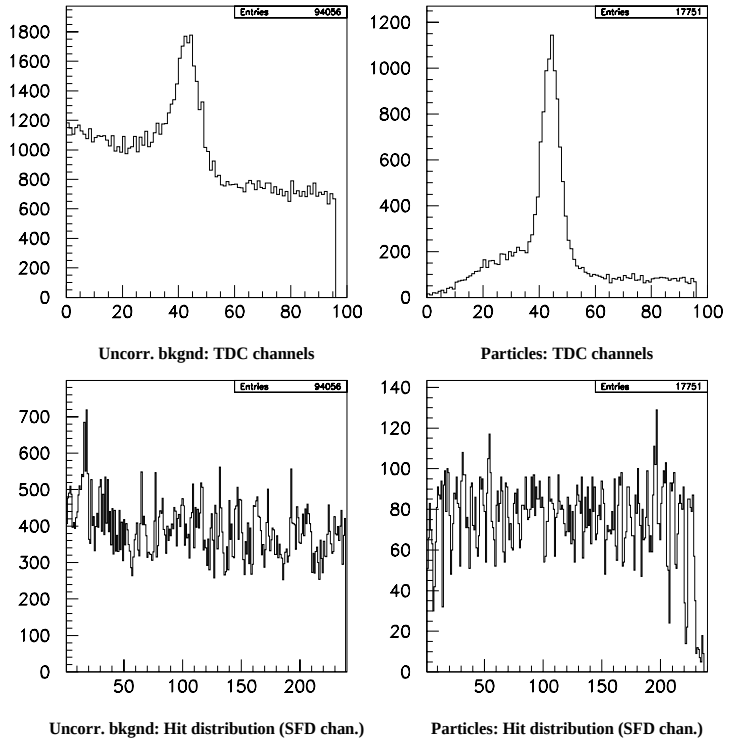

Fig. 5: Time and hit distributions for correlated and uncorrelated background.

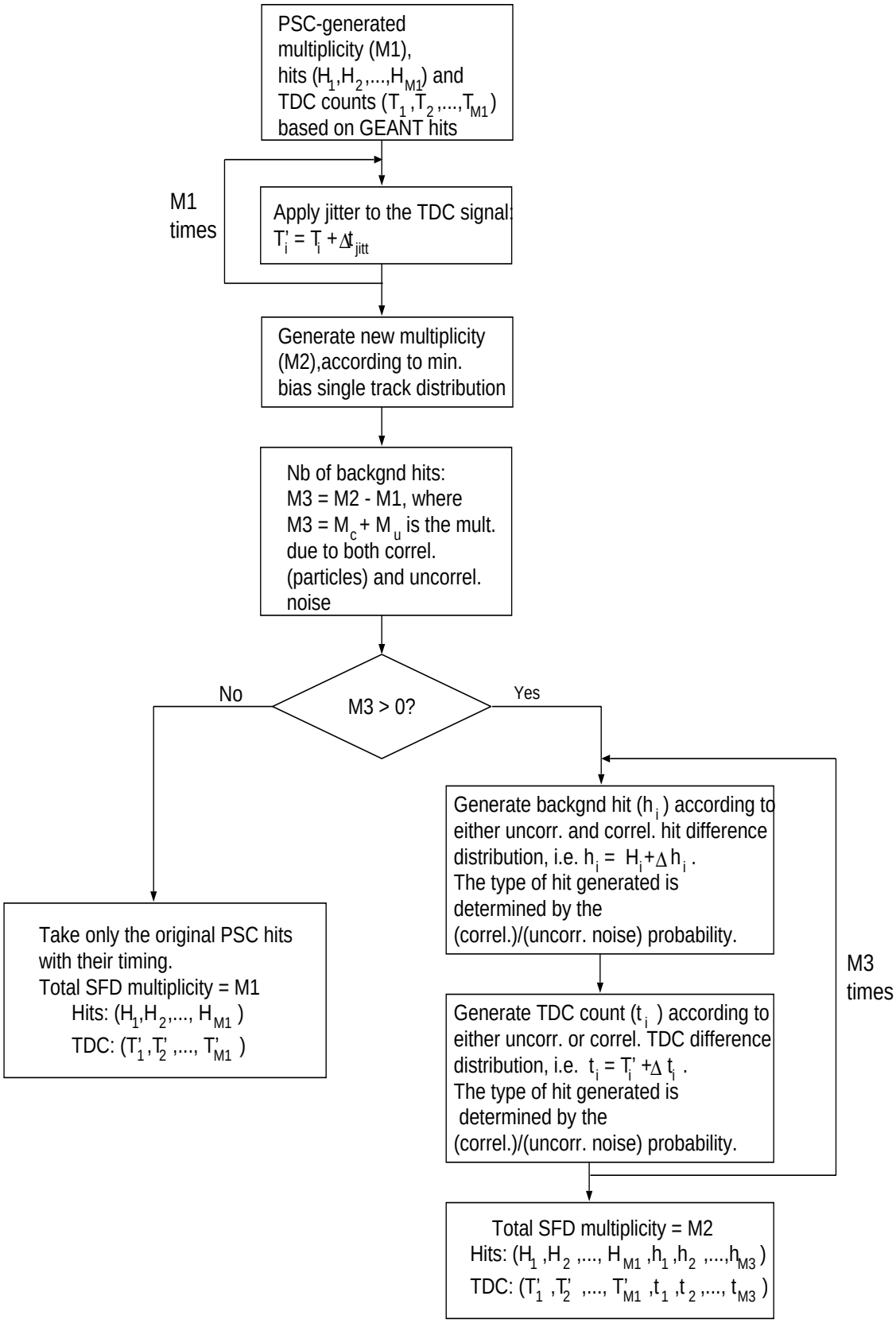

Fig. 6: SFD background simulation algorithm.

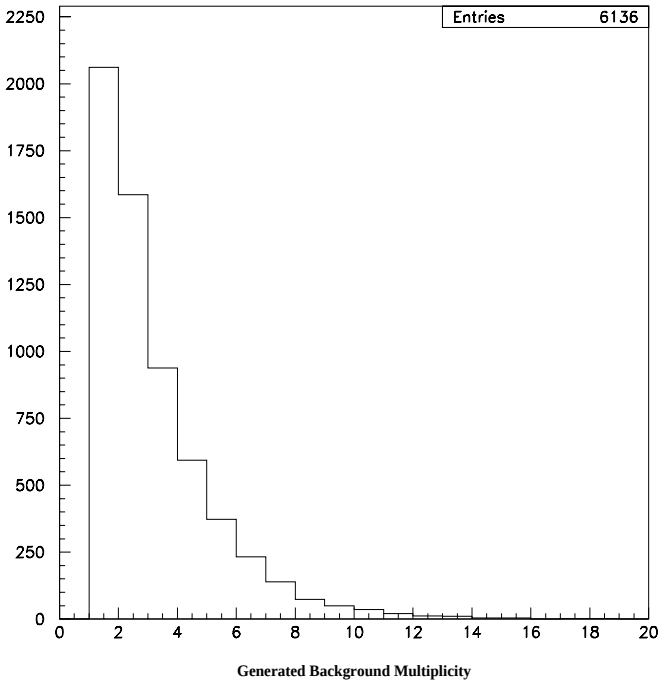

Fig. 7: Generated background multiplicity.

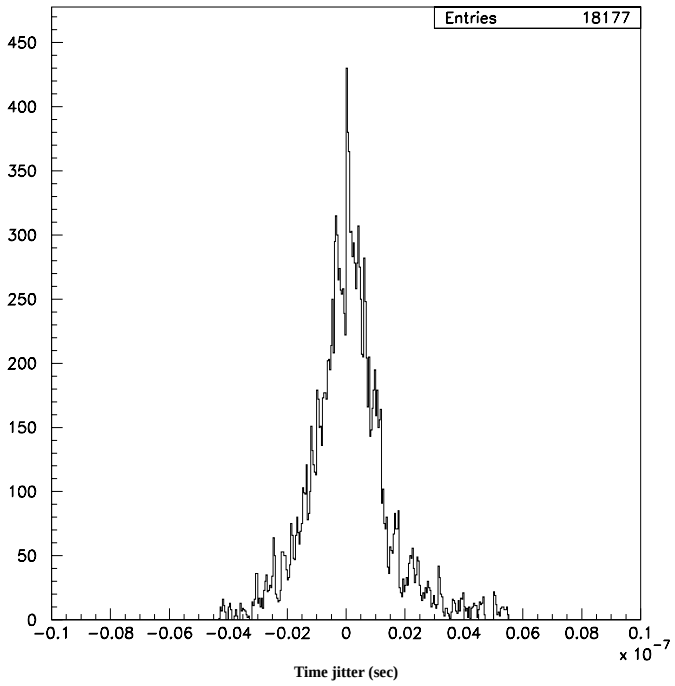

Fig. 8: Generated jitter in SFD timing.

by the PSC. This time is used in the subsequent background simulation.

The code is designed to detect whether the input event was generated by a single particle or a double particle (such as an atomic or a Coulomb pair) event. The single particle multiplicity for the x and y-plane was found from the single (π^+) track minimum bias results. If a double track event, such as $\pi^+\pi^-$ pair, is detected, every multiplicity bin except 0, 1 and 2 are multiplied by a factor of 2. Following that, the background multiplicity (designated by M3 in Fig. 6) is generated as a result of subtraction of the PSC-generated multiplicity Ml from the overall multiplicity M2.

If M3 is less or equal to 0, the subroutine exits having executed only the time smearing. Otherwise, it proceeds to the next step of choosing whether the newly found hit is uncorrelated or correlated. The type of hit to be generated is determined by the probability ratio of uncorrelated hits to particles (calculated from the ratio of the number of entries of both types). This ratio was determined to be roughly 3:2 for the x-plane and 3:4 for the y-plane of the SFD based on minimum bias data. Once the choice is made, the subroutine produces the hit-PSC generated hit difference based on the distributions in Fig. 4. If several PSC hits are present, only one hit is selected at random.

Analogous procedure is used to find the associated TDC information. Since it is already known whether the hit comes from the correlated or uncorrelated noise, the only remaining step is to generate a relevant TDC count difference (based on Fig. 4), from which the TDC count is found. In the final step the generated background multiplicity, hit channel numbers and the timing information are passed back to the calling subroutine.

B.3 Comparison of the simulation and experimental results

Below we compare the results of the simulated performance of the SFD for generated and real data pion pair events. Real data events came from the T1$\pi^+\pi^-$-coplanarity run with no imposed cuts. The generated events were obtained from the

same run, with the input file containing lab momenta and time differences between two pion tracks. This input was run through GEANT and, finally, processed by Ariane[3].

In Fig. 9-12 we plot multiplicities, hit maps and timing for both sets of data. These plots show a good overall agreement between both types of data. Normalized multiplicity distributions differ only by a few percent for multiplicities higher than 2 and are close to within one percent for multi multiplicities higher than 2. Some differences may also be observed in the shape of y-plane distributions and the timing. However, we find that the slight deviations from the real life SFD response do not have any adverse effect on the quality of the track reconstruction.

In Fig. 13 we compare relative momentum distributions for accidental events (-15 to -5 ns VH time difference) from the $\pi^+\pi^-$-coplanarity run and the generated accidentals (input file contained lab momenta and timing for the accidentals in the -15 to -5 ns time interval). Evidently, we are able to reproduce the desirable flatness of the ratios of the relative momenta of the accidental pairs (except for a slight enhancement in the low Q region of the y-distribution attributable, perhaps, to the differences between artificially generated accidentals and real data).

B.4 Influence of the background on the Q reconstruction

Finally, we used our simulation to investigate the effect of background on the relative momentum reconstruction of atomic, coulomb and accidental pairs. We use generated pionium and coulomb pairs (both input files provided by Cibran Santamarina) and accidental pairs (input file containing lab momenta and time differences between the two pion tracks was produced from the accidentals in the -15 to -5 ns time interval in the T1$\pi^+\pi^-$-coplanarity run) and compare the Q-distributions with and without background (with only PSC active) (Fig. 14-17). The ratios of the

[3]We used 'PrshMuFinder' subroutine to reduce the muon background and thresholds of 62 ADC channels in the positive arm and 75 in the negative to reduce the e^+e^- back ground.

distributions are flat in the low momentum region (from -2 to 2 MeV), with background contribution evident in longer tails, which are due to mismatched track-hit assignments. We conclude that:

1. Adding background does not reduce the efficiency of the reconstruction. All the events simulated without the background are also reconstructed when the background is added.

2. As is evident from the ratios of the relative momenta with and without background, relative momenta distributions are minimally distorted by the added background. To make the difference more quantitative, one can also plot the differences per event between the Q's with and without the added background (Fig. 15). The deviations from the background-free values are all of the order of only a few tens of keV, and which, taking into account the comparable resolution of the SFD, are compatible with zero.

B.5 Conclusions

Correlated and uncorrelated background in the SFD was analyzed. The results of the analysis were used in constructing the background simulation for the SFD. With the background simulation active, we compared its output (multiplicity, hit map and timing) to the real data. Relative momenta reconstruction was tested on the accidentals for both types of data. The response of the simulation was found to be in good agreement with experimental results. By considering atomic pair events with and without the background we found that the influence of the background on the Q reconstruction is minimal.

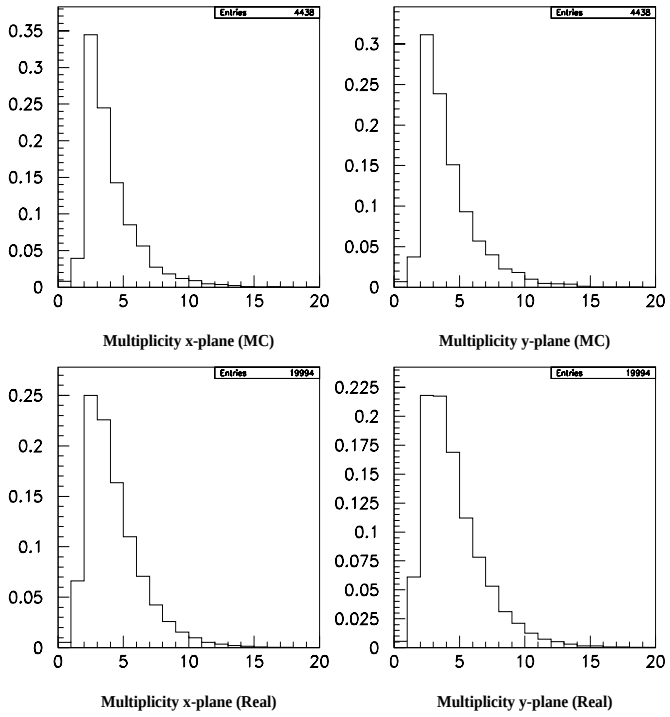

Fig. 9: Multiplicities, normalized to 1 (top: Monte Carlo events, bottom: real data).

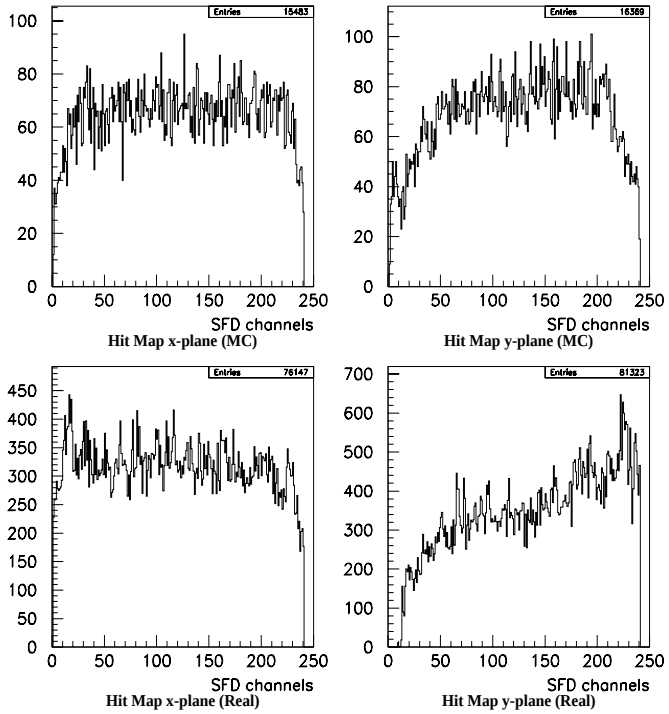

Fig. 10: Hit maps (top: Monte Carlo events, bottom: real data).

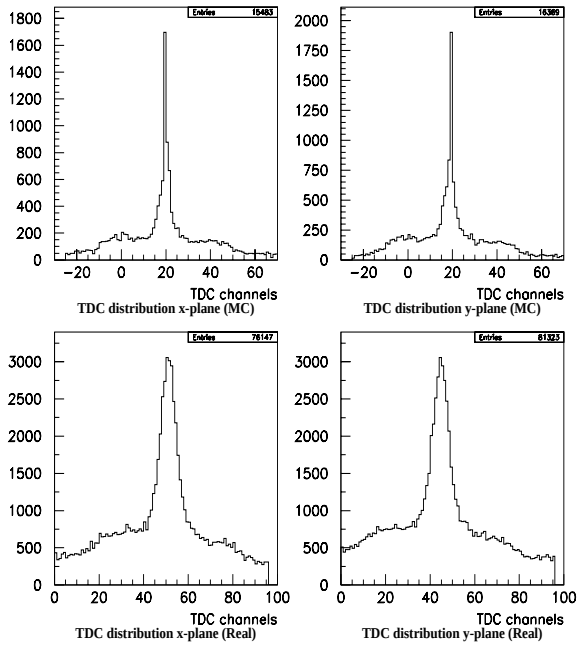

Fig. 11: TDC signals (top: Monte Carlo events, bottom: real data). Note that the real data signals are shifted relative to the simulation due to delays in electronics.

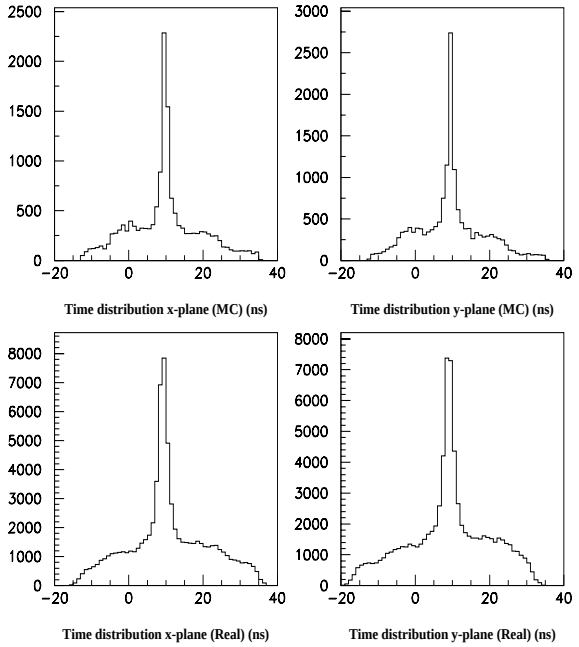

Fig. 12: Timing (top: Monte Carlo events, bottom: real data).

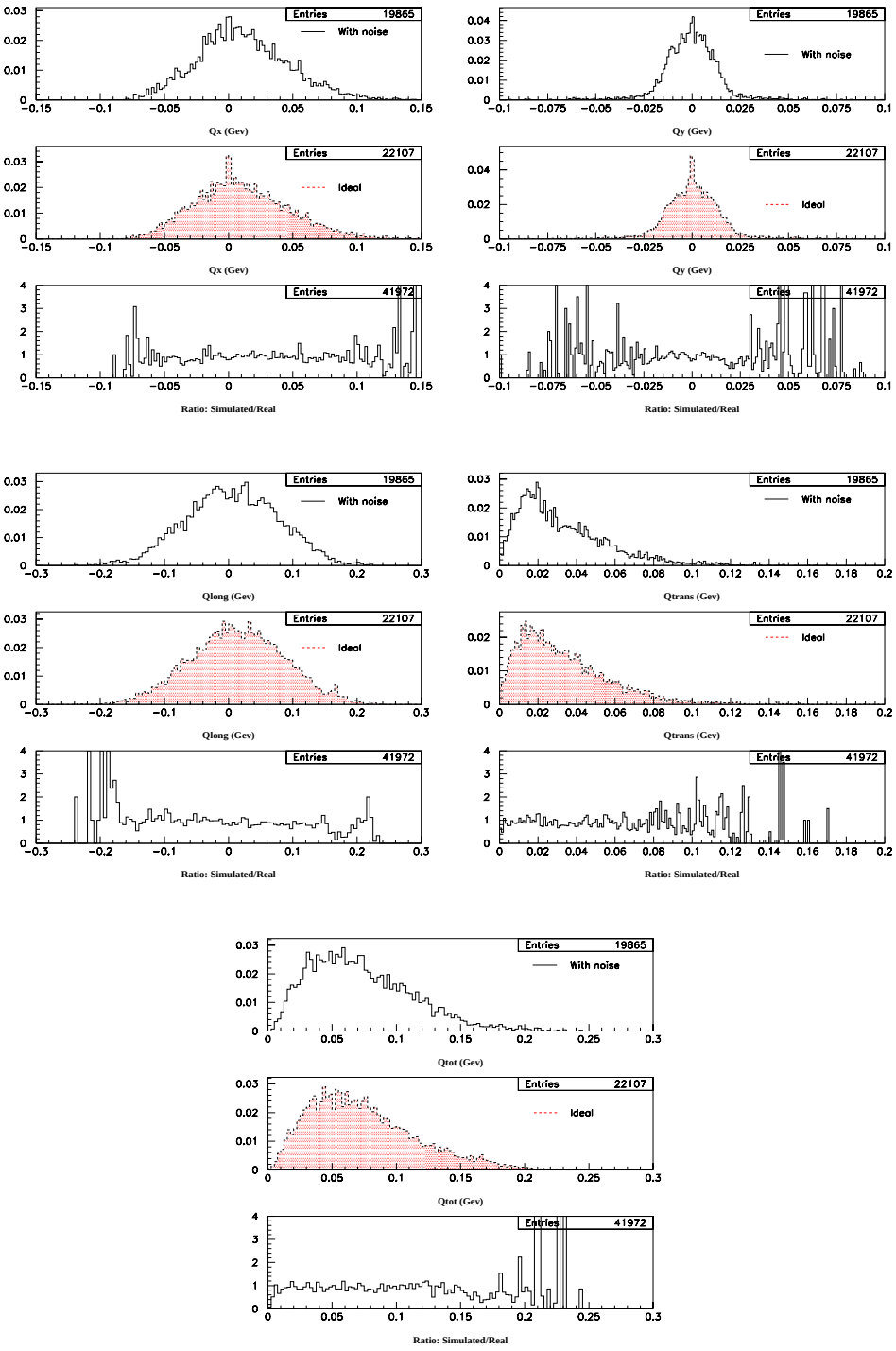

Fig. 13: Relative momenta for simulated and real accidental $\pi^+\pi^-$ pairs with their corresponding ratios. The flatness of the ratios indicate that the SFD simulation is working correctly.

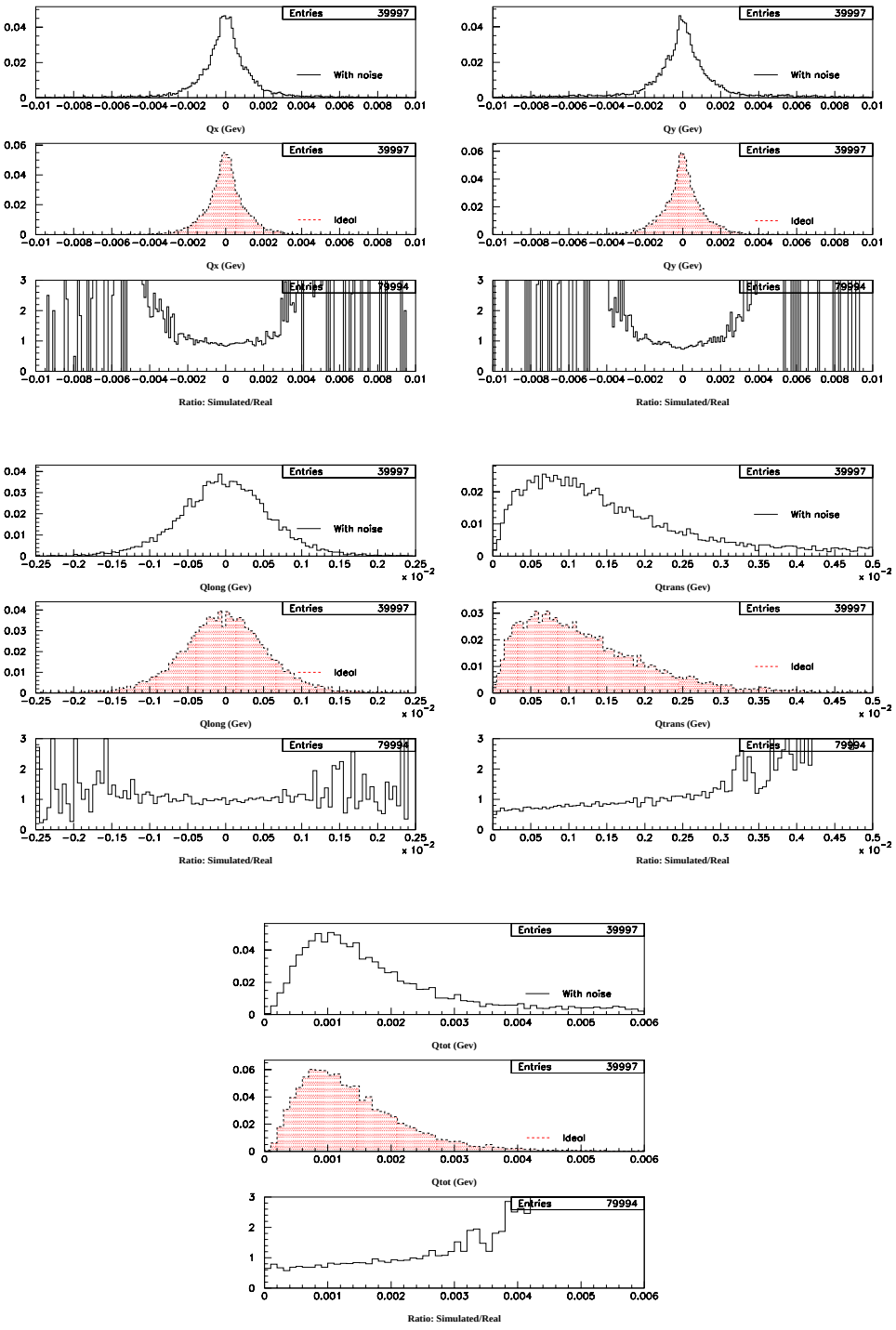

Fig. 14: Relative momenta of atomic pairs and ratios with and without the SFD background. The ratios are flat and the original number of events is preserved with the background on.

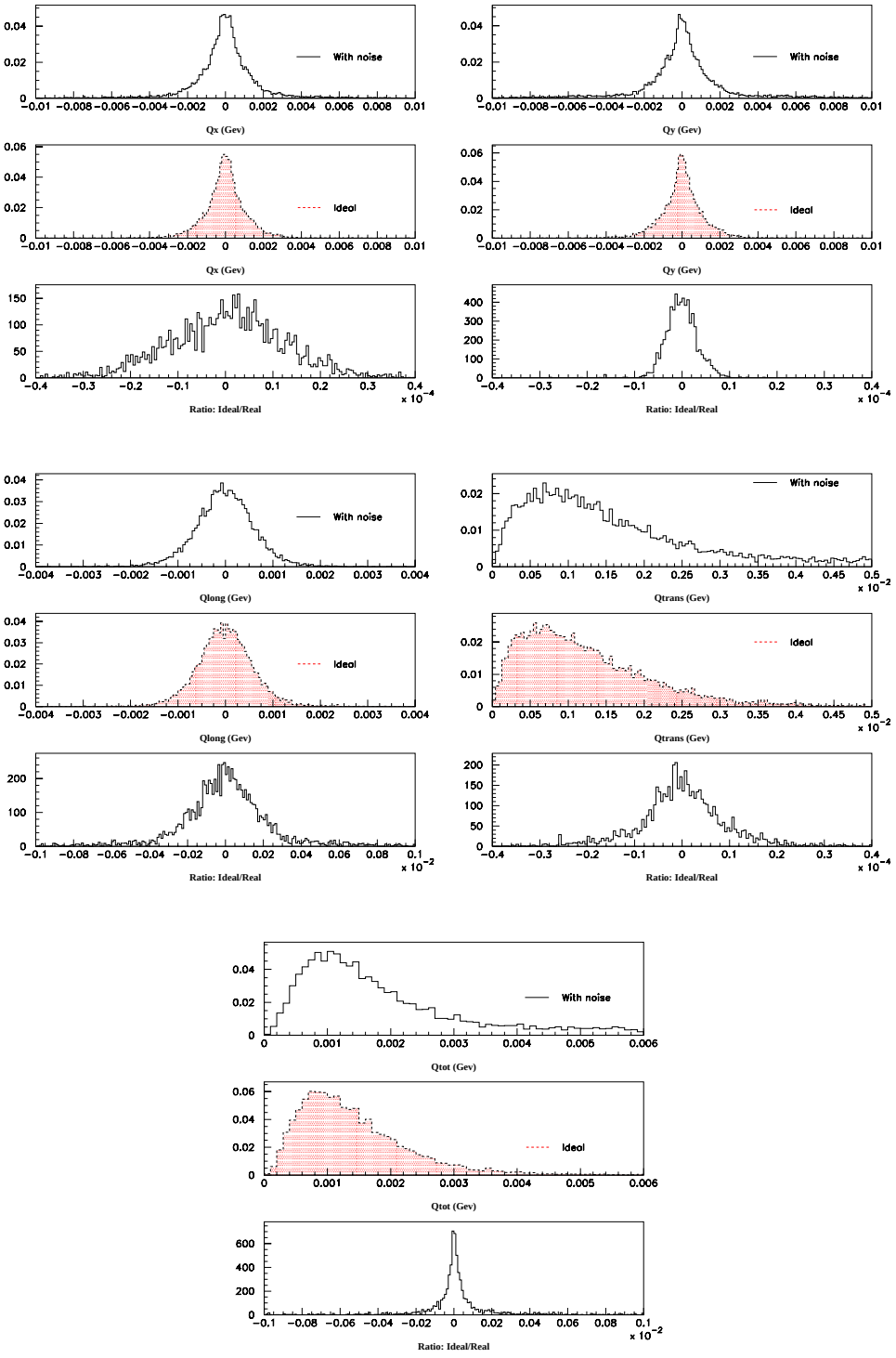

Fig. 15: The deviations of the relative momenta per event with background included relative to the background-free values are small ($A_{2\pi}$ sample).

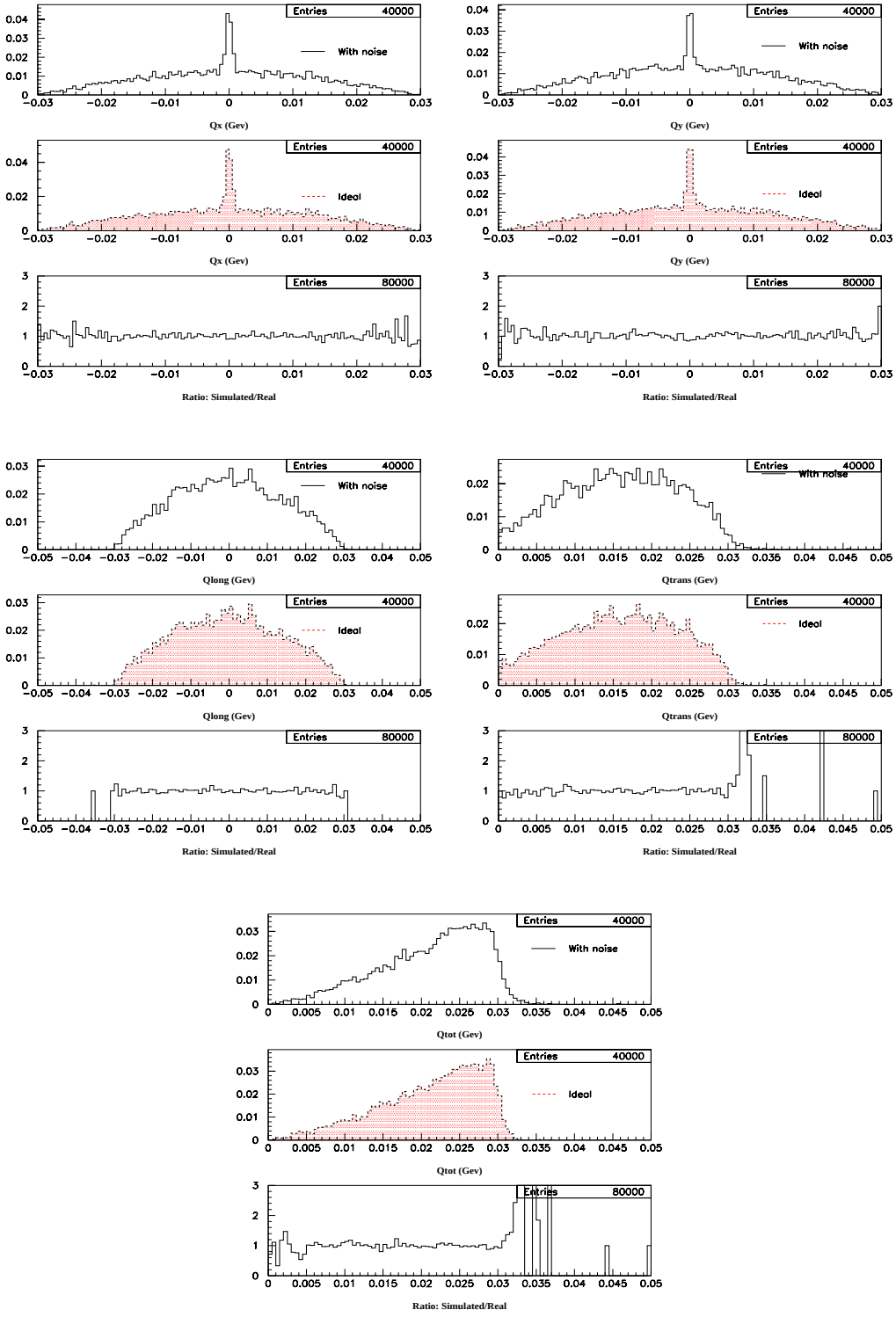

Fig. 16: Coulomb pairs with and without background.

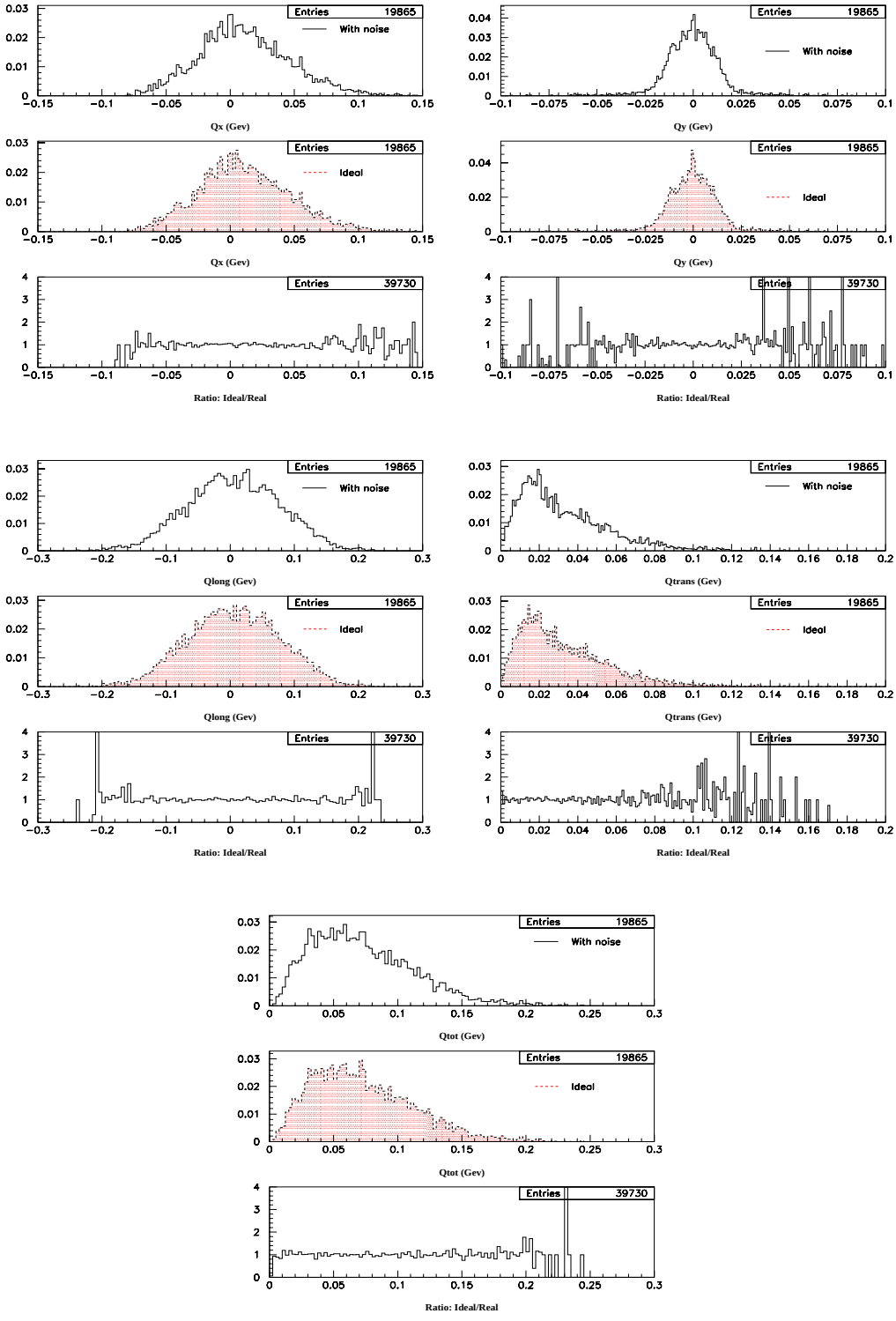

Fig. 17: Accidentals with and without background.

Appendix C

MC-Generated Single and Multilayer Backgrounds

In the plots below we justify the claim (found in Chapter 6) that the Monte Carlo backgrounds for the single and multilayer backgrounds are, indeed, identical. All single and multilayer distributions have been normalized to 1.

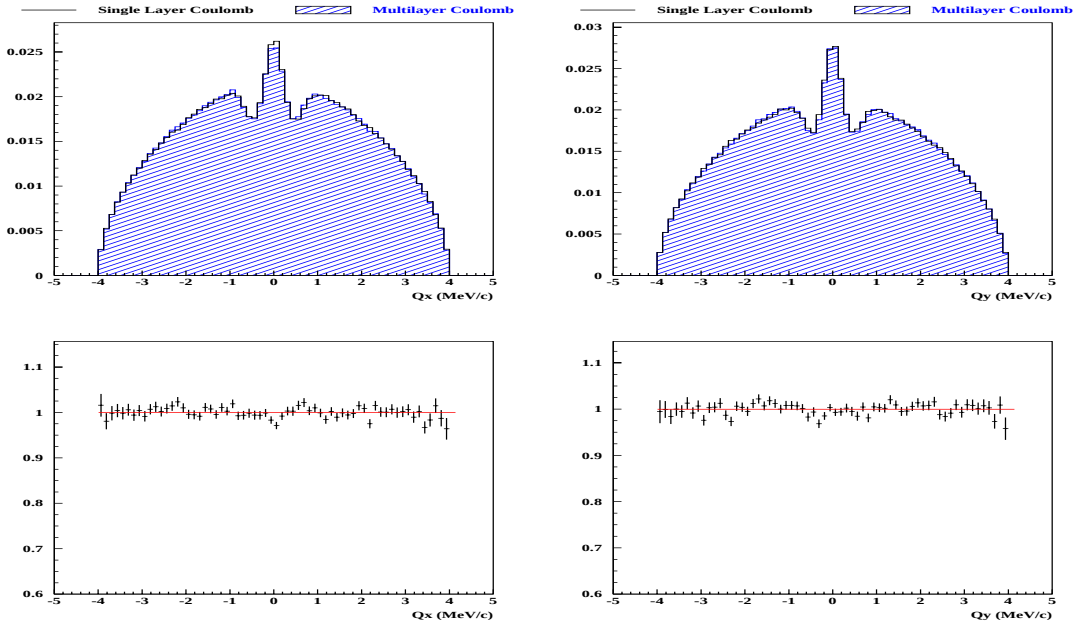

Fig. C.1: Q_x and Q_y distributions for single and multilayer *Coulomb* events with corresponding ratios (below).

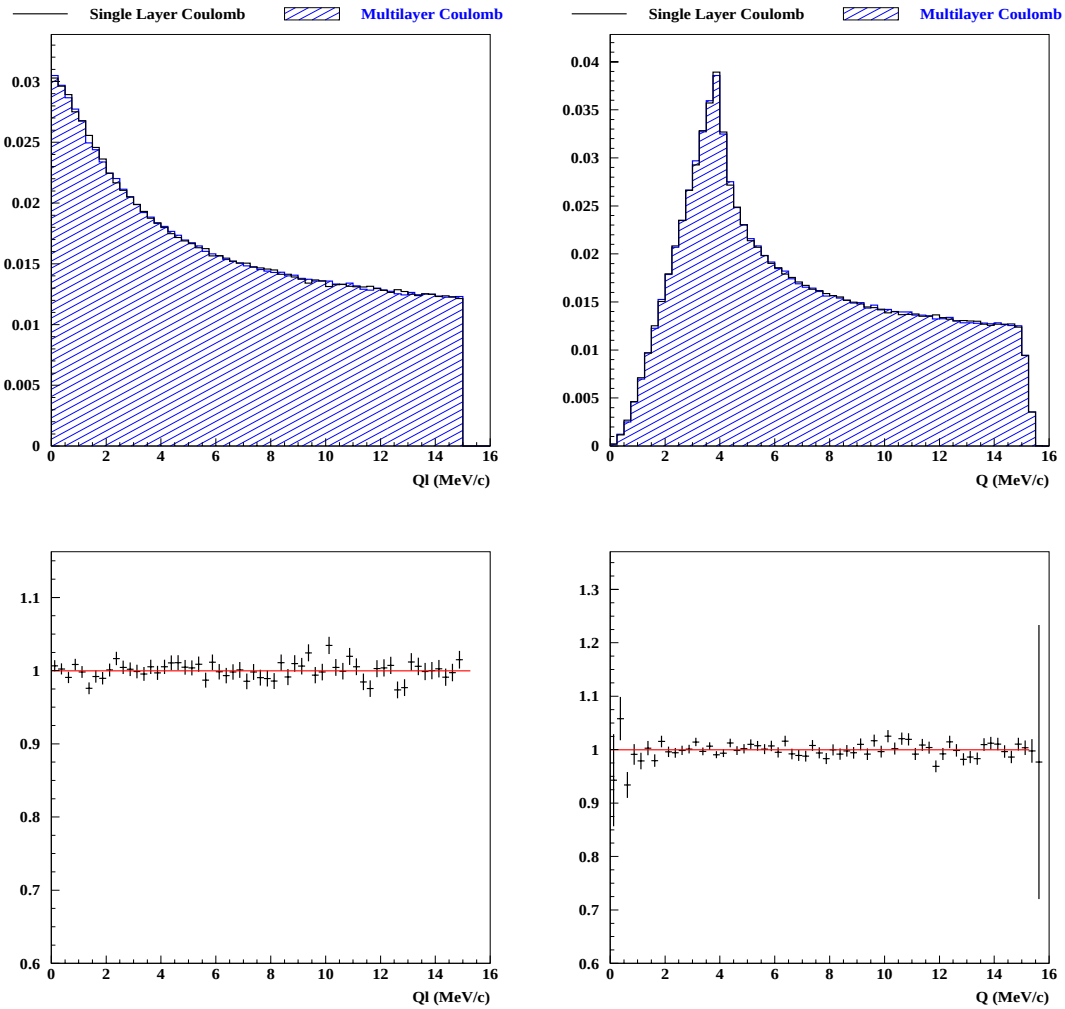

Fig. C.2: Q_l and Q distributions for single and multilayer *Coulomb* events with corresponding ratios (below).

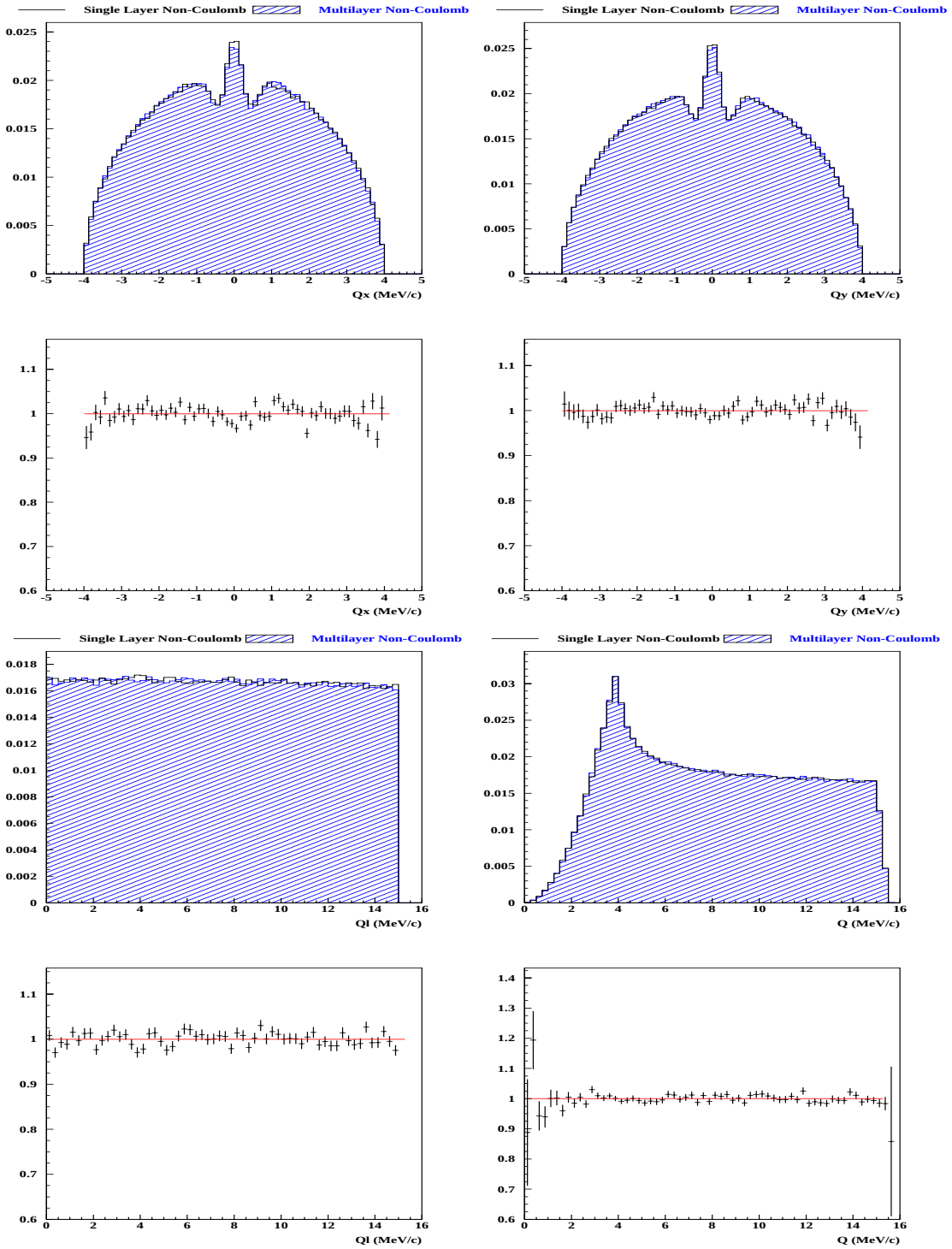

Fig. C.3: Q_x, Q_y, Q_l and Q distributions for single and multilayer *non-Coulomb* events with corresponding ratios (below).

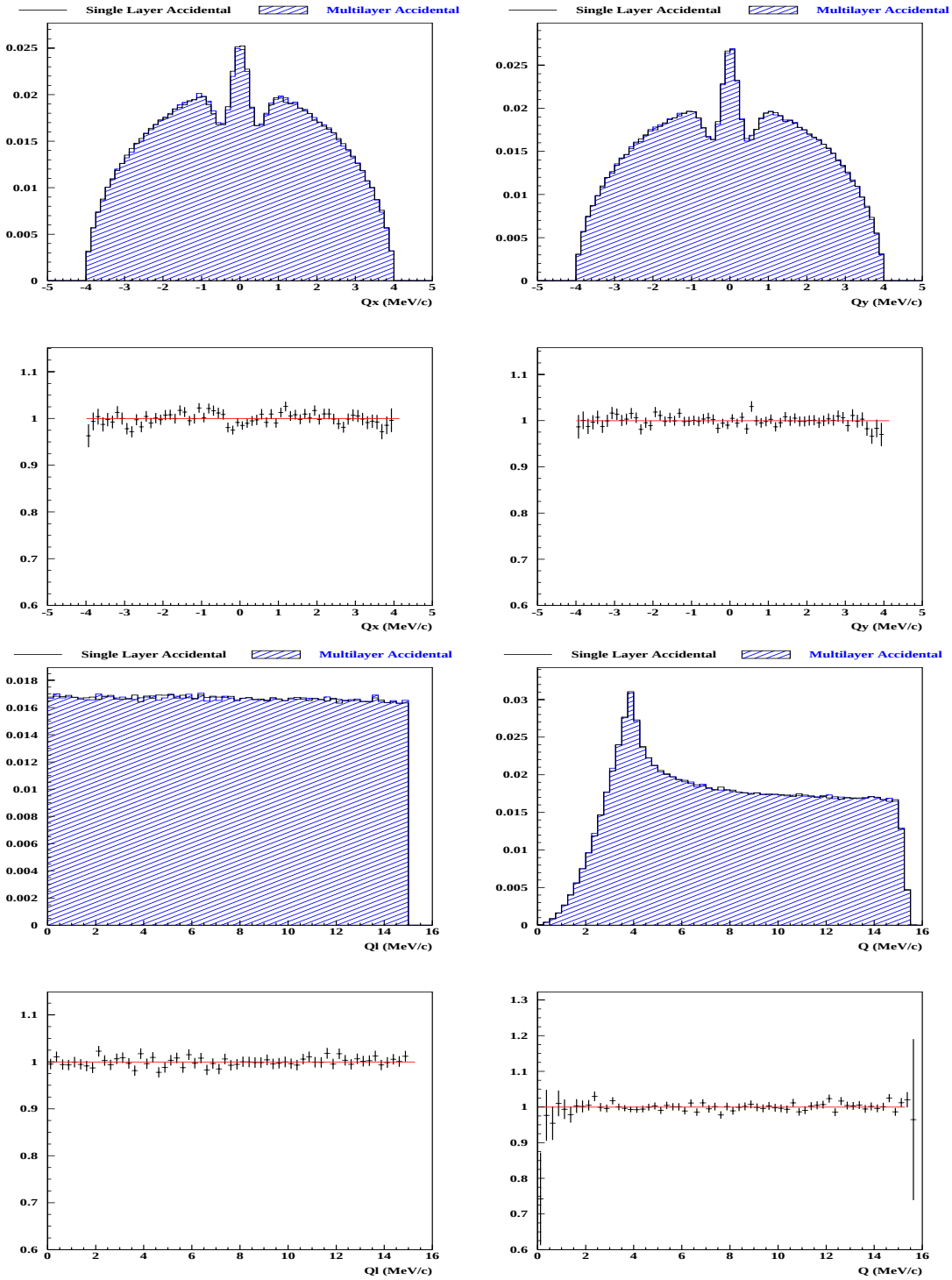

Fig. C.4: Q_x, Q_y, Q_l and Q distributions for single and multilayer *accidental* events with corresponding ratios (below).